Searches for rare exclusive Higgs boson decays to a meson and an associated photon with the ATLAS detector

James Harry Broughton

Thesis submitted for the degree of
Doctor of Philosophy

Particle Physics Group,
School of Physics and Astronomy,
University of Birmingham.

November, 2018

ABSTRACT

Searches for the Higgs boson decaying into a meson and an associated photon are presented using $\sqrt{s} = 13$ TeV proton-proton collision data collected by the ATLAS experiment during LHC Run II in 2015 and 2016. No significant excess of events is observed above the expected backgrounds. 95% confidence-level upper limits on the branching fractions of the Higgs boson decays to $J/\psi\,\gamma$, $\psi(2S)\,\gamma$, and $\Upsilon(nS)\,\gamma$ of 3.5×10^{-4}, 2.0×10^{-3}, and $(4.9, 5.9, 5.7)\times10^{-4}$ $(n = 1, 2, 3)$, respectively, are obtained assuming Standard Model Higgs production with 36.1 fb^{-1} of data. Analogous limits on the branching fractions of the Higgs boson decays to $\phi\,\gamma$ and $\rho\,\gamma$ of 4.8×10^{-4} and 8.8×10^{-4}, respectively, are also found using up to 35.6 fb^{-1} of data at $\sqrt{s} = 13$ TeV.

In the next decade, the LHC will undergo an upgrade to increase the delivered instantaneous luminosity, which will aim to collect 3000 fb^{-1}of integrated luminosity over its lifetime. With this improvement the searches for Higgs boson decays into a meson and an associated photon will have a sensitivity closer to the Standard Model predicted branching fractions. The ATLAS detector will be upgraded to sustain performance with the higher rate of collisions. The University of Birmingham is among a consortium of facilities that irradiate and test prototype silicon sensors intended for the upgrade of the ATLAS detector. This thesis also presents early results during the commissioning of the sensor test system.

DECLARATION OF AUTHOR'S CONTRIBUTION

The contents of this thesis represent the work I have performed and contributed to over the course of my post-graduate studies. Much of this work has been reliant on the efforts of other people.

All results published by the ATLAS collaboration are founded upon the endeavours of thousands of people, in the design, construction and operation of the ATLAS experiment, as well as the LHC, and the development of shared tools to simplify the analysis procedures. In 2016, I was fortunate to have the opportunity to contribute to the operation of the ATLAS experiment in a data quality monitoring role.

Chapters 2, 3 and 4 detail background physics and detector information of relevance to the thesis. Chapter 5 describes my contribution to a project at the University of Birmingham, developing a prototype silicon sensor test system, to diagnose issues with the Birmingham Medical Cyclotron and to have the university commissioned as an irradiation site. My role was specifically in the construction of the test system and the measurements of the sensors between September 2014 and November 2015, whilst several other collaborators provided guidance and irradiated the sensors in the cyclotron.

The main focus of this thesis is on the Higgs and Z boson decays to a meson and a photon, detailed in Refs. [1–3]. For these analyses, I worked in a small analysis group, in which we shared tools and each had different roles. The $H(Z) \to \psi(kS)\,\gamma$ and $H(Z) \to \Upsilon(nS)\,\gamma$ analyses, which are described in the most detail in Chapters 6 and 7 of this thesis, were almost entirely my own work. I used and built upon tools developed by the analysis team, and benefited from their advice and guidance throughout. For the $H(Z) \to \phi\,\gamma$ analysis, which is described in Chapter 8, the roles in the analysis were shared among the analysis team. My primary focus was

on the initial analysis development, calculation of efficiencies and production of validation plots. The background model development and statistical analysis were performed by other members of the team. Finally, Section 8.6 details an extension to the $H(Z) \to \phi\gamma$ analysis and the inclusion of a search for $H(Z) \to \rho\gamma$. My contribution to this analysis was minor, with the calculation of efficiencies and the effects of polarisation on the kinematic acceptance. This section is included in the thesis to give a complete picture and is described in more detail in the thesis of the main analyser in Ref. [4].

Chapters 6, 7 and 8 use some verbatim text from my publications in Refs. [1, 2].

ACKNOWLEDGEMENTS

It is not lost on me how fortunate I am to have a great number of people to thank for helping me achieve my ambitions of, if all goes according to plan, earning a Doctorate in Particle Physics. Though I could most definitely write a long-winded thesis of praise and thanks to every single person that has positively impacted my PhD journey and experience, which they would all deserve, I will attempt to consolidate all of that gratitude in the next few paragraphs, hopefully conveying just how appreciative I am for the unfaltering help and support I have received.

I would like to begin by thanking the STFC for their financial support as, without it, this PhD would never have been possible. Their funding has enabled me to participate in informative, exciting particle physics projects, as well as the opportunity to directly experience the operation of international experiments. Notably, I would like to thank my analysis team, comprised of Andy, Chris, Kostas and Rhys, as they have expended a considerable amount of their time in guiding and assisting me through several projects. Much of my analysis work has been dependent on their contributions and I want them to know that their input has been recognised and valued by me throughout the years. A special thanks must be extended to Chris, my primary supervisor, for his patience, understanding and support throughout my years as a PhD student. He has frequently gone beyond the call-of-duty to advise and help me, and I am greatly indebted to him. I would also like to give thanks to John Wilson and Phil Allport for their encouragement and guidance in the first year of my PhD.

I would like to continue by acknowledging and highlighting those who I have shared an office with: Benedict, Muddly, Javier, Mark, Matt, Andy, Alasdair, Kendrick, Briglin, Elliot, Russell, Jack, Rob, Gov, Dan and Nandish, for both their academic help and insight, and for facilitating a friendly environment to work in. I wish them all tremendous success in completing their PhDs, as well as embarking on incredible careers with incredible, well-earned, opportunities. I can only hope they found me

as helpful as I found them.

Those that know me well know that I have a special place in my heart for The Dilshad restaurant, as they have hosted our curries since I started my PhD, as well as introducing me to superior-tasting curries at the start of my undergraduate studies, eight long years ago. As well as the great food, I have a long list of names to thank for regularly being the good company that made the curries so enjoyable throughout the years: Alasdair, Andy Foster, Andy Chisholm, Benedict, Dan, Jack, John, Katy, Muddly, Robbie, Russell, Sammy, Tim, Zoe and, of course, Sam and the Dilshad staff.

As current World Champions of UK Particle Physics Football (and as 2016 winners too!), I want to give thanks to all of the team members over the years. Firstly, thank you for having me as team captain and not forming a mutiny, despite Andy's attempts. Secondly, thank you all for the effort at each tournament and setting an example I can only hope the future generations of Birmingham students will continue. Finally, a big thank you for the entertainment in the build-up, on-the-day, and post-football celebrations/commiserations. I will remember it all fondly and I feel lucky to have shared the experience with all of you.

Over the course of this PhD, I hope I have made some friends for life, most notably the BAPS crew: Alasdair, Alison, Andy, Abby, Chisholm, Sarah, Katy, Tim, Muddly and Sammy. They have all been nothing short of fantastic, genuine friends to me. I hope our friendships continue long into the future, or at least as long as it takes for me to win the FPL league, so probably forever. A special thanks to Andy Foster for living with me for a year in Geneva and a year in Birmingham, and to Briglin for the 3-months in Geneva. I hope I was not too much of a burden to live with and that they enjoyed themselves as much as I did during that time.

A big thank you to my Abingdon friends: Aaron, Andrew, Chris, Richard and Shaun-who have always made home feel like home and who I can always rely on to give me a break from working. I hope in the future I will be able to live closer to you all, as eight years away has been much too long already. I would also like to express my gratitude to my extended family, who have continuously motivated and inspired me over the years.

I want to thank my partner, Tammy, for her support in the final months of my PhD, and especially in the writing of this thesis. I have loved every minute of being with her and I can only hope we have a long and bright relationship into the future.

Last, but definitely most importantly, I want to thank my mum, dad and brother, who have supported me through, not only all of my years of University, but all the days of my life. They have advised and encouraged me throughout this journey with great insight and wisdom, never failing to show love and respect, and I will remain eternally grateful for their presence in my life. I will always cherish the experiences mentioned above and I am thankful to have already come this far, as I remain excited for what is to come in the future.

You can't put a limit on anything.
... The more you dream, the further you get.

- Michael Phelps

Contents

CHAPTER 1

INTRODUCTION

Since the first physics data taking began at the Large Hadron Collider (LHC) in 2010, the "A Toroidal LHC Apparatus" (ATLAS) experiment has greatly contributed towards our understanding of particle physics. Just over two years later, the ATLAS and Compact Muon Solenoid (CMS) collaborations published the first observation of a Higgs boson with a mass, m_H, around 125 GeV [5, 6]. This discovery was the culmination of decades of progress and results from other experimental facilities. Nevertheless, much of particle physics has still to be fully understood.

Our current best understanding is described by the Standard Model of particle physics (SM). There are a number of observations unexplained by this model, such as the existence of dark matter, the measurement of non-zero neutrino mass, and the asymmetry of matter to antimatter in the observed universe. Many different models have been theorised that would help give an explanation for these observations. They also tend to have characteristics that would impact the properties of the particles that have already been observed. One such particle that is highly sensitive to Beyond

the Standard Model (BSM) theories is the Higgs boson. Currently, not all the Higgs boson's properties and couplings to other particles have been precisely measured and a significant effort from the ATLAS collaboration is devoted to constraining these to help test the different models. The main discussion of this thesis is related to several different analyses [1–3] that probe the couplings of the Higgs boson to quarks.

Chapter 2 provides an overview of the current understanding of particle physics, focussing in particular on the Higgs boson and the relevant theoretical background. Chapter 3 gives details of the LHC and the ATLAS experiment. An outline of the methods used by ATLAS to reconstruct physics objects is given in Chapter 4. Chapter 5 reports a project performed at the University of Birmingham to irradiate and test silicon sensors for use in the future development of the LHC detectors. The silicon sensors must be able to perform adequately after the expected total dosage of the LHC, which the Birmingham Medical cyclotron is capable of providing within a short time frame.

The physics analyses are described in Chapters 6, 7 and 8, which focus on the Higgs boson decaying exclusively into a meson with an associated photon. Two distinct periods of running have taken place at the LHC, a period between 2009 and 2013 where the LHC produced $\sqrt{s} = 7$ and 8 TeV beam collisions that is referred to as Run I, and a Run II period between 2015 and 2018 where beams collided at $\sqrt{s} = 13$ TeV. The results in this thesis were obtained using data collected during the Run II operation of the LHC. The principle analysis of this thesis, where the mesons searched for are the $\psi(kS)$ (where k=1,2) and $\Upsilon(nS)$ (where n=1,2,3), is presented in Chapters 6 and 7. Chapter 8 primarily describes a search for the Higgs boson decaying into a ϕ meson and an associated photon, with a short section describing an extension of this analysis to include more data, as well as the addition of a further search for the Higgs boson decaying into a ρ meson with a photon.

Lastly, Chapter 9 provides an overview of the thesis with some concluding remarks.

CHAPTER 2

THEORETICAL BACKGROUND TO HIGGS PHYSICS AND OVERVIEW OF EXPERIMENTAL RESULTS

2.1 The Standard Model of Particle Physics

The current best description of the interactions of fundamental particles is given by the Standard Model of particle physics (SM). In this model twelve fundamental matter particles with half-integer spin, called fermions, are described, whose interactions are mediated by the strong, weak and electromagnetic (EM) forces, as summarised in Table 2.1. Each of these fermions has an associated anti-particle, which possesses the same mass but opposite charge. Each of the forces has associated "force carrier" particles with integer spin, known as gauge bosons. The properties of all of these particles and their interactions are determined by Quantum Chromodynam-

ics (QCD) and the Electroweak (EW) sectors of the SM, which are summarised in Section 2.2 and Section 2.3, respectively.

The final particle of the SM is the spin-zero Higgs Boson, which was predicted in 1964 by Brout, Englert, and Higgs [7, 8], as well as Guralnik, Hagen and Kibble [9], and discovered by the ATLAS and CMS experiments in 2012 [5, 6] using the data collected during Run I operation of the LHC. The LHC, now operating in Run II, is continuing its testing of the SM. An overview of the current measurements of the properties of the Higgs boson is given in Section 2.4.

Table 2.1: Standard model of particle physics excluding the Higgs boson. The table shows the three generations of fermions and the fundamental interactions.

	I	II	III	Interaction (mediator)		
Quarks	u d	c s	t b	strong (gluon)	el.-mag. (photon)	weak ($W^{\pm}$,Z^0)
Leptons	e ν_e	μ ν_μ	τ ν_τ			

2.2 Quantum Chromodynamics

The strong interaction has $SU(3)$ symmetry, and is described by Quantum Chromodynamics (QCD), a non-abelian gauge theory. The twelve fundamental matter particles can be distinguished into two categories, quarks and leptons. Quarks carry colour charge, with which the mediator of the strong force, the gluon, interacts. Colour charge has six possible values (R,G,B,$\bar{R}$,$\bar{G}$,$\bar{B}$) and, as described by the theory, coloured particles are unobservable and must exist in net-zero colour charge composites (hadrons) to be observed in isolation. The most common colour neutral composite particles are either a pair of colour and anti-colour ($R\bar{R}$,$G\bar{G}$,$B\bar{B}$) quarks, known as mesons, or all three colours combined (RGB,$\bar{R}\bar{G}\bar{B}$), known as baryons. Unlike photons that do not carry electric charge, gluons carry a colour charge and, therefore, also self-interact. As a result, the quarks produced in experiments become part of bound states in a process known as hadronisation. This process results in

final state quarks or gluons (partons) usually being observed as collimated cones of hadrons known as jets. Jets are not easily matched to the original parton and algorithms are used to associate the observed jet with its most likely origin.

The nature of QCD colour charge results in the internal structure of hadrons being hidden from direct observation. Instead, the variation of parton densities within the hadrons can be studied. Several models have been developed from experimental data, which are known as parton distribution functions (PDFs). These PDFs provide crucial information for the prediction of jet production at the LHC, which form a common signal and background in analyses. Jets can either be misidentified directly as other particles, or produce particles during the hadronic showering that replicate the signal. This background is often referred to as QCD background.

The coupling of the strong force, α_S, varies as a function of the 4-momentum transfer in an interaction [10, 11]. The behaviour of α_S is crucial for the modelling of particle interactions in the LHC. An important property of the QCD coupling is that two types of divergences occur: ultraviolet (UV) ones, which occur at large momenta; and infrared (IR) ones, which occur in part due to massless particles radiating other massless particles. For simplification reasons, two QCD scales are introduced to resolve these divergences. In the UV case, the renormalisation scale, μ_R, is used and for the IR case the factorisation scale, μ_F. At these energy scales the α_S parameter becomes a function of μ_R or μ_F. Calculations involving these scales form a significant uncertainty in the theoretical modelling of particle interactions. For instance, applying perturbative theory to calculations of high energy cross sections yields logarithmic terms involving the masses [12]. This is the result of the cross section being a combination of short and long-distance behaviour and is generally not computable directly in perturbation theory for QCD. Instead, factorisation theorems are applied to separate the long-distance from the short-distance behaviour and give terms for which perturbation theory can be applied alongside terms that may be measured experimentally.

2.3 Electroweak Theory

At low energies, the electromagnetic and weak interactions are observed to behave differently, one has a long range and is relatively strong, while the other has a short range and interacts weakly. Electroweak theory describes how the two forces are two different aspects of the same force, which unify at high energies to form a single electroweak force. Therefore, the electromagnetic and weak interactions can be described by a single Quantum Field Theory based on the $SU(2)_L \bigotimes U(1)_Y$ gauge group, where Y is defined as the weak hypercharge; a quantum number that relates the electric charge with the third component of weak isospin. Fermions consist of left-handed and right-handed fields. Weak interactions only interact with the left-handed components. Left-handed components transform as doublets under $SU(2)$ and the right-handed components transform as singlets.

The requirement for local gauge invariance results in four gauge bosons: B_μ hypercharge and three W^a_μ bosons isospin. The combination of these fields produces the four physically-observed bosons: photon (γ), Z^0 boson and the charged W^+ and W^- bosons.

2.4 The Brout-Englert-Higgs Mechanism

As initially described by EW gauge theory, all of the associated force-carrying particles are predicted without an associated mass. The solution to this problem was devised in the Brout-Englert-Higgs (BEH) mechanism, which describes the generation of masses for the W and Z vector bosons. The discovery of these bosons by the UA1 and UA2 collaborations confirmed the prediction of the W and Z bosons to be massive, whilst the photon and gluons are massless under extensive observations.

A key foundation of gauge theory is local gauge invariance. The addition of a simple mass term to the Lagrangian causes this invariance to be broken. Instead, the BEH mechanism proposes the inclusion of a new scalar field with a specific potential that

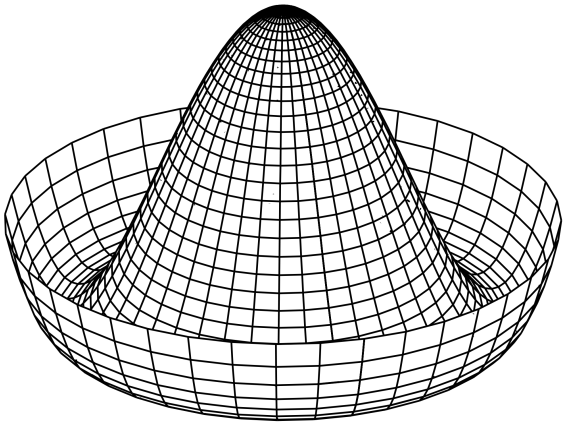

Figure 2.1: Shape of the Higgs potential. Figure taken from Ref. [13].

maintains the invariance of the full Lagrangian under $SU(2)_L \bigotimes U(1)_Y$, but causes the vacuum not to be invariant under this symmetry. This is known as spontaneous symmetry breaking of a locally gauge invariant theory.

To break the $SU(2)_L \bigotimes U(1)_Y$ symmetry, first a complex, left-handed isospin doublet is introduced:

$$\phi = \begin{pmatrix} \phi^+ \\ \phi^0 \end{pmatrix} = \frac{1}{\sqrt{2}} \begin{pmatrix} \phi_1 + i\phi_2 \\ \phi_3 + i\phi_4 \end{pmatrix},$$

with a potential that spontaneously breaks the symmetry, as shown in Figure 2.1. This is described by:

$$V(\phi) = \mu^2(\phi^\dagger\phi) + \lambda(\phi^\dagger\phi)^2,$$

where λ is the self coupling parameter ($\lambda > 0$ due to vacuum stability) and where $\mu^2 < 0$ is chosen. From this, the vacuum has $\phi_1 = \phi_2 = \phi_4 = 0$ and $\phi_3 = \nu$:

$$\text{Vacuum} = \phi = \frac{1}{\sqrt{2}} \begin{pmatrix} 0 \\ \nu + h \end{pmatrix},$$

where ν is the vacuum expectation value of the Higgs field ($\nu \approx 246\,\text{GeV}$) and h is the real scalar Higgs field with one degree of freedom.

The result of this is that the $SU(2)_L$ and $U(1)_Y$ generators are spontaneously broken and all four gauge bosons (W_1, W_2, W_3 and B) acquire mass. The W_1 and W_2 bosons

mix to form the charged $W^{\pm}$ bosons and the W_3 and B bosons mix to form the Z boson and the photon. Computing the masses of these mixed states, one of the combinations (the photon) remains massless, but the $W^{\pm}$ and Z bosons all have finite masses. The resulting Lagrangian contains terms describing the interaction of the additional field with the massive gauge bosons, as well as a term describing a massive scalar particle, the Higgs boson, and its self-interactions. The mass of the Higgs boson is given by

$$m_H = \sqrt{2\lambda}\,\nu.$$

Due to λ being a free parameter, unconstrained in the SM, the Higgs boson mass is also not predicted by the SM.

2.5 Yukawa Interactions

As described by the BEH mechanism, the origin of massive bosons can be directly explained by the existence of a Higgs boson. However, this mechanism alone does not directly imply the masses of the fermions. The solution for this is to insert gauge invariant fermion mass terms into the Lagrangian. For this to be an $SU(2)_L \bigotimes U(1)_Y$ invariant term it must be a singlet under $SU(2)_L$ and $U(1)_Y$. This can be done using the complex doublet, ϕ, described previously, which has the right quantum numbers to form an $SU(2)_L$ and $U(1)_Y$ singlet in the vertex: $-\lambda_f \bar{\psi}_L \phi \psi_R$, where λ_f is the Yukawa coupling of the fermion with the Higgs. The resulting couplings, $g_{Hf\bar{f}}$, can be calculated in the SM and depend linearly on the fermion mass, m_f, whereas the Higgs boson-vector boson couplings, g_{HVV}, depend on the vector boson mass, m_V, squared:

$$g_{Hf\bar{f}} = \frac{m_f}{\nu}, \qquad g_{HVV} = \frac{2m_V^2}{\nu}.$$

2.6 Higgs Boson Measurements at the LHC

Many measurements of the Higgs boson have now been performed and the LHC experiments frequently publish new studies. The measurements and theory discussed in this section and Section 2.7 are relevant to the searches performed in this thesis and, therefore, some of the text has been taken verbatim from the publication in Ref. [1]. These results were up-to-date as of August 2018.

Higgs bosons are produced via several different modes at the LHC. The Feynman diagrams of the Higgs boson production mechanisms relevant to the analyses discussed in this thesis are shown in Figure 2.2.

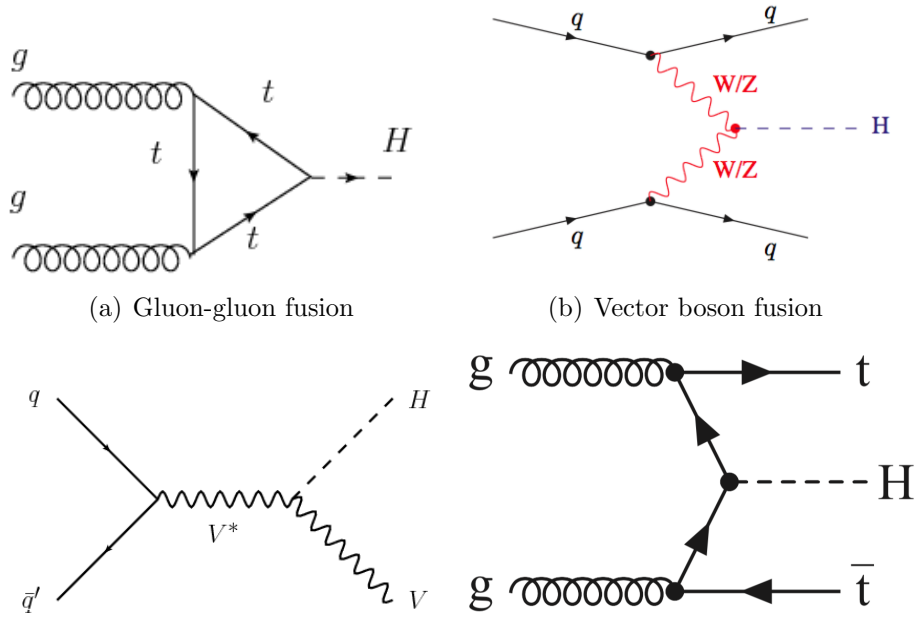

(a) Gluon-gluon fusion (b) Vector boson fusion

(c) Vector boson associated production (d) Quark associated production

Figure 2.2: Feynman diagrams of the most common Higgs production mechanisms.

A detailed report of the SM predicted Higgs boson production cross sections and their corresponding uncertainties can be found in Ref. [14]. The dominant production mechanism is through gluon-gluon fusion (ggH), where the Higgs boson is produced by two gluons fusing through a heavy quark loop. This mode is predicted to contribute 87% of the Higgs bosons produced in $\sqrt{s}$=13 TeV pp collisions at the

LHC. About 7% of the Higgs bosons originate from vector boson fusion (VBF). A further 4% come from processes where the Higgs boson is produced in association with a vector boson (WH/ZH). The production of a Higgs boson in association with a top-quark pair ($t\bar{t}$H) or a bottom-quark pair ($b\bar{b}$H) contributes 2%.

Since the discovery of a Higgs boson in 2012 by the ATLAS and CMS experiments, many analyses have focussed on studying the properties of this particle. This is essential not only for understanding the particle, but also to probe alternative models to the SM. Many models arise by using more complicated fields in the electroweak symmetry breaking than the scalar field described in Section 2.4. Such modifications to the SM can lead to significant differences in the Yukawa couplings and even to the existence of additional Higgs-like bosons.

The ATLAS collaboration reported a total cross section measurement for $pp \to H + X$ of $57.0^{+6.0}_{-5.9}(\text{stat.})^{+4.0}_{-3.3}(\text{syst.})$pb [15] using 36.1 fb^{-1} of data at a centre-of-mass energy of $\sqrt{s} = 13$ TeV, which is consistent with the SM prediction of $55.6^{+2.4}_{-3.4}$ pb [14]. Using the same Run II dataset and combining with the Run I dataset, ATLAS has also measured the mass of the Higgs boson, m_H, in the $H \to ZZ^* \to 4\ell$ and $H \to \gamma\gamma$ channels. A simultaneous fit in the two channels provides a value of $m_H = 124.97 \pm 0.19\,(\text{stat.}) \pm 0.13\,(\text{syst.})$ GeV [16]. The value reported by ATLAS and CMS from the $\sqrt{s} = 7$ TeV and $\sqrt{s} = 8$ TeV datasets is $m_H = 125.09 \pm 0.21(\text{stat.}) \pm 0.11(\text{syst.})$ GeV [17]. A full comparison of the mass measurements in the individual channels and combined is shown in Figure 2.3.

Similarly, with their own independent dataset collected at centre-of-mass energy $\sqrt{s} = 13$ TeV, the CMS collaboration has also reported measurements of the Higgs boson production cross section and the mass of the Higgs boson in the $H \to ZZ^* \to 4\ell$ channel [18]. The observed cross section for this Higgs boson decay mode of $2.92^{+6.0}_{-5.9}\,(\text{stat.})\,^{+4.0}_{-3.3}\,(\text{syst.})$ fb is consistent with SM predictions and the measured Higgs boson mass $m_H = 125.26 \pm 0.20\,(\text{stat.}) \pm 0.08\,(\text{syst.})$ GeV is compatible with the combined ATLAS and CMS measurement at $\sqrt{s} = 7$ TeV and $\sqrt{s} = 8$ TeV. An analysis of the $H \to \gamma\gamma$ channel has also been performed by CMS, yielding a best

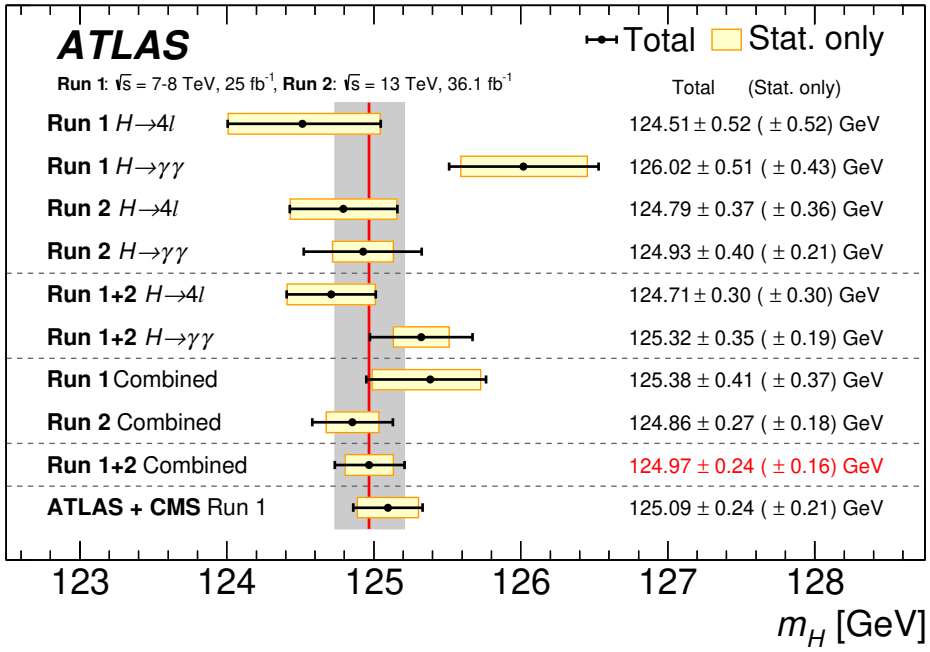

Figure 2.3: Summary of the Higgs boson mass measurements from the individual $H \to ZZ^* \to 4\ell$ and $H \to \gamma\gamma$ channels and combined analyses, compared to the Run I analyses and combined Run I measurement by ATLAS and CMS [17]. The statistical-only (yellow-shaded bands), and total (black error bars) uncertainties are indicated. The (red) vertical line and corresponding (gray) shaded column indicate the central value and the total uncertainty of the combined measurement, respectively. Figure taken from Ref. [16].

fit mass of $m_H = 125.4 \pm 0.20\,(\text{stat.}) \pm 0.20\,(\text{syst.})$ GeV [19].

Experimental observations of the Higgs boson have been performed mainly using its decays to other bosons. Currently all of the measurements of the Higgs boson in this sector are consistent with SM predictions. However, the Higgs boson coupling to fermions proceeds via a different mechanism, which is also susceptible to large modifications in BSM models. A broad spectrum of studies are being performed on the Higgs boson decaying to fermions with some channels already yielding experimental evidence.

The first observation reported of the Higgs coupling to a third-generation fermion was in the $H \to \tau^+\tau^-$ channel [20–22]. This result combines the analyses of both ATLAS and CMS on the $\sqrt{s} = 7$ TeV and $\sqrt{s} = 8$ TeV datasets and provides the first experimental evidence for Yukawa couplings. In addition, progress has been made in the third-generation quark sector with indirect evidence for the coupling of the Higgs boson to the top-quark [20]. This was recently complemented by direct observation of the associated production of the Higgs boson with a top quark pair ($t\bar{t}H$) [23, 24].

The Higgs boson decays into $b\bar{b}$ have recently been observed by both ATLAS and CMS [25, 26]. The $b\bar{b}$ decay mode has the largest branching ratio for the Higgs boson due to it being the most massive particle pair into which a 125 GeV boson can decay. Unfortunately, the final state of this decay, two hadronic jets, is a common background from QCD processes in the underlying pp collisions of the LHC. A significant effort has been made to develop algorithms that can consistently identify jets originating from a b quark [27].

No experimental evidence has yet been found for the couplings to the first and second generation fermions, but direct searches were recently performed by the ATLAS Collaboration for $H \to c\bar{c}$ [28] and $H \to \mu^+\mu^-$ [29, 30], while the CMS Collaboration has performed searches for $H \to \mu^+\mu^-$ and $H \to e^+e^-$ decays [31].

2.7 $H \to \mathcal{Q}\,\gamma$ theory and motivation

As mentioned in the previous section, deviations in the quark Yukawa couplings from the SM expectations can lead to significant increases in the branching fractions for exclusive Higgs decays. These deviations can arise in BSM theories; for example, the quark masses might not originate entirely from the BEH mechanism, but could also be induced by other subdominant sources of electroweak symmetry breaking [32]. Other scenarios include the minimal flavour violation framework [33], the Froggatt–Nielsen mechanism [34], the Higgs-dependent Yukawa couplings model [35], the Randall–Sundrum family of models [36], and the possibility of the Higgs boson being a composite pseudo-Goldstone boson [37]. An overview of relevant models of new physics is provided in Ref. [14].

Progress in jet-tagging has enabled studies of the Higgs decays to b and c quarks. Measuring these decays directly is inhibited by a large background from QCD processes. Complementary methods of providing sensitivity to the Yukawa couplings have been developed by searching for the exclusive decays of the Higgs boson into flavour-neutral vector mesons, V, and associated photons, γ. These decays are sensitive to both the "direct" and "indirect" amplitudes shown in Figure 2.4. The direct decay proceeds through the $H \to q\bar{q}$ coupling, with a subsequent photon emission before the $q\bar{q}$ hadronisation to V. The indirect decay is via the $H\gamma\gamma$ coupling followed by the fragmentation $\gamma^* \to V$. The topology of these decays, a high-p_T photon back-to-back with a meson decay, is a comparatively clean signal, albeit with a small branching fraction.

Decays of the Higgs boson to a heavy vector quarkonium state, $\mathcal{Q} \equiv J/\psi$ or $\Upsilon(nS)$, and a photon have previously been sought by the ATLAS Collaboration with up to 19.2 fb^{-1} of data collected at $\sqrt{s} = 8$ TeV [38], resulting in 95% confidence level (CL) upper limits of 1.5×10^{-3} for $\mathcal{B}(H \to J/\psi\,\gamma)$, and $(1.3, 1.9, 1.3) \times 10^{-3}$ for $\mathcal{B}(H \to \Upsilon(nS)\,\gamma)$ $(n = 1, 2, 3)$. The former has also been sought by the CMS Collaboration [39], yielding a similar upper limit. The branching fractions for these decays

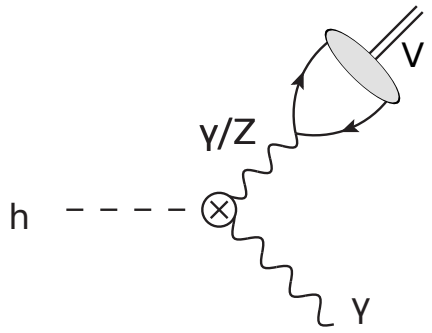

(a) Indirect

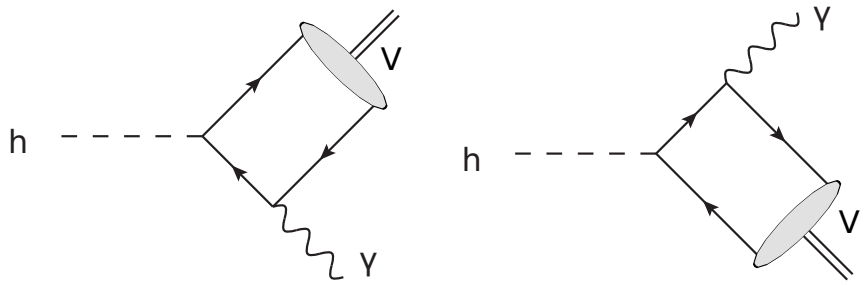

(b) Direct

Figure 2.4: Feynman diagrams of (a) indirect and (b) direct $H(Z) \to V\gamma$ decays.

have been calculated within the SM to be $\mathcal{B}(H \to J/\psi\,\gamma) = (2.99^{+0.16}_{-0.15}) \times 10^{-6}$ [40–43] and $\mathcal{B}(H \to \Upsilon(nS)\,\gamma) = (5.22^{+2.02}_{-1.70}, 1.42^{+0.72}_{-0.57}, 0.91^{+0.48}_{-0.38}) \times 10^{-9}$ $(n = 1, 2, 3)$ [40, 41]. The $\Upsilon(nS)\,\gamma$ branching fractions are significantly smaller than the $J/\psi\,\gamma$ branching fraction due to a cancellation between the direct and indirect amplitudes. The branching fraction of the $H \to \psi(2S)\,\gamma$ decay is currently unconstrained by experimental data. It has a branching fraction calculated within the SM to be $\mathcal{B}(H \to \psi(2S)\,\gamma) = (1.03 \pm 0.06) \times 10^{-6}$ [44], and the first search for this decay is described in Chapters 6 and 7.

In addition, light-quark (u,d,s) couplings to the Higgs boson can be constrained in analogous rare exclusive decays of the Higgs boson. The Higgs boson decays to a ϕ or ρ meson and a photon provide a unique probe to measure directly its couplings to the strange quark and the up and down quark, respectively.

Owing to the large Z boson production cross section at the LHC, rare Z boson decays can be probed at levels much lower than for Higgs boson decays to the same final state. Branching fractions for $Z \to \mathcal{Q}\,\gamma$ decays have been calculated to be between 10^{-8} and 10^{-7} for both $Z \to J/\psi\,\gamma$ and $Z \to \Upsilon(nS)\,\gamma$ decays [45–47]. Measurements of the branching fractions for such decays would provide a sensitive test of the SM and the factorisation approach in QCD, since the power corrections in terms of the QCD energy scale over the vector boson mass are small [46]. ATLAS has searched for Z decays to J/ψ or $\Upsilon(nS)$ $(n = 1, 2, 3)$ plus a photon with 20.3 fb^{-1} of data collected at $\sqrt{s} = 8$ TeV [38], resulting in 95% confidence level (CL) upper limits of 2.6×10^{-6} and $(3.4, 6.5, 5.4) \times 10^{-6}$ on their corresponding branching fractions, respectively.

This thesis covers the searches for $H(Z) \to J/\psi\,\gamma$ and $H(Z) \to \Upsilon(nS)\,\gamma$ decays, as well as a search for $H(Z) \to \psi(2S)\,\gamma$ decays, all of which are described in Chapters 6 and 7 and have been performed using the 2015 and 2016 $\sqrt{s} = 13$ TeV ATLAS dataset. Chapter 8 describes the first searches for the analogous decays of $H(Z) \to \phi\,\gamma$ and $H(Z) \to \rho\,\gamma$ using the same ATLAS dataset.

CHAPTER 3

THE ATLAS EXPERIMENT

3.1 The Large Hadron Collider

The LHC is a particle accelerator that occupies a 26.7 km circumference tunnel at CERN, near Geneva, Switzerland, which was originally constructed to house the preceding Large Electron Positron Collider (LEP). A detailed description of all aspects of the LHC is given in Ref [48], but only the key points will be described here. A series of accelerators supply the LHC with protons via the injector complex shown in Figure 3.1. Two different proton beams orbit in opposite directions in the two rings of the LHC tunnel; their orbit is sustained by 1232 superconducting dipole and 392 quadrupole magnets, which bend and focus the beams, respectively. These powerful magnets have been designed to allow the LHC to accelerate the protons in each ring up to an energy of 7 TeV per proton to deliver proton-proton (pp) collisions at centre-of-mass energy of up to $\sqrt{s} = 14$ TeV. The LHC is also capable of accelerating heavier ions, most commonly lead, to supply heavy-ion collisions.

There are four Interaction Points (IPs) on the LHC ring, each surrounded by a particle physics detector experiment:

- ATLAS and CMS are general purpose experiments focussed on high-luminosity operation (up to a peak instantaneous luminosity of $\mathcal{L} = 2.1 \times 10^{34}$ cm^{-2} s^{-1}). The ATLAS experiment is discussed in more detail later in this chapter and is the experiment of focus for this thesis.

- LHC beauty (LHCb) is designed to study B-physics using a forward spectrometer at a lower instantaneous luminosity of around $\mathcal{L}$ =10^{32} cm^{-2} s^{-1}. LHCb studies B-physics via various processes, giving sensitivity to Charge-Conjugation Parity (CP) violation and indirectly to BSM theories.

- A Large Ion Collider Experiment (ALICE) is an experiment operating at an instantaneous luminosity of around $\mathcal{L} = 2 \times 10^{30}$ cm^{-2} s^{-1} and is designed specifically for the heavy ion collisions produced at the LHC. Such collisions, at around 2.6 TeV per nucleon, can replicate the conditions of the early universe.

To reach the peak instantaneous luminosity of $\mathcal{L} = 2.1 \times 10^{34}$ cm^{-2} s^{-1}, the LHC is designed to orbit 2808 bunches per proton beam, each with 10^{11} protons. The bunches of the two beams cross every 25 ns at each collision point, with up to 60 pp interactions at each crossing, resulting in around 1 billion collisions per second. Many interactions occurring at such a high rate is called pile-up, which presents two challenges. One is the effect where multiple interactions happen in the same bunch crossing and the particles produced from the different collisions overlap and interfere with the reconstruction of each collision. The second is from "deadtime", which is data lost while the trigger and DAQ process an earlier event. The presence of pile-up increases the amount of data per event to be processed, and so can increase the level of deadtime. In general, all of the particles created in the collisions, excluding the final state particles of interest, are referred to as the underlying event.

The integrated delivered luminosity for each year of operation of the ATLAS detector is shown in Figure 3.2. Each year has surpassed the delivered luminosity of

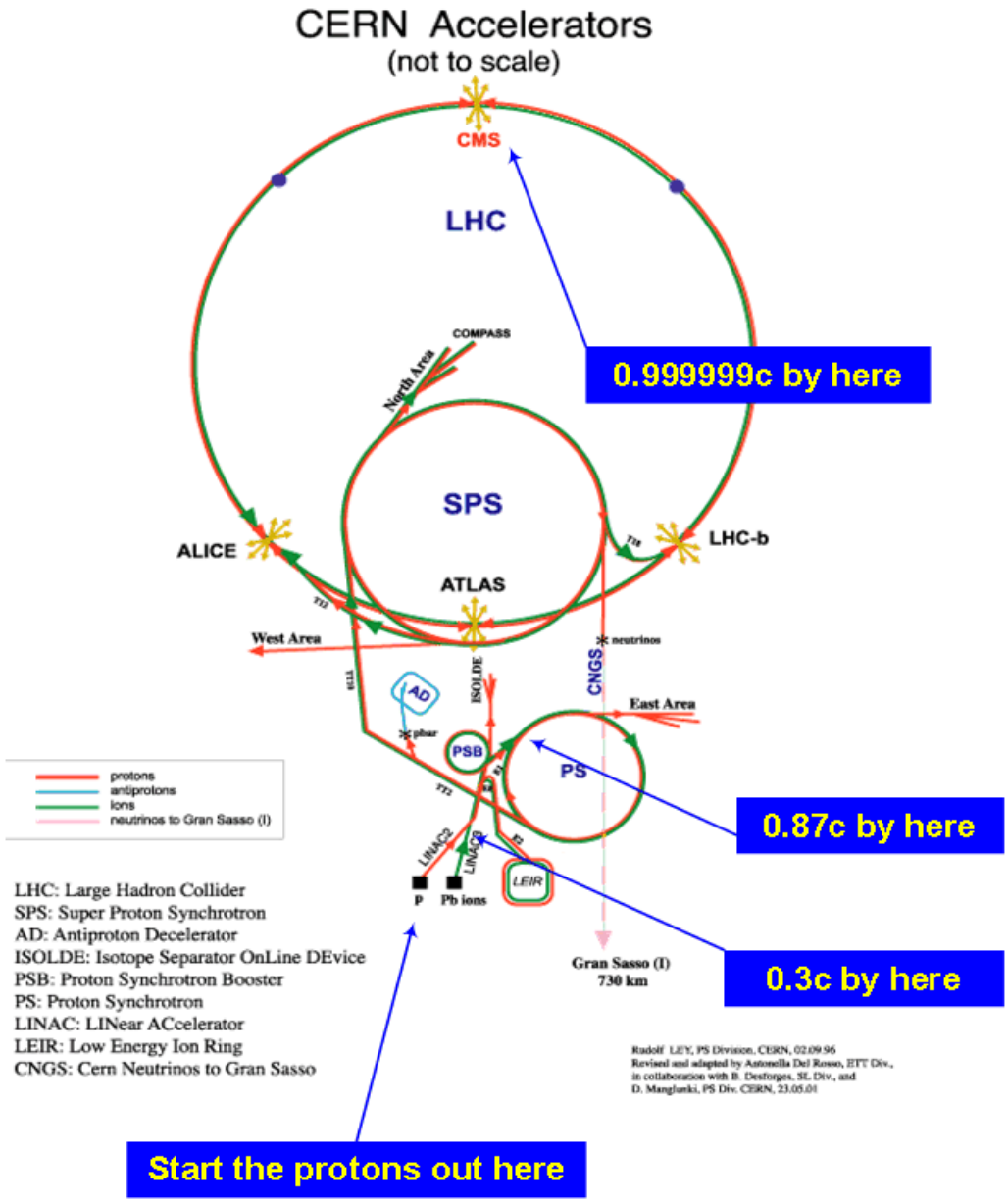

Figure 3.1: A schematic diagram of CERN's accelerator complex. A series of lower-energy accelerators increment the speed of the protons before injecting them into the 26.7 km ring of the LHC. ©CERN 2008

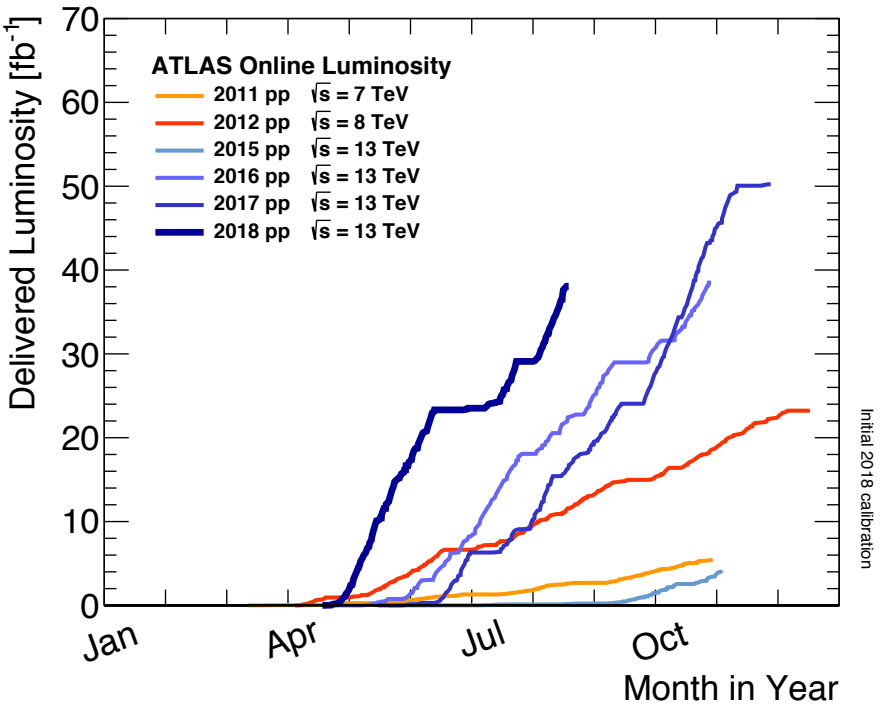

Figure 3.2: Integrated luminosity versus day delivered to ATLAS for 2011 to 2018 *pp* collisions. Figure taken from Ref. [49].

the previous year, excluding 2015, where operation began late in the year after an increase in centre-of-mass energy.

3.2 Introduction to the ATLAS Detector

As a general-purpose detector, ATLAS must be sensitive to a broad range of processes and, therefore, requires a well-balanced system of sub-detectors and triggers. The sub-detectors are arranged to provide an almost hermetic coverage that is both forward-backward and axially symmetric. These sub-detectors enclose the beam axis in layers and consist of a central "barrel" section and two "endcap" sections. An overview of the ATLAS design and operation is described here, which is based on a more detailed description in Ref. [50]. A schematic view of the ATLAS detector is shown in Figure 3.3.

The ATLAS coordinate system is defined based around the nominal IP, where the

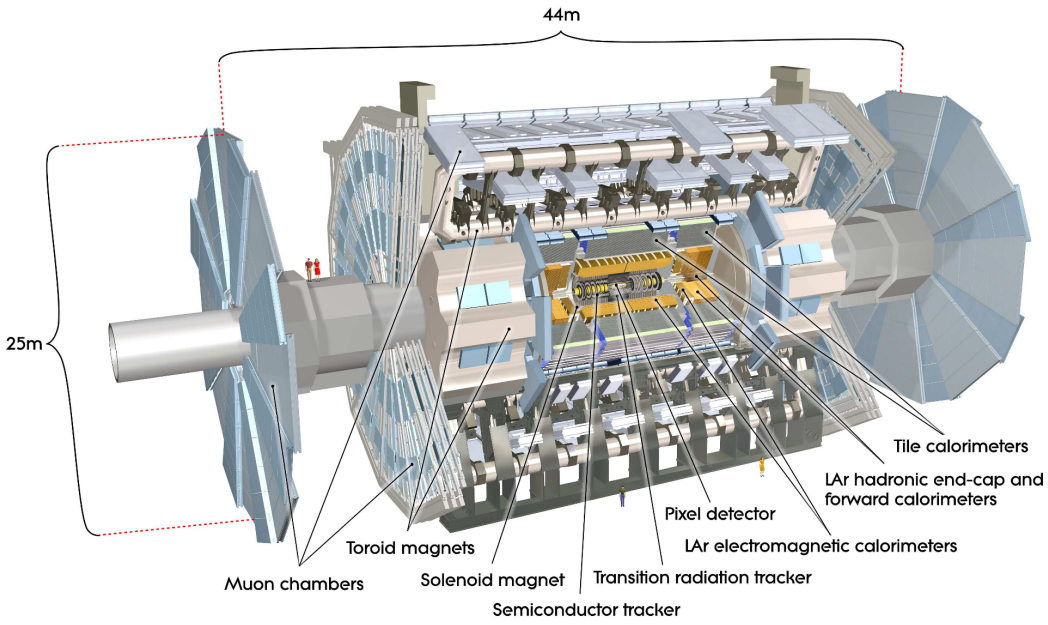

Figure 3.3: Cut-away schematic view of the ATLAS detector. Figure taken from Ref. [50].

z-axis is defined to point along the beam direction, the x-axis points from the IP towards the centre of the LHC ring, and the y-axis points vertically upwards. The azimuthal angle around the beam axis in the x-y plane is labelled ϕ and the angle from the beam axis is labelled θ. The radius in the x-y plane from the beam pipe is defined by $R = \sqrt{x^2 + y^2}$.

For convenience, the angular variable rapidity, y, is used to describe massive particles travelling at relativistic speeds,

$$y = \frac{1}{2} \ln \left[\frac{(E + p_z)}{(E - p_z)} \right], \tag{3.1}$$

where $E = \sqrt{|\vec{p}|^2 + M^2}$ is the energy of a particle of mass M travelling with momentum $\vec{p}$, and p_z is the component of $\vec{p}$ in the direction of the beam axis (z). Furthermore, in the case of massless or highly relativistic particles ($E \approx |\vec{p}|$), the pseudorapidity, η, is used,

$$\eta = -\ln \left[\tan(\frac{\theta}{2}) \right], \tag{3.2}$$

which gives a quantity whose difference between two particles, $\delta\eta$, is Lorentz in-

variant under boosts along the z-axis. Often the transverse momentum p_T and transverse energy E_T are used, which are defined in the x-y plane as $p_T^2 = p_x^2 + p_y^2$ and $E_T = E\ \sin(\theta)$, respectively.

3.3 Magnet System

A powerful magnet system is utilised in the ATLAS detector to cause the high-energy charged particles to curve as they traverse the layers of sub-detectors. The curved trajectory of a charged particle can be used to determine the transverse momentum of the particle. The ATLAS magnet system is composed of a 2 T solenoid magnet surrounding the Inner Detector and three toroid magnets surrounding the Muon Spectrometer. The toroid in the barrel region provides approximately a 0.5 T magnetic field, while the toroid magnets in the end-caps provide a 1.0 T magnetic field.

3.4 The Inner Detector

The ATLAS Inner Detector (ID) is designed and built to provide excellent momentum resolution and the ability to extrapolate the trajectory of charged particle tracks to find the IP (also known as the primary vertex) and the particle decay points (secondary vertices) [50]. To do this, the ID must be capable of making precise spatial measurements in the demanding environment caused by approximately 1000 particles emerging for every 25 ns bunch crossing. As shown in Figure 3.4, the ID is composed of three different sections: the Pixel Detector occupies the inner-most radii (31<R<242 mm); followed by the Semiconductor Tracker (SCT) barrel (255<R<549 mm) and endcap (251<R<610 mm); and finally at the outer-most radii the Transition Radiation Tracker (TRT) barrel (554<R<1082 mm) and end-cap (617<R<1106 mm). The ID also has good angular coverage up to $|\eta| < 2.5$. Outside these three sub-detectors is a superconducting solenoidal magnet, which

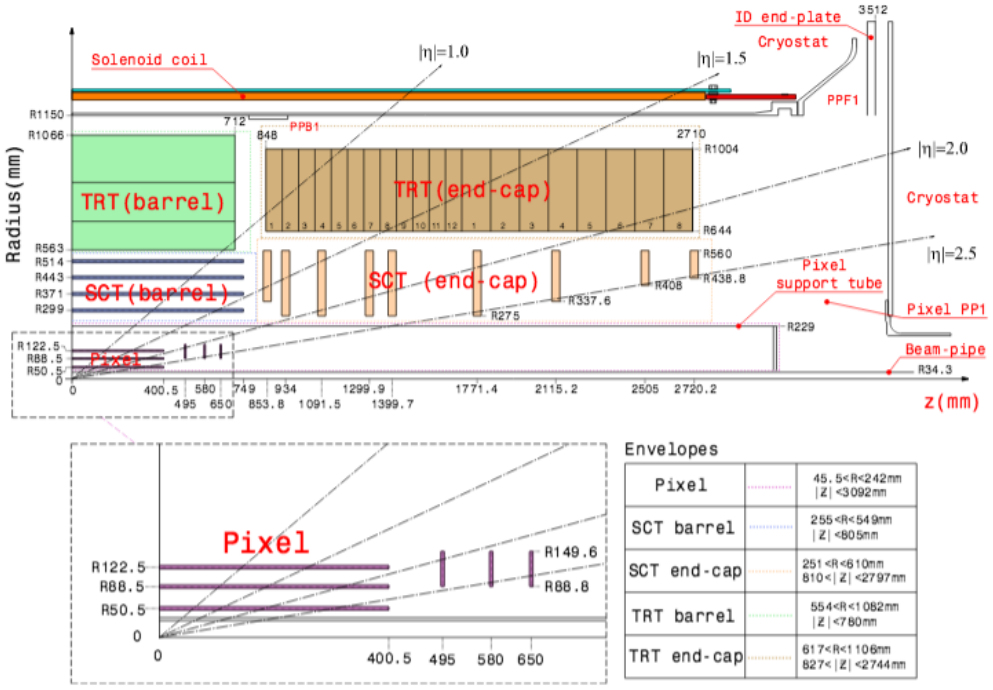

Figure 3.4: A plan view of a quarter section of the ATLAS Inner Detector. Figure taken from Ref. [50].

provides a uniform axial magnetic field of 2 T to allow the measurement of charged particle transverse momenta in the ID.

3.4.1 Pixel Detector

There are 1744 silicon sensors forming the pixel detector, arranged in three barrel layers and two end-caps each with three disk layers [50]. The sensors are 250 μm in thickness and have area 19 $\times$ 63 mm^2. Pixel sensors provide the best spatial resolution of all the tracking detectors: 10 μm (R-ϕ) and 115 μm (z) in the barrel and 10 μm (R-ϕ) and 115 μm (R) in the end-cap disks [51]. During the shutdown before Run II, the pixel detector was upgraded with an extra layer of pixel detectors known as the Insertable B-Layer (IBL) [52]. This extra layer was installed to improve the vertex finding ability of the ATLAS detector. The improvement in the longitudinal impact parameter resolution between data collected in Run I compared with Run 2 is shown in Figure 3.5 as functions of p_T and η. In the regions of $0.0 < \eta < 0.2$ and

$0.4\,\text{GeV} < p_T < 0.5\,\text{GeV}$ around a 40% improvement is found with respect to the Run I impact parameter resolution [53].

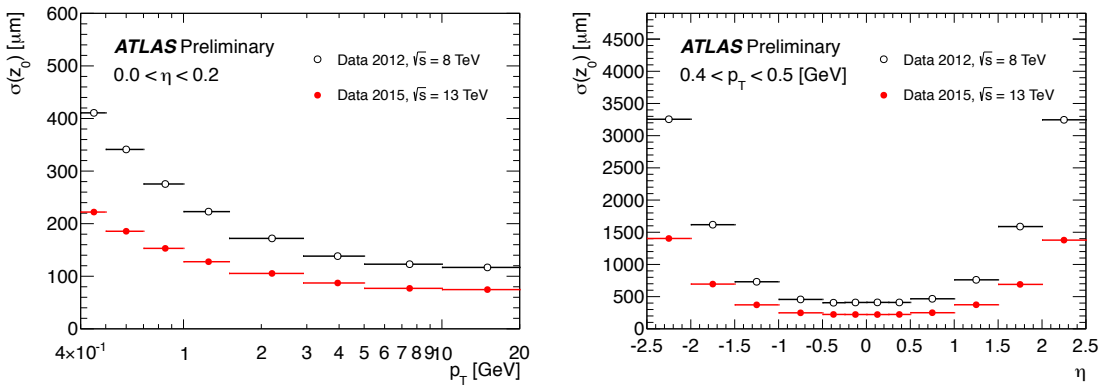

(a) (b)

Figure 3.5: Longitudinal mpact parameter resolution measured from data in 2015, $\sqrt{s} = 13$ TeV, with the ID including the IBL, as a function of (a) p_T in the region $0.0 < \eta < 0.2$, and (b) η for values of $0.4\,\text{GeV} < p_T < 0.5\,\text{GeV}$, compared to that measured from data in 2012, $\sqrt{s} = 8$ TeV. Figure taken from Ref. [53].

3.4.2 Semiconductor Tracker

The ATLAS Semiconductor Tracker (SCT) is a silicon tracking chamber that is arranged in four concentric barrel layers and two endcaps each containing nine disks perpendicular to the beam axis. Each layer or disk contains silicon strip modules providing further spatial measurements. Most strip modules contain four strip sensors: a first pair, which is parallel to the z-axis in the barrel and perpendicular to it in the endcaps; and a second pair on the other side of the module, which is aligned at a stereo angle of 40mrad with respect to the first. In total there are 4088 modules, with 15,912 silicon sensors of 285±15 μm in thickness and 80 μm in strip pitch, providing a spatial precision of around 17 μm in R-ϕ [51]. Charge deposited in the strips is received by radiation-hard read-out chips and registered as a hit if the charge exceeds a predetermined threshold. Each chip reads out 128 strips.

3.4.3 Transition Radiation Tracker

The Transition Radiation Tracker (TRT) uses 298,304 gaseous proportional drift tubes. Each tube is 144 cm long in the barrel and 37 cm long in the endcap; they are 4 mm in diameter and filled with a mixture of 77% Xe, 27% CO_2 and 3% O_2 [50]. A charged particle with $p_T > 0.5$ GeV and $|\eta| < 2.0$ will traverse around 36 tubes, providing many 130 μm spatial resolution points for precision momentum measurements in R-ϕ [50].

The TRT has a lower precision per measurement than the silicon components; however, it still contributes considerably to momentum measurements with its larger number of measurement points and longer track length. An added benefit of the TRT is its role in electron identification, where traversing electrons create a larger signal than other particles.

3.5 Calorimeter Systems

Calorimeters are used in many detectors to measure the energy deposited as well as to provide position and direction information for electrons, photons and hadrons. A particle is forced to interact with the calorimeter material, causing it to shower into many other particles. The depth of the calorimeter is chosen such that it can fully contain the EM and hadronic showers, allowing the full measurement of the shower energy and to minimise the number of particles reaching the Muon Spectrometer (MS). Different technologies are employed in different regions of the calorimeter system based on the interesting physics processes and the radiation environment. All of the calorimeters in ATLAS utilise the sampling calorimeter method, with alternating layers of absorber material and active material. There are three types of calorimeter used in ATLAS, as shown in Figure 3.6: a Liquid Argon (LAr) EM calorimeter, designed to absorb and measure the energy of particles that interact via the EM force (electrons, photons etc.) in the pseudorapidity region

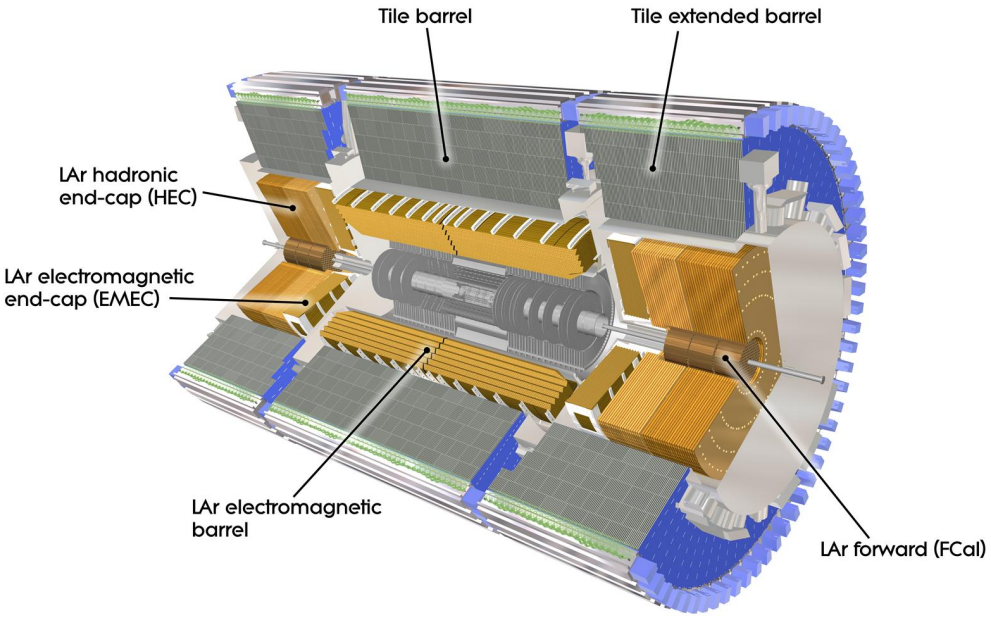

Figure 3.6: Computer generated image of the ATLAS calorimeter. Figure taken from [54].

$|\eta| < 3.2$; a scintillator-tile hadronic calorimeter concentric to the EM calorimeter in the barrel region ($|\eta| < 1.7$), to measure the energy of hadrons, and a LAr EM and hadronic calorimeter in the forward region up to $|\eta| < 4.9$.

3.5.1 Electromagnetic Calorimeter

The whole EM calorimeter rapidity range utilises LAr calorimeters, separated into one barrel section and two endcap sections. A lead absorber layer with electrodes is assembled in an accordion geometry to provide complete ϕ symmetry without azimuthal cracks [50]. The barrel section contains 32 modules, each covering $\Delta\phi = 22.50°$. A module, as shown in Figure 3.7, has three layers in depth. Layer 1 uses thin strip cells to provide high granularity in η. Layer 2 has larger square cells and collects the majority of the energy of the EM shower. Layer 3 collects only the tail of the EM shower and so has a coarser granularity. Neighbouring calorimeter cells that are within a region of $\Delta\eta \times \Delta\phi = 0.1 \times 0.1$ are defined as a "trigger tower". The signals obtained by the cells of a tower are combined. Information

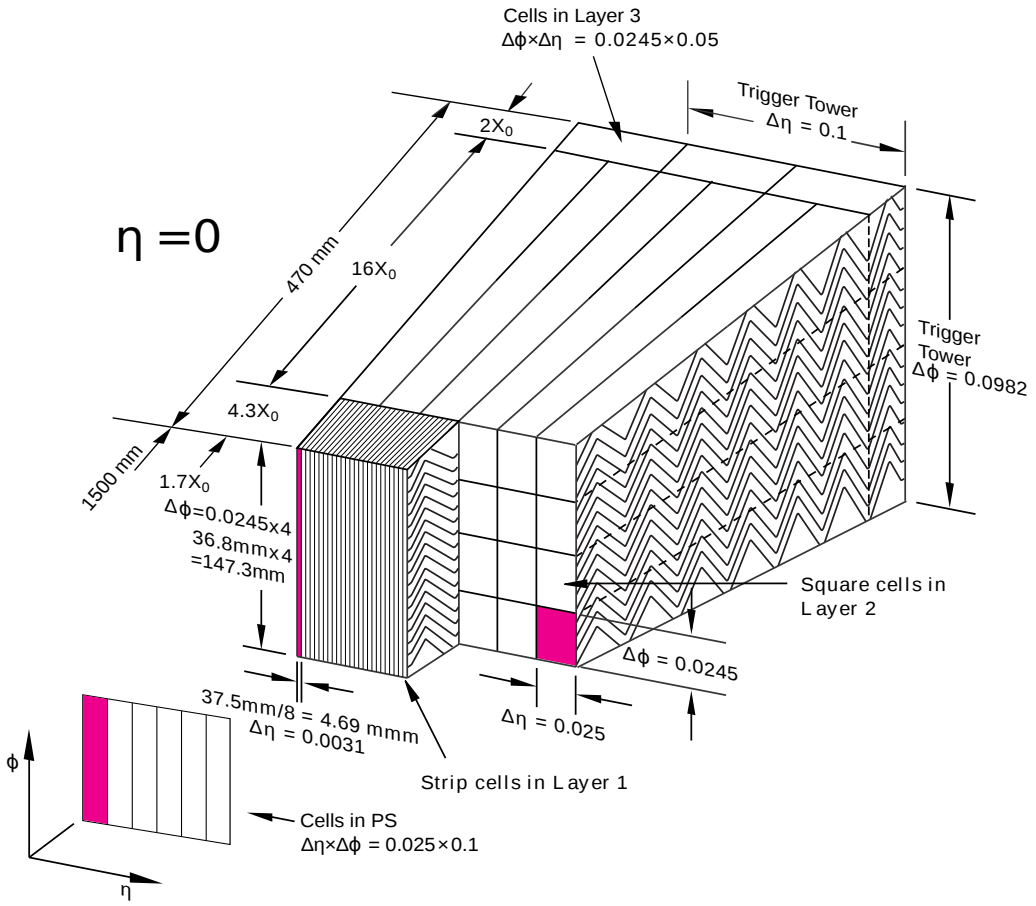

Figure 3.7: Sketch of a module of the EM calorimeter, showing the different layers in the accordion geometry. Granularity in η and ϕ of the cells of each of the three layers and of the trigger towers is also shown. What is referred to as a cell in each layer is highlighted pink. X_0 is the radiation length of the material [10]. Figure taken from Ref. [50].

from neighbouring towers is then provided as input to an algorithm used to identify interesting events. One such algorithm combines information from neighbouring calorimeter cells, while suppressing noise contributions, based on the structure of different physics objects to form topological clusters [55]. The resulting clusters have both shape and location information stored, which provide essential information for reconstruction of the physics object.

3.5.2 Hadronic Calorimeter

The Tile calorimeter uses steel as the absorber material and scintillator as the active medium. The calorimeter is divided into a barrel section ($|\eta| < 1.0$) and two extended barrel sections ($0.8 < |\eta| < 1.7$). It is located directly outside the EM calorimeter and is also segmented into three layers. The barrel and extended barrels are divided azimuthally into 64 modules. Cells of the hadronic calorimeter also form trigger towers with the EM calorimeter.

In the endcaps, an LAr calorimeter is used. The Hadronic Endcap Calorimeter consists of two separate wheels per endcap, located directly behind the EM calorimeter. Each wheel is built from 32 wedge-shaped modules, which are two layers in depth.

3.5.3 Forward Calorimeter

The Forward calorimeter is an LAr calorimeter integrated into each endcap, which contains three modules in each endcap. The first module is made of copper and is optimised for EM measurements, while the other two are made of tungsten and are predominantly used to measure hadronic interactions.

3.6 Muon Spectrometer

The outer part of ATLAS is occupied by the Muon Spectrometer (MS), designed to detect charged particles that have escaped the calorimeters with minimal interaction. Muons are the most common particles to escape due to interacting via only the weak and electromagnetic forces, and their relatively high mass. The MS provides tracking coverage across the region $|\eta| < 2.7$ and a trigger detector within the region $|\eta| < 2.4$. Figure 3.8 shows the layout of the ATLAS MS. A set of large superconducting toroid magnets is constructed within the MS and designed to produce a field orthogonal to the muon trajectories where possible. The MS, which is arranged into a barrel

and two endcap sections, is used in combination with the ID to provide a precise momentum measurement and good track reconstruction for charged particles. In particular, muon candidates are defined based on different combinations of tracks in the ID and MS. The tracking chambers are arranged in three cylindrical layers in the barrel region and three layers in the form of wheels in each of the endcaps.

The ATLAS MS is composed of four different varieties of chambers: two are used for tracking and two for triggering. All utilise different designs and technologies. Monitored Drift Tube (MDT) chambers provide the precision tracking measurements in the region $|\eta| < 2.7$. These are supplemented by Cathode Strip Chambers (CSC) in the innermost layer for the region $2.0 < |\eta| < 2.7$, because they provide both η and ϕ coordinates, with higher rate capability and time resolution, making them better suited for the higher background rates in this region.

Fast triggering information is provided by the Resistive Plate Chambers (RPC) in the barrel and Thin Gap Chambers (TGC) in the endcaps in the region $|\eta| < 2.0$. Both chambers are designed to detect signals quickly enough that the correct bunch crossing can be associated with the event.

3.7 Luminosity Measurement

Monitoring the delivered luminosity is a crucial part of any particle physics experiment. The measurement is necessary for estimating the number of signal events expected, which is a requirement for calculating branching fraction limits and cross section measurements. In ATLAS, the main luminosity measurement and monitoring is performed by a system of photomultiplier tubes (PMTs), known as LUCID [50], which are positioned ± 17 m along the beampipe from the interaction point. Its primary purpose is to detect inelastic pp scattering in the forward direction, from which the instantaneous luminosity can be determined using the methods in Ref. [57]. The detector is calibrated using special runs of the LHC called van der Meer scans, where the two beams are scanned across each other, first in the horizon-

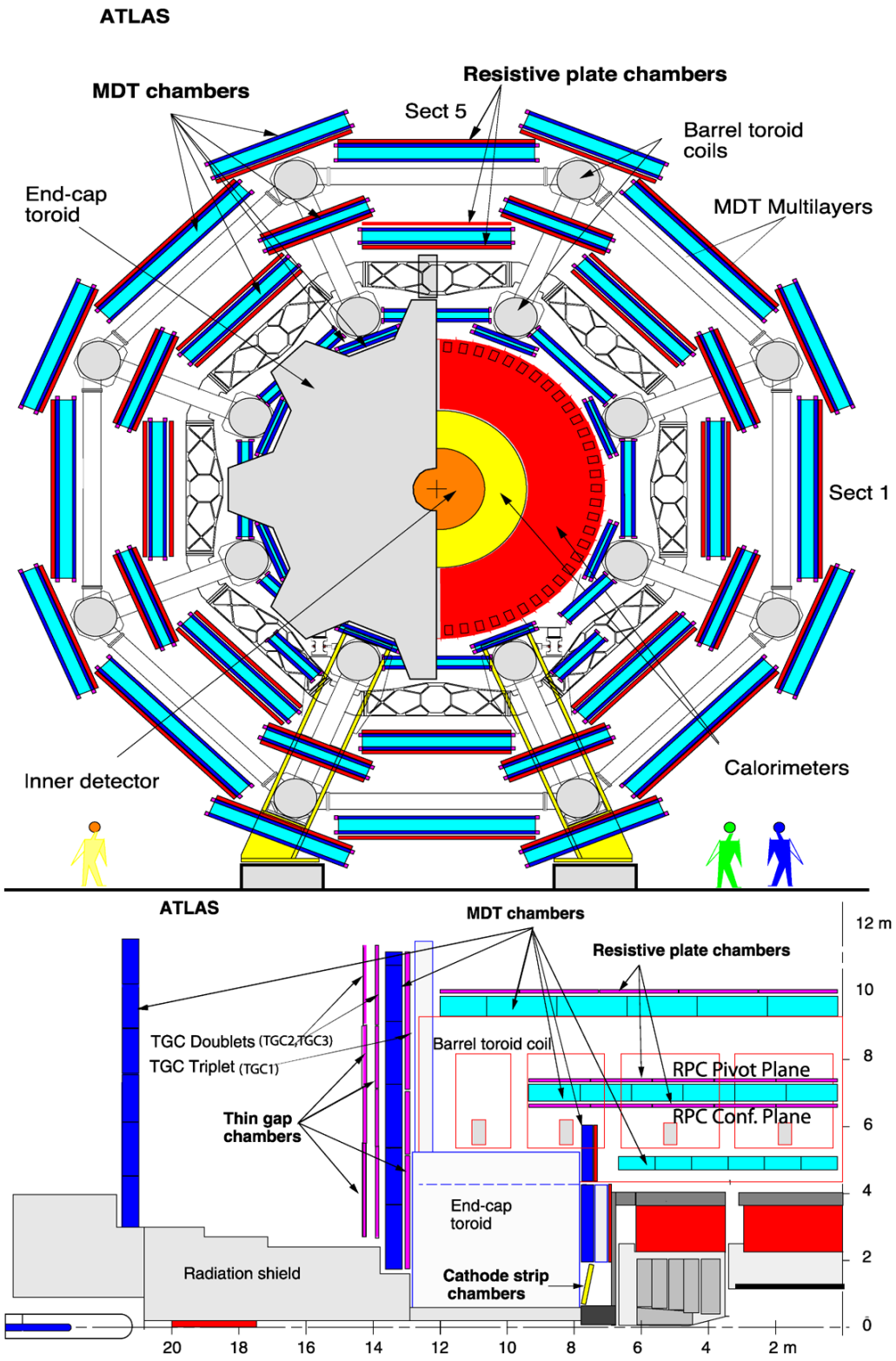

Figure 3.8: Schematic layout of the ATLAS Muon Spectrometer (MS) in the x–y (top) and z-y (bottom) projections. Figure taken from Ref. [56].

tal (x) direction, then in the vertical (y). This provides two bell shaped curves, from which the position of the beam centre and width of the beam can be determined.

In 2014, LUCID was upgraded in an effort to cope with the higher pile-up rate that occurred in the Run II operation of the LHC [58]. The principle behind the detector remains the same, but with some improvements to the electronics and hardware, and added protection against the magnetic fields of ATLAS.

3.8 Data Acquisition and Trigger System

The high rate of pp collisions in the ATLAS detector surpasses the read out and recording capabilities of current technology. Therefore, a sophisticated trigger system is required to use a coarse selection of detector information to determine whether an event is interesting or not. In ATLAS, the trigger system consists of a hardware-based first level trigger (Level-1) and a software-based High Level Trigger (HLT) [59]. Figure 3.9 shows the ATLAS trigger and data acquisition system.

The Level-1 trigger combines information from the calorimeter and muon detectors, which provide a fast read out, to reduce the event rate from the bunch-crossing frequency of around 40 MHz down to 100 kHz in a decision time of 2.5 μs. The Level-1 trigger subsystems feed their information to the central trigger processor (CTP), where a decision is made, based on a programmable menu, to transmit the Level-1 accept message to the various ATLAS sub-detectors. Once broadcast, this triggers all of the subsystems to read out their data to the data acquisition system. During the read out process, the information from the various sub-detectors is cached together for each collision.

Once an event has been assembled, the HLT begins to process the information. The HLT has the capability to combine the Level-1 trigger information with a basic reconstruction of physics objects, which allows more selective criteria to be applied. The HLT trigger menu takes the form of so-called “chains”. Typically around 2500

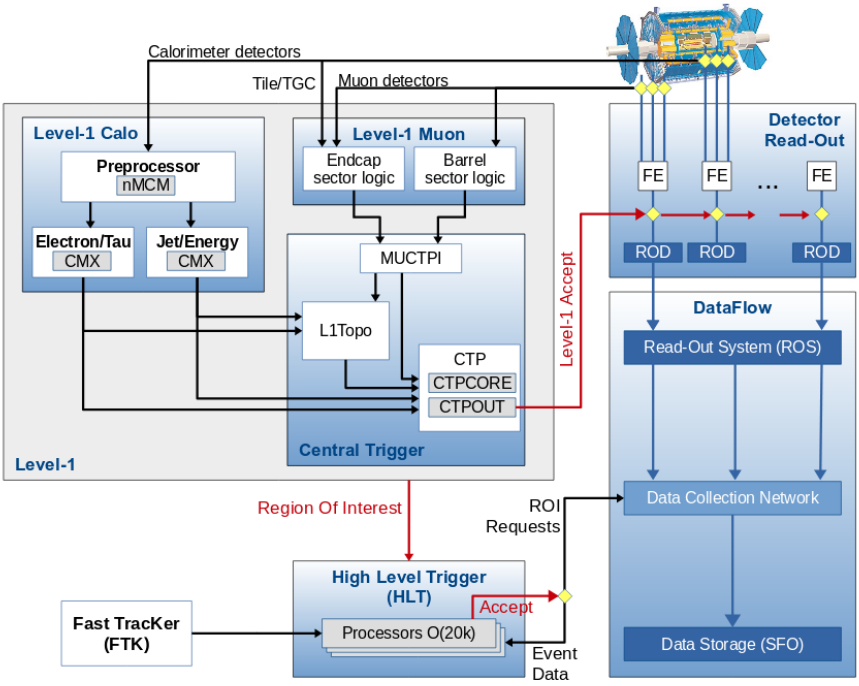

Figure 3.9: Schematic layout of the ATLAS trigger and data acquisition system. Figure taken from Ref. [59].

independent trigger chains are applied. The trigger chains can be focussed on certain reconstructed particles and apply thresholds to tighten the selection. Some chains use loose criteria that can be used by a broad range of analyses; others are more sophisticated and are developed for a specific analysis. Multi-object chains are also possible. A good balance must be found between a loose threshold, to allow freedom to change the analysis selection after data collection, with a suitably tight threshold to avoid the collection rate becoming too high. At the HLT, the event rate is reduced from approximately 100 kHz to around 1 kHz in a processing time of about 200 ms.

3.9 Simulation

An essential part of particle physics analysis involves precisely simulating the pp collisions, the behaviour and interactions of the created particles and their reconstruction in the ATLAS detector. Having this information enables analysts to model

the signatures of important decays and optimise their analysis to separate the interesting signal events from the background events. A range of different event generator programs are available that use Monte Carlo (MC) simulation to model the acceptance of events. Event generators simulate the pp interaction and the subsequent decays based on a set of pre-determined parameters ("tunes"). They also model parton showers, hadronisation and underlying event processes. In some cases, the event generator is only used to simulate the hard interaction and a 'showering program' is used to simulate the other processes. The constituents of the colliding protons are modelled using PDFs; a few different model PDFs are available and each can be applied in the simulation.

The generated events are passed through a detailed GEANT4 simulation of the ATLAS detector [60, 61]. This simulates the interaction of the particles with the detector geometry and material composition. A copy of the generated events is also kept prior to the detector simulation and reconstruction. This is called the truth-sample and represents the exact particles that were produced in each decay and their properties. This provides essential information for understanding the acceptance effects on the data.

Inconsistencies between the reconstruction of events in MC and data are accounted for within analyses by using scale factors and systematic uncertainties. These inconsistencies are measured by using high rate decays and comparing the expected signal with the measured signal.

3.10 Data Sample

The results presented in this thesis are based on the data collected by ATLAS in 2015 and 2016, when the LHC operated at $\sqrt{s} = 13$ TeV during its Run II period. Figure 3.10 illustrates the ATLAS collected integrated luminosity during LHC Run II. Data is classified "good quality" if ATLAS recorded it with all of its systems running well. The peak instantaneous luminosity delivered during each fill

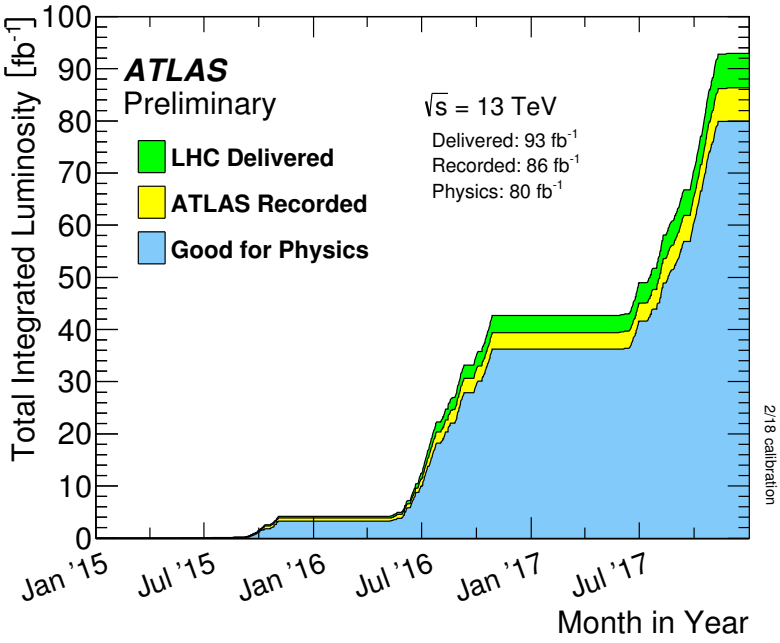

Figure 3.10: Integrated luminosity versus time delivered to ATLAS (green), recorded by ATLAS (yellow) and certified to be "good quality" data (blue) during stable beams for *pp* collisions at 13 TeV centre-of-mass energy in 2015-2017. Figure taken from Ref. [49].

of the 2015 and 2016 data taking is shown in Figure 3.11.

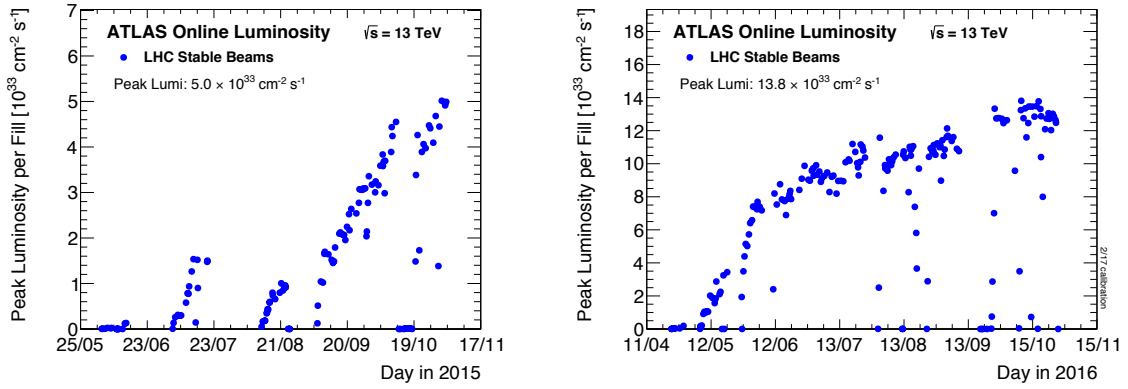

(a) (b)

Figure 3.11: The peak instantaneous luminosity delivered to ATLAS during stable beams for *pp* collisions at $\sqrt{s} = 13$ TeV is shown for each LHC fill as a function of time in (a) 2015 and (b) 2016. Figure taken from Ref. [49].

The average number of interactions per bunch crossing for the $\sqrt{s} = 13$ TeV dataset collected in 2015–2017, is shown in Figure 3.12. The double-peak distribution present in 2017 data collection is due to the implementation of luminosity level-

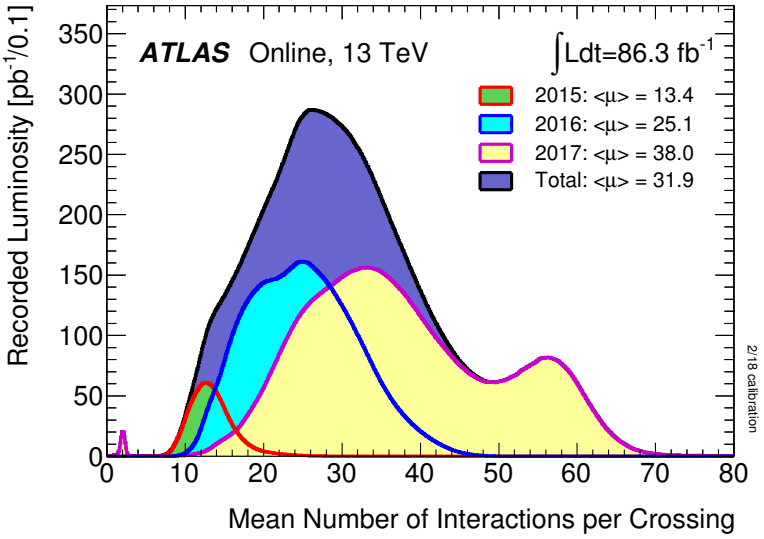

Figure 3.12: Luminosity-weighted distribution of the mean number of interactions per bunch crossing (μ) for the 2015–2017 pp collision data at 13 TeV centre-of-mass energy. The $\langle\mu\rangle$ values given correspond to the average μ value over the year of operation. Figure taken from Ref. [49].

ling. This procedure constrains the pile-up to a manageable level by limiting the instantaneous luminosity from peaks of above 2×10^{34} cm^{-2} s^{-1} to a maximum of 1.5×10^{34} cm^{-2} s^{-1}.

A breakdown of the data samples used for the results presented in this thesis is given in Table 3.1.

Table 3.1: Summary of the $\sqrt{s} = 13$ TeV data samples collected by the ATLAS detector and used for the results presented in this thesis. *IBLOFF* represents a period of running during which the IBL detector was inactive, but data were nevertheless recorded.

Dataset	Data Collected	Data Taking Efficiency	Peak Luminosity [$\times 10^{33}$ cm^{-2} s^{-1}]	Average peak pile-up
2015 - IBLOFF	0.2 fb^{-1}	Unavailable	Unavailable	Unavailable
2015	3.2 fb^{-1}	92.1%	5.0	13.7
2016	32.9 fb^{-1}	92.4%	13.8	24.9

CHAPTER 4

ATLAS PARTICLE RECONSTRUCTION AND IDENTIFICATION

The ATLAS detector applies different criteria to identify the various long-lived particles passing through the detector. The criteria are optimised to minimise the misidentification of particles, whilst maintaining a high efficiency for correct identification. In this section the strategies used by ATLAS are outlined with particular focus on the muon and photon reconstruction due to their crucial role in the $H(Z) \to \mathcal{Q}\gamma$ analysis that is the subject of this thesis.

4.1 Tracks

The reconstruction of charged particle trajectories (tracks) forms an important first step in identifying particles traversing the detector. Comprehensive descriptions of the reconstruction method are given in Refs. [62, 63]. Layers of position sensitive detectors in a magnetic field allow the path of the charged particle to be measured. This trajectory can be extrapolated towards the IP to find where it intersects the path of another particle, in space and time, so as to determine its production vertex. The curvature of the track in the magnetic field enables a momentum measurement to be made. In the simplest terms, the chord length, L, and the distance from the centre of the arc to the centre of its base, known as the sagitta, s, can be combined with the axial magnetic field of the detector, B, to calculate the transverse momentum with

$$p_T = \frac{0.3BL^2}{8s}.$$

A diagram of the geometry is shown in Figure 4.1. The sagitta and chord length can be calculated from its trajectory through multiple layers of detector. In reality, the calculation is more complex and has to take into account energy losses and scattering in the detector, and imperfections in the magnetic field.

In the pixel and SCT detectors, clusters are assembled from the raw measurements. Neighbouring pixels and strips are grouped together when the deposited charge exceeds a certain threshold. Based on these clusters, three-dimensional (3D) measurements of the points where the particle traversed the detector are made, known as space-points. Track seeds are formed from sets of three space-points. The reconstruction algorithm then attempts to build track candidates by incorporating compatible space-points from the remaining layers of the pixel and SCT detectors. It is possible for multiple track candidates to be formed from a seed, for which an ambiguity-solver compares and rates the individual candidates based on their track qualities. A high-resolution track fit is then performed using all of the information for the track candidate. If the track candidate has too many missing space points, too few clusters or contains problematic pixel clusters then the track candidate will

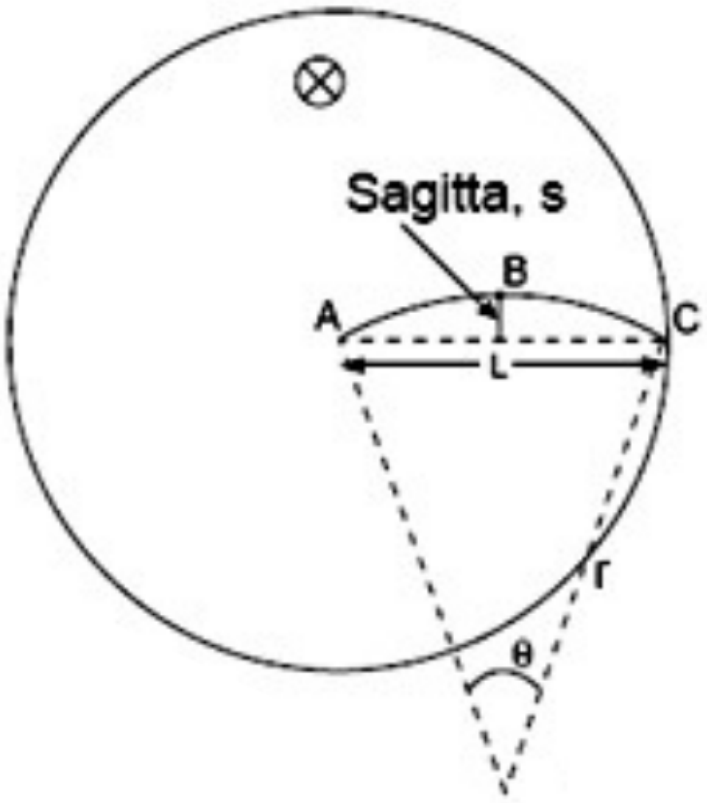

Figure 4.1: Geometry used in particle momentum measurements.

be rejected. Otherwise, the track candidate will be kept for the final collection. An extension into the TRT subdetectors is also performed, where compatible TRT measurements are included using an extension algorithm. Consecutively, an outside-in sequence is used, where track seeds are found in the TRT and then matched to clusters in the pixel and SCT detectors. This reverse process can find small track segments in the pixel and SCT, which might have been unable to form their own track seeds.

4.2 Muons

In ATLAS, muons can be detected in both the ID and MS, as well as in the calorimeters. Their momentum is measured separately in the ID and MS. A more detailed summary of the muon reconstruction, identification and performance can be found in Ref. [64], with a general overview given here. Four different muon 'types' are defined based on which subdetectors are used in reconstruction:

- **Combined (CB) muons** are the most common type used in ATLAS analyses. A combined track is formed using the hits in both the ID and MS subdetectors. CB muons have the lowest misidentification frequency of the muon types.
- **Segment-Tagged (ST) muons** are used when muons cross only one layer of MS chambers, either due to their low p_T or because their trajectory is within a region of reduced MS acceptance. These muons are identified by an ID track, which can be extrapolated to a hit in an MS segment. In such a case, the ST muons adopt the parameters of the reconstructed ID track.
- **Calorimeter-Tagged (CT) muons** have the lowest purity of all of the muon types. They are the result of an ID track being matched to an energy deposit in the calorimeter that is compatible with a minimum-ionising particle. The track parameters of the ID track are assigned to the muon.

- **Extrapolated (ME) muons** are defined when the reconstruction is based only on an MS track and with a loose requirement that the track originates from the IP. In the barrel, two layers of MS chambers recording hits are required, while three layers are required in the forward region. The track parameters are determined by extrapolating the MS track back to the IP, accounting for the estimated energy loss of the muon in the calorimeters.

Various algorithms based on the information provided by the ID, MS and calorimeters are used to sort the muons into the different types. These muon types are defined exclusively. Overlaps between different muon types are resolved before producing the collection of muons used in physics analyses. When an ID track is shared, preference is given to CB muons, then ST, with CT receiving lowest priority. Overlap of muon types with tracks in the MS are resolved by selecting the track with more hits and a better track fit quality.

The ATLAS muon group provides four operating points for muon identification and selection (*Loose*, *Medium*, *Tight* and *High-*p_T), which are designed to meet the varying needs of different physics analyses:

- **Loose muons** are designed to maximise the reconstruction efficiency while providing good-quality muon tracks. All of the muon types are used.
- **Medium muons** are the default selection for muons in ATLAS. Only CB and ME muons are used. This selection is optimised to minimise the systematic uncertainties associated with muon reconstruction and calibration. A loose requirement on the compatibility between ID and MS momentum measurements is applied to suppress the contamination due to hadrons misidentified as muons.
- **Tight muons** are selected to maximise the purity of muons, but at the cost of some efficiency. Only CB muons with hits in at least two layers of the MS are considered.

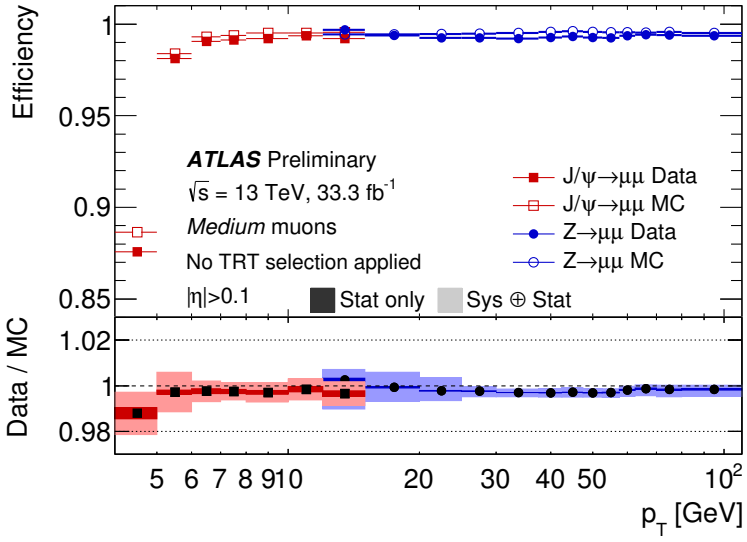

Figure 4.2: Muon reconstruction efficiencies for the Medium identification algorithm measured in $J/\psi \to \mu^+\mu^-$ and $Z \to \mu^+\mu^-$ events as a function of the muon momentum. Figure taken from Ref. [65].

- **High-p_T muons** aim to maximise the momentum resolution for tracks with transverse momentum above 100 GeV. CB muons passing the Medium selection and having at least three MS hits are selected. This selection results in a 30% improvement on the p_T resolution of muons above 1.5 TeV compared to the other muon types.

The Loose, Medium and Tight selections are inclusive, i.e. the muons within the tighter selection are also included in the looser selection.

The focus of most ATLAS analyses is on the identification of heavy particles such as the W, Z, or Higgs bosons. The decay of these into muons usually results in the muons being isolated from other particles. Therefore, a useful discriminant from background events is to measure the detector activity near a muon track, which is known as the muon isolation. Two variables are used; one variable sums the p_{T} of all tracks within a variable cone size of $\Delta R = \sqrt{(\Delta\phi)^2 + (\Delta\eta)^2} = 10\ \mathrm{GeV}/p_T^{\mu}$, up to a maximum cone size of $\Delta R = 0.3$, around the muon; while the second is a calorimeter-based isolation variable, which is the sum of the transverse energy of topological clusters in a cone of size $\Delta R = 0.2$ around the muon. The selected muon

p_{T} and energy deposit, as well as pile-up effects, are accounted for in both variables.

4.3 Electrons

A thorough description of the electron reconstruction and identification used by ATLAS in Run II can be found in Ref. [66]. Electron objects are reconstructed by first finding electron-like deposits in the EM calorimeter and then checking the ID for any tracks along the same trajectory. The selected ID track is then refitted with the centre of the EM cluster as an added hit. This final combination of the EM cluster and refitted track is defined as the electron candidate. In a similar manner to the muon identification, three levels of identification operating points are defined: *Loose*, *Medium* and *Tight*. The level is determined using algorithms in which a range of cut-based and likelihood-based methods are implemented.

The electron identification efficiency as a function of the transverse energy for the three different operating levels can be seen in Figure 4.3. In general, ATLAS operates at a 90% or higher efficiency for high energy electrons.

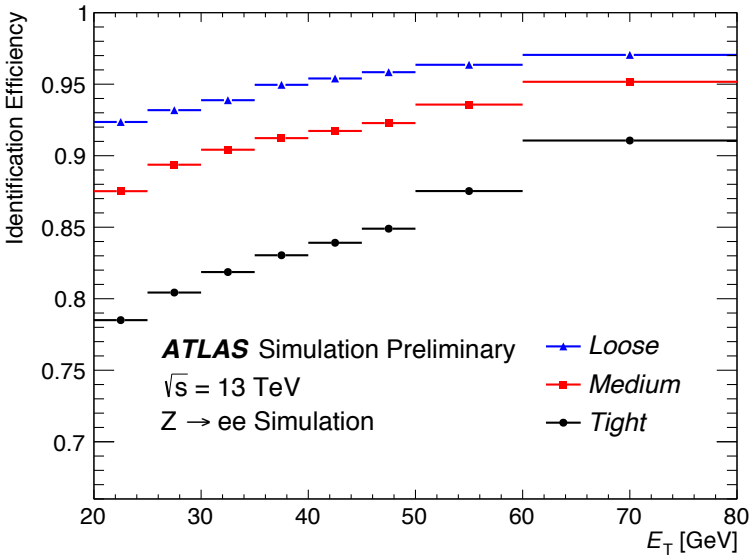

Figure 4.3: The efficiency to identify electrons from $Z \to e^+e^-$ decays. Figure taken from Ref. [66].

ATLAS also defines electron isolation variables to provide a further discriminant

between signal and background. The variables quantify the energy of the particles produced around the electron candidate to provide a distinction between isolated electrons, originating from heavy resonance decays, and non-isolated electrons that originate from converted photons, heavy flavour hadron decays or light hadrons misidentified as electrons. Two different variables are used: a calorimeter isolation variable and a track isolation variable. ATLAS analyses that search for electrons use either or both of these variables to reduce the number of background events.

4.4 Photons

Photon reconstruction begins in a similar manner to electron reconstruction. The EM calorimeter is searched for energy deposits resembling a photon; however, no matching tracks in the ID are required. A detailed description of the reconstruction and identification of photons with the ATLAS detector is given in Ref. [67]. The ID is searched for any tracks that are loosely matched to the EM clusters in order to identify and reconstruct electrons and photon conversions. Tracks consistent with originating from a photon conversion are used to create conversion vertex candidates, which are then matched to the EM clusters. Once determined, an algorithm is used to decide whether an EM cluster corresponds to an unconverted photon, a converted photon or an electron. It does this based on matching the cluster to conversion vertices or tracks and also on the four momenta of the cluster and tracks.

Two sets of reference identification selection criteria are used for photons: *Loose* and *Tight*. The Loose selection is based only on shower shapes in the second layer of the EM calorimeter and on the energy deposited in the hadronic calorimeter. It is designed to provide a high prompt-photon identification efficiency with respect to reconstruction, where prompt photons are those that have not originated from the decay of hadrons. The efficiency rises from 97% at $E_T^\gamma = 20$ GeV to above 99% for $E_T^\gamma > 40$ GeV for both converted and unconverted photons. The Tight selection includes extra information from the finely segmented strip layer of the calorimeter.

The efficiency of the Tight selection as a function of transverse energy is shown in Figures 4.4 and 4.5 for the unconverted and converted photons, respectively. The efficiency is calculated using three different data-driven methods as described in Ref. [68] and increases from 53–64% (47–61%) for unconverted (converted) photons at $E_T \approx 10$ GeV to 88–92% (96–98%) for $E_T \approx 100$ GeV.

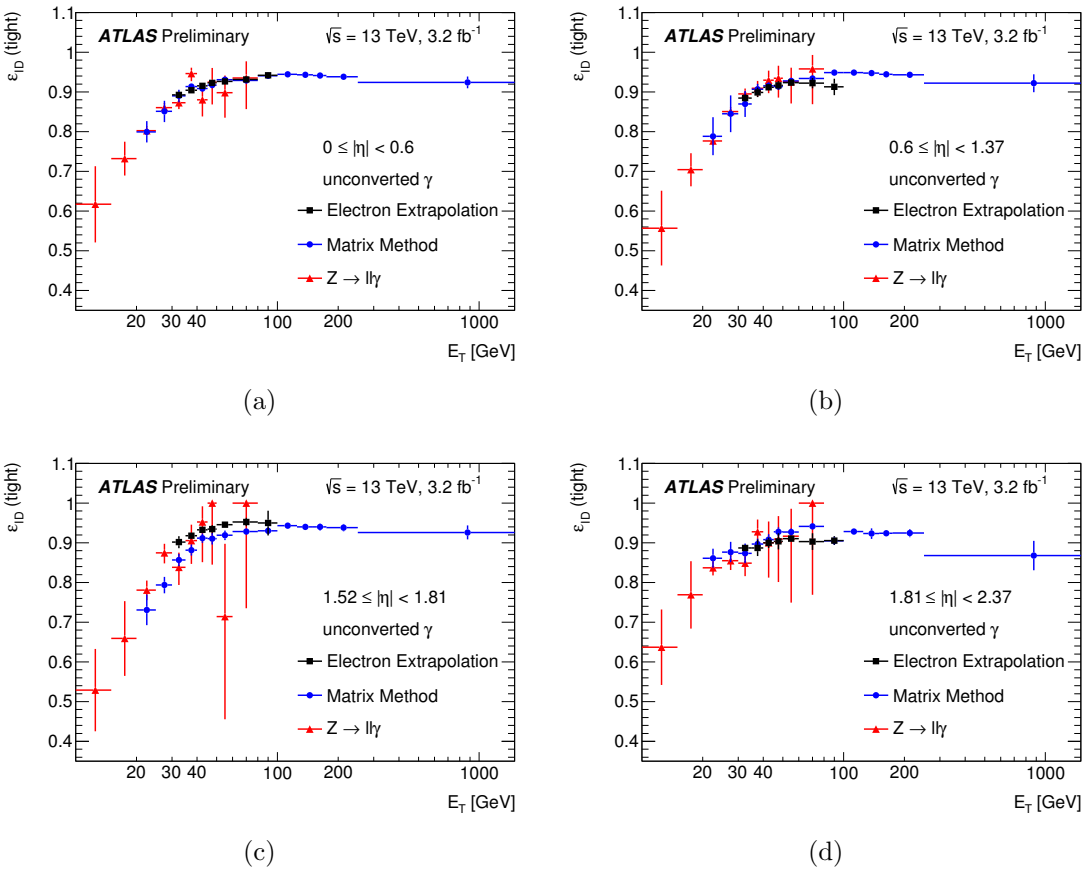

Figure 4.4: Tight identification efficiency using three different data-driven measurements for unconverted photons as a function of the transverse energy, E_T, in the region 10 GeV $\leq E_T \leq$ 1500 GeV, for four pseudorapidity intervals. Figure taken from Ref. [68].

Track and calorimeter isolation variables can be used to reduce hadronic background. The calorimeter isolation variables, E_T^{iso}, are computed from three-dimensional topological clusters of calorimeter cells [69] in a cone around the photon candidate. Contributions from the photon, the underlying event and pile-up are all subtracted from the E_T^{iso} variables. Two different calorimeter isolation variables are used: one with a cone size of $\Delta R = 0.2$ and another with $\Delta R = 0.4$. For the track isolation variable,

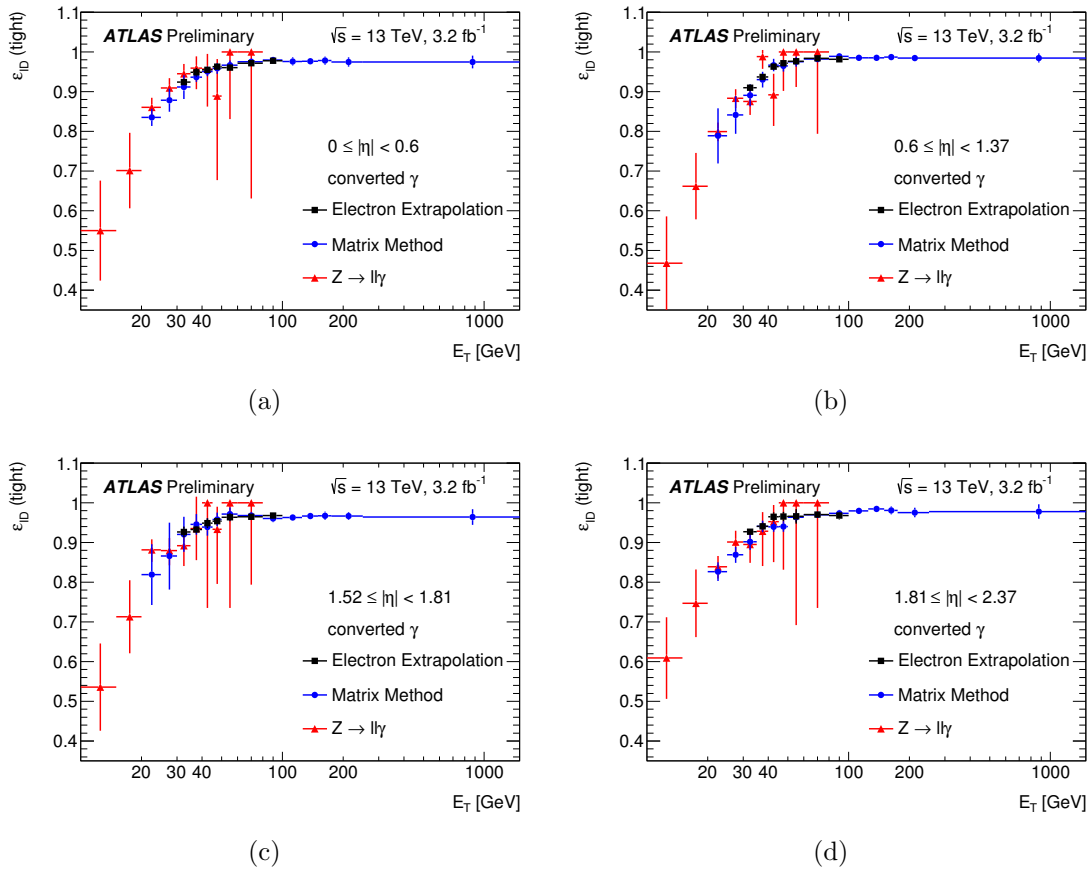

Figure 4.5: Tight identification efficiency using three different data-driven measurements for converted photons as a function of the transverse energy, E_T in the region 10 GeV $\leq E_T \leq$ 1500 GeV, for four pseudorapidity intervals. Figure taken from Ref. [68].

one cone size of $\Delta R = 0.2$ is used.

4.5 Jets

For the analyses of Higgs and Z boson decays to a meson and a photon, none of the final state objects are observed as a jet within the detector. Jets do, however, form an important background in the analyses, either as the origin of particles of interest or through misidentification as a photon. A complete discussion of the jet reconstruction in ATLAS is beyond the scope of this thesis; however, a detailed account can be found in Ref. [51]. Essentially, jets are reconstructed in ATLAS

using the anti-k_t algorithm [70], which combines information from topological clusters of calorimeter cells. Further algorithms are used to "tag" jets based on the assumed original particle. These algorithms distinguish jets produced by b and c quarks from lighter quarks by using features of the jet such as opening angles, displaced secondary vertices, impact parameters and transverse momenta of the decay products. Optimising the performance of these taggers plays an essential part in the direct analyses of $H \to b\bar{b}$ and $H \to c\bar{c}$, which are complementary to the searches described in this thesis.

4.6 Other Physics Objects

A description of the methods for reconstruction of other physics objects in ATLAS, such as tau leptons and missing transverse energy, is outside the field of reference for this thesis. A comprehensive review of all of the reconstruction methods used by ATLAS can be found in Ref. [51].

CHAPTER 5

TESTING THE IRRADIATION HARDNESS OF SILICON SENSORS AT THE UNIVERSITY OF BIRMINGHAM

5.1 Introduction

The University of Birmingham is one of a consortium of institutes that characterises prototype silicon strip sensors pre- and post-irradiation using the University of Birmingham Medical Physics cyclotron [71]. This is to assess the consequences for detector performance after a high dose (10^{15} 1MeVn$_{eq}$/cm^2) of proton irradiation, equivalent to the expected dosage over the High Luminosity-LHC lifetime. This chapter describes the commissioning of a silicon sensor test system at Birmingham. This involved the design and implementation of the system, as well as the analysis of several silicon sensors in an effort to obtain certification of the Birmingham

cyclotron as an irradiation centre.

5.2 High-Luminosity Upgrade of the LHC

Plans have been devised and approved to upgrade the peak luminosity of the LHC starting at the end of 2023 in order to obtain as much data from the collider as possible in the phase named the High Luminosity (HL) LHC. The upgrade will increase the annual integrated luminosity by a factor of 10 and the peak luminosity up to $\mathcal{L}$ =7.5 $\times$ 10^{34}cm^{-2}s^{-1} [72]. The predicted evolution of the peak and integrated luminosities are shown in Figure 5.1, with the third long shutdown (LS3), referred to as the Phase II upgrade period, expected to last around 30 months.

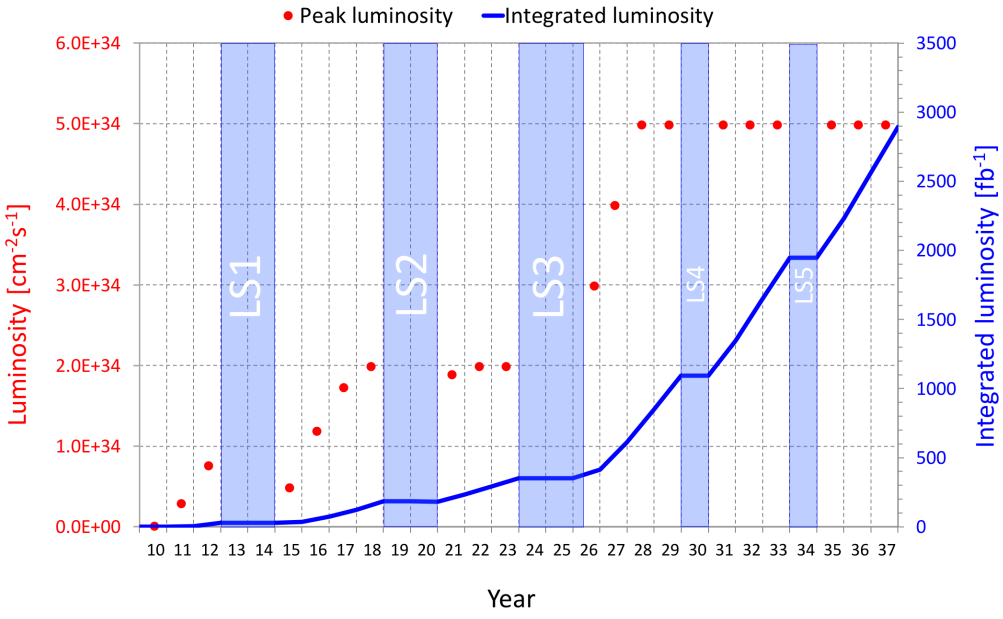

Figure 5.1: LHC luminosity forecast until 2037, both peak (red dots) and integrated (blue line). Main Long Shutdown (LS) periods are indicated. Figure taken from [73].

The implication of such a large increase in peak luminosity during the upgrade is that there will be a corresponding increase in the rate of particles requiring detection. In preparation for this planned upgrade of the LHC, ATLAS will require large improvements to sustain its performance in the future. There are two main areas of focus for the changes to the ATLAS detector. Firstly, the new detector systems

must be resistant to higher levels of radiation damage at this unprecedented luminosity. Secondly, they need to be capable of handling an increase in trigger rates and detector occupancy[i] to minimise deadtime and, consequently, lost events [74].

During the HL-LHC operation, the calorimeters can expect particle fluxes and the average energy deposited in the calorimeters to be five to ten times higher than the original LHC design values [75]. At these levels, the 15-20 year old read out electronics will need to be replaced and upgraded. Similarly, the MS requires an upgraded read out system to cope with the greater particle fluxes.

The ID will undergo the largest change for the HL-LHC; an all-silicon replacement known as the Inner Tracker (ITk) will succeed the ID. The relatively poor occupancy capabilities of the TRT will result in it being replaced by an extended silicon strip tracker. There will be six full-length barrel layers stretching across radii in the range 405 mm $\leq$ R $\leq$ 1000 mm; three inner layers with strips of 23.8 mm in length and two outer layers with 47.8 mm long strips [74]. A 'stub' layer, with 47.8 mm long strips, provides an extra layer of detection, as shown in Figure 5.2. The pixel detector will utilise n^+-in-n sensors of size 25 $\times$ 150 μm^2, close to the beam pipe between radii 39 mm $\leq$ R $\leq$ 250 mm. For cost reasons, outer pixel sensors will use n-in-p technology and be of a larger 50 $\times$ 250 μm^2 size [74]. The pixel detector will have 8.2 m^2 of active silicon area and 638 million channels, compared to the 193 m^2 of active silicon area and 74 million channels in the strip detector [74].

[i]Occupancy is the number of particles traversing a detector per bunch crossing

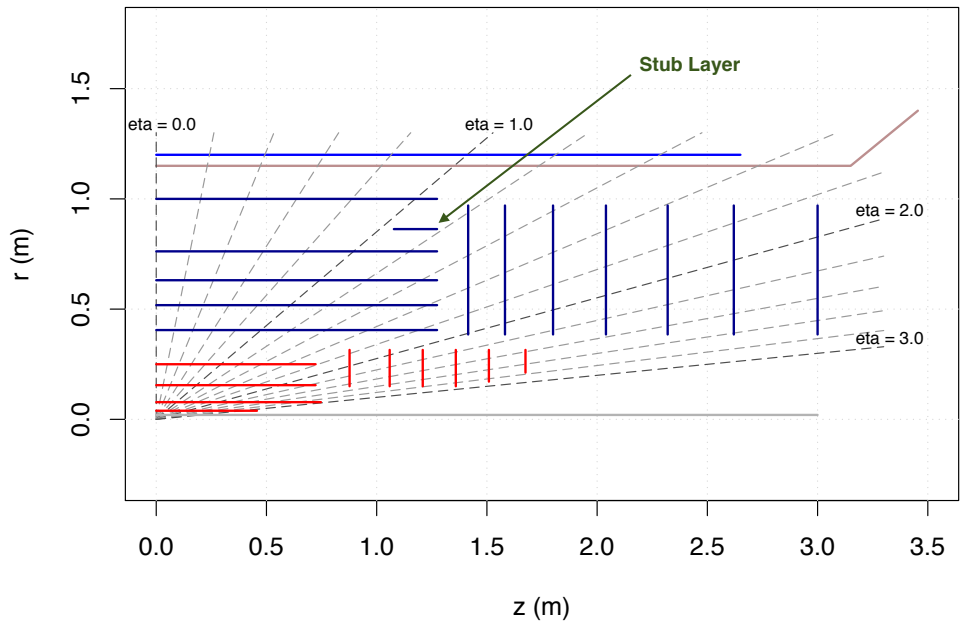

Figure 5.2: Proposed layout of the ATLAS Inner Tracker (ITk); pixels in red and strips in blue. Figure taken from Ref. [74]

5.3 Physics of Silicon Sensors

Silicon is a well-understood type IV element with low intrinsic conductivity. A passing Minimum Ionising Particle (MIP)[ii] will most likely deposit 3.5 fC of charge in 300 μm of silicon [76]. This charge is negligible compared to the intrinsic free charge of silicon that originates from thermal excitation. Silicon is doped with type III (boron) and V (phosphor) elements to increase the conductivity by providing extra holes (p-type acceptors) and electrons (n-type donors), respectively. The notation n^+ and p^+ are used to represent high doping levels, n and p represent moderate levels, and n^- and p^- are used for low dopant concentrations. The interface between p- and n-type silicon (p-n junction) creates a 'depletion region', where diffusion of the free charges across the junction results in a region of recombination and removal of free charges.

[ii] A MIP is a particle that is at such a momentum that it loses only a small fraction of its energy by interactions with the matter it passes through.

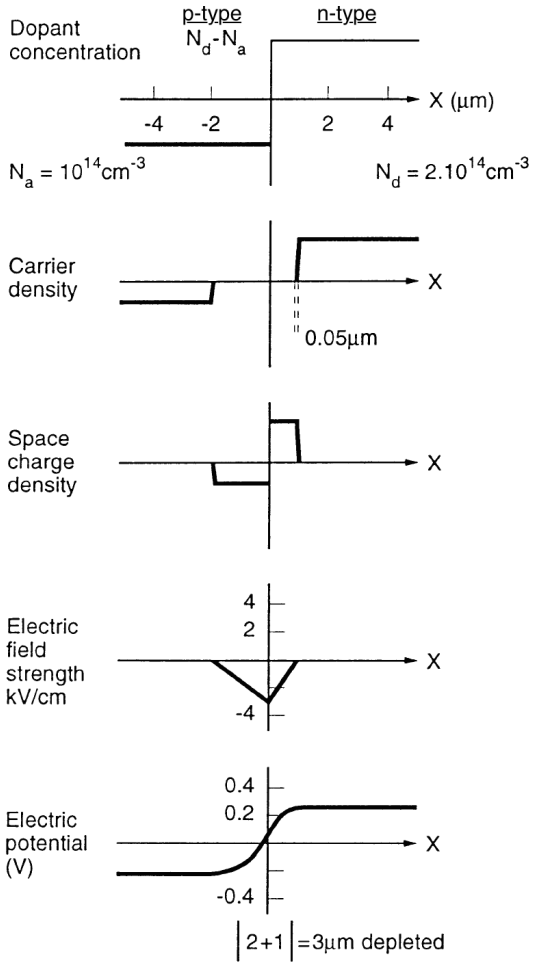

Figure 5.3: Summary of various quantities across an unbiased p-n junction. N_d and N_a are the dopant concentration of donors and acceptors respectively. Carrier density is the density of free charge carriers, where at the p-n junction the charge carriers are depleted. Space charge originates from an excess or lack of electric charge in the material as a result of the small current across the junction. The effect of the space charge is that it alters the electric field in the region, which gives rise to a gradual step in the electric potential. Figure taken from [77].

Figure 5.3 gives a summary of some of the characteristics induced by the p-n junction. In the depletion region, the free-charge carrier density is reduced to zero and an excess of charge (space charge) is contained within the region. This is exemplified by the change in electric potential over the region, which results in an electric field being created that behaves as a potential barrier. An equilibrium is reached, where electron-hole pairs are generated by thermal excitation in the depleted silicon

but are balanced by charge carriers with sufficient energy that drift in the opposing direction across the region.

A bias voltage applied across the sensor will result in diode behaviour. Current flow rises exponentially when the voltage polarity has p-implants positive with respect to n-implants, while in the opposite,"reverse biased" configuration, increased voltage simply increases the width of the depletion region, with a small current resulting from thermal generation of electron-hole pairs in this region. Up to the sensor depth[iii], the thickness of the depletion region, W, follows a square-root relationship with the voltage,

$$W = \sqrt{\frac{2\epsilon}{q_e} \times \frac{V}{N}}, \tag{5.1}$$

where V is the bias voltage, q_e is the electron charge, N is the density of dopants and ϵ is the permittivity of silicon [77]. There is a linearly decreasing field with distance from the p-n junction.

A passing charged particle will liberate electrons and holes by ionisation inside the depleted region, which will drift in the electric field towards and away from the p-n junction. The energy directly deposited by the MIP is formed by two separate components: a Gaussian distribution from low-energy transfers in the ionisation of the silicon's atoms and a high-energy component that originates from a small number of electrons being excited via collisional scattering. These scattered electrons create a separate trail of ionisation, which contributes to the overall energy deposited and gives rise to a high-energy tail in the signal distribution. This shape of distribution is known as the Landau distribution [78] and an example is shown in Figure 5.4. The most probable signal value (the position of the maximum) is approximately proportional to the thickness of the depletion region and therefore has the same $\sqrt{V}$ relationship as Equation 5.1.

Damerell's review [77] provides a detailed account of the physics behind silicon sensors; a general overview, based on [77], is given in this chapter. A typical schematic

[iii]The sensor depth is the depth of the silicon bulk in the sensor (usually 300μm thick)

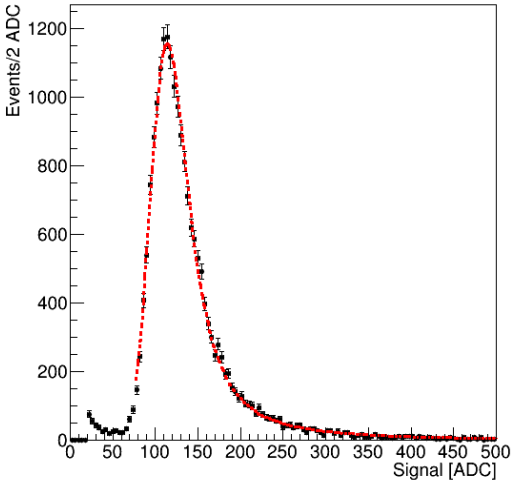

Figure 5.4: An example of the Landau-shaped signal distribution for a sensor pre-irradiation. Signal is in Analog-to-Digital Converter units (ADC). Each entry corresponds to the signal detected from a passing MIP. The dashed red line is the best-fit of a Landau distribution to the signal distribution.

diagram of a silicon sensor is shown in Figure 5.5. In this design, the sensor is composed of a bulk material of n-type silicon, with a thin and narrow strip of p-type silicon embedded in the front surface of the sensor. Holes formed in the depletion region will be pulled toward the p-strip and be received by aluminium electrodes connected to the p-strips, which pass the signal to external circuitry. A heavily doped n^+ backplane provides a low-resistance ohmic contact.

The damage caused by irradiation to silicon sensors can be divided into two dominating effects: bulk damage and surface damage. Michael Moll's thesis [79] has a thorough discussion of his research into the radiation damage caused to the bulk material of silicon sensors. Only a condensed summary of this material will be given here, but a significant portion of the thesis is relevant in understanding the issues that can develop during the investigations conducted in this project.

The primary cause of bulk damage is due to high energy hadrons displacing a Primary Knock-on Atom (PKA) out of its lattice site, which results in a Frenkel pair[iv]

[iv] A Frenkel pair is a vacant lattice site and a dislodged atom that has become interstitial between other lattice atoms

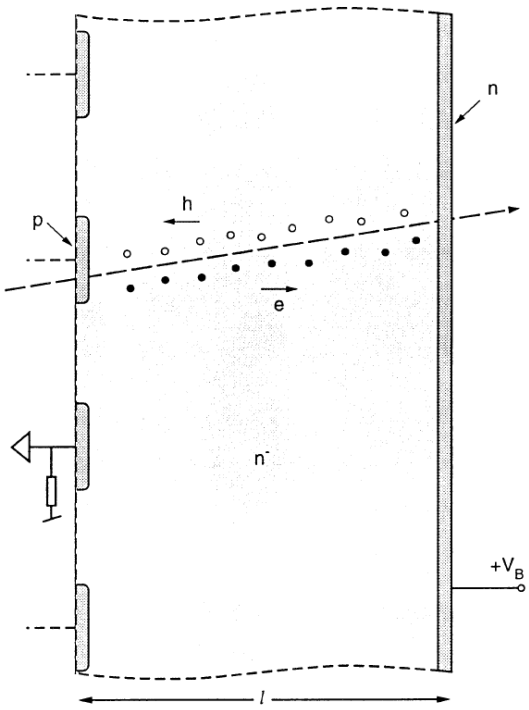

Figure 5.5: Schematic diagram of a typical silicon sensor. Figure taken from Ref. [77].

that can migrate through the lattice and develop into a defect in the silicon. Further displacement and ionisation will occur if the recoiling atom is suitably energetic, as shown in Figure 5.6. At the end of a recoiling atom's path, the energy loss due to the displacing of further PKAs will dominate and a dense agglomeration of defects is formed (a cluster). The essential radiation-induced changes in macroscopic detector properties due to bulk damage are an increase in leakage current[v], a degradation in charge collection efficiency[vi] and a change in the effective doping concentration[vii]. The last of these effects corresponds to a change in the depletion voltage and has the most detrimental impact on detector operation.

A problem with the p-in-n arrangement (shown in Figure 5.5) is that defects created

[v]The consequence of some defects having a smaller threshold for ionisation by thermal energy compared to the non-defected atoms

[vi]Some defects will capture drifting charge carriers and the delay of re-emission will be longer than the shaping time of the electronic readout

[vii]Defects contribute to the number of free charge carriers

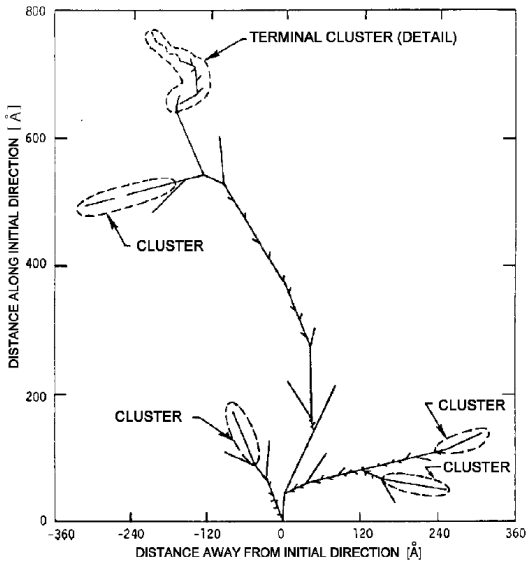

Figure 5.6: Monte Carlo simulation of a recoil-atom track causing damage to the bulk of the detector. Figure taken from Ref. [79].

by radiation damage from hadronic particles (pions, protons, neutrons, etc.) remove donor atoms and generate acceptor-like states in the silicon bulk. In the fluences of the HL-LHC, the radiation damage will have such an effect that the n-type silicon will change to behave as p-type silicon and increase the voltage required to reach full depletion. If the arrangement is instead reversed to have n-in-p, the bulk p-type silicon will behave even more like heavily p-doped silicon as the fluence of radiation damage increases. The n-in-p silicon sensors are much more radiation hard, but have a new issue of their own; silicon dioxide is used as a protective layer on the front end of the sensor and after accumulated damage this will create an excess positive charge at the surface, which attracts a thin layer of electrons from the bulk material [80]. Surface damage is predominantly the result of ionisation in the silicon dioxide layer. As illustrated in Figure 5.7, the ionisation liberates many holes and pairs in the dioxide layer; after an initial recombination, the charge begins to drift depending on the voltage applied. A build up of charge begins to form at the interface between the dioxide layer and the silicon, which causes a similar effect in the bulk. In the original p-in-n type sensor, the electrons are opposed by the negatively charged dopant atoms in the strips. The n-in-p type does not repel the negative charge

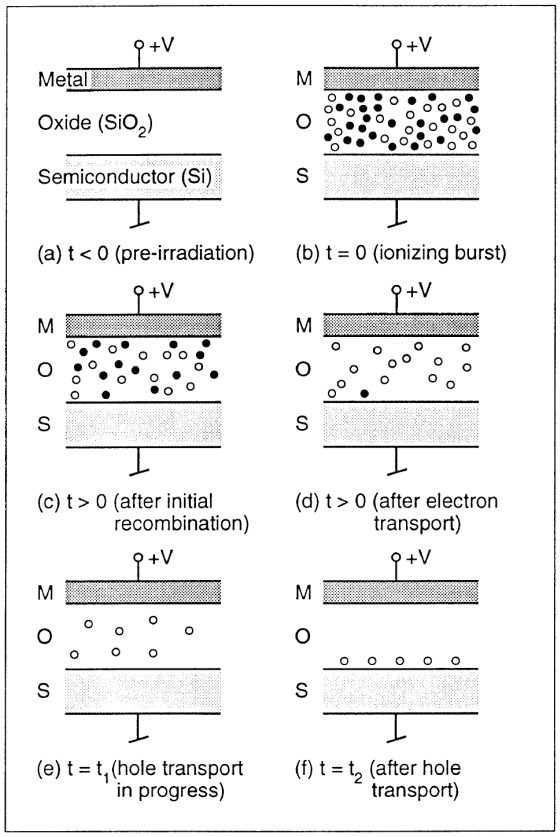

Figure 5.7: A step-by-step diagram of the surface damage in the silicon dioxide. Figure taken from Ref. [77].

build up and instead the electrons form a bridge between strips that allows signal electrons to flow easily between neighbouring strips. An innovative solution to this problem involves adding heavily doped p^+ silicon implants (p-stop) in between the n-strips, which effectively remove the negative charge build up at the surface [77]. A second, alternative solution is to use a p^+ spray, which covers the entire surface in a p^+ layer.

Moll's thesis [79] also covers the effect of annealing silicon in considerable detail, i.e. the diffusion of defects within the material accelerated by heat. The Frenkel pairs are very mobile at room temperature causing them to migrate through the silicon lattice until they are almost completely trapped at impurities and defects. This process gives rise to further defects and defect reactions, so it is essential to minimise this effect by storing irradiated sensors in a freezer. An interesting property

of annealing devices is that there is a short term beneficial annealing component N_A, shown in Figure 5.8, which is the result of the very mobile process of Frenkel pairs recombining. The result of this component is that heating the sensor at 60°C for 80 minutes will reduce the depletion voltage. Longer than this time period will result in an increase in depletion voltage. Another characteristic of annealing is a reduction in leakage current, which continuously decreases with respect to the duration of the annealing. Therefore, the change in current after annealing can be used to ensure that annealing has been successfully performed on the sensor.

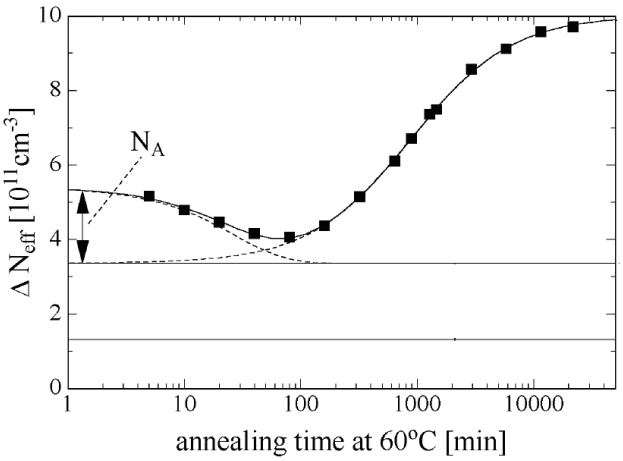

Figure 5.8: Annealing behaviour of the radiation induced change in the effective doping concentration, ΔN_{eff}, where ΔN_{eff} is the difference between the doping concentration before irradiation and at its current state. Figure taken from Ref. [79].

Characterising the effects of irradiation and annealing on silicon sensors is essential for predicting their performance in the fluences of the HL-LHC. The degradation of signal resulting from damage to the bulk of the silicon has been well-researched before and during the operation of previous detectors; however, the consequences of surface damage from choosing the less familiar n-in-p silicon sensors is still not fully understood. Measurements described in Section 5.6 aim to replicate the effects of the HL-LHC on n-in-p silicon sensors and provide valuable insight into the damage caused.

5.4 ATLAS Silicon Sensors

Prototype n-in-p silicon strip sensors are being developed for the ATLAS ITk upgrade. Two different generations of ATLAS n^+-in-p silicon miniature sensors were irradiated and tested for the studies presented in this chapter: ATLAS07 sensors [81], which have an unirradiated depletion voltage of around 200V; and ATLAS12 sensors with a higher depletion voltage of around 300V. A comprehensive journal article on the ATLAS12 design and specifications describes the new features present in the sensor [82]. The change in depletion voltage originates from the different resistivities of the sensors. The miniature sensors are developed with 104 strips compared to the nominal 1280 strips, where each strip corresponds to a readout channel. The depths of the sensors are 320 μm and 310 μm for the ATLAS07 and ATLAS12 sensors, respectively. Both sensors have a strip pitch width of 74.5 μm. The miniature sensors use the same material and structure as the main design, but their smaller size makes them easier for production and testing. In the following sections, all references to sensors imply these miniature sensors.

The Birmingham cyclotron [71] is among several facilities around the world that test the silicon strip sensors for radiation hardness by irradiating them at the fluences expected at the HL-LHC. The University of Birmingham ITk Group is part of the consortium testing the performance of sensors before and after irradiation. Sections 5.5 and 5.6 describe the assembling and commissioning of a silicon sensor testing facility in Birmingham, similar to ones already used elsewhere.

5.5 Sensor Testing and Irradiation

All testing is carried out using "A Liverpool Barcelona Valencia" (ALiBaVa), which is a commercially-available portable readout system designed for prototype microstrip detectors [83]. The silicon sensor is connected to a daughter board that contains 128 channel readout chips, and which receives commands from a mother

board linked to a PC. An external trigger system must be constructed to synchronise the readout with the passing charged particles. A basic schematic diagram is shown in Figure 5.9.

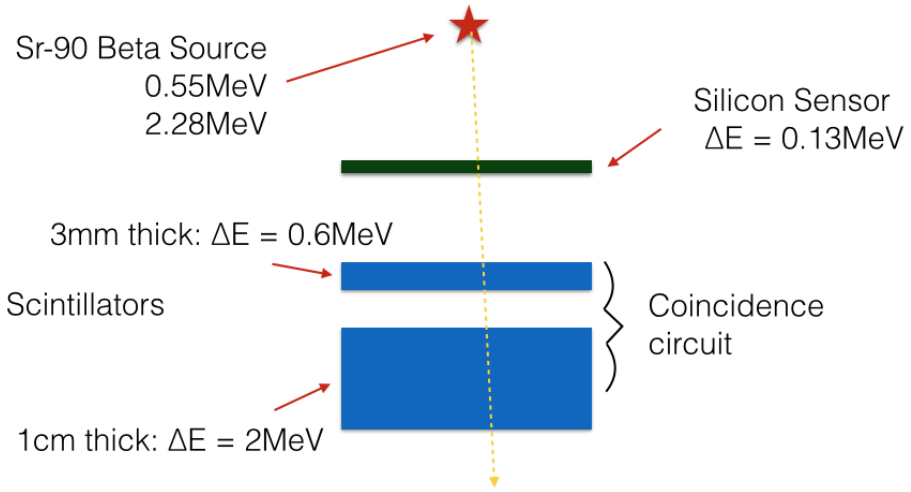

Figure 5.9: A simple schematic diagram of the silicon microsensor test system. A strontium-90 source is positioned above the silicon sensor; β particles emitted by the source pass through the sensor and also through two scintillators that are aligned beneath the sensor. The two scintillators are connected to photo-multiplier tubes and behave as triggers for the signal to be read off the sensor.

An 80 MBq ^{90}Sr source is used for its β^--emitting decay chain, shown in Figure 5.10; ^{90}Sr decays to ^{90}Y with the emission of a 0.55 MeV β^- particle, and the daughter ^{90}Y nucleus decays to ^{90}Zr via 2.28 MeV β^- emission. The electrons from the 2.28 MeV decay mostly behave as MIPs and are therefore ideal for testing the sensors.

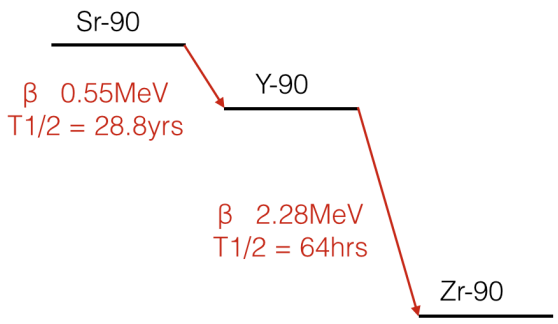

Figure 5.10: The β-emitting decay chain of ^{90}Sr. ^{90}Sr decays via a 0.55 MeV β emission to ^{90}Y, which subsequently decays to ^{90}Zr by a 2.28 MeV β emission.

Two scintillators connected to photo-multiplier tubes are used as a trigger system. The scintillators, sensor and source are all aligned such that an emitted β particle incident on the sensor will also trigger the readout. The ALiBaVa mother board has a coincidence circuit built in to minimise spurious triggers. The components are assembled in a modified box for portability and protection. A 3D design drawing of the setup is shown in Figure 5.11.

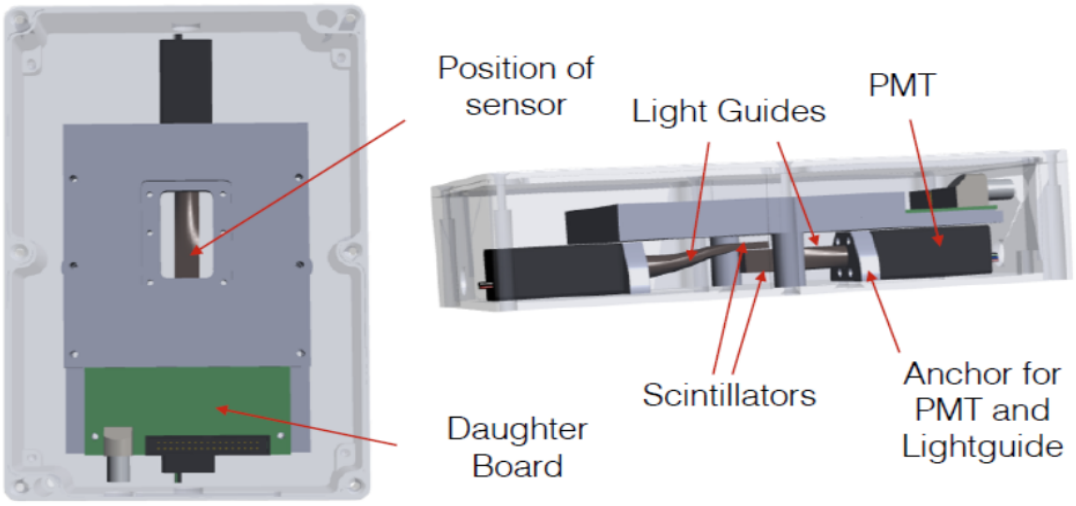

Figure 5.11: A 3D rendered drawing of the box containing the ALiBaVa daughter card and scintillator triggers. The position of the sensor is aligned with the scintillators and source.

Silicon sensors are tested both before and after irradiation and then after annealing at 60°C for 80 minutes (see Section 5.3). Sensors are irradiated with 27 MeV protons (beam currents 50-500 nA) at the Birmingham MC40 Cyclotron [71, 84]. The fluence of proton irradiation, once corrected to the equivalent dose for 1 MeV neutrons (10^{15} n_{eq}/cm^2), is representative of the expected dosage from operation over the lifetime of the HL-LHC. Sensors are mounted in 3×3 frames using Kapton tape and string, as shown in Figure 5.12. The frame is then fixed inside a temperature-regulated cold box. This cold box, or thermal chamber, allows accurate control of temperature, humidity, light tightness and electrical shielding. A nitrogen gas feed controls the humidity inside the box and a thin double-skinned Polyamide window is used to allow beam entry. The box is placed on a scanning robot, which moves the box on

a pre-programmed path in the irradiation area. As shown in the simple schematic diagram in Figure 5.13, a Faraday cup is placed behind the mounted sensors to measure the beam current and allow accurate beam monitoring. This system scans the beam across the 3×3 frame of sensors, in a pre-determined path, with calculated settings to irradiate sensors for the required time to reach the expected dosage of the HL-LHC.

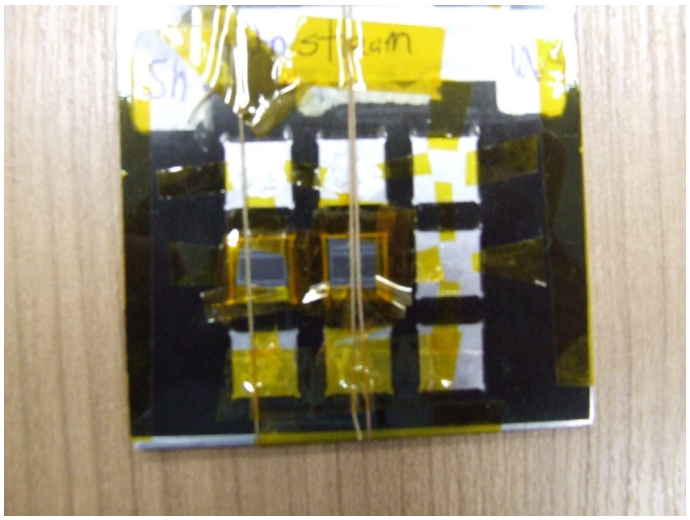

Figure 5.12: Photograph of two sensors mounted in a 3×3 frame using Kapton tape and string.

While the silicon sensors are being tested, ALiBaVa reads out the raw signal of every channel in the sensor each time the system is triggered by a signal from the photo-multiplier tubes. The software then subtracts the strip's offset (pedestals) as well as the shared offset (common mode) of all the strips to obtain each channel's response at the time of the trigger. Each channel's noise is also recorded to determine whether an excess signal is consistent with a fluctuation in the noise. If a channel has a signal greater than 3.5 times the noise then it is considered to be a signal originating from the β particle passing through and begins the cluster. The neighbouring channels are analysed and if their signal is greater than 1.8 times their noise then their signals will be included in the cluster. All of the strips with a signal exceeding the threshold are referred to as "hits". The cluster expands until the channels on either side of the cluster have a signal that is less than 1.8 times the noise. The sum of the signals in the cluster is taken to be the signal deposited by the β particle. For every trigger,

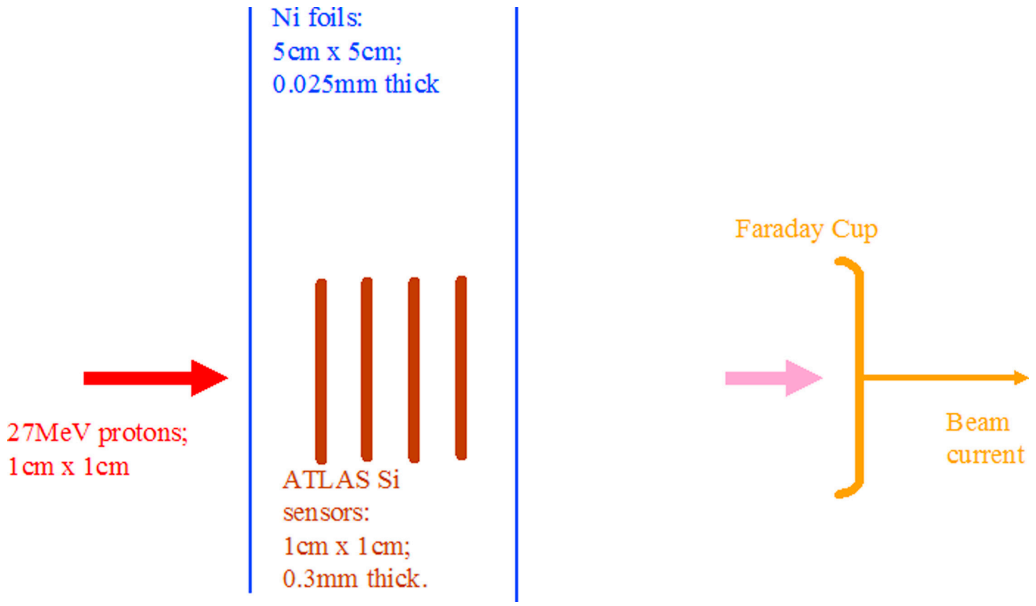

Figure 5.13: Setup of the Birmingham irradiation facility. Silicon sensors are mounted in front of the 27 MeV beam of protons. The sensor is moved along a pre-programmed path to irradiate several sensors. A Faraday cup is used to measure the beam current.

this signal is output to a signal distribution plot to form the Landau distribution.

There are three different sets of data that are usually used to quantify the sensors' performance: Charge Collection Efficiency (CCE) scans, Current-Voltage (IV) scans and the relative cluster sizes. CCE scans take the most probable signal value from the fit of the Landau-shaped signal distribution (see Figure 5.4) and compare how this varies as a function of voltage, as shown in Figure 5.14. The IV scans display the dependence of current on voltage over a similar range of voltages to the CCE scan (see Figure 5.15). The cluster size is the number of neighbouring channels (hits) contributing to a cluster. The relative cluster size distributions (see Figure 5.16) show how the fraction of each size of cluster varies as a function of bias voltage. This provides useful information on the broadness of the clusters, which hints at how successful the strip isolation is. Typically a good sensor will show a decrease in signal after irradiation, with a small increase (or remaining the same) after annealing. The IV curve will be considerably higher post-irradiation and decrease slightly after annealing. The cluster sizes will be narrow at low voltages and become broader at

higher voltages for all three stages during the process, but becoming slightly narrower after irradiation (due to the decreased signal for the same voltage), followed by an overall broadening after annealing.

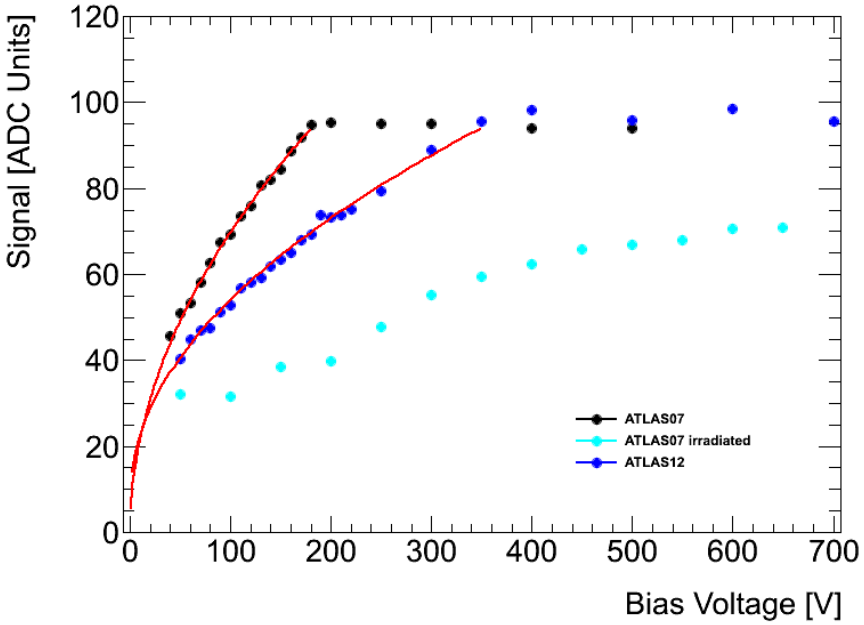

Figure 5.14: Most probable signal against voltage comparison (CCE scan) of the ATLAS07 and ATLAS12 sensors before irradiation and the ATLAS07 curve after irradiation. The red curves show the fits of a $\sqrt{V}$ function to each set of data as described by Equation 5.1.

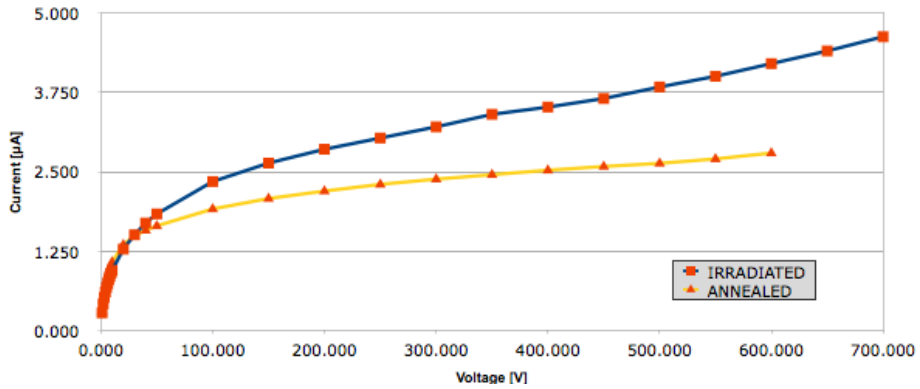

Figure 5.15: IV scan of an ATLAS12 silicon sensor irradiated in a 50 nA proton beam.

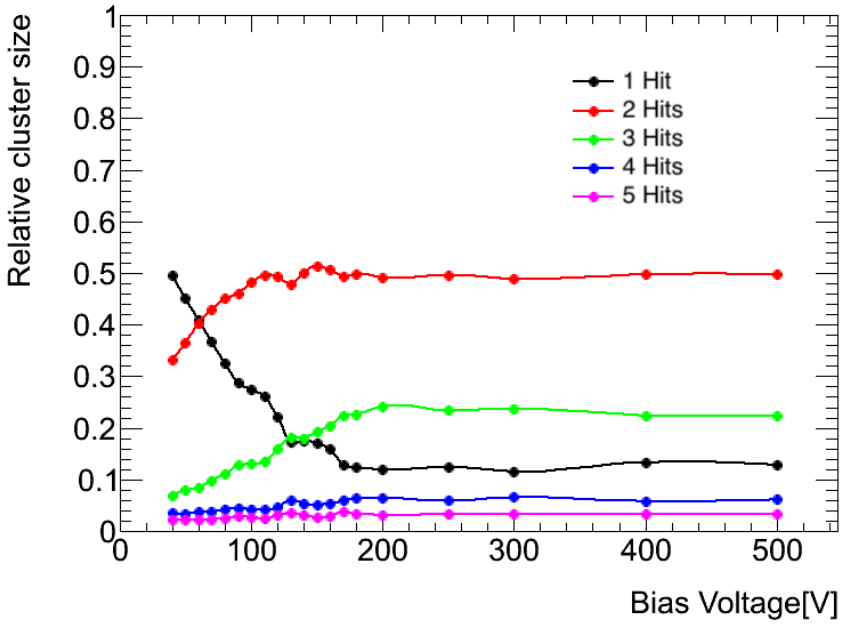

Figure 5.16: Relative cluster sizes of an unirradiated ATLAS12 silicon sensor. Each line shows how the fraction of each size of cluster (1 hit strip up to 5 hit strips) varies as a function of bias voltage.

5.6 Measurements of the Performance of Silicon Sensors Irradiated in Birmingham

Irradiation of new prototype n-in-p silicon sensors is conducted at multiple irradiation facilities around the world, with different high-energy particles used at different locations. There are four proton beam facilities: Tohuku University's CYRIC in Japan, Los Alamos, Karlsruhe and Birmingham; a pion beam at PSI in Switzerland; a neutron beam from a nuclear reactor at Ljubljana and a gamma ray beam from a ^{60}Co source at BNL in the USA. The Birmingham cyclotron is relatively new to this group and is one of the lowest energy beam irradiations available. Having a broad range of irradiation facilities enables a thorough testing of sensors designed for the HL-LHC operation of the ATLAS detector.

During the commissioning of the Birmingham cyclotron as an irradiation facility, it had to be shown that results from irradiations of sensors in the cyclotron gave consistent results to those irradiated at other facilities. To this end, an ALiBaVa test system was assembled at the University of Birmingham to provide quick analysis of irradiated sensors, in an effort to diagnose any problems with the Birmingham procedure. The ambition was to become a dependable irradiation site for testing the hardness of a broad range of sensors and materials for scientific groups around the world.

An example of the expected behaviour is shown in Figure 5.17 with ATLAS12 sensors irradiated at the Ljubljana facility. The signal after annealing is equal to or greater than the signal before annealing at a given voltage. The initial irradiations by the Birmingham cyclotron gave unexpected results in tests performed by the University of Liverpool. The first sensor tested at the University of Birmingham confirmed Liverpool's observations and the CCE plot in Figure 5.18 shows this behaviour. After irradiation, the response decreases as expected; however, after then annealing the sensor the response decreases again, which is inconsistent with expectations and the behaviour found elsewhere. Such observations could be due to a number

of reasons. One possibility was that sensors were being overheated in the proton beam, which would have induced the annealing effect early and therefore the silicon would be beyond the short-term beneficial component of annealing before testing began. Another possibility was that the sensors had a susceptibility that might be exposed uniquely during the Birmingham irradiations, which would be problematic if the ATLAS experiment also produced these effects. One more hypothesis was that surface damage was taking place, either directly as a result of the proton beam or indirectly from scattered particles showering onto the sensor. A programme of irradiation studies was begun at the University of Birmingham, in which the different possible origins could be tested systematically.

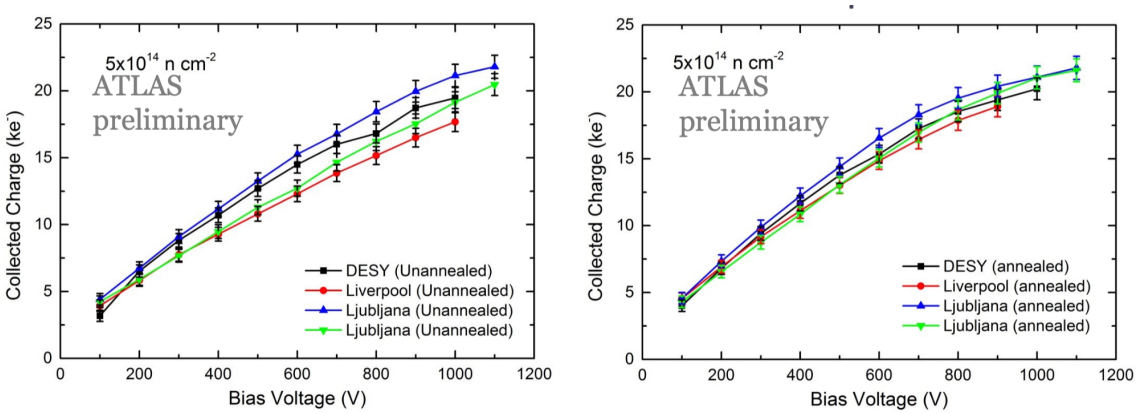

Figure 5.17: Two CCE plots for ATLAS12 sensors irradiated at 5×10^{14} 1 MeV n_{eq}/cm^2 at Ljubljana, before (left) and after (right) annealing. Different coloured data points correspond to sensors tested at the different sites, DESY, Liverpool and Ljubljana. Figure taken from Ref. [85].

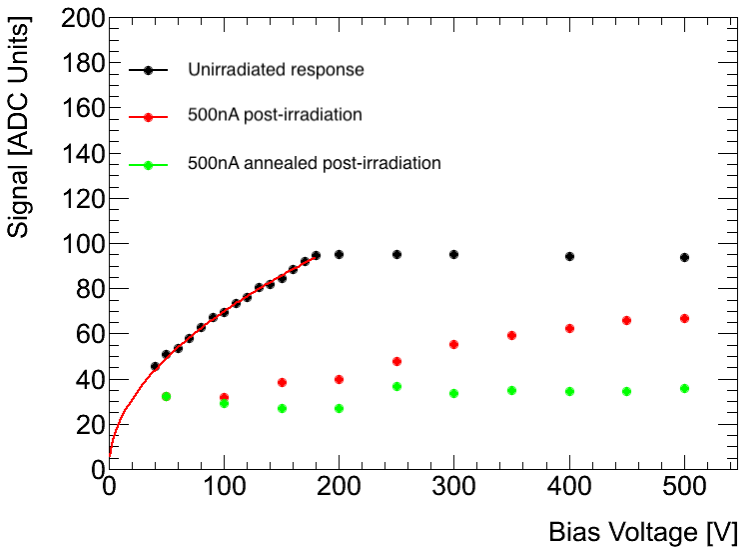

Figure 5.18: Most probable signal against voltage for an ATLAS07 sensor at three different stages: unirradiated (black), irradiated (red) and annealed after irradiation (green). Irradiated on the 15^{th} July 2015 in a 500nA proton beam.

An ATLAS12 sensor was tested in the Birmingham facility to check whether the effect was unique to the ATLAS07 sensors. The CCE plot in Figure 5.19 for an ATLAS12 sensor shows a similar behaviour to that observed for the ATLAS07 sensor. The relative cluster sizes are shown in Figure 5.20. Unexpectedly, the number of hit channels combining into a cluster increases after irradiation compared to before. This is counter-intuitive with respect to the reduced signal detected and is a strong indication that surface damage has occurred, which reduces the inter-strip isolation and therefore results in charge spreading across neighbouring strips. A more diffuse signal means more strips have a small signal, not exceeding the threshold above noise required to seed a new cluster. After annealing, the clusters continue to broaden, as expected, but do not show the recovery towards pre-irradiation behaviour as required.

More samples were obtained by irradiating four different ATLAS12 sensors, which were exposed to different beam currents: 50 nA, 200 nA, 400 nA and 500 nA. This check would determine whether the beam current had any effect for the same total dosage of 5×10^{34} 1 MeV n_{eq}/cm^2. Surprisingly, all four of these sensors showed

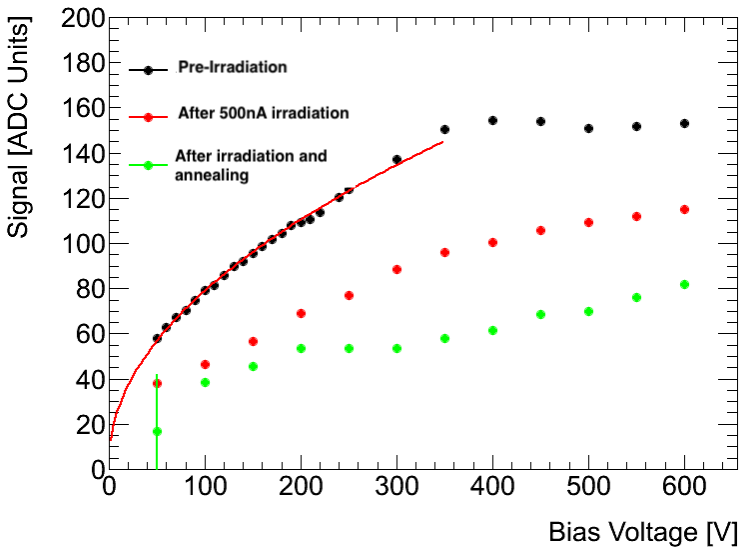

Figure 5.19: Most probable signal against voltage for an ATLAS12 sensor at three different stages: unirradiated (black), irradiated (red) and annealed after irradiation (green). Irradiated on the 22^{nd} July 2015 in a 500nA proton beam for a dosage of 5×10^{34} 1 MeV n_{eq}/cm^2 at the Birmingham cyclotron.

consistent and reasonable behaviour. As shown in Figure 5.21, the sensors annealed after irradiation had signals consistent or improved compared to those irradiated without annealing. An IV scan, such as that shown in Figure 5.22, validates that the sensors were successfully annealed due to the reduced current for the same voltage, i.e. the leakage current has been somewhat reduced by annealing. These results were unexpected as the 500 nA beam current irradiated sample should have been a direct repeat of the first ATLAS12 sensor irradiated.

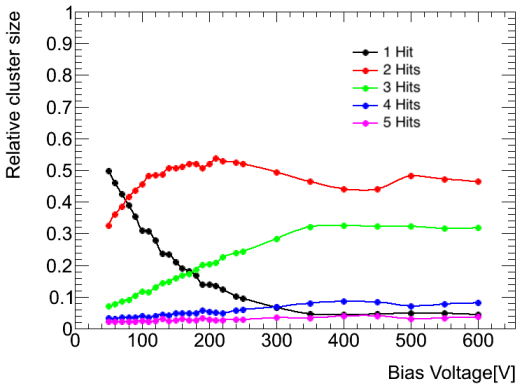

(a) Before irradiation

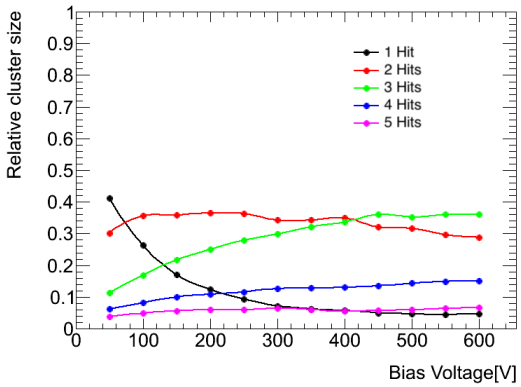

(b) After irradiation

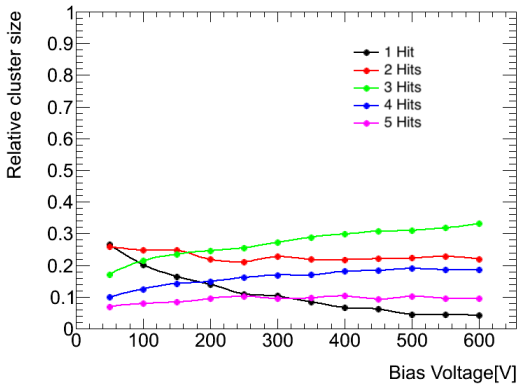

(c) After irradiation and annealing

Figure 5.20: Relative cluster sizes at three different stages in the testing process for an ATLAS12 sensor irradiated at 500 nA beam current for a dosage of 5×10^{34} 1 MeV n_{eq}/cm^2 at the Birmingham cyclotron.

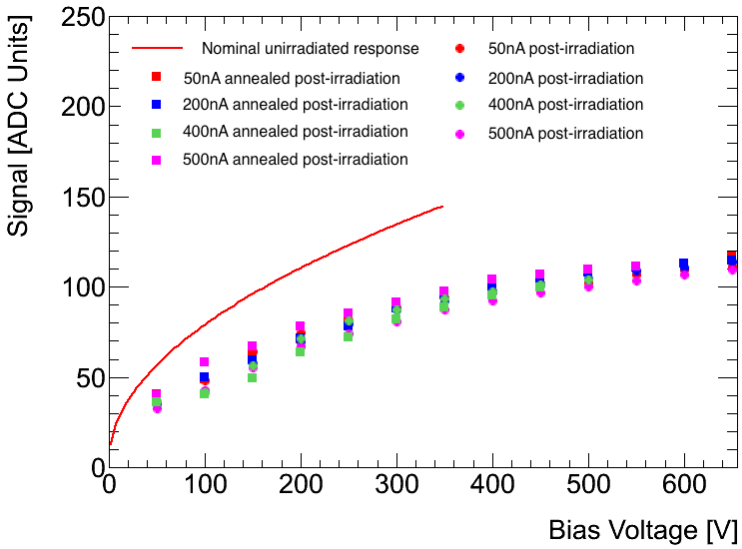

Figure 5.21: Most probable signal against voltage for ATLAS12 sensors irradiated with different beam currents for a dosage of 5×10^{34} 1 MeV n_{eq}/cm^2 at the Birmingham cyclotron. Each sensor is distinguished with different coloured points where circles are used for the response after irradiation and squares for the annealed after irradiation. The red line indicates the nominal shape for an unirradiated sensor.

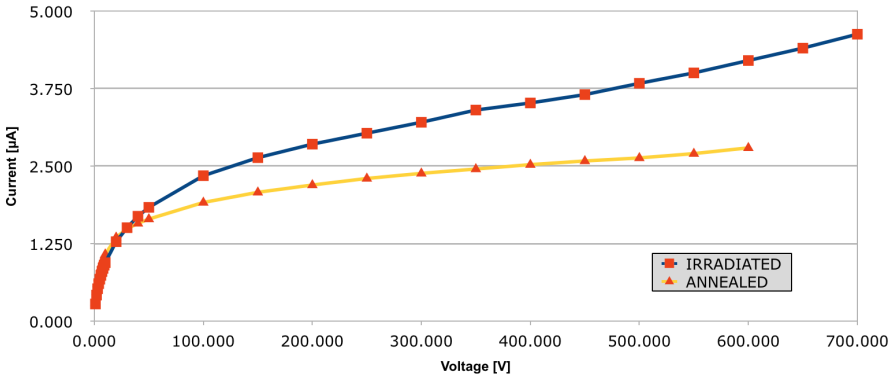

Figure 5.22: An IV scan of an ATLAS12 sensor irradiated in a 50 nA proton beam for a dosage of 5×10^{34} 1 MeV n_{eq}/cm^2 at the Birmingham cyclotron.

Another sensor was irradiated in a 500 nA proton beam, whilst also having a second sensor placed within the cold box, but never directly exposed to the beam. The unirradiated sensor performed as expected in tests and, as a result, it could be assumed there were no environmental effects damaging the sensors, such as ions being present in the gas. The irradiated sensor showed almost identical behaviour to the poor performance of the ATLAS07 sensor and the first ATLAS12 sensor.

A peculiar observation was made in the signal distributions, an example of which can be seen in Figure 5.23 for a 200 V bias voltage, where a second signal peak appears to be present in the distribution. Viewing the individual signal responses for all clusters on each strip, shown in Figure 5.24, two separate regions of the detector can be seen to give different signals on average over all of the triggers. One region, from channels 170 to 220 of ALiBaVa, has very little response detected for the triggers. The second region, from channels 220 to 230, behaves much more reasonably, similar to the "good" sensors tested previously. This indicates that the cause of the damage appears not to be affecting the entire sensor.

A series of further irradiations were performed, which tested different possibilities: the strip orientation was varied with some sensors having vertically aligned strips, others horizontally aligned and some sensors placed face down; a thermally conductive paste was used to ensure good contact between the sensor and conductor to keep the sensor cool; and various checks of the humidity within the cold box were made. All of the sensors tested showed the same erratic behaviour as the ATLAS07 sensor. However, from these checks a similar repeat of the regional behaviour, shown before in Figure 5.24, was observed, but this time with more than two regions and in different positions. It was realised that the position of the regions was consistent with the position of the string, which was used to mount the sensors. A rough projection from a photograph, taken prior to irradiation, onto a plot of the signal response for each cluster on each strip is shown in Figure 5.25. This led to the discovery of the problem with the Birmingham cyclotron irradiations as being due to a scattering of low-energy ions produced by the proton beam. These would settle into the sensors, causing surface damage. In the case of the regions shielded beneath the string, the

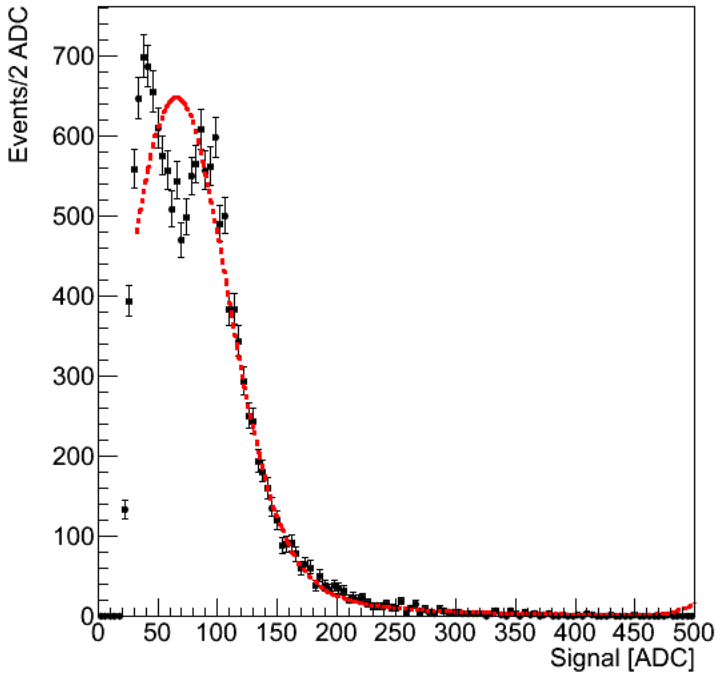

Figure 5.23: Signal distribution for a 200V bias voltage showing an unusual double peak for an ATLAS12 sensor irradiated at 500nA for a dosage of 5×10^{34} 1 MeV n_{eq}/cm^2 at the Birmingham cyclotron. Each entry corresponds to the signal recorded by ALiBaVa at the reception of a trigger. The dashed red line is the best-fit of the expected Landau distribution to the data.

string had absorbed the low energy particles and protected the strips behind it.

The exact source of the low-energy particles could not be located. Some further studies, as described in Ref. [86], trialled different combinations of Kapton, nickel foils and 300 μm thick aluminium foil in front of the sensors. It was found that the aluminium was most suitable for absorbing the low-energy particles and, as shown in Figure 5.26, subsequent CCE scans performed for sensors irradiated by the Birmingham cyclotron behaved consistently with those irradiated by other facilities. The University of Birmingham Medical Physics cyclotron is now fully commissioned as an irradiation facility and can be used for further radiation tolerance studies [86].

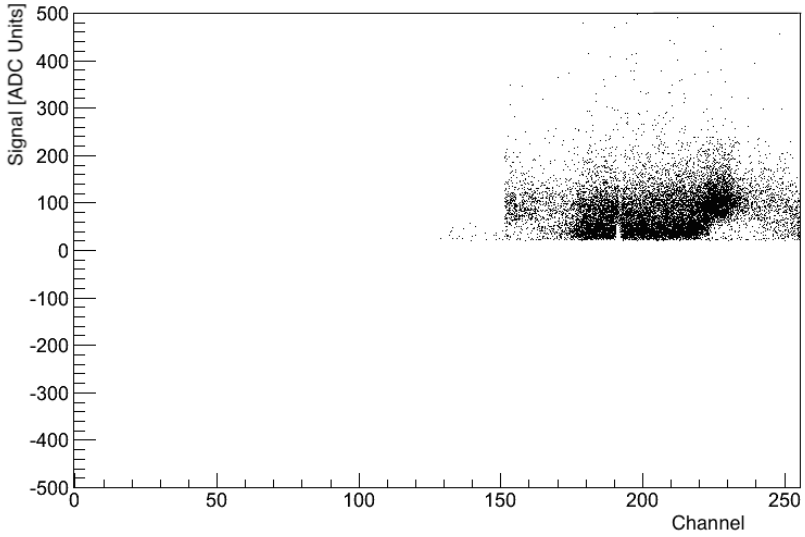

Figure 5.24: Scatter plot of signal against channel number for all the clusters on an ATLAS12 sensor irradiated at 500nA for a dosage of 5×10^{14} 1 MeV n_{eq}/cm^2 at the Birmingham cyclotron. Each channel represents an ALiBaVa readout connection, which can be wire-bonded to silicon strips. The 104-channel ATLAS12 sensor is bonded to channels 152 to 256. Each dot represents the signal recorded for each cluster, with the channel number corresponding to the seed strip. The collimation of β particles causes the clusters to appear predominantly between channels 170 to 230.

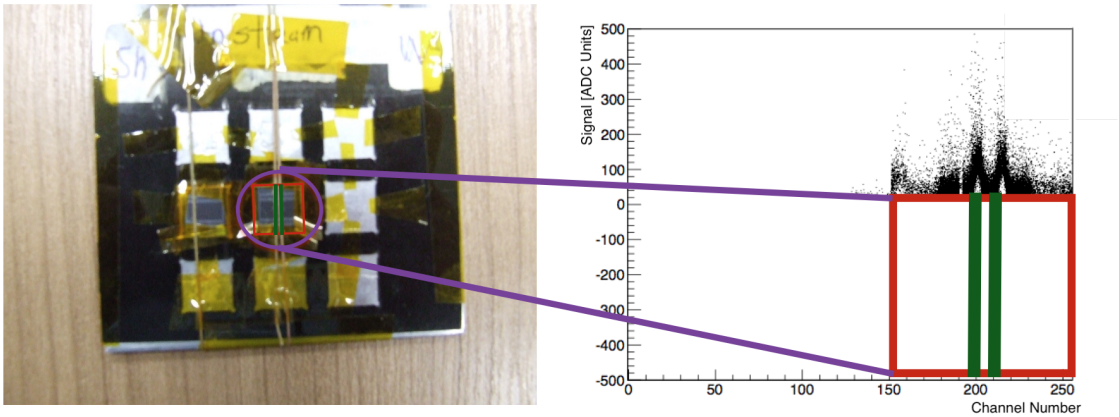

Figure 5.25: Photograph of an ATLAS12 sensor mounted for irradiation with strings used to fix the sensor in position (left). The photographed sensor is projected onto the scatter plot of signal against channel number for all the clusters of the same sensor. The ATLAS12 sensor was irradiated at 500nA for a dosage of 5×10^{14} 1 MeV n_{eq}/cm^2 at the Birmingham cyclotron. Figure 5.24 provides more information for the scatter plot.

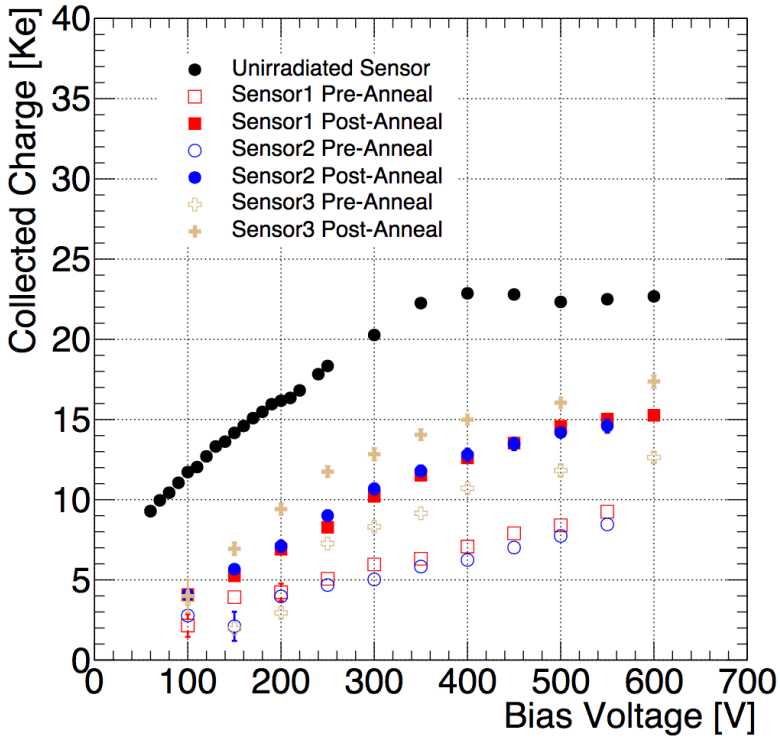

Figure 5.26: Charge collection measurements for sensors irradiated behind 300 μm of aluminium. Sensor 1 was irradiated to 7×10^{14} 1 MeV $n_{\text{eq}}/\text{cm}^2$; Sensor 2 was irradiated to 9×10^{14} 1 MeV $n_{\text{eq}}/\text{cm}^2$ and Sensor 3 was irradiated to 10×10^{14} 1 MeV $n_{\text{eq}}/\text{cm}^2$. The units of collected charge, Ke, correspond to thousands times the charge of the electron, i.e. 1.6×10^{-16} Coulombs. This is found by calibrating the measurements to convert from an ADC to a Ke. Figure taken from Ref. [86].

CHAPTER 6

SEARCH FOR THE HIGGS AND Z BOSON DECAYS TO $\psi(kS)\gamma$ AND $\Upsilon(nS)\gamma$: ANALYSIS DEVELOPMENT

6.1 Introduction

This chapter and the next describe a search for the exclusive decays of the Higgs and Z bosons to $J/\psi\,\gamma$, $\psi(2S)\,\gamma$ and $\Upsilon(nS)\,\gamma\,(n = 1, 2, 3)$. The Higgs boson search probes the Yukawa couplings of the c and b quarks in a complementary manner to the direct measurements. The Z boson search provides a useful reference channel for the Higgs boson decay search, as well as giving a unique precision test of the SM and the factorisation approach in QCD [46]. This chapter contains some figures and verbatim text from a publication of the analysis, Ref. [1].

Throughout this chapter and the next, the mesons J/ψ and $\psi(2S)$ will be collectively referred to as $\psi(kS)$ where $k = 1$ or 2. When referring to both $\psi(kS)$ and $\Upsilon(nS)$ states, they will be collectively called quarkonium, $\mathcal{Q}$.

The analysis is performed by reconstructing the decays $\mathcal{Q} \to \mu^+\mu^-$ exclusively, whilst $\mathcal{Q} \to e^+e^-$ decays are not investigated. The $\mathcal{Q} \to \mu^+\mu^-$ decays are preferred since the final state leptons in $H(Z) \to \mathcal{Q}\,\gamma \to \ell\ell\gamma$ decays are typically very collimated and boosted $\mathcal{Q} \to e^+e^-$ decays will often form a merged electromagnetic shower that is more difficult to reconstruct reliably.

As described in Section 2.7, the $H(Z) \to J/\psi\,\gamma$ and $H(Z) \to \Upsilon(nS)\,\gamma$ searches have been performed before using the ATLAS dataset recorded at centre-of-mass energy $\sqrt{s} = 8$ TeV. The analysis described in this chapter is performed on the $\sqrt{s} = 13$ TeV dataset. At this higher energy, the search benefits from a Higgs boson production cross section increased by approximately a factor of two. Further improvements are achieved from new dedicated triggers with increased signal efficiency and improvements to the data-driven method used to model the background. The analysis also includes a new channel, $H(Z) \to \psi(2S)\,\gamma$, which has not been measured before. The Run I limits and the corresponding predicted branching fractions for all of the channels are shown in Table 6.1.

This chapter focusses on the development of the search for $H(Z) \to \mathcal{Q}\,\gamma$ decays. The next three sections of this chapter (Sections 6.2, 6.3 and 6.4) describe the dataset and the MC simulation samples used, treatment of the polarisation of the particles involved and how the extension to include the $H(Z) \to \psi(2S)\,\gamma$ channel is handled. A description of the triggers is given in Section 6.5 and the event selection in Section 6.6. Chapter 7 discusses the modelling of the signal and background components and the results obtained from the final fitting procedure.

Table 6.1: $\mathcal{B}(H(Z) \to \psi(kS)\,\gamma)$ and $\mathcal{B}(H(Z) \to \Upsilon(nS)\,\gamma)$ 95% CL upper limits obtained in Run I [38] and the SM expected values.

Branching Fraction	Observed Limit (95% CL) Run I	SM expectation
$\mathcal{B}(H \to J/\psi\,\gamma)$	1.5×10^{-3}	3.0×10^{-6} [40]
$\mathcal{B}(Z \to J/\psi\,\gamma)$	2.6×10^{-6}	9.0×10^{-8} [45]
$\mathcal{B}(H \to \psi(2S)\,\gamma)$	No measurement	1.0×10^{-6} [44]
$\mathcal{B}(Z \to \psi(2S)\,\gamma)$	No measurement	No calculation
$\mathcal{B}(H \to \Upsilon(1S)\,\gamma)$	1.3×10^{-3}	5.2×10^{-9} [40]
$\mathcal{B}(H \to \Upsilon(2S)\,\gamma)$	1.9×10^{-3}	1.4×10^{-9} [40]
$\mathcal{B}(H \to \Upsilon(3S)\,\gamma)$	1.3×10^{-3}	0.91×10^{-9} [40]
$\mathcal{B}(Z \to \Upsilon(1S)\,\gamma)$	3.4×10^{-6}	4.8×10^{-8} [45]
$\mathcal{B}(Z \to \Upsilon(2S)\,\gamma)$	6.5×10^{-6}	2.4×10^{-8} [45]
$\mathcal{B}(Z \to \Upsilon(3S)\,\gamma)$	5.4×10^{-6}	1.9×10^{-8} [45]

6.2 Data and Simulation Samples

The analysis is performed using the full 2015 and 2016 data samples collected by the ATLAS experiment at $\sqrt{s} = 13$ TeV. The total integrated luminosity used is 36.1 fb^{-1}, with a corresponding 2.1% uncertainty derived using the method described in Ref. [87]. All runs are required to be included in the "Good Run List" [88], which defines the successful data taking runs in which all components of ATLAS were operating satisfactorily. A common procedure in ATLAS to save computational time is to create a smaller data sample (derivation) from the full dataset by applying a loose initial selection, which is motivated by simulated signal events. The `DxAOD_HIGG2D5` derivation [89] is used, which retains events based on the following requirements:

- The event must contain at least one oppositely charged di-muon pair;
- The leading p_T^μ muon must satisfy $p_T^\mu > 15\,\text{GeV}$;
- The sub-leading p_T^μ muon must satisfy $p_T^\mu > 2.5\,\text{GeV}$;
- A fit of the di-muon vertex must have $\chi^2 < 200$;

- The di-muon invariant mass must satisfy $2.0 < m_{\mu^+\mu^-} < 4.2\,\text{GeV}$ for a $\psi(kS)$ candidate and $8.0 < m_{\mu^+\mu^-} < 12.0\,\text{GeV}$ for an $\Upsilon(nS)$ candidate;
- The event must also contain one photon with $p_T^\gamma > 15\,\text{GeV}$.

Only events included in this derivation are used in the analysis.

The Higgs and Z boson signal contributions are modelled with MC samples. For the ggH and VBF processes, the production is modelled using the POWHEG-BOX v2 MC event generator [90–94]. Both processes use the CT10 parton distribution functions [95] and are calculated up to next-to-leading-order (NLO) in α_S. The PYTHIA 8.186 event generator [96, 97] is combined with POWHEG-BOX to model parton showering, hadronisation and the underlying event with parameters set according to the AZNLO tune [98]. Additional contributions from the associated production of a Higgs boson and a W or Z boson (denoted WH and ZH, respectively) are obtained at leading-order (LO) from PYTHIA 8.186 using the NNPDF23LO parton distribution functions [99] and the A14 tune for hadronisation and the underlying event [100]. The Z boson production samples were also produced using POWHEG-BOX, interfaced with PYTHIA 8.186 and the CTEQ6L1 parton distribution functions [101], to model the parton shower, hadronisation and underlying event, with parameters set according to the AZNLO tune.

The simulation samples used to model the $H(Z) \to \mathcal{Q}\gamma$ signals are detailed in Table 6.2. Each $J/\psi\,\gamma$ sample had approximately 50k events generated, whereas the $\Upsilon(nS)\,\gamma$ samples had 100k events (approximately 33k per Υ state).

The simulated events used in the $H(Z) \to J/\psi\,\gamma$ analysis can also be used in the $H(Z) \to \psi(2S)\,\gamma$ analysis due to their very similar decay kinematics. Throughout the analysis, the same MC is used for both, with the $H(Z) \to \psi(2S)\,\gamma$ analysis having an adjustment made for the expected di-muon mass and resolution.

These simulated events are used throughout the analysis to model the signal contributions and to determine the efficiencies and systematic uncertainties. The Higgs

Table 6.2: The MC simulation samples used to model the $H(Z) \to \mathcal{Q}\gamma$ signals.

Analysis	Production	Generator	Generator tune	PDF	Events (J/ψ)
$J/\psi\,\gamma$	ggH	PowhegPythia8	AZNLO	CT10	48380
	VBF	PowhegPythia8	AZNLO	CT10	47537
	WH	Pythia8	A14	NNPDF23LO	48471
	ZH	Pythia8	A14	NNPDF23LO	45508
	Z	PowhegPythia8	AZNLO	CTEQ6L1	48437
					$(1S, 2S, 3S)$
$\Upsilon(nS)\,\gamma$	ggH	PowhegPythia8	AZNLO	CT10	(31694,32173,32074)
	VBF	PowhegPythia8	AZNLO	CT10	(30283,30392,30461)
	WH	Pythia8	A14	NNPDF23LO	(31645,31752,31616)
	ZH	Pythia8	A14	NNPDF23LO	(32254,32278,32445)
	Z	PowhegPythia8	AZNLO	CTEQ6L1	(32006,31906,31939)

boson production cross sections and decay branching ratios, as well as their uncertainties, are taken from Ref. [14]. A next-to-next-to-next-to-leading-order (N^3LO) QCD calculation with NLO electroweak corrections applied [102–105] is used to determine the normalisation of the ggH production sample. The VBF normalisation is calculated using an approximate next-to-next-to-leading-order (NNLO) QCD cross section with NLO electroweak corrections applied [106–108]. Similarly for the WH and ZH normalisations, an NNLO calculation is used with NLO electroweak corrections [109, 110]. These normalisations also include NLO QCD corrections [111] for $gg \to ZH$. The two next-most dominant production mechanisms $t\bar{t}H$ and $b\bar{b}H$, for which no MC simulation was available, are included in the signal yield assuming the signal efficiency to be equal to that for ggH. The addition of $t\bar{t}H$ and $b\bar{b}H$ to ggH leads to a change in the signal acceptance of less than 1%.

As will be described in Section 7.2, one sample of MC is used in the modelling of the background contribution. This background model uses a sample of simulated $Z \to \mu^+\mu^-$ events, produced using POWHEG-BOX, which includes Quantum Electrodynamics (QED) final state radiation (FSR) generated using the `PHOTOS` package [112]. The other components of the background composition are from a complicated mixture of other processes and, therefore, are too complex to model using MC simulation and instead use a data-driven approach.

6.3 Polarisation Effects

The Higgs and Z boson decays are simulated as a cascade of two-body decays. The polarisation effects are not inherently modelled in the MC simulation samples, but they do play an important role in the final-state decay kinematics and, therefore, the signal acceptances. The effect on the distributions can be estimated and accounted for in the analysis by reweighting the signal MC events by a factor dependent on the angular distribution of the final decay products. The factor is calculated using the four-momentum of the truth particles of the simulated events, incorporating their relative angles of trajectory and reweighting according to the predicted angular distribution of the decays. The polarisations are calculated following the method described in Ref. [113] and detailed below.

6.3.1 Higgs boson decays to $\mathcal{Q}\,\gamma \to \mu^+\mu^-\,\gamma$

The Higgs boson has spin 0. The quarkonium state, $\mathcal{Q}$, has $J^{PC} = 1^{--}$ and the photon is a massless vector boson with $J = 1$, $m_J = \pm 1$. For μ^+ we have $J = \frac{1}{2}$.

For the decays $H \to \psi(kS)\,\gamma \to \mu^+\mu^-\,\gamma$ and $H \to \Upsilon(nS)\,\gamma \to \mu^+\mu^-\,\gamma$ in the helicity basis [113], the angular distribution, $I(\theta')$, is given by:

$$I(\theta') = \frac{1}{\Gamma_1\Gamma_2}\frac{2s_2+1}{2}\sum_{\lambda_1\lambda_2\lambda_3\lambda_4}\left|d^{s_2}_{\lambda_2,\lambda_4-\lambda_5}\right|^2\left|A_{\lambda_2\lambda_3}\right|^2\left|B_{\lambda_4\lambda_5}\right|^2 \tag{6.1}$$

where particle 1 is the Higgs, 2 is quarkonium, 3 is the photon, and 4 and 5 are the positively and negatively charged decay products of quarkonium, respectively. θ' is the angle between the momentum of particle 4 in the rest frame of particle 2, with respect to the spin quantisation axis of particle 2 (i.e. the direction of particle 2 in the rest frame of particle 1). s_i, Γ_i and λ_i are the spin, decay rate, and helicity of particle i measured in the rest frame of its parent. $A_{\lambda_2\lambda_3}$ are the helicity amplitudes for the $1 \to 23$ decay and $B_{\lambda_4\lambda_5}$ the helicity amplitudes for $2 \to 34$. $d^{s_2}_{\lambda_2,\lambda_4-\lambda_5}$ is

known as the "d function" [10], which describes the limiting angular distribution.

The helicity amplitudes allowed by conservation of angular momentum, given the selection rules $|\lambda_2 - \lambda_3| \leq s_1$ and $|\lambda_3 - \lambda_4| \leq s_2$, are $A_{1,1}$ and $A_{-1,-1}$. This means that the quarkonium should be transversely polarised, given $s_1 = 0$ and the photon does not have the longitudinal polarisation. Correspondingly for $B_{\lambda_4\lambda_5}$ we have $B_{1/2,-1/2}$, $B_{-1/2,1/2}$ as the only options, because $B_{-1/2,-1/2}$ and $B_{1/2,1/2}$ are not allowed due to chirality conservation.

Thus, the only contributions to the angular distributions are: $d^1_{1,1} = d^1_{-1,-1} = \frac{1+\cos\theta'}{2}$ and $d^1_{-1,1} = d^1_{1,-1} = \frac{1-\cos\theta'}{2}$, up to unobservable relative signs. The relative angular distribution is therefore $\frac{1}{2}\Big[(1+\cos\theta')^2 + (1-\cos\theta')^2\Big] = 1 + \cos^2\theta'$.

6.3.2 Z boson decays to $\mathcal{Q}\gamma \to \mu^+\mu^-\gamma$

For the Z boson decays, $s_1 = 1$ and the Z boson is produced with a mixture of polarisations. However, as pointed out in Ref. [47], the transversely-polarized quarkonium states vanish to leading order in $m^2_{\mathcal{Q}}/M^2_Z$. Thus, the quarkonium in the decay will be longitudinally polarised. The allowed helicity amplitudes, given the selection rule $|\lambda_2 - \lambda_3| \leq s_1$, are therefore $A_{0,1}$ and $A_{0,-1}$.

Then, according to the selection rule $|\lambda_3 - \lambda_4| \leq s_2$, for $B_{\lambda_4\lambda_5}$ the only options are $B_{1/2,-1/2}$ and $B_{-1/2,1/2}$, because $B_{1/2,1/2}$ and $B_{-1/2,-1/2}$ are not allowed due to chirality conservation.

Thus, the only contributions to the angular distributions are $d^1_{0,1} = d^1_{0,-1} = \frac{\sin\theta'}{\sqrt{2}}$, up to an unobservable sign difference, and the relative angular distribution is therefore $1 - \cos^2\theta'$.

6.4 Simulation of $H(Z) \to \psi(2S)\,\gamma$ decays

In the initial development of the analysis, the $H(Z) \to \psi(2S)\,\gamma$ decays were overlooked due to the low expected branching fraction of $\psi(2S)\,\gamma \to \mu^+\mu^-\gamma$. For this reason, no simulation samples were generated to model this decay. However, the kinematic distributions of the $\psi(2S)\,\gamma$ decay are expected to be similar to the $J/\psi\,\gamma$ decay. This can be shown using simple truth MC samples of the $H(Z) \to J/\psi\,\gamma$ and $H(Z) \to \psi(2S)\,\gamma$ decays. Figure 6.1 shows almost identical kinematic distributions for both samples. The mass difference between the two mesons causes a slightly wider $\Delta R(\mu^+, \mu^-)$ separation between the muons of the $\psi(2S)\,\gamma$ decay. Overall, the change in meson mass results in less than 0.5% change in the acceptance of the analysis selection (described in Section 6.6), relative to the $H(Z) \to J/\psi\,\gamma$ analysis.

As a result of this study, the signal modelling performed in the $H(Z) \to J/\psi\,\gamma$ analysis can be cloned for the $\psi(2S)\,\gamma$ analysis, but with some adjustments made. The method of modelling the $H(Z) \to J/\psi\gamma$ signal distributions in $m_{\mu^+\mu^-\gamma}$ and $m_{\mu^+\mu^-}$ is described in Section 7.4. For the $\psi(2S)\,\gamma$ case, the mean value of the $m_{\mu^+\mu^-}$ distribution is shifted to the value given for the $\psi(2S)$ mass in Ref. [114] and the width of the distribution is found by scaling the J/ψ width by the ratio of the masses. The normalisation of the signal is also scaled by the ratio of the branching fractions of $\psi(2S) \to \mu^+\mu^-$ and $J/\psi \to \mu^+\mu^-$ using the values given in Ref. [114].

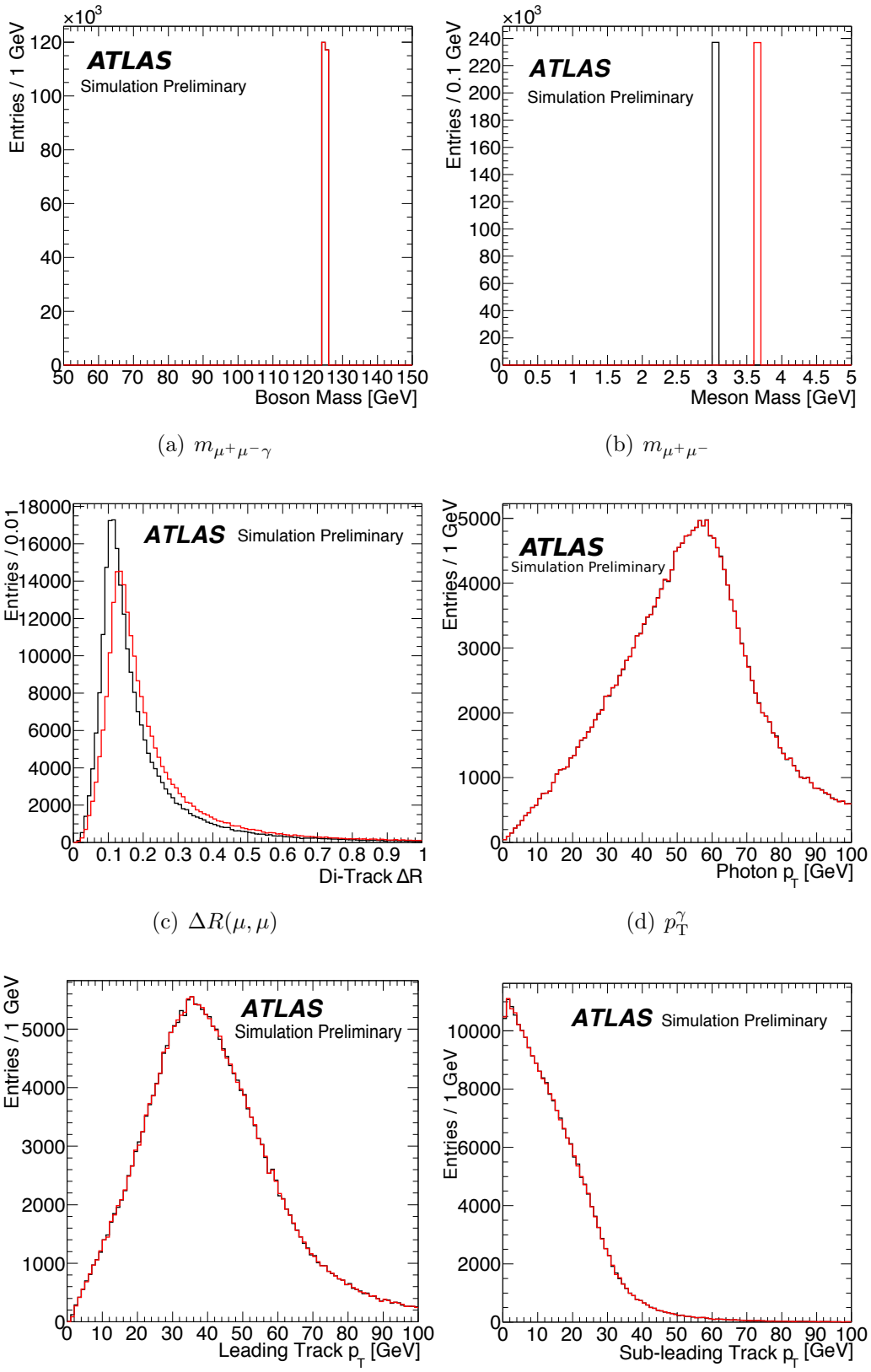

(a) $m_{\mu^+\mu^-\gamma}$

(b) $m_{\mu^+\mu^-}$

(c) $\Delta R(\mu,\mu)$

(d) p_{T}^{γ}

(e) Leading μ p_{T}

(f) Sub-leading μ p_{T}

Figure 6.1: Comparison between simple truth MC samples of $H \to J/\psi\,\gamma$ (black) and $H \to \psi(2S)\,\gamma$ (red) decays in various distributions of different kinematic variables.

6.5 Trigger

The unusual topology of a high-p$_T$ photon recoiling against two high-p$_T$ muons provides a distinctive signature used to implement dedicated triggers, which are included in the ATLAS trigger menu. The high boost of the $\mathcal{Q} \to \mu^+\mu^-$ decay typically results in the muons being close together. A single muon trigger has to be used due to the small separation between the two muons and in such a situation the trigger efficiency is poor. In the Run I analysis, the trigger efficiency was around 70% (80%) for the $J/\psi\gamma$ ($\Upsilon(nS)\gamma$) analysis with respect to the full analysis selection. This trigger is greatly affected by acceptance limitations of the detector, with important structures built in the lower muon chambers to support the weight of the ATLAS detector and for the magnets [115]. For the Run 2 analysis, a single-muon trigger is used, which is seeded by a Level-1 EM object to avoid the Level-1 muon inefficiency. This trigger is then combined with a photon trigger. The thresholds used for the triggers are based on simulated distributions of the kinematic variables.

The dedicated trigger used is a composition of subchains and thresholds. The trigger is part of the high-level trigger chain with a 35 GeV transverse energy threshold for the photon trigger component. A Level-1 EM object, representing a photon deposit, is then used to seed a search by muon trigger for muons with $p_{\mathrm{T}}^{\mu^\pm} > 18$ GeV. Using this dedicated trigger, a trigger efficiency of around 95% is obtained in signal MC, after the full selection has been applied, as described in Section 6.6.

To increase the efficiency further, a second trigger is used, which combines a $p_{\mathrm{T}}^{\gamma} > 25$ GeV photon trigger with a $p_{\mathrm{T}}^{\mu^\pm} > 24$ GeV muon trigger. This increases the trigger efficiency to 97%, an increase of 20% with respect to the Run-I analysis, which was inhibited by the Level-1 muon inefficiencies.

Both of the triggers used were active in ATLAS between runs 276262 (16^{th} August) and 284484 (3^{rd} November) of the 2015 data collection and runs 297730 (28^{th} April) and 311481 (26^{th} October) of the 2016 data collection periods. All events included in the final analysis selection were required to pass at least one of the two triggers

described.

6.6 Event Selection

The topology of the decay is used to define further selection requirements to reduce the number of background events but retain as much signal as possible. The $\psi(kS)$ and $\Upsilon(nS)$ analyses use almost identical selections, except for different di-muon mass and p_T requirements. The same analysis selection is used for both the Higgs and Z boson candidates, except for the final $m_{\mu^+\mu^-\gamma}$ ranges used.

In the development of the event selection, candidates in data that satisfy the requirements $86\,\text{GeV} < m_{\mu^+\mu^-\gamma} < 96\,\text{GeV}$ and $122\,\text{GeV} < m_{\mu^+\mu^-\gamma} < 128\,\text{GeV}$ were hidden (blinded). Once the final selection was frozen these data events were unblinded.

6.6.1 $\mathcal{Q} \to \mu^+\mu^-$ Selection

Candidate $\mathcal{Q} \to \mu^+\mu^-$ decays are selected from di-muon pairs that satisfy the following. The minimum requirement for muons is that they are reconstructed from ID tracks combined with independent muon spectrometer tracks or track segments [116], with $p_{\text{T}}^{\mu^\pm} > 3$ GeV and pseudorapidity $|\eta^{\mu^\pm}| < 2.5$. $\mathcal{Q}$ candidates are reconstructed from pairs of oppositely charged muons, which are identified as originating from a common vertex. The leading muon of the pair must have $p_{\text{T}}^{\mu^\pm} > 18$ GeV. Generator-level $p_{\text{T}}^{\mu^\pm}$ distributions using simulated signal events for the leading and sub-leading muons are shown in Figure 6.3 and used in the decision of the $p_{\text{T}}^{\mu^\pm}$ selection requirements.

Events are separated depending on the $\mathcal{Q}$ candidate's mass. Di-muons with a mass, $m_{\mu^+\mu^-}$, within the ranges $2.0 < m_{\mu^+\mu^-} < 4.2$ GeV or $8.0 < m_{\mu^+\mu^-} < 12.0$ GeV are identified as $\psi(kS) \to \mu^+\mu^-$ candidates or $\Upsilon(nS) \to \mu^+\mu^-$ candidates, respectively.

Further isolation and vertex quality requirements are applied to the $\mathcal{Q}$ candidates,

following an ATLAS working point called "FixedCutTightTrackOnly" [64]. The scalar sum of the p_T of the reconstructed inner detector tracks within a cone of variable half-angle size $\Delta R = 10$ GeV$/p_T^\mu$, up to a maximum cone size of $\Delta R = 0.3$, around the leading muon must be less than 6% of that muon's p_{T} [64]. The p_T of the ID track associated with the leading muon is subtracted from this isolation sum. In the case where the opening angle between the muons is small, $\Delta R < 0.2$, the p_{T} of the lower-p_{T} muon is also subtracted from the isolation sum of the leading muon. For di-muon pairs with $\Delta R > 0.2$, no correction is applied. To mitigate the effects of multiple pp interactions in the same or neighbouring bunch crossings, only ID tracks that originate from the primary vertex are considered, defined as the reconstructed vertex with the highest $\Sigma_i \, p_{\mathrm{T}i}^2$ of all associated tracks used to form the vertex.

A common background comes from $\psi(kS) \to \mu^+\mu^-$ decays originating from "non-prompt" b-hadron decays. These b-hadrons have a longer lifetime than the $\mathcal{Q}$ (whose decay is "prompt") and can therefore be rejected by applying a requirement on the signed projection, L_{xy}, of the $\mathcal{Q}$ candidate flight distance, between the primary pp vertex and the di-muon vertex, onto the direction of its transverse momentum, $p_T^{\mathcal{Q}}$. This is required to be less than three times its uncertainty $\sigma_{L_{xy}}$. An example plot of this quantity is shown in Figure 6.2 for $\psi(kS)\,\gamma$ candidates in data. The prompt contribution forms the symmetric peak around $L_{xy} = 0$ and the non-prompt background forms the linearly reducing plateau that extends to high values of $L_{xy}/\sigma_{L_{xy}}$.

Section 6.6.4 describes an optimisation procedure used to determine the best requirement for the transverse momentum of the $\mathcal{Q}$ candidate, $p_{\mathrm{T}}^{\mathcal{Q}}$. In this study the optimal values differ between the Higgs and Z boson analyses. To ensure near-optimal sensitivity in both analyses while using a single search region, the requirement on $p_{\mathrm{T}}^{\mathcal{Q}}$ therefore varies as a function of the invariant mass of the three-body system, $m_{\mathcal{Q}\gamma}$. For the $\psi(kS) \to \mu^+\mu^-$ ($\Upsilon(nS) \to \mu^+\mu^-$) selection, thresholds on $p_{\mathrm{T}}^{\mathcal{Q}}$ of 40.0 GeV (34.0 GeV) and 54.4 GeV (52.7 GeV) are imposed for the regions $m_{\mathcal{Q}\gamma} \leq 91$ GeV and $m_{\mathcal{Q}\gamma} \geq 140$ GeV, respectively. The thresholds are varied between their minimum and maximum values as a linear function of $m_{\mathcal{Q}\gamma}$ in the region 91 GeV $< m_{\mathcal{Q}\gamma} <$ 140 GeV. These requirements are shown in Equations 6.2 and 6.3

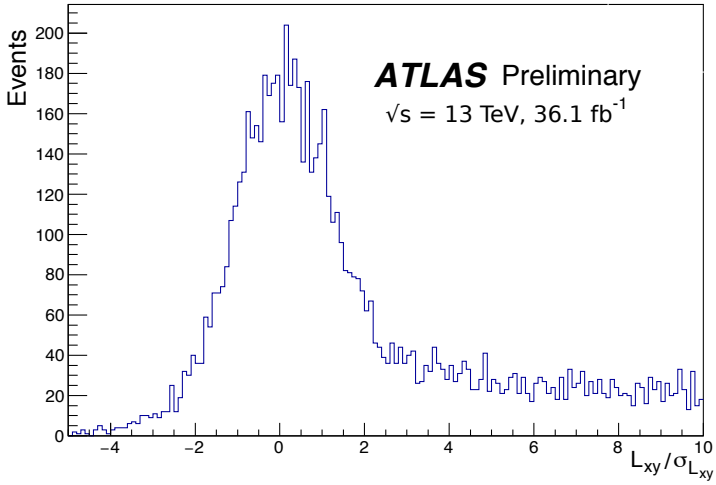

Figure 6.2: $L_{xy}/\sigma_{L_{xy}}$ distribution for $\psi(kS)\,\gamma$ candidates in data passing the Generation Region selection, as described in Section 6.6.5, but with the requirement on $L_{xy}/\sigma_{L_{xy}}$ relaxed. The prompt component of the background can be observed as the peak around $L_{xy}/\sigma_{L_{xy}} = 0$.

for the $\psi(kS) \to \mu^+\mu^-$ and $\Upsilon(nS) \to \mu^+\mu^-$ analyses, respectively.

- For $H(Z) \to \psi(kS)\,\gamma$ candidates, the di-muon system transverse momentum must satisfy:

$$p_T^{\mu^+\mu^-} > \begin{cases} 40 \text{ GeV}, & \text{if } m_{\mu^+\mu^-\gamma} \leq 91 \text{ GeV} \\ 40 + 10/34 \times (m_{\mu^+\mu^-\gamma} - 91) \text{ GeV}, & \text{if } 91 \text{ GeV} < m_{\mu^+\mu^-\gamma} < 140 \text{ GeV} \\ 54.41 \text{ GeV}, & \text{if } m_{\mu^+\mu^-\gamma} \geq 140 \text{ GeV}. \end{cases} \quad (6.2)$$

- For $H(Z) \to \Upsilon(nS)\,\gamma$ candidates, the di-muon system transverse momentum must satisfy:

$$p_T^{\mu^+\mu^-} > \begin{cases} 34 \text{ GeV}, & \text{if } m_{\mu^+\mu^-\gamma} \leq 91 \text{ GeV} \\ 34 + 13/34 \times (m_{\mu^+\mu^-\gamma} - 91) \text{ GeV}, & \text{if } 91 \text{ GeV} < m_{\mu^+\mu^-\gamma} < 140 \text{ GeV} \\ 52.74 \text{ GeV}, & \text{if } m_{\mu^+\mu^-\gamma} \geq 140 \text{ GeV}. \end{cases} \quad (6.3)$$

6.6.2 Photon Selection

Photons are reconstructed from clusters of energy in the electromagnetic calorimeter. Clusters without matching ID tracks are classified as unconverted photon candidates

while clusters matched to ID tracks and consistent with the hypothesis of a photon conversion into e^+e^- are classified as converted photon candidates [67]. Reconstructed photon candidates are required to have transverse momentum $p_{\mathrm{T}}^{\gamma} > 35$ GeV, pseudorapidity $|\eta^{\gamma}| < 2.37$, but excluding the barrel/endcap calorimeter transition region $1.37 < |\eta^{\gamma}| < 1.52$, and also to satisfy the "tight" photon identification criteria, as outlined in Section 4.4. The p_{T}^{γ} requirement is based on the optimisation study described in Section 6.6.4 and the generator-level p_{T}^{γ} distributions shown in Figure 6.3. Isolation requirements are imposed to suppress the contamination from jets, following an ATLAS working point called "FixedCutTight". The scalar sum of the transverse momenta of all tracks originating from the primary vertex, within $\Delta R = 0.2$ of the photon direction, excluding those associated with the reconstructed photon, is required to be less than 5% of p_{T}^{γ}. In addition to this track isolation, a calorimeter isolation requirement is applied, where the sum of the transverse momenta of calorimeter energy clusters within $\Delta R = 0.4$ of the photon direction, excluding the energy of the reconstructed photon, is required to be less than $(2.45\ \mathrm{GeV} + 0.022 \times p_{\mathrm{T}}^{\gamma})$. The effects of multiple pp interactions in the events are also accounted for in the calorimeter isolation measurements using a calculation of the median transverse energy density from low-p_{T} jets [67].

6.6.3 $H(Z) \to \mathcal{Q}\,\gamma$ Selection

Combinations of a $\mathcal{Q} \to \mu^+\mu^-$ candidate and a photon, with a separation in azimuthal angle satisfying $\Delta\phi(\mathcal{Q}, \gamma) > \pi/2$, are retained for further analysis. When multiple combinations are possible, a situation that arises in only a few percent of the events, the combination of the highest-p_{T} photon and the $\mathcal{Q}$ candidate with invariant mass closest to the respective quarkonium mass is retained. To improve the sensitivity of the $\Upsilon(nS)\gamma$ analysis in resolving the individual $\Upsilon(nS)$ states, the events are classified into two exclusive categories, based upon the pseudorapidity of the muons. Events where both muons are within the region $|\eta^{\mu^{\pm}}| < 1.05$ constitute the "barrel" (B) category. Events where at least one of the muons is outside the

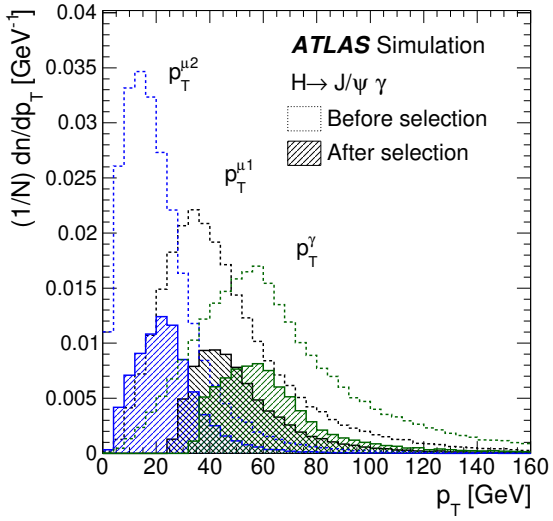

(a) $H \to J/\psi\,\gamma$

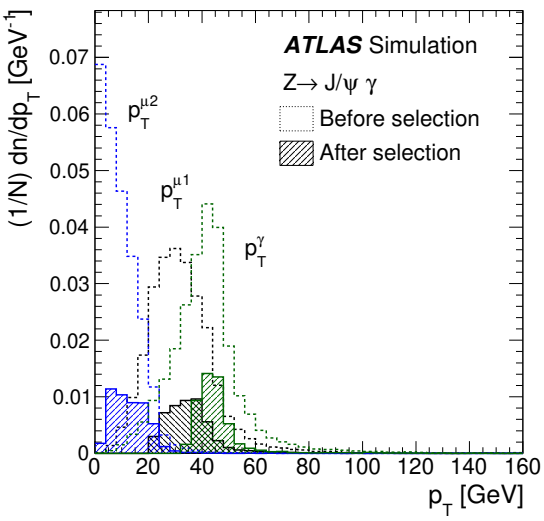

(b) $Z \to J/\psi\,\gamma$

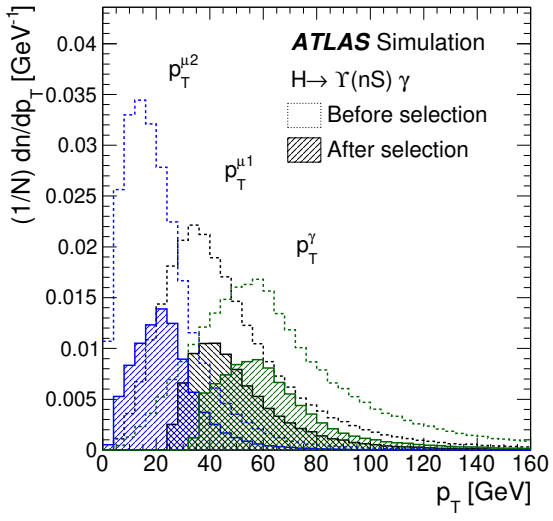

(c) $H \to \Upsilon(nS)\,\gamma$

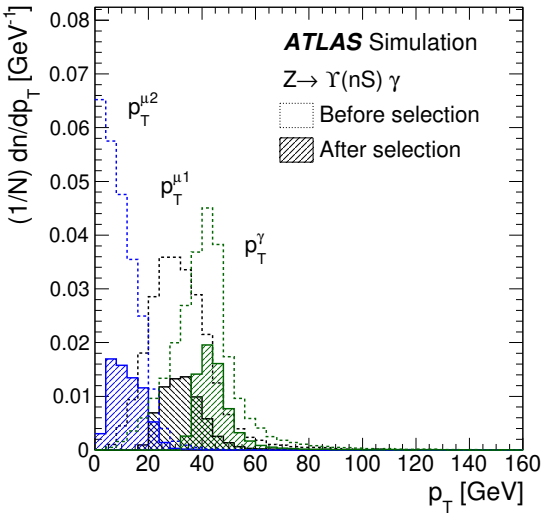

(d) $Z \to \Upsilon(nS)\,\gamma$

Figure 6.3: Generator-level p_{T} distributions of the photon and of the muons, ordered in p_{T}, for (a) $H \to J/\psi\,\gamma$, (b) $Z \to J/\psi\,\gamma$, (c) $H \to \Upsilon(nS)\,\gamma$ and (d) $Z \to \Upsilon(nS)\,\gamma$ simulated signal events, respectively. The hatched histograms denote the full event selection while the dashed histograms show the events at generator level that fall within the analysis geometric acceptance (both muons are required to have $|\eta^{\mu^{\pm}}| < 2.5$ while the photon is required to have $|\eta^{\gamma}| < 2.37$, excluding the region $1.37 < |\eta^{\gamma}| < 1.52$). The dashed histograms are normalised to unity, and the relative difference between the two sets of distributions corresponds to the effects of reconstruction, trigger, and event selection efficiencies. The leading muon candidate is denoted by $p_{\mathrm{T}}^{\mu 1}$ and the sub-leading candidate by $p_{\mathrm{T}}^{\mu 2}$. Figure taken from Ref. [1].

region $|\eta^{\mu^{\pm}}| < 1.05$ constitute the "endcap" (EC) category. The $m_{\mu^+\mu^-}$ resolution is different in each of these categories, giving the required improved separation of the $\Upsilon(nS)$ states.

6.6.4 Selection Requirement Optimisation Procedure

The majority of the requirements described in the previous section are chosen based on the limitations of the detector or on several pieces of external information. The p_{T}^{γ} and $p_{\mathrm{T}}^{\mu^+\mu^-}$ selections have more freedom to be varied. These are optimised, with the other requirements fixed to the values described in Section 6.6. The p_{T}^{γ} and $p_{\mathrm{T}}^{\mu^+\mu^-}$ requirements are varied systematically and the yields of signal MC and estimated background events are recorded within the ranges 120 GeV $< m_{\mu^+\mu^-\gamma} <$ 130 GeV and 80 GeV $< m_{\mu^+\mu^-\gamma} <$ 100 GeV for the Higgs and Z bosons, respectively. A simple Poisson likelihood function is assumed using the yields of signal and background events for each combination of selection requirements, to obtain distributions of the expected 95% confidence level upper limits on the Higgs and Z branching fractions to $\mathcal{Q}\,\gamma$. Figures 6.4 and 6.6 show these distributions for the $H \to \psi(kS)\,\gamma$ and $Z \to \psi(kS)\,\gamma$ analyses, and Figures 6.5 and 6.7 show the distributions for the $H \to \Upsilon(nS)\,\gamma$ and $Z \to \Upsilon(nS)\,\gamma$ analyses, respectively. Also shown in these figures are the signal and background efficiencies relative to the numbers of events passing the loosest cuts. Ultimately, the aim is to achieve the lowest 95% confidence level upper limits with the selection requirements; however, consideration must also be made to retain a high signal efficiency. In the figures shown, the optimum values for the selection are shown by the lightest shade of colour.

Based on this study, the optimal selection requirements are to use the lowest possible p_{T}^{γ} requirement, limited to 35 GeV by the trigger requirement. A varying $p_{\mathrm{T}}^{\mu^+\mu^-}$ requirement is chosen, which increases linearly between the Higgs and Z boson masses, such that the optimal $p_{\mathrm{T}}^{\mu^+\mu^-}$ values are achieved for the Higgs and Z boson analyses. The requirements to achieve this are given in Equations 6.2 and 6.3 for the $\psi(kS) \to \mu^+\mu^-$ and $\Upsilon(nS) \to \mu^+\mu^-$ analyses, respectively.

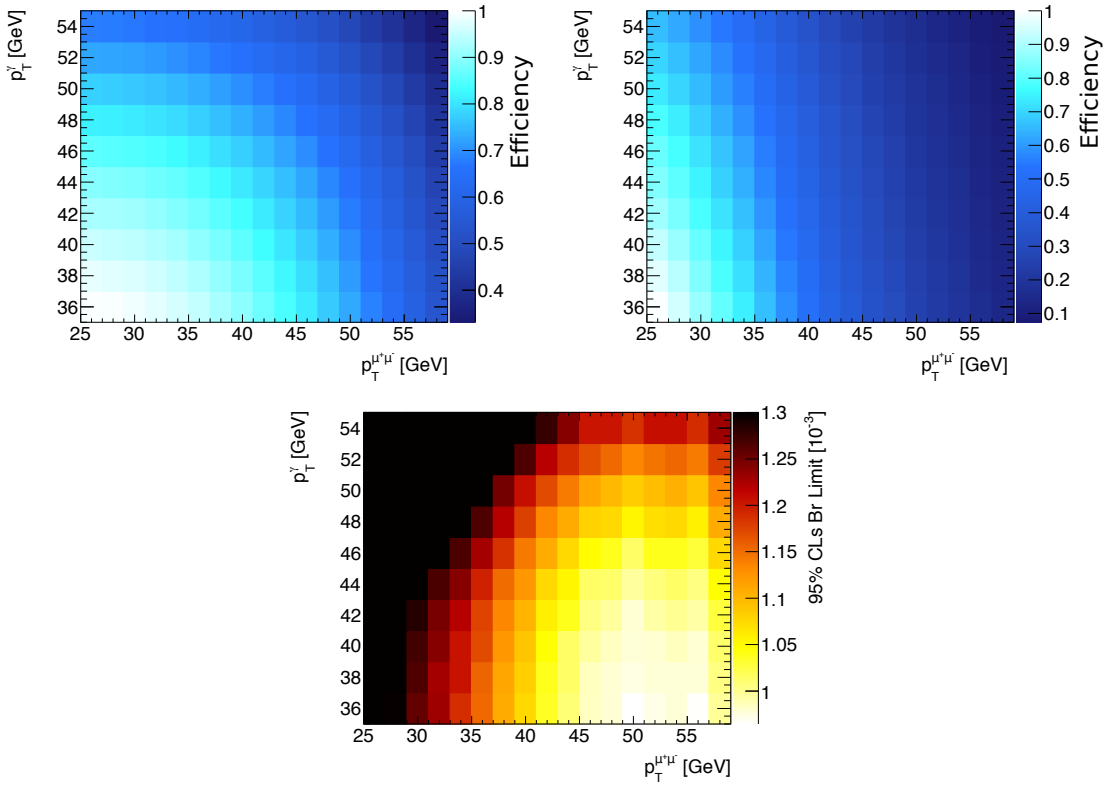

Figure 6.4: Optimisation of the p_{T}^{γ} and $p_{\mathrm{T}}^{\mu^+\mu^-}$ selection requirements for $H \to \psi(kS)\,\gamma \to \mu^+\mu^-\gamma$ decays using an estimation of the expected 95% CL upper limit as the figure of merit (bottom plot). The top two figures show the signal (left) and background (right) efficiencies relative to the numbers of events passing the loosest cuts (bottom left bin).

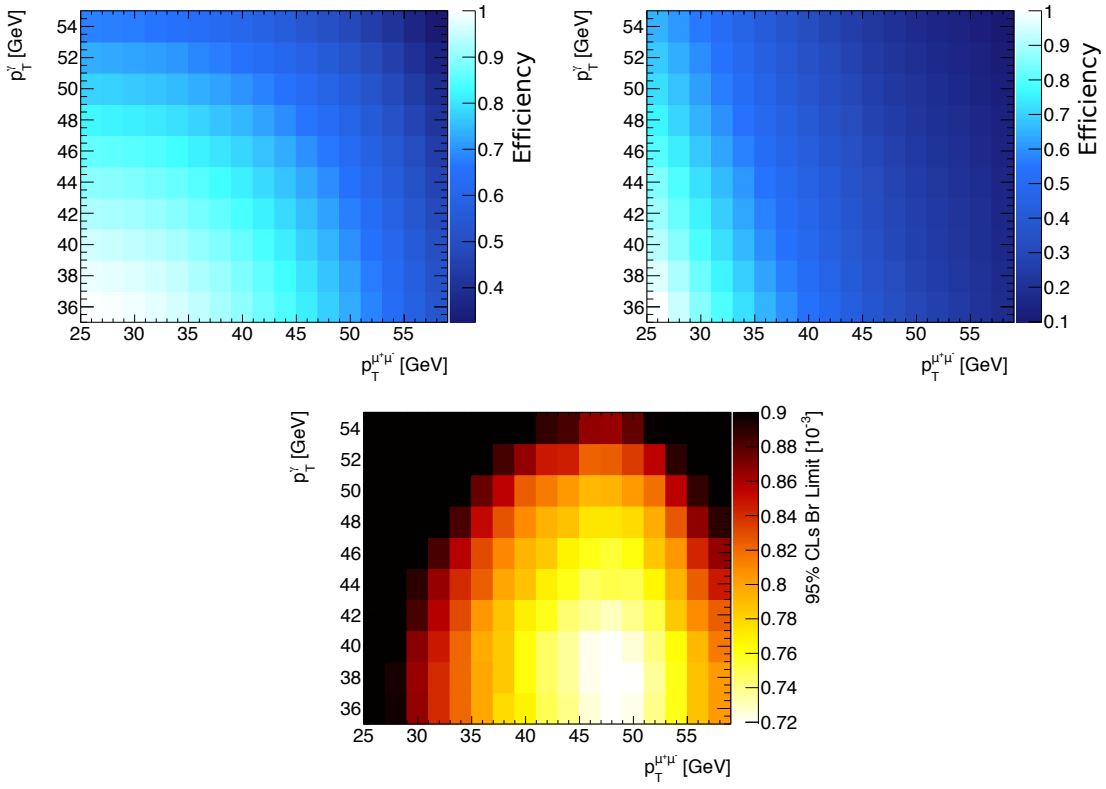

Figure 6.5: Optimisation of the p_{T}^{γ} and $p_{\mathrm{T}}^{\mu^+\mu^-}$ selection requirements for $H \to \Upsilon(nS)\,\gamma \to \mu^+\mu^-\gamma$ decays using an estimation of the expected 95% CL upper limit as the figure of merit (bottom plot). The top two figures show the signal (left) and background (right) efficiencies relative to the numbers of events passing the loosest cuts (bottom left bin).

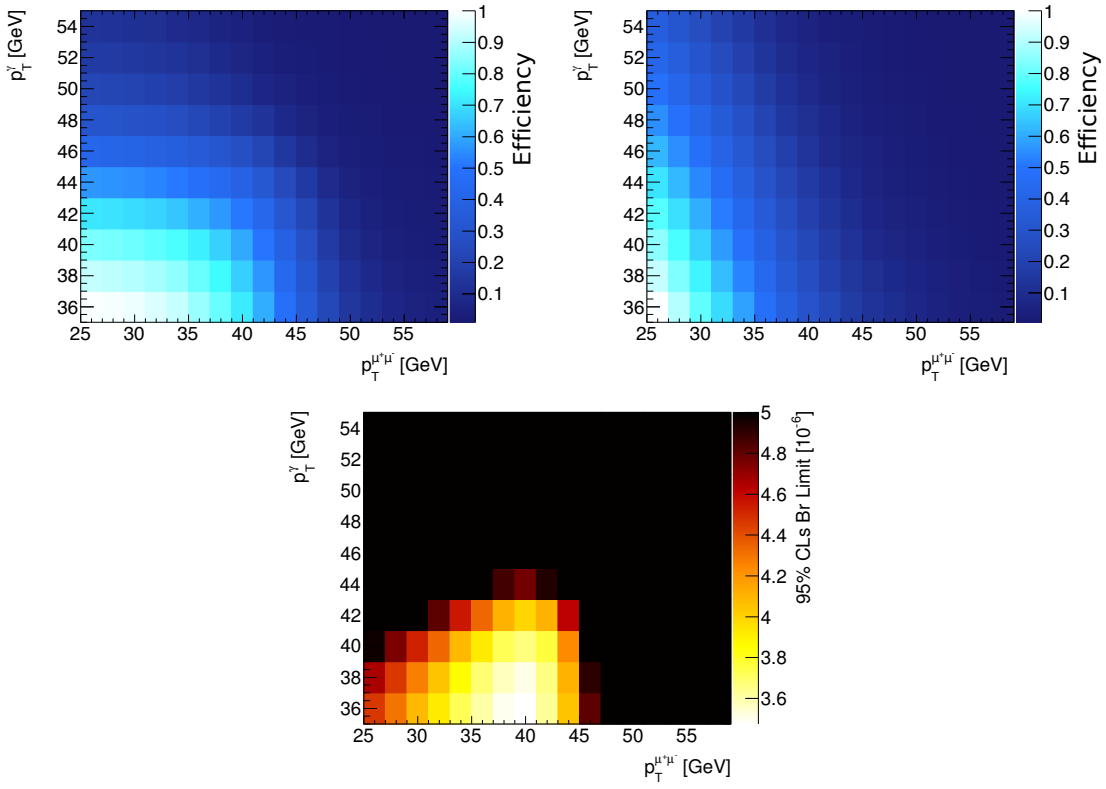

Figure 6.6: Optimisation of the p_{T}^{γ} and $p_{\mathrm{T}}^{\mu^+\mu^-}$ selection requirements for $Z \to \psi(kS)\,\gamma \to \mu^+\mu^-\gamma$ using an estimation of the expected 95% CL upper limit as the figure of merit (bottom plot). The top two figures show the signal (left) and background (right) efficiencies relative to the numbers of events passing the loosest cuts (bottom left bin).

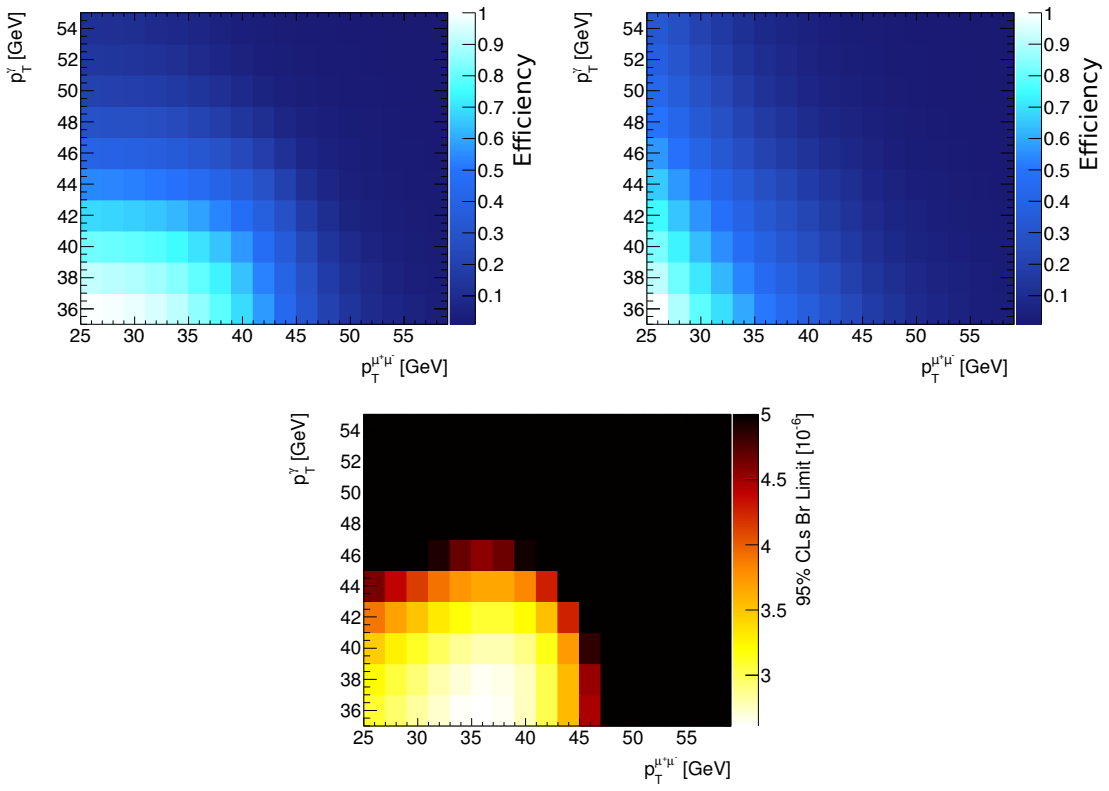

Figure 6.7: Optimisation of the p_{T}^{γ} and $p_{\mathrm{T}}^{\mu^+\mu^-}$ selection requirements for $Z \to \Upsilon(nS)\,\gamma \to \mu^+\mu^-\gamma$ using an estimation of the expected 95% CL upper limit as the figure of merit (bottom plot). The top two figures show the signal (left) and background (right) efficiencies relative to the numbers of events passing the loosest cuts (bottom left bin).

6.6.5 Selection and Validation Regions

Multiple regions are defined using different selection requirements, which are needed for the generation and validation of the background model. The nominal selection, as described above, is defined as the Signal Region (SR); this is the final selection used to perform the analysis and search for the Higgs and Z boson decays. For the generation of the background model, a looser selection is required to create a region dominated by background events, with negligible signal contributions, in which the background can be modelled accurately, as described in Section 7.2. In this region, referred to as the Generation Region (GR), the isolation criteria of the photon and $\mathcal{Q}$ candidates are removed and a looser requirement of $p_{\mathrm{T}}^{\mu^+\mu^-} > 30\,\mathrm{GeV}$ is imposed. Three further regions are defined: Validation Region 1 (VR1), which is the same as GR, but with the inclusion of the standard $p_{\mathrm{T}}^{\mu^+\mu^-}$ requirement; VR2, which uses the GR selection but with the $\mathcal{Q}$ isolation requirement imposed; and VR3, which uses the GR selection as well as imposing the photon isolation requirements. The validation regions are used to check the performance of the modelling of key kinematic quantities within the background sample, after each tighter selection requirement has been applied. The regions defined are summarised in Table 6.3.

Table 6.3: Summary of the five control regions and the selection requirements applied on top of the loose GR selection.

Region	$p_{\mathrm{T}}^{\mu^+\mu^-}$	Photon Isolation	$\mathcal{Q}$ Isolation
GR	-	-	-
VR1	Eqs. 6.2 and 6.3	-	-
VR2	-	-	FixedCutTightTrackOnly
VR3	-	FixedCutTight	-
SR	Eqs. 6.2 and 6.3	FixedCutTight	FixedCutTightTrackOnly

6.6.6 Passing of $H(Z) \to J/\psi\,\gamma$ Events through Selection Criteria

The passing of events through the different selection criteria ("cut flow") is studied using the $H \to J/\psi\,\gamma$ and $Z \to J/\psi\,\gamma$ signal MC samples and the 2015–2016 data samples. Table 6.4 presents the impact of each requirement. The starting events for the signal is based on the generated $H(Z) \to J/\psi\,\gamma$ events, whereas the data events start at the "preselection". The preselection applies the derivation requirements and further slightly tighter requirements, which includes the following:

- Photons must pass the medium quality requirements and have $p_{\mathrm{T}}^{\gamma} > 15$ GeV, with the detector η requirements;
- Muons must be segment tagged or combined with $p_{\mathrm{T}}^{\mu^{\pm}} > 3$ GeV and $|\eta^{\mu}| < 2.5$, and the di-muon mass must be within 2 GeV $< m_{\mu\mu} <$ 14 GeV.

Table 6.4: $J/\psi\,\gamma$ cut flow in signal MC. Branching fractions of $\mathcal{B}(H \to J/\psi\,\gamma) = 10^{-3}$ and $\mathcal{B}(Z \to J/\psi\,\gamma) = 10^{-6}$ are assumed along with an integrated luminosity of 36.1 fb^{-1}. Preselection is defined in the main text.

	Signal					**Data**
	ggH	VBF	WH	ZH	Z	
`Starting events`	105.71	8.04	2.92	1.88	124.85	173 081
`Preselection`	43.95	3.54	1.14	0.75	41.06	173 081
`Passed Trigger`	39.69	3.09	1.01	0.66	31.07	71 332
`Leading` $p_T^{\mu} >$ `18 GeV`,	39.54	3.07	1.00	0.66	30.75	66 148
`Photon:- tight,`p_T^{γ} `> 35 GeV`,	37.70	2.85	0.93	0.61	27.17	52 339
$p_T^{\mu\mu}$ `>30 GeV`,	37.00	2.75	0.90	0.59	26.18	36 487
$m_{\mu\mu}$ `requirement`,	37.00	2.75	0.90	0.59	26.18	26 710
$\Delta\phi(\mathcal{Q}, \gamma) > \pi/2$	33.82	1.94	0.65	0.42	25.34	22 793
$\lvert L_{xy}/\sigma(L_{xy})\rvert < 3.0$	33.52	1.92	0.65	0.42	25.11	9848
`Pass GR`	32.73	1.87	0.62	0.41	24.54	5485
`Pass SR`	20.44	1.13	0.37	0.24	13.66	1101

6.6.7 Passing of $H(Z) \to \Upsilon(nS)\,\gamma$ Events through Selection Criteria

The cut flow is studied using the $H(Z) \to \Upsilon(nS)\,\gamma$ signal MC and the 2015–2016 data samples. Tables 6.5, 6.6 and 6.7 present the impact of each requirement. The

starting events for the signal is based on the generated $H(Z) \to \Upsilon(nS)\,\gamma$ events, whereas the data events start at the "preselection". The preselection applies the derivation requirements and further slightly tighter requirements, which includes the following:

- Photons must pass the medium quality requirements and have $p_{\mathrm{T}}^{\gamma} > 15$ GeV, with the detector η requirements;
- Muons must be segment tagged or combined with $p_{\mathrm{T}}^{\mu^{\pm}} > 3$ GeV and $|\eta^{\mu}| < 2.5$, and the di-muon mass must be within 2 GeV $< m_{\mu\mu} <$ 14 GeV.

Table 6.5: $\Upsilon(1S)\,\gamma$ cut flow in signal MC. Branching fractions of $\mathcal{B}(H \to \Upsilon(1S)\,\gamma) = 10^{-3}$ and $\mathcal{B}(Z \to \Upsilon(1S)\,\gamma) = 10^{-6}$ are assumed along with an integrated luminosity of 36.1 fb^{-1}. Preselection is defined in the main text.

	Signal					**Data**
	ggH	VBF	WH	ZH	Z	
`Starting events`	44.66	3.41	1.24	0.80	52.89	173 081
`Preselection`	18.91	1.55	0.49	0.32	17.02	173 081
`Passed Trigger`	17.29	1.38	0.44	0.29	12.97	71 332
`Leading` $p_T^{\mu} >$ `18 GeV`,	17.19	1.37	0.44	0.28	12.82	66 148
`Photon:- tight,` p_T^{γ} `> 35 GeV`,	16.28	1.25	0.40	0.26	11.26	52 339
$p_T^{\mu\mu}$ `>30 GeV`,	15.96	1.20	0.39	0.25	10.80	36 487
$m_{\mu\mu}$ `requirement`,	15.96	1.20	0.39	0.25	10.64	6447
$\Delta\phi(\mathcal{Q}, \gamma) > \pi/2$	14.64	0.83	0.28	0.18	10.32	5375
$\lvert L_{xy}/\sigma(L_{xy})\rvert < 3.0$	14.54	0.82	0.27	0.18	10.25	3480
`Pass GR`	14.23	0.80	0.26	0.17	10.05	2328
`Pass SR`	9.87	0.53	0.17	0.11	7.76	943

Table 6.6: $\Upsilon(2S)\,\gamma$ cut flow in signal MC. Branching fractions of $\mathcal{B}(H \to \Upsilon(2S)\,\gamma) = 10^{-3}$ and $\mathcal{B}(Z \to \Upsilon(2S)\,\gamma) = 10^{-6}$ are assumed along with an integrated luminosity of 36.1 fb^{-1}. Preselection is defined in the main text.

	Signal					**Data**
	ggH	VBF	WH	ZH	Z	
`Starting events`	34.13	2.60	0.94	0.61	40.13	173 081
`Preselection`	14.45	1.17	0.37	0.24	13.06	173 081
`Passed Trigger`	13.28	1.04	0.33	0.22	10.04	71 332
`Leading` $p_T^\mu >$ `18 GeV`,	13.20	1.03	0.33	0.22	9.94	66 148
`Photon:- tight,` $p_T^\gamma >$ `35 GeV`,	12.44	0.95	0.30	0.20	8.57	52 339
$p_T^{\mu\mu}$ `>30 GeV`,	12.17	0.91	0.29	0.19	8.20	36 487
$m_{\mu\mu}$ `requirement`,	12.16	0.91	0.29	0.19	8.14	6447
$\Delta\phi(\mathcal{Q}, \gamma) > \pi/2$	11.12	0.63	0.21	0.14	7.88	5375
$\lvert L_{xy}/\sigma(L_{xy})\rvert < 3.0$	11.04	0.62	0.21	0.13	7.83	3480
`Pass GR`	10.79	0.61	0.20	0.13	7.67	2328
`Pass SR`	7.47	0.40	0.13	0.08	5.89	943

Table 6.7: $\Upsilon(3S)\,\gamma$ cut flow in signal MC. Branching fractions of $\mathcal{B}(H \to \Upsilon(3S)\,\gamma) = 10^{-3}$ and $\mathcal{B}(Z \to \Upsilon(3S)\,\gamma) = 10^{-6}$ are assumed along with an integrated luminosity of 36.1 fb^{-1}. Preselection is defined in the main text.

	Signal					**Data**
	ggH	VBF	WH	ZH	Z	
`Starting events`	39.47	3.00	1.09	0.70	46.69	173 081
`Preselection`	16.64	1.36	0.43	0.28	15.17	173 081
`Passed Trigger`	15.29	1.21	0.39	0.25	11.88	71 332
`Leading` $p_T^\mu >$ `18 GeV`,	15.21	1.20	0.38	0.25	11.78	66 148
`Photon:- tight,` $p_T^\gamma >$ `35 GeV`,	14.37	1.11	0.35	0.23	10.33	52 339
$p_T^{\mu\mu}$ `>30 GeV`,	14.09	1.06	0.34	0.22	9.84	36 487
$m_{\mu\mu}$ `requirement`,	14.08	1.06	0.34	0.22	9.78	6447
$\Delta\phi(\mathcal{Q}, \gamma) > \pi/2$	12.93	0.73	0.24	0.16	9.43	5375
$\lvert L_{xy}/\sigma(L_{xy})\rvert < 3.0$	12.81	0.73	0.24	0.16	9.35	3480
`Pass GR`	12.52	0.71	0.23	0.15	9.11	2328
`Pass SR`	8.51	0.47	0.15	0.10	7.06	943

6.6.8 $\psi(kS)$ and $\Upsilon(nS)$ Candidates

The $m_{\mu^+\mu^-}$ distribution for selected $\psi(kS)\,\gamma$ candidates in the GR is shown in Figure 6.8(a), and exhibits clear peaks at the J/ψ and $\psi(2S)$ masses. In Figure 6.8(b) and Figure 6.8(c), the corresponding GR distributions for the selected $\Upsilon(nS)\,\gamma$ candidates in the barrel and endcap categories, respectively, are shown, where the $\Upsilon(1S, 2S, 3S)$ peaks can be observed. The $\psi(kS)$ and $\Upsilon(nS)$ peaks are fitted with Gaussian probability density functions (pdfs), while the distribution of the non-resonant events is modelled with a Chebychev polynomial function. The experimental resolution in $m_{\mu^+\mu^-}$ is around 54 MeV for the $J/\psi\,\gamma$ candidates (43 MeV for events in the barrel category and 64 MeV for events in the endcap category).

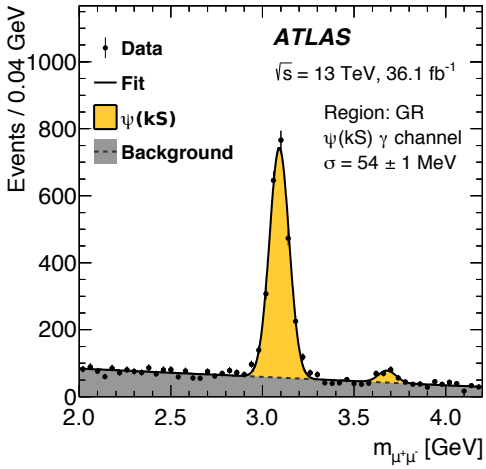

(a) $\psi(kS)$ candidates

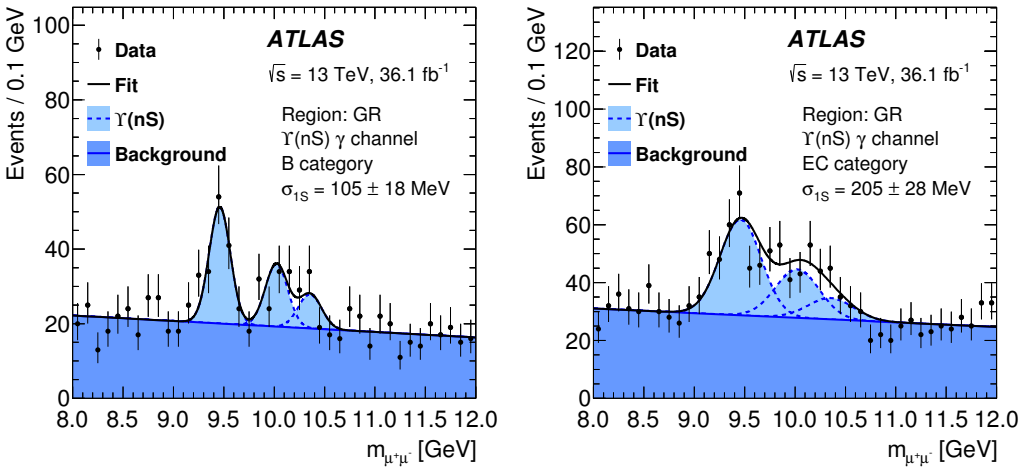

(b) $\Upsilon(nS)$ candidates in the barrel category (c) $\Upsilon(nS)$ candidates in the endcap category

Figure 6.8: Distribution of $\mu^+\mu^-$ invariant mass for $\psi(kS)\,\gamma$ (a) and $\Upsilon(nS)\,\gamma$ (barrel (b) and endcap (c) categories) candidates, respectively. The candidates fulfil the event selection, but without the nominal isolation requirements and with a looser minimum $p_{\mathrm{T}}^{\mathcal{Q}}$ requirement of 30 GeV. These events define the background dominated Generation Region (GR). The signal and background models are discussed in the text. Figure taken from Ref. [1].

CHAPTER 7

SEARCH FOR THE HIGGS AND Z BOSON DECAYS TO $\psi(kS)\gamma$ AND $\Upsilon(nS)\gamma$: SIGNAL AND BACKGROUND MODEL AND RESULTS

In the previous chapter the basis of the search for Higgs and Z boson decays to $\psi(kS)\gamma$ and $\Upsilon(nS)\gamma$ was discussed. The chapter provided details of the datasets, simulation samples and triggers used, as well as a description of the selection requirements applied and their motivation. This chapter focusses on the signal and background models and the details of the final fitting procedure. An overview of the fitting procedure is given in Section 7.1. Section 7.2 provides a detailed account of the background modelling method and Section 7.3 presents an assortment of kinematic distributions, which serve to validate the background model. The signal

modelling is discussed in Section 7.4 and the systematic uncertainties of the normalisation of the signal yields are given in Section 7.5. The final fitting procedure is performed and the results are described in Section 7.6.

7.1 Fitting Procedure

Throughout the analysis many fits are employed to estimate both the background and signal contributions, and to perform the final fitting procedure to measure the signal present in the data. This section provides an overview of the different fits used in the analysis.

7.1.1 Signal Modelling

The signal is modelled by fitting analytical functions to the signal MC events that pass the full SR event selection. The parameters obtained from this fit are fixed for the final fitting procedure. A complete discussion of the different signal models and the measured parameters is given in Section 7.4.

7.1.2 Background Modelling

Fits are used in two areas for the generation of the background model. Firstly, a fit is performed to the $m_{\mu^+\mu^-\gamma}$ distribution of GR data events to separate the exclusive background (from $Z \to \mu^+\mu^-\gamma$) from the inclusive combinatoric background. The results from this fit are used to remove the exclusive background events when sampling data for construction of the data-driven background model. A second fit is performed on the $m_{\mu^+\mu^-}$ distribution of GR data events. This fit models the inclusive background shape with analytical functions, which are described by parameters that are then fixed to these values for the final fitting procedure on the SR data events. The exclusive background for the $\Upsilon(nS)\gamma$ case is fitted to the $m_{\mu^+\mu^-}$ distribution in

a sample of MC events, whereas for $\psi(kS)\gamma$ the parameters of this distribution are determined by the final fitting procedure. The full background method is described in Section 7.2.

7.1.3 Overview of Fitting Procedure

A final fit is performed to the data using the background and signal models described below. This fit is initially tested on a dataset constructed from the predicted background distributions to obtain the expected sensitivity of the experiment, as explained in Section 7.6.1. The results from this final fit are reported in Section 7.6.3.

For these analyses two discriminant variables are used during the fit: the invariant mass of the $\mu^+\mu^-\gamma$ system ($m_{\mu^+\mu^-\gamma}$) and the invariant mass of the $\mu^+\mu^-$ system ($m_{\mu^+\mu^-}$). A simultaneous two-dimensional (2D) unbinned maximum-likelihood fit is performed to these two variables to better separate the non-resonant backgrounds from the resonant backgrounds and signal. In the case that no signal is observed, the 95% CL limits on the branching fractions, $\mathcal{B}(H/Z \to \mathcal{Q}\gamma)$ are extracted from the fitting procedure.

The fits include pdfs for the signal ($H/Z \to \mathcal{Q}\gamma$) and the background processes, whilst the normalisation of each is free to float in the fit. The pdfs used to model the signal are described in Section 7.4. For the background $m_{\mu^+\mu^-\gamma}$ distribution, the data-driven method that is described in Section 7.2.1 is used to model the inclusive background with the exclusive Z FSR events modelled as described in Section 7.2.2. As will be described in Section 7.2.5, the $m_{\mu^+\mu^-}$ inclusive background distributions are modelled as Gaussian distributions for the resonant components and as a linear function for the non-resonant background. A linear function is used for the Z FSR background.

The statistical procedure uses the CL_s modified frequentist formalism [117] with the profile-likelihood ratio test statistic [118] and the asymptotic approximations derived in Ref. [119]. The signal and background pdfs are used to create a likelihood

function, $\mathcal{L}$, which depends on the signal strength parameter μ:

$$\mathcal{L}(\mu,\theta) = \prod_{j}^{\mathrm{N}_{bins}} \mathrm{Pois}(N_j|\mu\cdot S_j(\theta)+B_j(\theta)) \cdot \prod_{k=1}^{N_j} \mathcal{P}_k(m_{\mu^+\mu^-\gamma}, m_{\mu^+\mu^-}|\mu,\theta). \quad (7.1)$$

This likelihood function corresponds to the product over all the bins of the Poisson probability of observing N_j events in each bin, j, of the ($m_{\mu^+\mu^-\gamma}$, $m_{\mu^+\mu^-}$) distribution, given the expectation for the signal S_j and background B_j. This is multiplied by the product over the candidates in each bin of the values of the pdfs $\mathcal{P}_k$, which are constructed using the signal and background pdfs described below. The signal strength parameter, μ, represents the branching ratio of the signal of interest. The systematic uncertainties, which are described in Section 7.5, are introduced in the fit as nuisance parameters, θ. During the fit, these parameters are profiled to find their most likely value, whilst being constrained to their central value by a Gaussian dependence. The shapes of the pdfs of the background observables are also varied as described in Section 7.2.3. The shape systematic uncertainties are implemented using the interpolation technique described in Ref. [120]. The fit and limit setting are performed inclusively for the $\psi(kS)\gamma$ channel, while the $\Upsilon(nS)\gamma$ channel fits barrel and endcap categories separately, due to their different mass resolutions. In the case of the categorised $\Upsilon(nS)\gamma$ fit, the product of the likelihood functions of the two categories is taken to obtain the total likelihood function.

The 95% CL limits extracted are based on the profile likelihood ratio $\Lambda(\mu)$, which depends on the parameter of interest μ and on the nuisance parameters θ [119]:

$$\Lambda(\mu) = \frac{L\big(\mu,\hat{\hat{\theta}}(\mu)\big)}{L(\hat{\mu},\hat{\theta})} \quad . \quad (7.2)$$

Here $\hat{\hat{\theta}}$ corresponds to the value of θ that maximises $\mathcal{L}$ for the specified fixed value of μ, whereas $\hat{\mu}$ denotes the unconditional maximum likelihood estimate of μ, i.e.

where the likelihood is maximised for both θ and μ simultaneously.

While one signal (Higgs or Z) is being measured, the other is free and is profiled in the fit.

7.2 Background Modelling

Two distinct types of background events containing $\mathcal{Q}\gamma \to \mu^+\mu^-\gamma$ candidates are considered and are modelled with different approaches.

The "exclusive" backgrounds are mostly caused by fully or partially reconstructed decays of heavy bosons with FSR, most notably $Z \to \mu^+\mu^-\gamma$. These backgrounds lead to characteristic resonant distributions in $m_{\mu^+\mu^-\gamma}$ and a non-resonant distribution in $m_{\mu^+\mu^-}$.

The "inclusive" background is defined as a collection of sources that give rise to a quarkonium decay $\mathcal{Q} \to \mu^+\mu^-$, which is resonant in $m_{\mu^+\mu^-}$ (or a non-resonant di-muon pair with an invariant mass close to the $\psi(kS)$ or $\Upsilon(nS)$ masses), and an unrelated reconstructed high energy photon. These are generally combinatoric in nature or caused by an experimental misidentification (e.g. a jet misidentified as a photon). These backgrounds lead to a non-resonant distribution in $m_{\mu^+\mu^-\gamma}$.

Double/multi-parton interactions giving rise to a genuine isolated quarkonium decay $\mathcal{Q} \to \mu^+\mu^-$ (or non-resonant di-muon pair) and an isolated photon are expected to contribute at a relatively low level. Exclusive QCD processes, such as the associated production of $\mathcal{Q}\,\gamma$, have been found to be small compared to the inclusive background. Both of these sources are, nevertheless, included in the data-driven inclusive background estimation.

The same modelling procedure is used for the inclusive backgrounds in both the $\psi(kS)\,\gamma$ and $\Upsilon(nS)\,\gamma$ analyses. The method was developed for the Run I $J/\psi\,\gamma$ and $\Upsilon(nS)\,\gamma$ analyses [38] and improved upon in the later $\phi\gamma$ and $\rho\gamma$ analyses [2, 3].

7.2.1 Modelling of Inclusive Backgrounds

The main source of the inclusive background to $\mathcal{Q}\gamma \rightarrow \mu^+\mu^-\gamma$ signal events is inclusive quarkonium production in association with a jet, e.g. $gg \rightarrow \mathcal{Q}g$, in which the jet is subsequently misidentified as a single photon. The quarkonium state in such events can be well isolated while the photon candidate will, in general, be surrounded by hadronic activity. This prompt background can be effectively suppressed by requiring that the photon is well isolated, although the cross section of the underlying production mechanism is very large.

In the $\psi(kS)\,\gamma$ channel, the production of a $b\bar{b}$ pair can also give rise to a $\psi(kS)$ (from the decay of a b-hadron) recoiling against a hadronic system that could be misidentified as a single photon. In such a case, the decay vertex of the $\psi(kS)$ can be significantly displaced from the primary pp vertex and will generally be surrounded by hadronic activity from the fragmentation of the b quark and the subsequent decay of the b-hadron. This contribution can be suppressed effectively by requiring that the $\psi(kS)$ decay vertex is spatially consistent with the primary pp interaction vertex (with the decay length significance requirement discussed in Section 6.6) and requiring that the di-muon system is well isolated. Nevertheless this non-prompt source of $\psi(kS)$ represents the dominant contribution to $\psi(kS)$ production at $p_{\mathrm{T}}^{\mathcal{Q}} > 40$ GeV [121] and thus forms a significant contribution to the inclusive background.

Other contributions to the inclusive background include Drell-Yan production of $\mu^+\mu^-$ plus jets, or multi-jet, mostly $b\bar{b}$, events giving rise to a non-resonant di-muon pair and a single reconstructed photon.

The inclusive background cannot be reliably modelled with MC simulation due to the complicated mixture of the contributing processes. Inclusive backgrounds are instead described using a non-parametric data-driven approach. This involves using the kinematic and isolation distributions of a large sample of loose $\mathcal{Q}\gamma \rightarrow \mu^+\mu^-\gamma$ candidates in the data (the GR region defined in Section 6.6.5) to generate an

ensemble of "toy" $\mathcal{Q}\gamma \to \mu^+\mu^-\gamma$ candidates. These loose toy candidates are then subjected to the same final tight kinematic and isolation selection criteria as the data (the SR region) to form a sample that can be used to model the kinematic distributions of the inclusive background that remains after all the selection requirements have been applied.

The model is mostly based upon an investigation of the correlations between variables to which the $m_{\mu^+\mu^-\gamma}$ distribution is sensitive. The important correlations are shown in Figure 7.1. The key kinematic parameters that are modelled are the dimuon and photon transverse momentum $p_{\rm T}^{\mu^+\mu^-}$ and $p_{\rm T}^{\gamma}$; the muon track isolation relative to $p_{\rm T}^{\mu^+\mu^-}$ (μ TrkIso); photon track and calorimeter isolations relative to $p_{\rm T}^{\gamma}$ (γ TrkIso and γ CaloIso); the pseudorapidity difference between $\mathcal{Q}$ and γ, $\Delta\eta(\mathcal{Q},\gamma)$ (denoted $\Delta\eta$ in Figure 7.1), and the azimuthal angular separation between $\mathcal{Q}$ and γ, $\Delta\phi(\mathcal{Q},\gamma)$ (denoted $\Delta\phi$ in Figure 7.1)) .

The strongest correlation to $m_{\mu^+\mu^-\gamma}$ is $p_{\rm T}^{\mu^+\mu^-}$ and, therefore, $p_{\rm T}^{\mu^+\mu^-}$ is chosen as the basis for the correlations in the model. $p_{\rm T}^{\mu^+\mu^-}$ is also strongly correlated to $p_{\rm T}^{\gamma}$, and to the relative muon track isolation. The relative photon calorimeter isolation is strongly correlated to $p_{\rm T}^{\gamma}$ and to the relative photon track isolation. $\Delta\eta(\mathcal{Q},\gamma)$ is correlated strongly with $m_{\mu^+\mu^-\gamma}$ and loosely correlated with photon calorimeter isolation. The aim of the background model is to replicate the distributions of these kinematic variables, whilst retaining the key correlations. These correlations are retained by separating the GR data events into bins of one or two parameters. The parameter of interest is sampled from its kinematic distribution in a bin selected by the chosen values of the correlated parameters.

Based on the correlations, each toy background $\mathcal{Q}\gamma \to \mu^+\mu^-\gamma$ candidate is formed according to the following procedure:

i) Initially, a value for $p_{\rm T}^{\mathcal{Q}}$ is sampled from the corresponding pdf, which is formed by performing Kernel Density Estimation (KDE) smoothing [122] to the GR $p_{\rm T}^{\mu^+\mu^-}$ distributions shown in Figures 7.8(a) and 7.16(a).

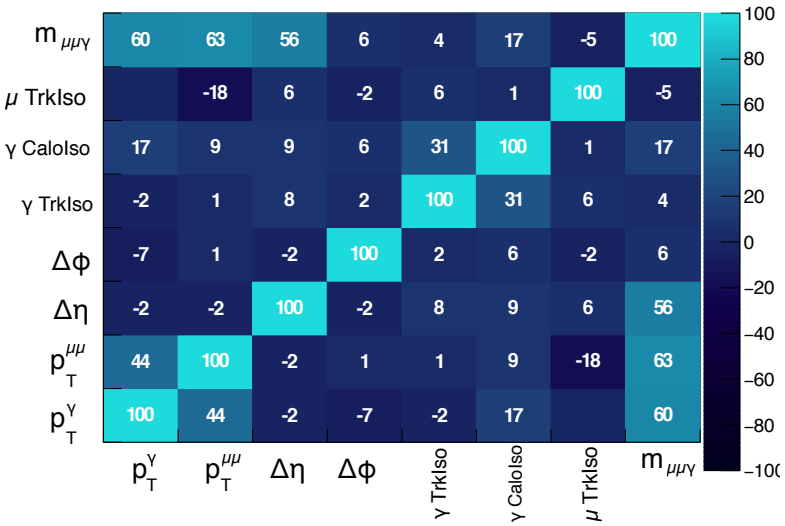

(a) Correlations observed in Data.

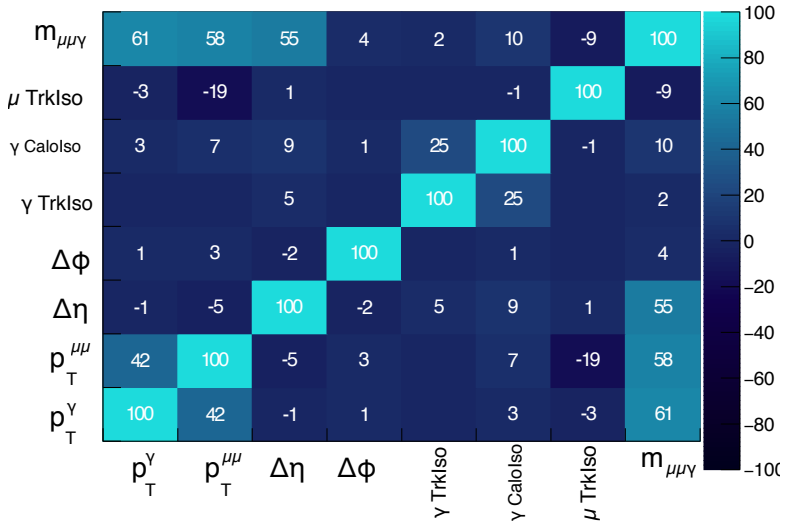

(b) Correlations produced by the Model.

Figure 7.1: Linear correlations between variables used in the background modelling shown for the (a) data events and (b) background model generated events. Distribution for the events within inclusive GR. The numbers in each bin are indicative of the strength of the correlation between variables. A value of 100 represents a perfect correlation, -100 a perfect negative correlation, and 0 completely uncorrelated. "TrkIso" represents the isolation variable for tracks, relative to the p_{T} of the particle; and "CaloIso" represents the isolation variable for calorimeter deposits, relative to the p_{T} of the particle. The azimuthal angular separation between $\mathcal{Q}$ and γ, $\Delta\phi(\mathcal{Q},\gamma)$, is denoted $\Delta\phi$. The pseudorapidity difference between $\mathcal{Q}$ and γ, $\Delta\eta(\mathcal{Q},\gamma)$, is denoted $\Delta\eta$.

ii) The distribution of p_{T}^{γ}, as shown in Figures 7.9(a) and 7.17(a), is parameterised in bins of $p_{\mathrm{T}}^{\mathcal{Q}}$, and a value is sampled from the corresponding bin, given the previously sampled value of $p_{\mathrm{T}}^{\mathcal{Q}}$. The muon isolation variable, as shown in Figures 7.14(a) and 7.22(a), is parameterised in bins of $p_{\mathrm{T}}^{\mathcal{Q}}$ and p_{T}^{γ}. The previously selected values of $p_{\mathrm{T}}^{\mathcal{Q}}$ and p_{T}^{γ} are then used to sample a value of the muon isolation from the corresponding bin.

iii) The distributions of $\Delta\eta(\mathcal{Q},\gamma)$ and the photon calorimeter isolation variable, shown in Figures 7.13(a) and 7.21(a), and their correlation, are parameterised in a binned 2D distribution. These 2D distributions are then separated into bins of $p_{\mathrm{T}}^{\mathcal{Q}}$. The same binning of $p_{\mathrm{T}}^{\mathcal{Q}}$ is used to describe the p_{T}^{γ} and muon isolation variables. Values of $\Delta\eta(\mathcal{Q},\gamma)$ and the photon calorimeter isolation variable are then sampled given the previously selected value of $p_{\mathrm{T}}^{\mathcal{Q}}$.

iv) The relative photon track isolation distribution, as shown in Figures 7.12(a) and 7.20(a), is split into bins of relative photon calorimeter isolation and $p_{\mathrm{T}}^{\mathcal{Q}}$. A value for the relative photon track isolation is then sampled using the given values for relative photon calorimeter isolation and $p_{\mathrm{T}}^{\mathcal{Q}}$.

v) The $\Delta\phi(\mathcal{Q},\gamma)$ distribution, as shown in Figures 7.11(a) and 7.19(a), is split into bins of $\Delta\eta(\mathcal{Q},\gamma)$ and $p_{\mathrm{T}}^{\mathcal{Q}}$. From the given values of $\Delta\eta(\mathcal{Q},\gamma)$ and $p_{\mathrm{T}}^{\mathcal{Q}}$, the value of $\Delta\phi(\mathcal{Q},\gamma)$ is sampled.

vi) Values for $\eta^{\mathcal{Q}}$ and $\phi^{\mathcal{Q}}$ are sampled from a binned histogram of the corresponding distributions in the GR data control sample. These are combined with $\Delta\eta(\mathcal{Q},\gamma)$ and $\Delta\phi(\mathcal{Q},\gamma)$, to give the values of η^{γ} and ϕ^{γ}.

vii) A value for $m_{\mathcal{Q}}$ is sampled directly from a binned distribution of the GR data within the required region of $m_{\mu^+\mu^-}$. This distribution is not used however, other than to obtain the four vector of the di-muon object. Separate pdfs are used in the fit to describe the $m_{\mu^+\mu^-}$ distributions of resonant $\psi(kS)$ and $\Upsilon(nS)$ production and the combinatoric non-resonant di-muons, as described in Section 7.2.5.

The above procedure yields the correlations shown in Figure 7.1(b). The majority of the strong correlations are replicated, confirming that the procedure is suitably modelling the kinematic distributions and their correlations. The validation of the background model procedure is discussed in Sections 7.2.4 and 7.3.

After an ensemble of toy candidates has been generated, the sample is normalised to the GR data control sample. Before unblinding, to obtain the "expected" normalisation of the background, the events observed in the $\mathcal{Q}\gamma$ mass distribution in the GR selection, outside the blinded regions of 86–96 GeV and 122–128 GeV, are used. The nominal tight cuts on the isolation of the di-muon system and the photon are then applied to these loose candidates to form a sample of toy candidates that provides a good description of the contributions from the inclusive backgrounds to the distributions used as signal discriminants. Given that the normalisation of the background sample is performed before any tight cuts are applied, this sample also provides a description of the background normalisation. However, this normalisation serves only as a validation of the consistency of the model and is not used in the final fit to data, where the background normalisation is a free parameter.

The final signal region background template is then generated using a KDE [122] of this sample of toy events corresponding to the signal region.

7.2.2 Modelling of Exclusive Backgrounds

The process of Z FSR represents an important exclusive background that leads to a resonant peak in the $m_{\mu^+\mu^-\gamma}$ distribution. While the probability for a $Z \to \mu^+\mu^-$ decay to emit such an energetic photon that the di-muon invariant mass falls within the mass windows of the $\psi(kS)$ or $\Upsilon(nS)$ is very low, the inclusive Z boson cross section is sufficiently large that it still represents a substantial contribution to the event count in the $Z \to \mathcal{Q}\gamma$ signal region.

This process represents a much larger background in the $\Upsilon(nS)\,\gamma$ channel than the $\psi(kS)\,\gamma$ channel, partially owing to the larger di-muon mass window allowed.

Therefore, in the $\Upsilon(nS)\,\gamma$ channel, the data-driven inclusive background method must be adjusted to exclude the data contribution from Z FSR.

$\Upsilon(nS)\,\gamma$ channel

This background is investigated using a sample of simulated $Z \to \mu^+\mu^-$ events, which covers the full fiducial region of the analysis and contains approximately 4×10^7 events of which 187 pass the full event selection for the $\Upsilon(nS)\,\gamma$ final state. From this sample, it is found that 484 exclusive background events are present in the 2343 event GR data sample, whereas a fit performed on the Z FSR peak in data (as described below) yields 425 events. A similar observation was found in the Run I analysis and, therefore, the MC is only used for the calculation of the relative acceptance between the GR and SR requirements, as well as modelling the shape of the $m_{\mu^+\mu^-}$ distribution.

Nominally, the data-driven method used to model the inclusive backgrounds incorporates all of the data found in the GR. This includes contamination from exclusive backgrounds. Therefore, it is important to model the shape and normalisation of the exclusive background found in the GR sample, and adjust the sampling of data to exclude these Z FSR events. The method for doing so is as follows:

- The Z FSR peak in the $m_{\mu^+\mu^-\gamma}$ distribution is modelled by an analytical convolution of a Breit-Wigner distribution and a Gaussian resolution function (Voigtian distribution). The width of the Breit-Wigner is fixed to the world average value of the Z boson width [114]. The peak position and Voigtian width (experimental resolution) are both extracted from a separate fit to a sample of simulated $Z \to \Upsilon(nS)\,\gamma$ events that pass the same event selection (GR), and they are then fixed in the fit to data.

- The combinatoric background is modelled using the method described in Section 7.2.1. An iterative procedure is used, whereby the fit of the Z FSR events in the GR is used to exclude Z FSR data events from the background model.

The adjusted background model is then refitted and the procedure is repeated until the ratio of Z FSR to combinatoric background events converges.

After five iterations, the modelling procedure converges and Figure 7.2 shows the resulting unbinned maximum likelihood fit to the $m_{\mu^+\mu^-\gamma}$ distribution for $\Upsilon(nS)\,\gamma$ candidates that satisfy the GR selection, in which the $Z \to \Upsilon(nS)\,\gamma$ signal yield is expected to be negligible.

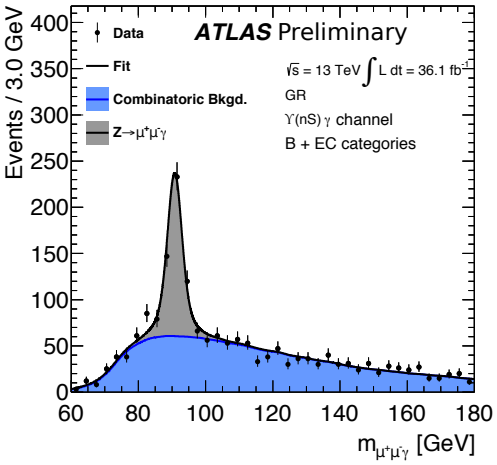

Figure 7.2: The results of an unbinned maximum likelihood fit to the $m_{\mu^+\mu^-\gamma}$ distribution of $\Upsilon(nS)\,\gamma$ candidates passing the loose selection used to generate the background GR.

It must be stressed that this MC prediction for the absolute normalisation of the Z FSR background contribution does not play any role in the estimation of the limits or the background prediction beyond a general cross-check and for visualisation in control plots. The normalisation of the Z FSR contribution used in the final analysis is extracted in the fit to the data.

$\psi(kS)\,\gamma$ channel

In the $\psi(kS)\,\gamma$ final state, the Z FSR contribution is more difficult to estimate. Only 35 MC events pass the GR event selection, which, when normalised, corresponds to 58 events out of a total of 5535 GR data events. The normalisation of the Z FSR background contribution to the $\psi(kS)\,\gamma$ final state can instead be estimated using the $Z \to \mu^+\mu^-\gamma$ MC and the $\Upsilon(nS)\,\gamma$ fit to the data.

The di-muon mass range is extended for the Z FSR MC to $2.0 < m_{\mu\mu} < 12.0\,\text{GeV}$. The GR selection requirements are consistent between the $\psi(kS)\,\gamma$ and $\Upsilon(nS)\,\gamma$ samples. A linear fit is applied to the full $m_{\mu^+\mu^-}$ distribution. The number of events estimated from the fit to the $\Upsilon(nS)\,\gamma$ GR data sample is extrapolated to the $\psi(kS)\,\gamma$ mass range. The acceptance of the MC can then be applied to estimate 39 Z FSR events expected in the $\psi(kS)\,\gamma$ signal region. Similarly to the $\Upsilon(nS)\,\gamma$ case, this prediction for the normalisation of the Z FSR background does not play any role in the estimation of the limits beyond a general cross-check. The normalisation of the Z FSR contribution used in the final fitting procedure is extracted in the fit to the data. However, in calculating the expected sensitivity of the analysis, prior to unblinding, these estimates of the exclusive background contributions are useful.

Several other H boson decay channels could give rise to events containing a reconstructed $\mu^+\mu^-\gamma$ candidate, such as $H \to \mu^+\mu^-\gamma$. In general, the expected rate for all of these decays is very low and, therefore, they are neglected in this analysis.

7.2.3 Background Systematic Uncertainties

Using the data-driven method to model the inclusive background provides a useful way to model the shape of complex backgrounds. However, the method is sensitive to fluctuations in the GR kinematic distributions, which can originate from a lack of statistics. Variations in the kinematic distributions will impact the shape of the predicted background in the SR $m_{\mu^+\mu^-\gamma}$ distribution. To allow the inclusive background model to be adjusted to the observed background distribution in data, alternative shapes can be devised. These are created either through the generation of alternative background models (for example, by applying a $p_{\text{T}}^{\mu^+\mu^-}$-shift or $\Delta\phi(\mu^+\mu^-,\gamma)$-distortion) or through distortion of the final $m_{\mu^+\mu^-\gamma}$ distribution shape (referred to as "tilt"). These techniques are motivated by experience gained in the analogous $\phi\gamma$ and $\rho\gamma$ searches [2, 3].

The overall effect of these shape variations is constrained in the fit to the data

through the implementation of shape morphing nuisance parameters [123]. With these parameters the shape of the background can morph between the nominal shape and the modified shapes. The final fit profiles the nuisance parameters to obtain the background shape that best fits the data. The alternative shapes chosen represent conservative upper/lower limits within which the interpolated pdf can operate. They correspond to $\pm 5\sigma$ variations of the associated profiled nuisance parameters in the final maximum likelihood fit. These $\pm 5\sigma$ variations are shown in Figure 7.3 for illustrative purposes. Tables 7.12 and 7.13 show the final fit values obtained for these nuisance parameters.

Each alternative model is generated with the same method that was used to generate the nominal background model, but with a single modification. For example, the parametrisation of the p_{T}^{γ} distributions (see Figures 7.9(a) and 7.17(a)) used is artificially shifted by ± 5 GeV. Figure 7.3(a) shows the effect of this variation of p_{T}^{γ} on the GR $m_{\mu^+\mu^-\gamma}$ distribution of the $\psi(kS)\,\gamma$ candidates.

Another alternative model is formed by re-weighting the $\Delta\phi(\mu^+\mu^-, \gamma)$ distributions, as shown in Figures 7.11(a) and 7.19(a). The re-weighting takes a linear form proportional to the value of $\Delta\phi$. For the "upward" variation, the higher values of $\Delta\phi$ are enhanced. This variation changes the weight of each bin to $1 + 10\Delta\phi/\pi$. The "downward" variation enhances the lower values of $\Delta\phi$ by changing the weight of each bin to $1 + 2(1 - \Delta\phi/\pi)$. The pre-factors (10 and 2) were chosen to give a symmetrical shift of approximately equal magnitude. Despite both the upward and downward shifts increasing the weights overall, the final normalisation is obtained from the GR data afterwards. The resulting effect of this $\Delta\phi$ shift can be observed in Figure 7.3(b) for the $\psi(kS)\,\gamma$ background distribution. The majority of the effect can be seen at masses in the range 50–70 GeV.

Both of these systematic shifts provide lateral movement to the peak of the $m_{\mu^+\mu^-\gamma}$ distribution. Another kind of distortion is an overall "tilt" of the distribution. To allow for such a possibility, an additional systematic template variation is included. A linear fit is performed to the ratio of the data and the prediction from the model for

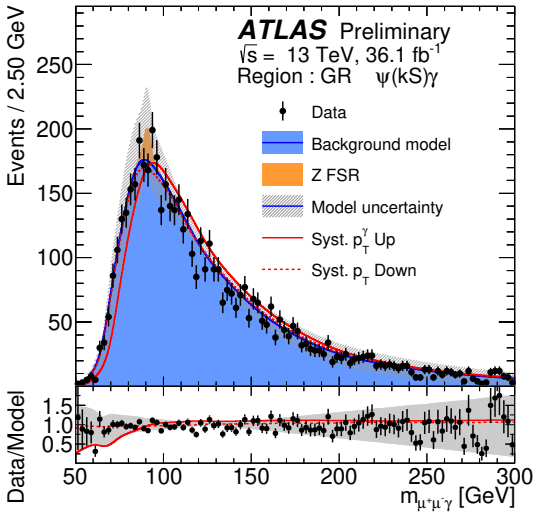

(a) p_{T}^{γ} shift

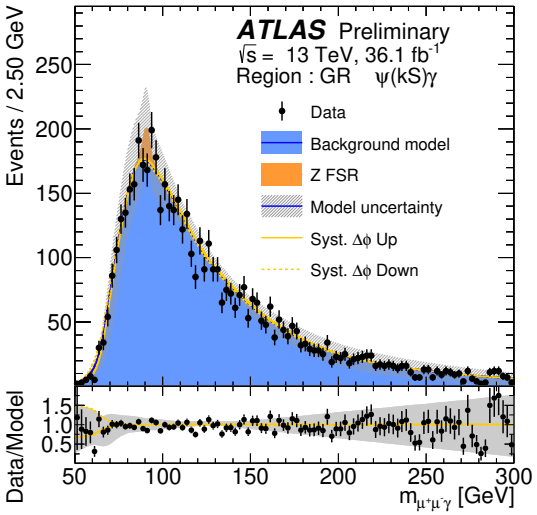

(b) $\Delta\phi$ shift

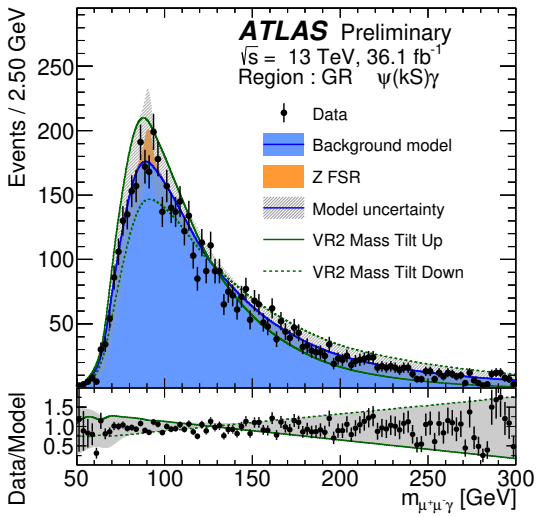

(c) Tilt

Figure 7.3: $m_{\mu^+\mu^-\gamma}$ distribution for the $\psi(kS)\,\gamma$ candidates showing the changes in the background model due to the systematic shape variations. These correspond to the $\pm5\sigma$ variation of the associated profiled nuisance parameter.

the $m_{\mu^+\mu^-\gamma}$ distribution in the VR2 region (originally motivated by a discrepancy observed in this region in the $\phi\gamma$ analysis [3]). The parameters from this fit are used to re-weight the model to match the data, which provides freedom for the background model to adjust for a mismodelling of the isolation variable. Fitting a linear function to the ratio of the data to the background model gives the re-weighting factor, $f = -0.0023 m_{\mu^+\mu^-\gamma}/[\mathrm{GeV}] + 1.27$. This tilts the background

shape such that at masses lower than 117 GeV the background is increased and above 117 GeV the background model is reduced; this is referred to as the "upward" variation. To provide a symmetric envelope, a "downward" variation is applied, where the upward variation is reflected about the line $f = 1$ to obtain the equation $f = 0.0023 m_{\mu^+\mu^-\gamma}/[\text{GeV}] + 0.73$. The $\pm 5\sigma$ systematic shifts are taken to be the weighting factors modified to $2f - 1$, for both the upward and downward variations. The effect of this variation can be seen in Figure 7.3(c). Unlike the previous two variations, this "tilt" is left without a constraint in the fit and the final value is fully determined from the data (as is the normalisation).

The exclusive background must also account for mismodelling in the shape of the $m_{\mu^+\mu^-\gamma}$ distribution. A further nuisance parameter is included to account for the effects of the energy/momentum scale and resolution uncertainties on the mean of the Z FSR background shape. This effect was investigated and the uncertainty found to be $\pm 0.2\%$. This resulted in a $\pm 0.5\%$ change to the expected limits in the $Z \to \Upsilon(nS)\,\gamma$ analyses and negligible changes in the other limits.

7.2.4 Background Control Plots

The background model is validated in each of the control regions defined in Section 6.6.5. Figures 7.4 and 7.5 show the expected $m_{\mu^+\mu^-\gamma}$ background distributions compared to data for the $\psi(kS)\gamma$ and $\Upsilon(nS)\gamma$ candidates. The GR and SR distributions in these figures also show the systematic uncertainty band from the background estimation. The uncertainty band represents the largest variation of the three systematic uncertainties on the inclusive background at each point in $m_{\mu^+\mu^-\gamma}$. In all of the validation regions the background $m_{\mu^+\mu^-\gamma}$ distributions model the data well, with the systematic uncertainty band allowing suitable freedom for the model to incorporate any changes in shape.

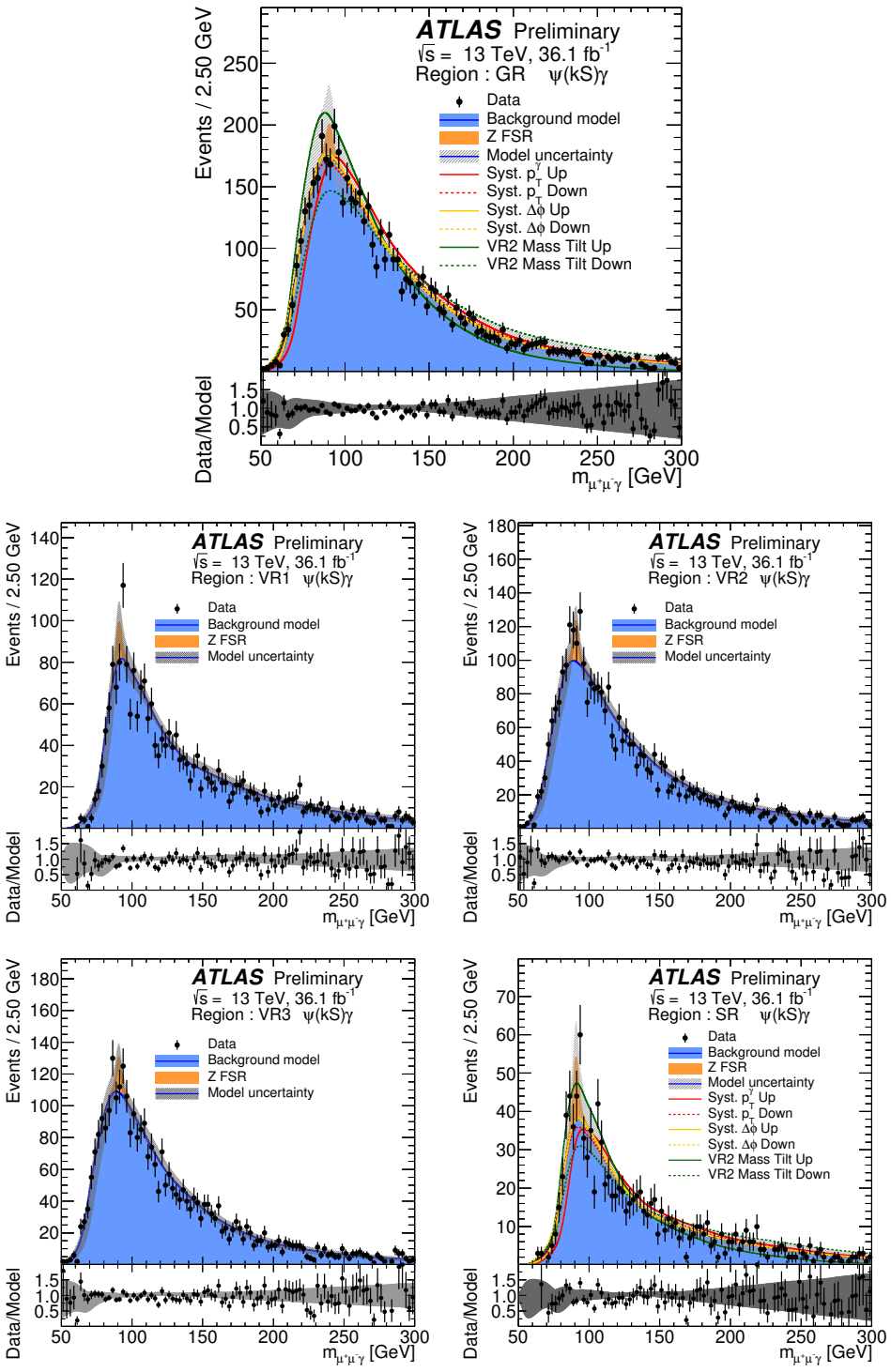

Figure 7.4: $m_{\mu^+\mu^-\gamma}$ distribution for the $\psi(kS)\,\gamma$ candidates in the various control regions showing the systematic uncertainty band from the background estimation.

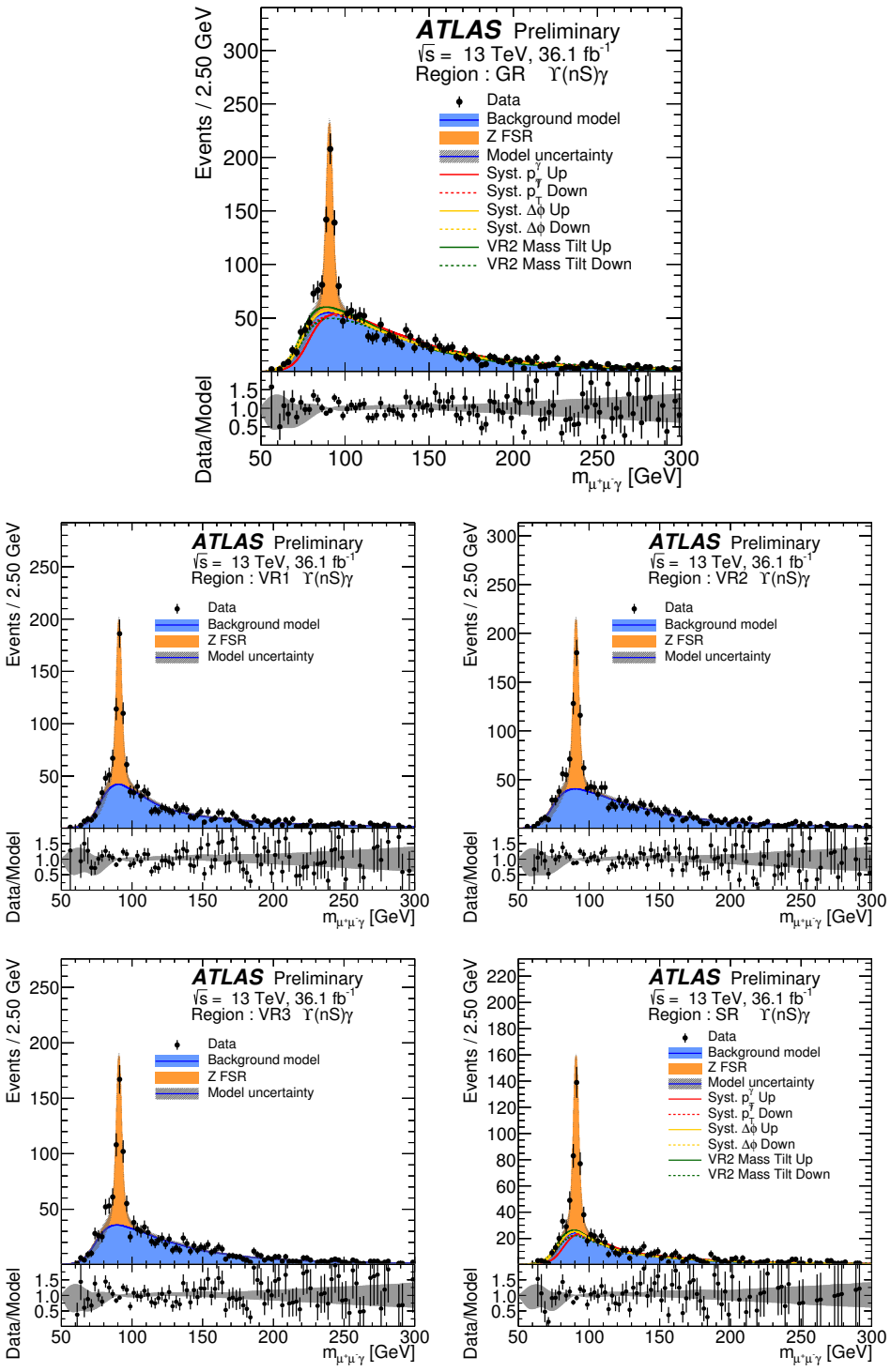

Figure 7.5: $m_{\mu^+\mu^-\gamma}$ distribution for the $\Upsilon(nS)\,\gamma$ candidates in the various control regions showing the systematic uncertainty band from the background estimation.

7.2.5 Di-Muon Mass Background Model

Unlike the background distributions in the three-body mass, all of the background components for the di-muon mass distributions can be modelled directly with analytical pdfs. There are three main sources of background to consider: the resonant and non-resonant inclusive backgrounds and the Z FSR background. The resonant backgrounds are modelled as Gaussian distributions, which are fitted to the data passing the GR selection. The shapes of the resonant backgrounds are assumed to remain the same between the GR and SR data and, therefore, parameters obtained from the fit of the Gaussian to GR data are fixed in the final fit to the SR data. The non-resonant and the Z FSR backgrounds can be modelled with linear functions. For the $\Upsilon(nS)\gamma$ analysis, the $Z \to \mu^+\mu^-\gamma$ MC signal sample is used to model the gradient of the Z FSR background distribution. As shown in Figure 7.6, the gradient in $m_{\mu^+\mu^-}$ for the Z FSR background is nearly flat in the Υ mass region. Using this Z FSR background shape, the non-resonant inclusive background shape can be determined in a fit to the GR data. In the $\psi(kS)\gamma$ case, the MC signal sample does not have sufficient statistics for it to be used. Thus, the gradient of the linear function of the Z FSR and non-resonant backgrounds is free to be determined in the final fitting procedure, using the regions of the $m_{\mu^+\mu^-}$ distribution outside the $\psi(kS)$ peak to constrain them.

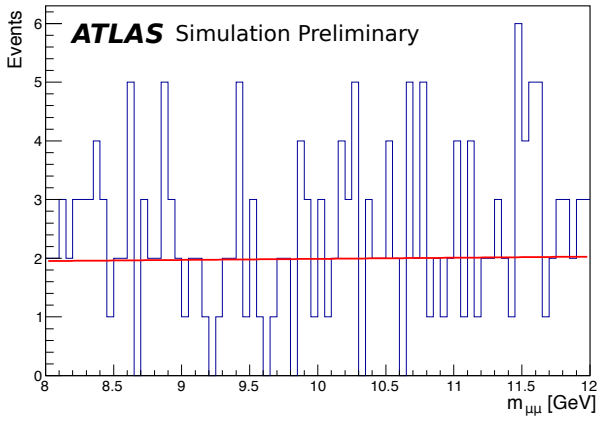

Figure 7.6: $m_{\mu^+\mu^-}$ distribution of the Z FSR background in $Z \to \mu^+\mu^-\gamma$ MC. The red line shows the best fit of a linear function to the data events.

7.2.6 Background Summary

The three main components of the $H(Z) \to \mathcal{Q}\gamma \to \mu^+\mu^-\gamma$ background, the non-resonant and resonant inclusive backgrounds, and the Z FSR exclusive background, are well modelled in both the $m_{\mu^+\mu^-\gamma}$ and $m_{\mu^+\mu^-}$ distributions. The $m_{\mu^+\mu^-\gamma}$ distributions for the inclusive background are modelled using a non-parametric data-driven approach, which is validated in different selection regions, while the Z FSR background is modelled with an analytical function determined from a fit to the $Z \to \mathcal{Q}\gamma$ signal MC. For the $m_{\mu^+\mu^-}$ distributions, the non-resonant inclusive background and the Z FSR backgrounds can be modelled using linear functions and the resonant backgrounds are modelled with Gaussian distributions.

7.3 Background Model Validation

In the construction of the background model, kinematic the variables of the generated pseudo-candidates should match the data events within the different selection regions of the analysis. The figures in this section show the background templates and data in distributions of the key kinematic variables.

The $p_{\mathrm{T}}^{\mu^+\mu^-\gamma}$ distributions shown in Figures 7.7 and 7.15 have no direct usage in the analysis; however, they provide a useful cross-check of the background model to ensure the momentum of the $\mu^+\mu^-\gamma$ system is being well modelled. In the $\psi(kS)\,\gamma$ analysis, the data and background model agree well, whereas in the $\Upsilon(nS)\gamma$ validation regions it is less well modelled at low values of $p_{\mathrm{T}}^{\mu^+\mu^-\gamma}$, where the Z FSR background is dominant. The $p_{\mathrm{T}}^{\mu^+\mu^-}$ and p_{T}^{γ} distributions are two of the most important variables to model well in the background procedure due to their large correlations with the three-body mass and other kinematic variables. As shown in Figures 7.8, 7.9, 7.16 and 7.17, the background distributions perform well at modelling the background in all of the selection regions of both the $\psi(kS)\,\gamma$ and $\Upsilon(nS)\,\gamma$ analyses. $p_{\mathrm{T}}^{\mu^+\mu^-}$ is used as one of the further selection requirements for

the SR relative to the GR. The effect of this requirement on the shape can be observed in Figure 7.8(c), and the model replicates this well. The $\Delta R(\mu^+\mu^-, \gamma)$ distributions shown in Figures 7.10 and 7.18 require good modelling of both the $\Delta\phi$ and $\Delta\eta$ kinematic variables. In general, this variable is well modelled for all the selection regions, but for the SR region of the $\psi(kS)\,\gamma$ analysis the background model underestimates the peak. The $\Delta\phi$ distributions are shown in Figures 7.11 and 7.19 and are well-modelled by the background distributions. The photon track and calorimeter isolation distributions are shown in Figures 7.12, 7.13, 7.20 and 7.21. On the whole, the background procedure models the shapes of these two kinematic variables well; however, when the photon isolation requirement is applied in VR3 and SR, the model underestimates the data slightly near to the threshold. The dimuon track isolation is shown in Figures 7.14 and 7.22 and is modelled well by the background distributions in all of the selection regions, including VR3 where the requirement of the dimuon track isolation is applied.

Despite minor mismodelling of some of the kinematic variables, ultimately the three-body mass distribution is the most important parameter to reproduce and, as shown in Section 7.2.4, the background model does this well.

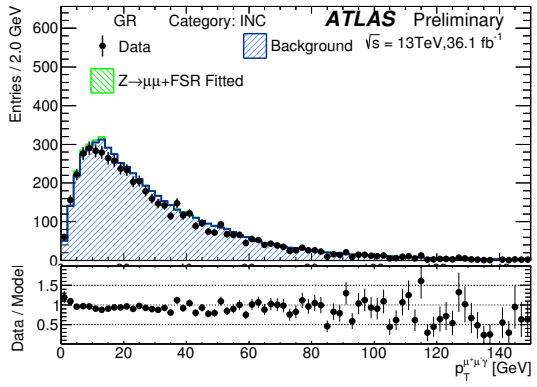

(a) GR

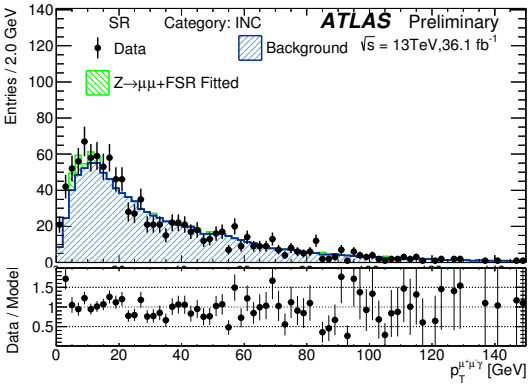

(b) SR

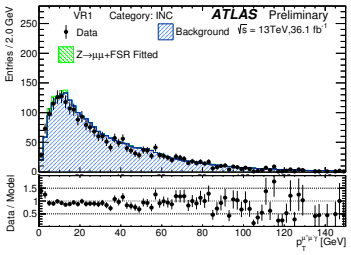

(c) VR1

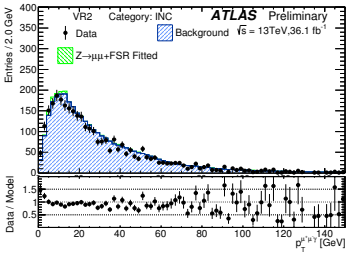

(d) VR2

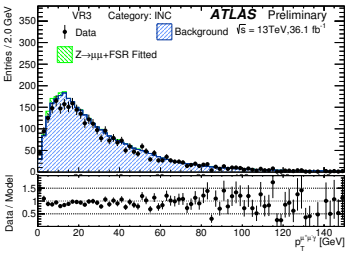

(e) VR3

Figure 7.7: Three-body transverse momentum control plots showing $\psi(kS)\,\gamma$ data (black markers) and the background modelling (inclusive in blue and Z FSR in green), within each of the selection regions. The background model is normalised to the data events in the GR sample and the $Z \to \mu^+\mu^-\gamma$ MC events and toy background candidates are passed through the remaining selection requirements to obtain the normalisation in the validation regions. Data/Model plots below the distributions show the ratio between the data and expected background distribution and emphasise discrepencies or systematic mismatching.

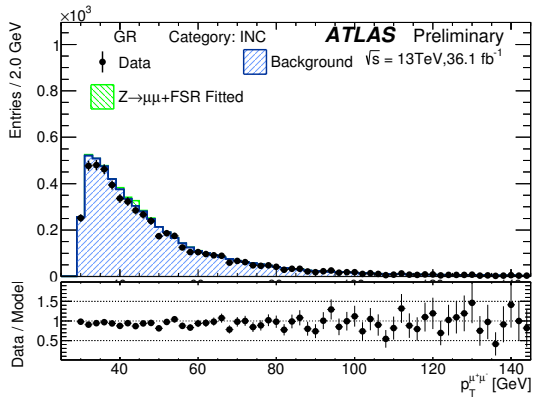

(a) GR

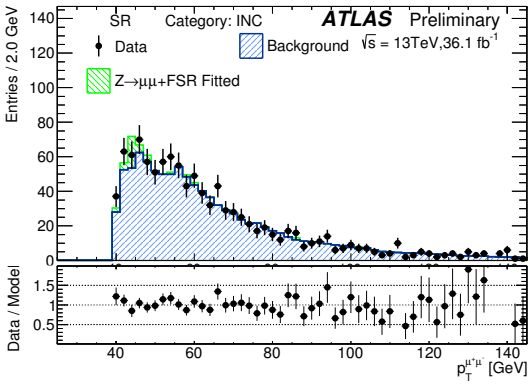

(b) SR

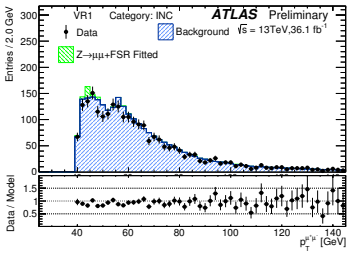

(c) VR1

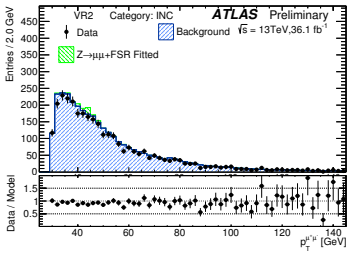

(d) VR2

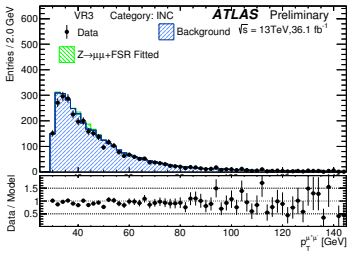

(e) VR3

Figure 7.8: Di-muon transverse momentum control plots showing $\psi(kS)\,\gamma$ data (black markers) and the background modelling (inclusive in blue and Z FSR in green), within each of the selection regions. The background model is normalised to the data events in the GR sample and the $Z \to \mu^+\mu^-\gamma$ MC events and toy background candidates are passed through the remaining selection requirements to obtain the normalisation in the validation regions. Data/Model plots below the distributions show the ratio between the data and expected background distribution and emphasise discrepencies or systematic mismatching.

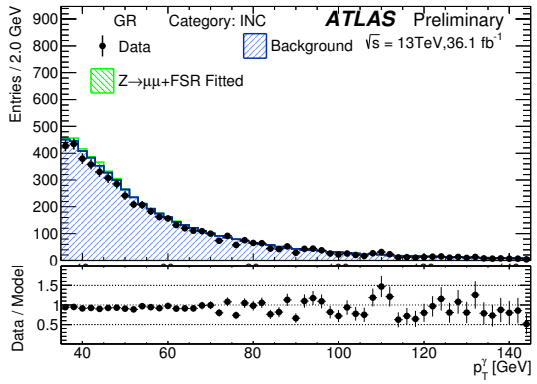

(a) GR

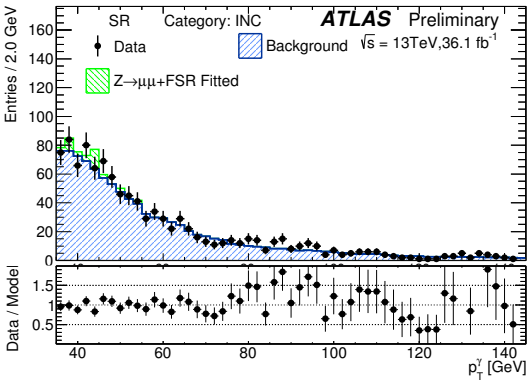

(b) SR

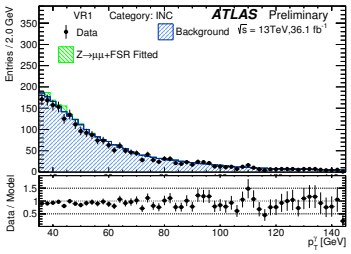

(c) VR1

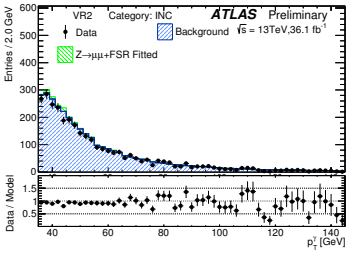

(d) VR2

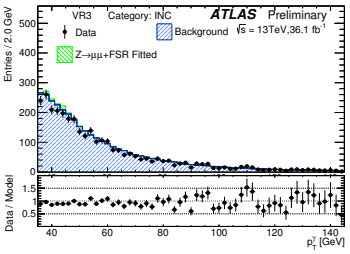

(e) VR3

Figure 7.9: Photon transverse momentum control plots showing $\psi(kS)\,\gamma$ data (black markers) and the background modelling (inclusive in blue and Z FSR in green), within each of the selection regions. The background model is normalised to the data events in the GR sample and the $Z \to \mu^+\mu^-\gamma$ MC events and toy background candidates are passed through the remaining selection requirements to obtain the normalisation in the validation regions. Data/Model plots below the distributions show the ratio between the data and expected background distribution and emphasise discrepencies or systematic mismatching.

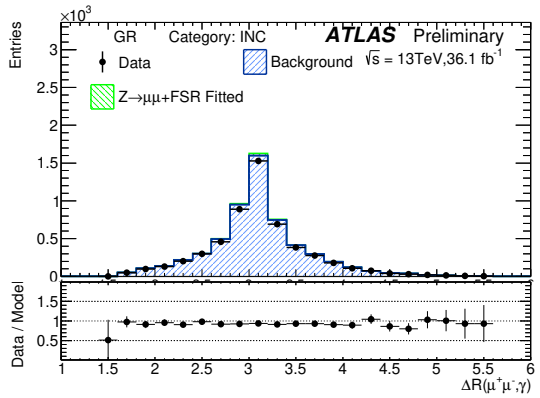

(a) GR

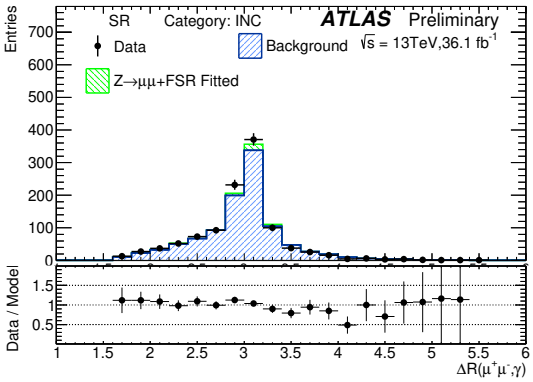

(b) SR

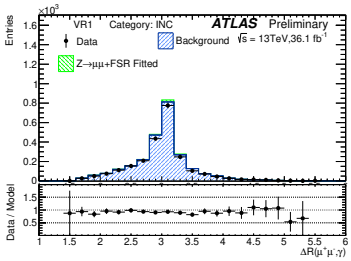

(c) VR1

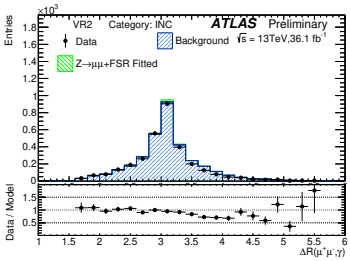

(d) VR2

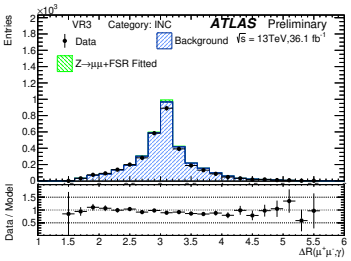

(e) VR3

Figure 7.10: $\Delta R(\mu^+\mu^-,\gamma)$ control plots showing $\psi(kS)\,\gamma$ data (black markers) and the background modelling (inclusive in blue and Z FSR in green), within each of the selection regions. The background model is normalised to the data events in the GR sample and the $Z \to \mu^+\mu^-\gamma$ MC events and toy background candidates are passed through the remaining selection requirements to obtain the normalisation in the validation regions. Data/Model plots below the distributions show the ratio between the data and expected background distribution and emphasise discrepencies or systematic mismatching.

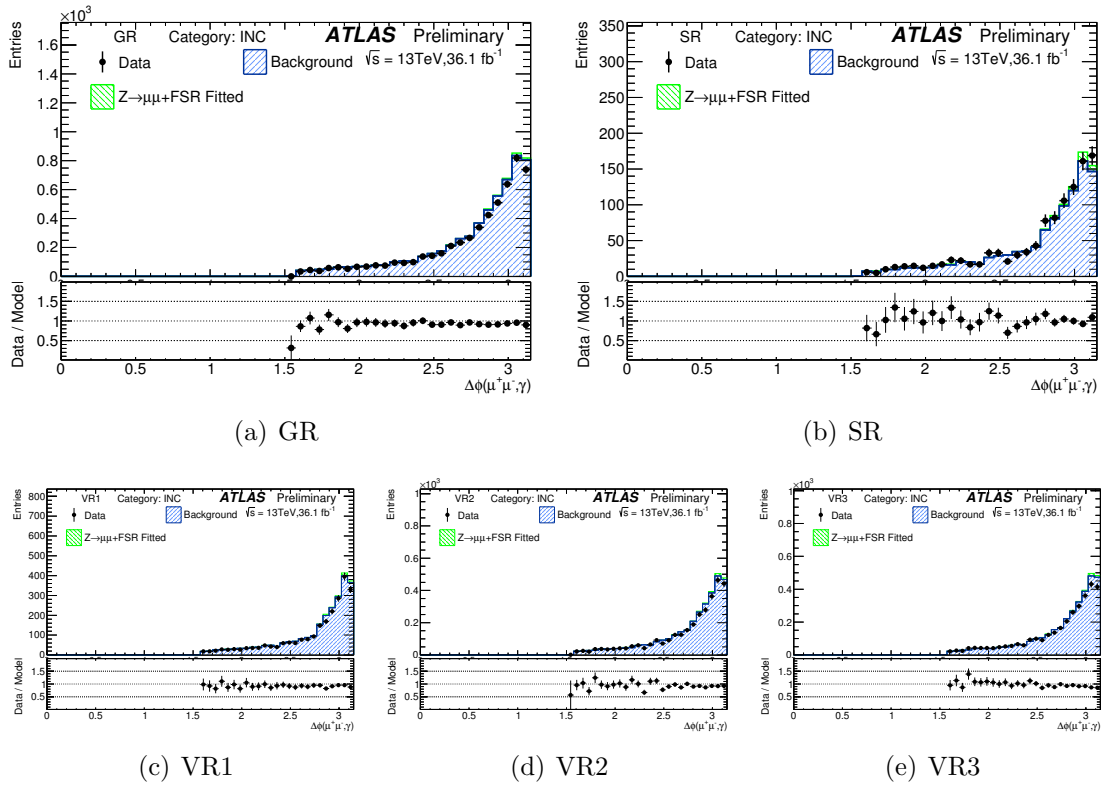

(a) GR (b) SR

(c) VR1 (d) VR2 (e) VR3

Figure 7.11: $\Delta\phi(\mu^+\mu^-,\gamma)$ control plots showing $\psi(kS)\,\gamma$ data (black markers) and the background modelling (inclusive in blue and Z FSR in green), within each of the selection regions. The background model is normalised to the data events in the GR sample and the $Z \to \mu^+\mu^-\gamma$ MC events and toy background candidates are passed through the remaining selection requirements to obtain the normalisation in the validation regions. Data/Model plots below the distributions show the ratio between the data and expected background distribution and emphasise discrepencies or systematic mismatching.

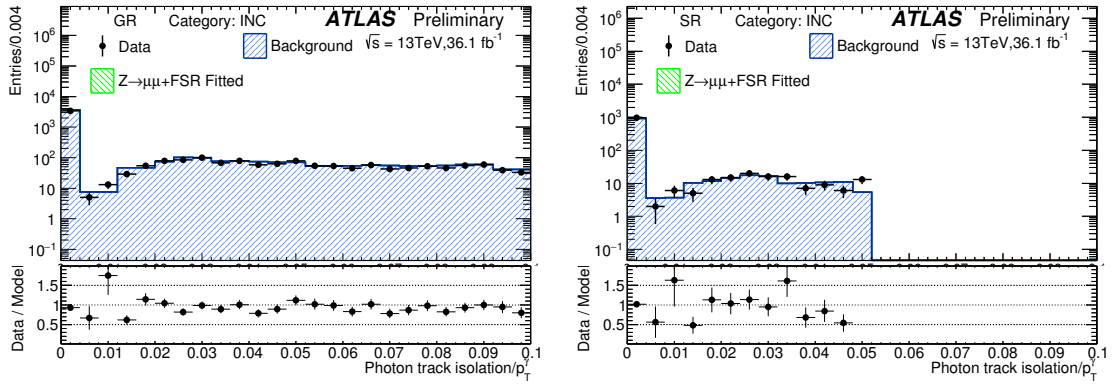

(a) GR

(b) SR

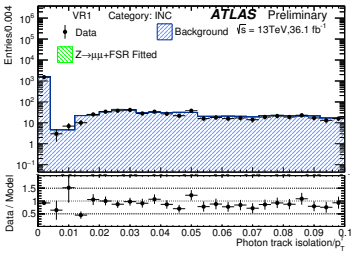

(c) VR1

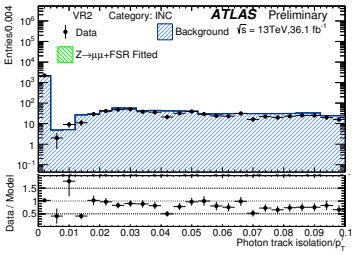

(d) VR2

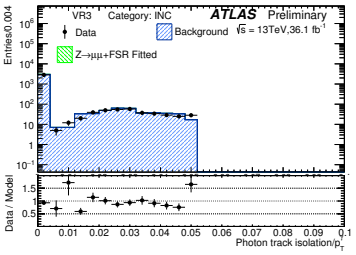

(e) VR3

Figure 7.12: Relative photon track isolation control plots showing $\psi(kS)\,\gamma$ data (black markers) and the background modelling (inclusive in blue and Z FSR in green), within each of the selection regions. The background model is normalised to the data events in the GR sample and the $Z \to \mu^+\mu^-\gamma$ MC events and toy background candidates are passed through the remaining selection requirements to obtain the normalisation in the validation regions. Data/Model plots below the distributions show the ratio between the data and expected background distribution and emphasise discrepencies or systematic mismatching.

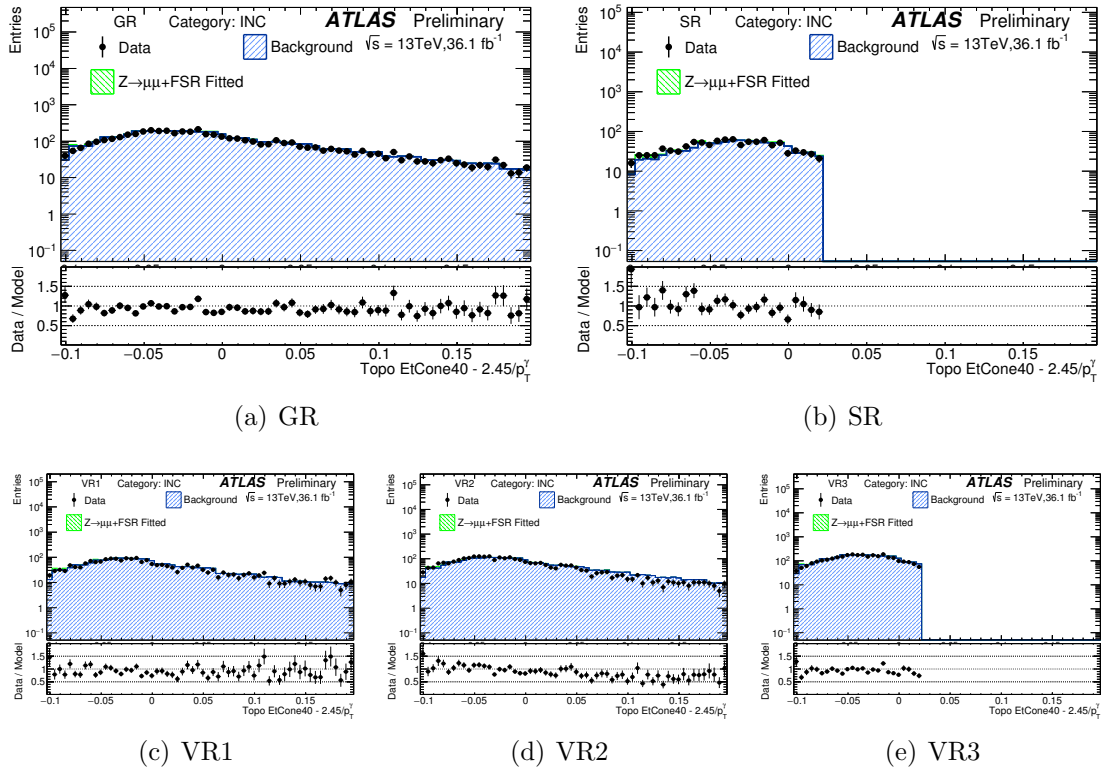

(a) GR (b) SR

(c) VR1 (d) VR2 (e) VR3

Figure 7.13: Relative photon calorimeter isolation control plots showing $\psi(kS)\,\gamma$ data (black markers) and the background modelling (inclusive in blue and Z FSR in green), within each of the selection regions. The background model is normalised to the data events in the GR sample and the $Z \to \mu^+\mu^-\gamma$ MC events and toy background candidates are passed through the remaining selection requirements to obtain the normalisation in the validation regions. Data/Model plots below the distributions show the ratio between the data and expected background distribution and emphasise discrepencies or systematic mismatching.

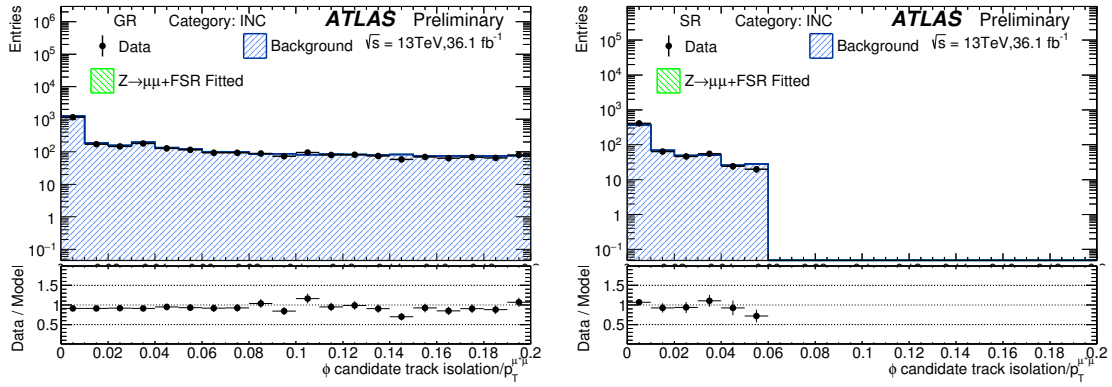

(a) GR

(b) SR

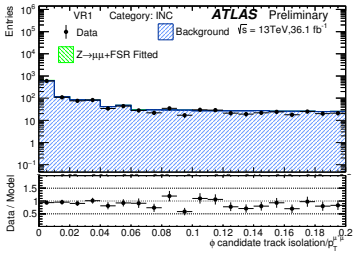

(c) VR1

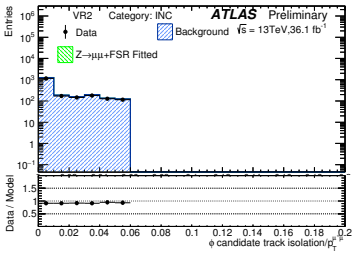

(d) VR2

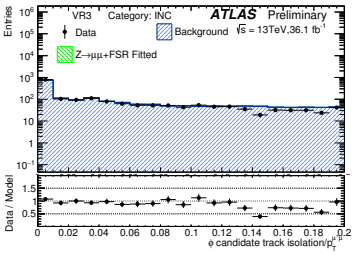

(e) VR3

Figure 7.14: Relative muon track isolation control plots showing $\psi(kS)\,\gamma$ data (black markers) and the background modelling (inclusive in blue and Z FSR in green), within each of the selection regions. The background model is normalised to the data events in the GR sample and the $Z \to \mu^+\mu^-\gamma$ MC events and toy background candidates are passed through the remaining selection requirements to obtain the normalisation in the validation regions. Data/Model plots below the distributions show the ratio between the data and expected background distribution and emphasise discrepencies or systematic mismatching.

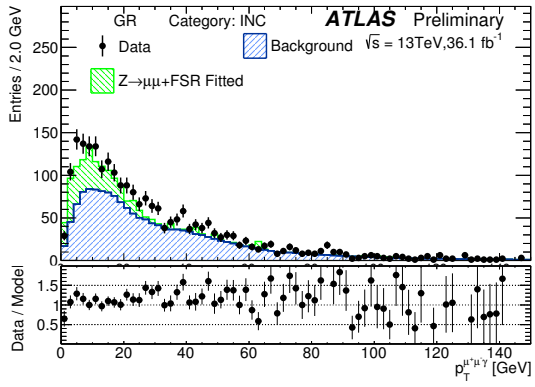

(a) GR

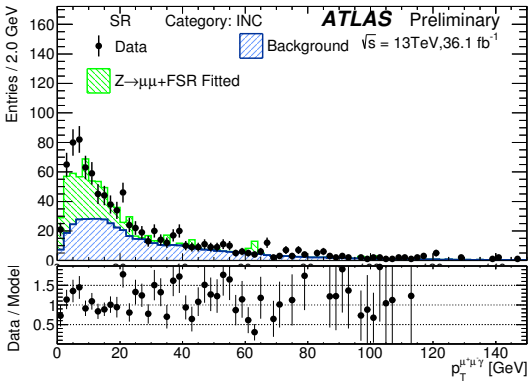

(b) SR

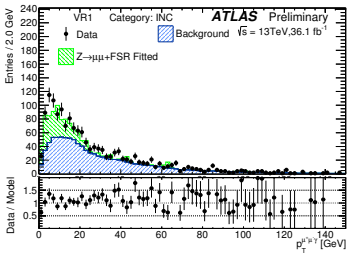

(c) VR1

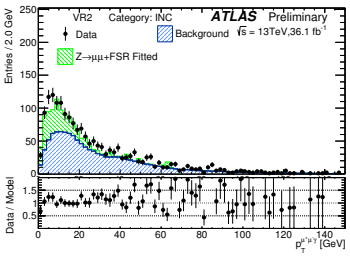

(d) VR2

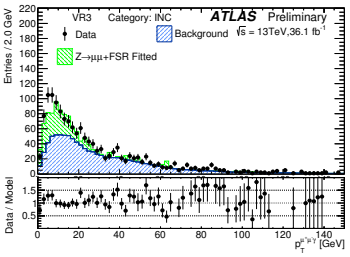

(e) VR3

Figure 7.15: Three-body transverse momentum control plots showing $\Upsilon(nS)\,\gamma$ data (black markers) and the background modelling (inclusive in blue and Z FSR in green), within each of the selection regions. The background model is normalised to the data events in the GR sample and the $Z \to \mu^+\mu^-\gamma$ MC events and toy background candidates are passed through the remaining selection requirements to obtain the normalisation in the validation regions. Data/Model plots below the distributions show the ratio between the data and expected background distribution and emphasise discrepencies or systematic mismatching.

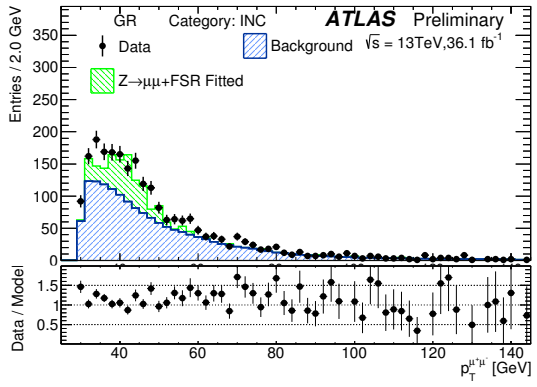

(a) GR

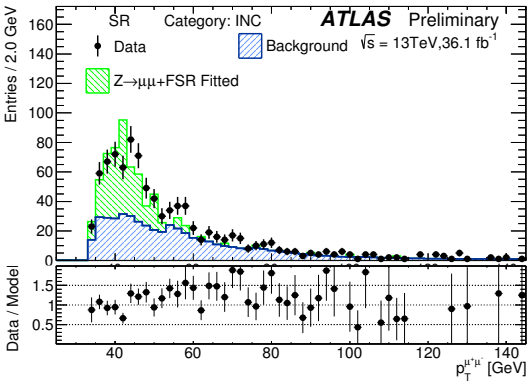

(b) SR

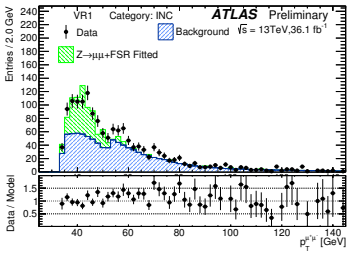

(c) VR1

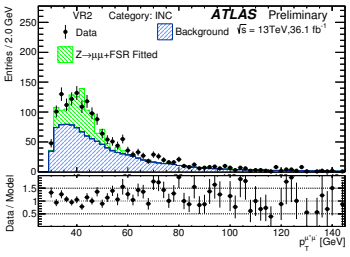

(d) VR2

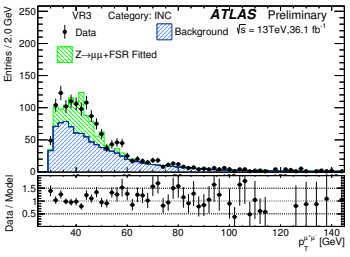

(e) VR3

Figure 7.16: Di-muon transverse momentum control plots showing $\Upsilon(nS)\,\gamma$ data (black markers) and the background modelling (inclusive in blue and Z FSR in green), within each of the selection regions. The background model is normalised to the data events in the GR sample and the $Z \to \mu^+\mu^-\gamma$ MC events and toy background candidates are passed through the remaining selection requirements to obtain the normalisation in the validation regions. Data/Model plots below the distributions show the ratio between the data and expected background distribution and emphasise discrepencies or systematic mismatching.

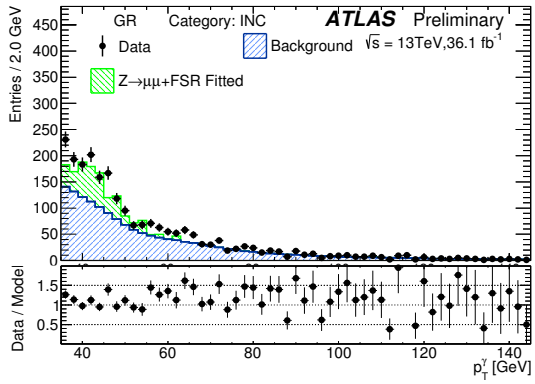

(a) GR

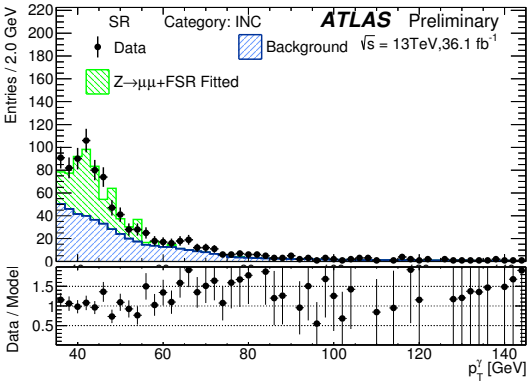

(b) SR

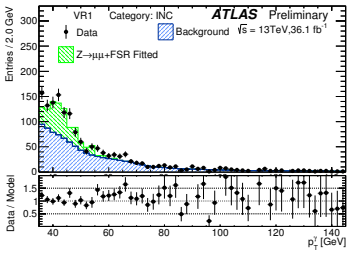

(c) VR1

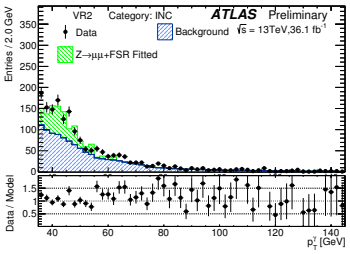

(d) VR2

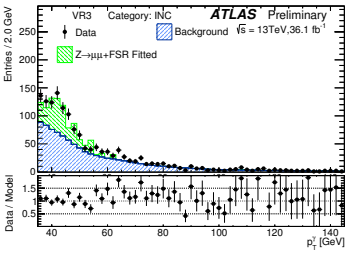

(e) VR3

Figure 7.17: Photon transverse momentum control plots showing $\Upsilon(nS)\,\gamma$ data (black markers) and the background modelling (inclusive in blue and Z FSR in green), within each of the selection regions. The background model is normalised to the data events in the GR sample and the $Z \to \mu^+\mu^-\gamma$ MC events and toy background candidates are passed through the remaining selection requirements to obtain the normalisation in the validation regions. Data/Model plots below the distributions show the ratio between the data and expected background distribution and emphasise discrepencies or systematic mismatching.

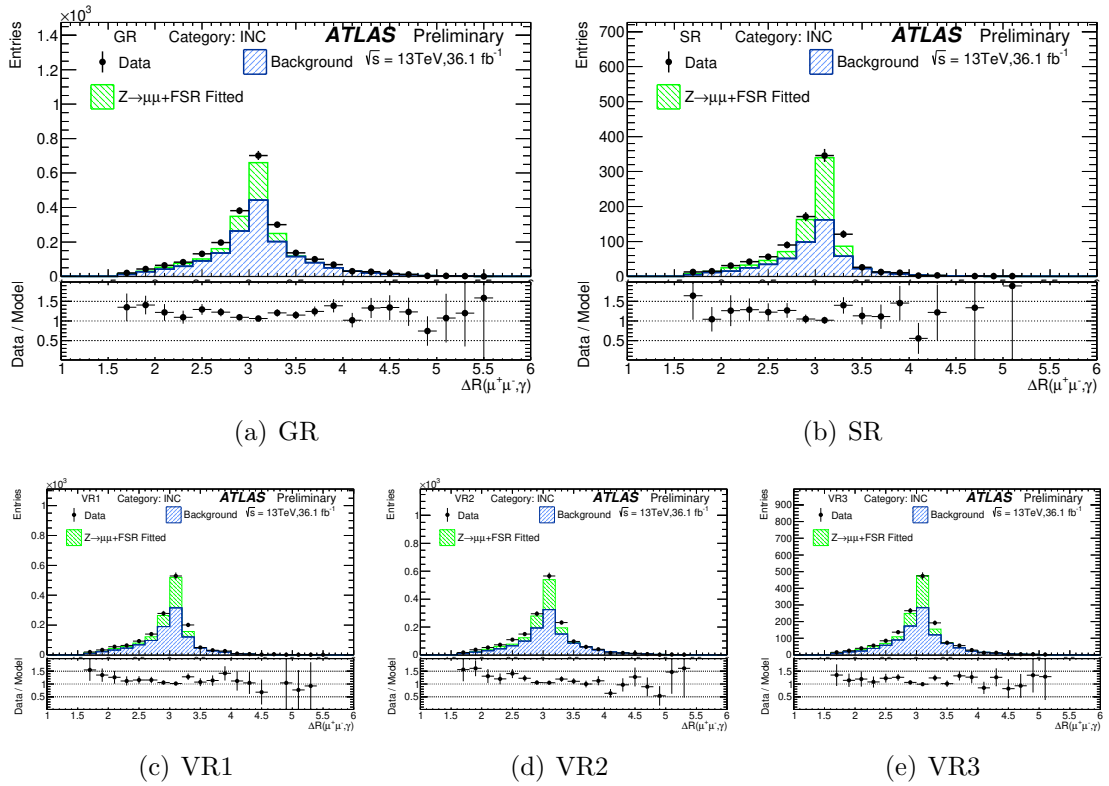

(a) GR (b) SR

(c) VR1 (d) VR2 (e) VR3

Figure 7.18: $\Delta R(\mu^+\mu^-,\gamma)$ control plots showing $\Upsilon(nS)\,\gamma$ data (black markers) and the background modelling (inclusive in blue and Z FSR in green), within each of the selection regions. The background model is normalised to the data events in the GR sample and the $Z \to \mu^+\mu^-\gamma$ MC events and toy background candidates are passed through the remaining selection requirements to obtain the normalisation in the validation regions. Data/Model plots below the distributions show the ratio between the data and expected background distribution and emphasise discrepencies or systematic mismatching.

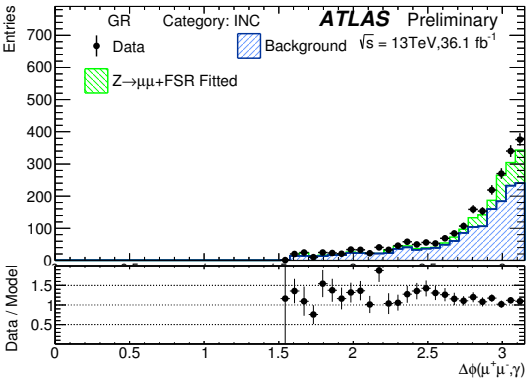

(a) GR

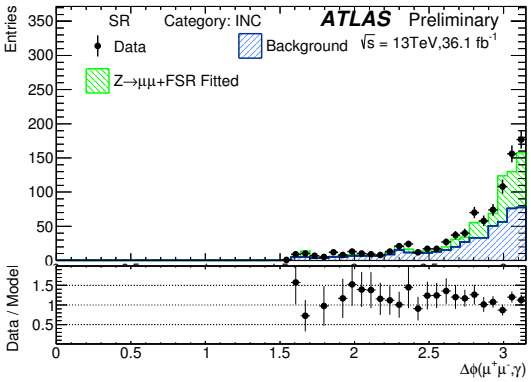

(b) SR

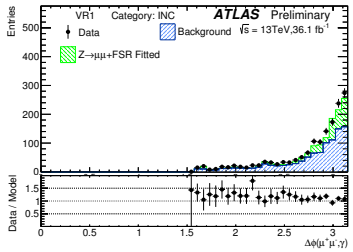

(c) VR1

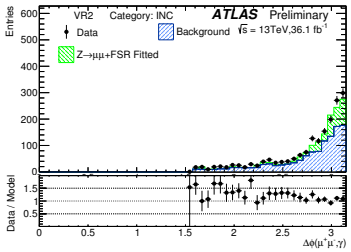

(d) VR2

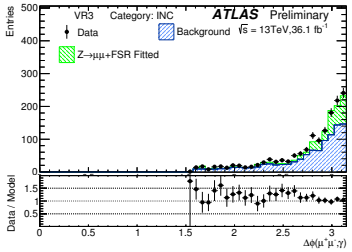

(e) VR3

Figure 7.19: $\Delta\phi(\mu^+\mu^-,\gamma)$ control plots showing $\Upsilon(nS)\,\gamma$ data (black markers) and the background modelling (inclusive in blue and Z FSR in green), within each of the selection regions. The background model is normalised to the data events in the GR sample and the $Z \to \mu^+\mu^-\gamma$ MC events and toy background candidates are passed through the remaining selection requirements to obtain the normalisation in the validation regions. Data/Model plots below the distributions show the ratio between the data and expected background distribution and emphasise discrepencies or systematic mismatching.

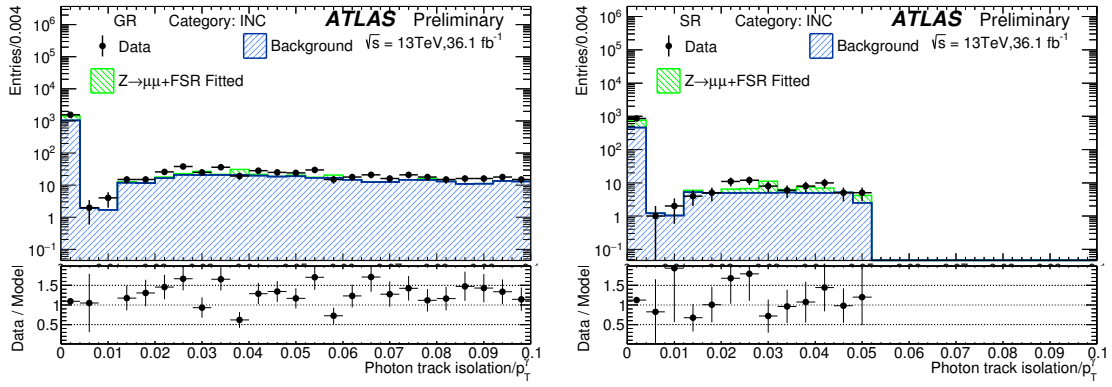

(a) GR

(b) SR

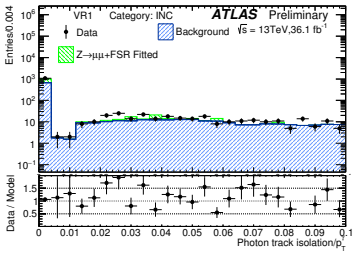

(c) VR1

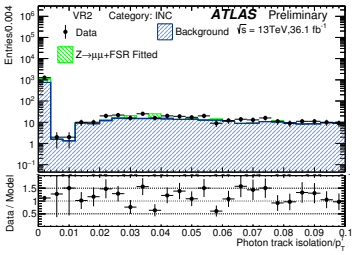

(d) VR2

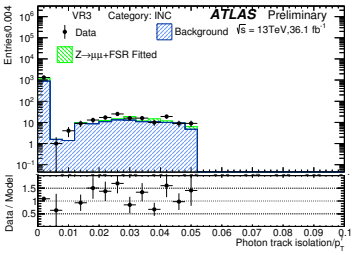

(e) VR3

Figure 7.20: Relative photon track isolation control plots showing $\Upsilon(nS)\,\gamma$ data (black markers) and the background modelling (inclusive in blue and Z FSR in green), within each of the selection regions. The background model is normalised to the data events in the GR sample and the $Z \to \mu^+\mu^-\gamma$ MC events and toy background candidates are passed through the remaining selection requirements to obtain the normalisation in the validation regions. Data/Model plots below the distributions show the ratio between the data and expected background distribution and emphasise discrepencies or systematic mismatching.

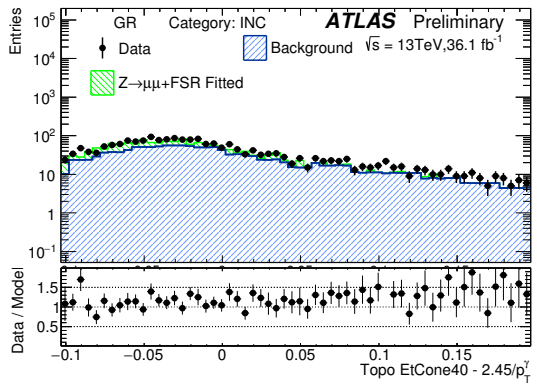

(a) GR

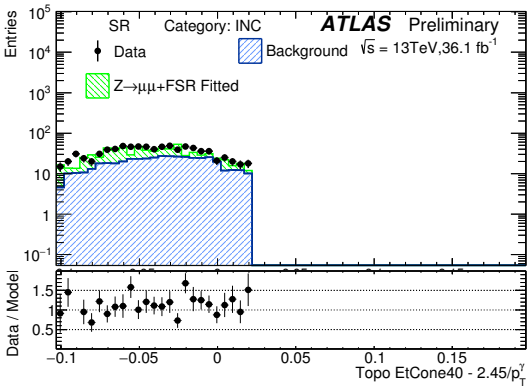

(b) SR

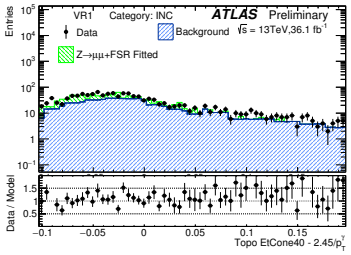

(c) VR1

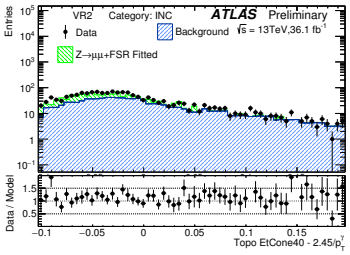

(d) VR2

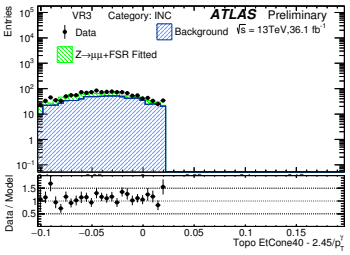

(e) VR3

Figure 7.21: Relative photon calorimeter isolation control plots showing $\Upsilon(nS)\,\gamma$ data (black markers) and the background modelling (inclusive in blue and Z FSR in green), within each of the selection regions. The background model is normalised to the data events in the GR sample and the $Z \to \mu^+\mu^-\gamma$ MC events and toy background candidates are passed through the remaining selection requirements to obtain the normalisation in the validation regions. Data/Model plots below the distributions show the ratio between the data and expected background distribution and emphasise discrepencies or systematic mismatching.

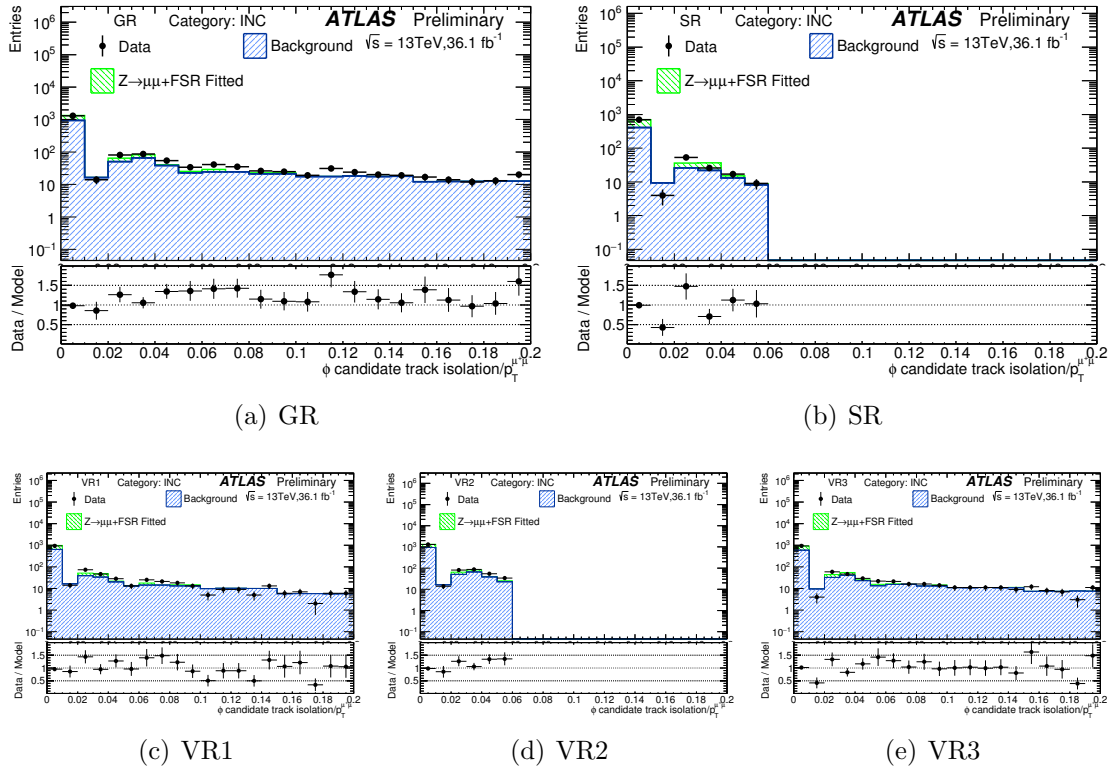

(a) GR (b) SR

(c) VR1 (d) VR2 (e) VR3

Figure 7.22: Relative muon track isolation control plots showing $\Upsilon(nS)\,\gamma$ data (black markers) and the background modelling (inclusive in blue and Z FSR in green), within each of the selection regions. The background model is normalised to the data events in the GR sample and the $Z \to \mu^+\mu^-\gamma$ MC events and toy background candidates are passed through the remaining selection requirements to obtain the normalisation in the validation regions. Data/Model plots below the distributions show the ratio between the data and expected background distribution and emphasise discrepencies or systematic mismatching.

7.4 Signal Modelling

For each of the final states, a two-dimensional ($m_{\mu^+\mu^-\gamma}$ and $m_{\mu^+\mu^-}$) pdf is used to model the signal. The Higgs boson signals are modelled with two-dimensional multivariate Gaussian distributions [124], which retain the correlation between $m_{\mu^+\mu^-\gamma}$ and $m_{\mu^+\mu^-}$ in the final states. Retaining this correlation allows further discrimination between the signal and the background events, which are uncorrelated. For the Z boson decays, the $m_{\mu^+\mu^-\gamma}$ distributions for the signal are modelled with Voigtian pdfs corrected with mass-dependent efficiency factors, and the $m_{\mu^+\mu^-}$ distributions

are modelled as Gaussian pdfs. The efficiency factors are required to account for the mass-dependent acceptance of the $\mu^+\mu^-\gamma$ system and their functions are shown in Figure 7.23. The large natural width of the Z boson causes the correlation between $m_{\mu^+\mu^-\gamma}$ and $m_{\mu^+\mu^-}$ to be small and, therefore, the correlation is not modelled. The mean and width parameters of the signal models are fixed to values found from fitting the models to MC signal events and are given in Tables 7.1 and 7.2. The MC signal event distributions used to model the signal are shown in Figures 7.24 and 7.25 for the $H \to \mathcal{Q}\gamma$ decays. Figure 7.26 shows the $m_{\mu^+\mu^-\gamma}$ MC signal event distribution for $Z \to J/\psi\,\gamma$ and Figure 7.27 shows the same distribution for the combination of $\Upsilon(nS)$ states for the $Z \to \Upsilon(nS)\,\gamma$ decays.

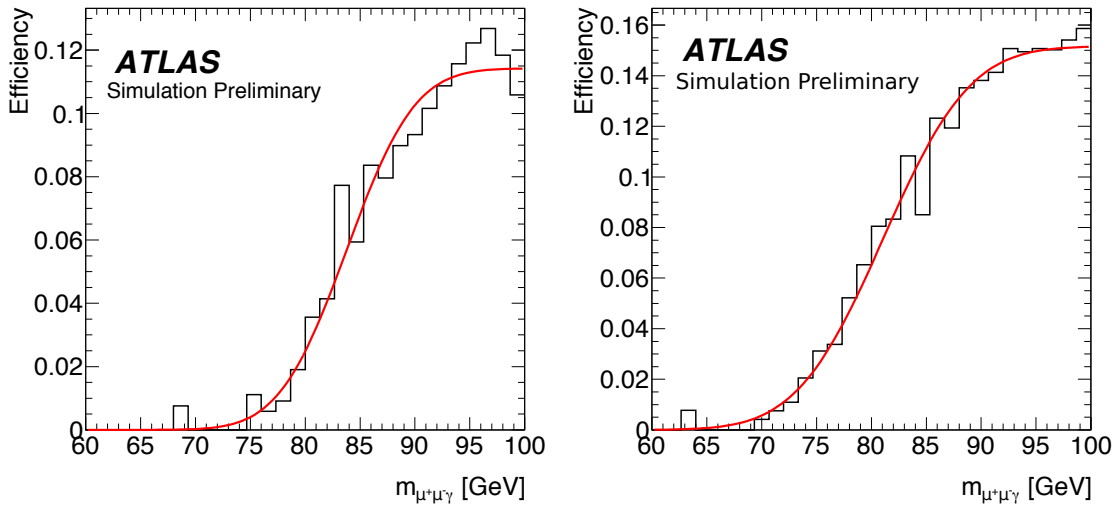

Figure 7.23: The mass-dependent efficiency function derived from the truth acceptance for the $Z \to \psi(kS)\,\gamma$ (left) and $Z \to \Upsilon(nS)\,\gamma$ (right) signal, respectively.

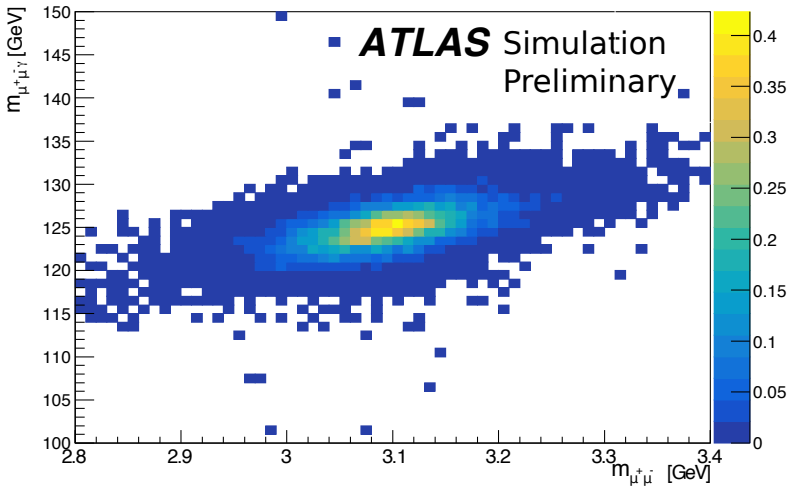

Figure 7.24: Two dimensional $m_{\mu^+\mu^-\gamma}$ and $m_{\mu^+\mu^-}$ distribution in $H \to J/\psi\,\gamma$ MC signal events. A fit of a two-dimensional multivariate Gaussian yields the parameters in Table 7.1.

Table 7.1: Parameters of the two-dimensional Gaussian used to model the Higgs signal. μ_H and σ_H describe the mean and standard deviation of the Gaussian distribution in $m_{\mu^+\mu^-\gamma}$. $\mu_{\mathcal{Q}}$ and $\sigma_{\mathcal{Q}}$ describe the mean and standard deviation of the Gaussian distribution in $m_{\mu^+\mu^-}$. The correlation parameter, ρ, describes the correlation between $m_{\mu^+\mu^-\gamma}$ and $m_{\mu^+\mu^-}$.

	μ_H [GeV]	$\mu_{\mathcal{Q}}$ [GeV]	σ_H [GeV]	$\sigma_{\mathcal{Q}}$ [GeV]	ρ (correlation)
$H \to J/\psi\gamma$	125.0	3.09	1.5	0.04	0.6
$H \to \psi(2S)\gamma$	125.0	3.68	1.5	0.05	0.6
$H \to \Upsilon(1S)\gamma$(barrel)	124.8	9.4	1.4	0.1	0.6
$H \to \Upsilon(1S)\gamma$(endcap)	124.9	9.5	1.7	0.2	0.7
$H \to \Upsilon(2S)\gamma$(barrel)	124.9	10.0	1.4	0.1	0.6
$H \to \Upsilon(2S)\gamma$(endcap)	124.8	10.0	1.7	0.2	0.6
$H \to \Upsilon(3S)\gamma$(barrel)	124.9	10.3	1.4	0.1	0.5
$H \to \Upsilon(3S)\gamma$(endcap)	124.9	10.3	1.7	0.2	0.6

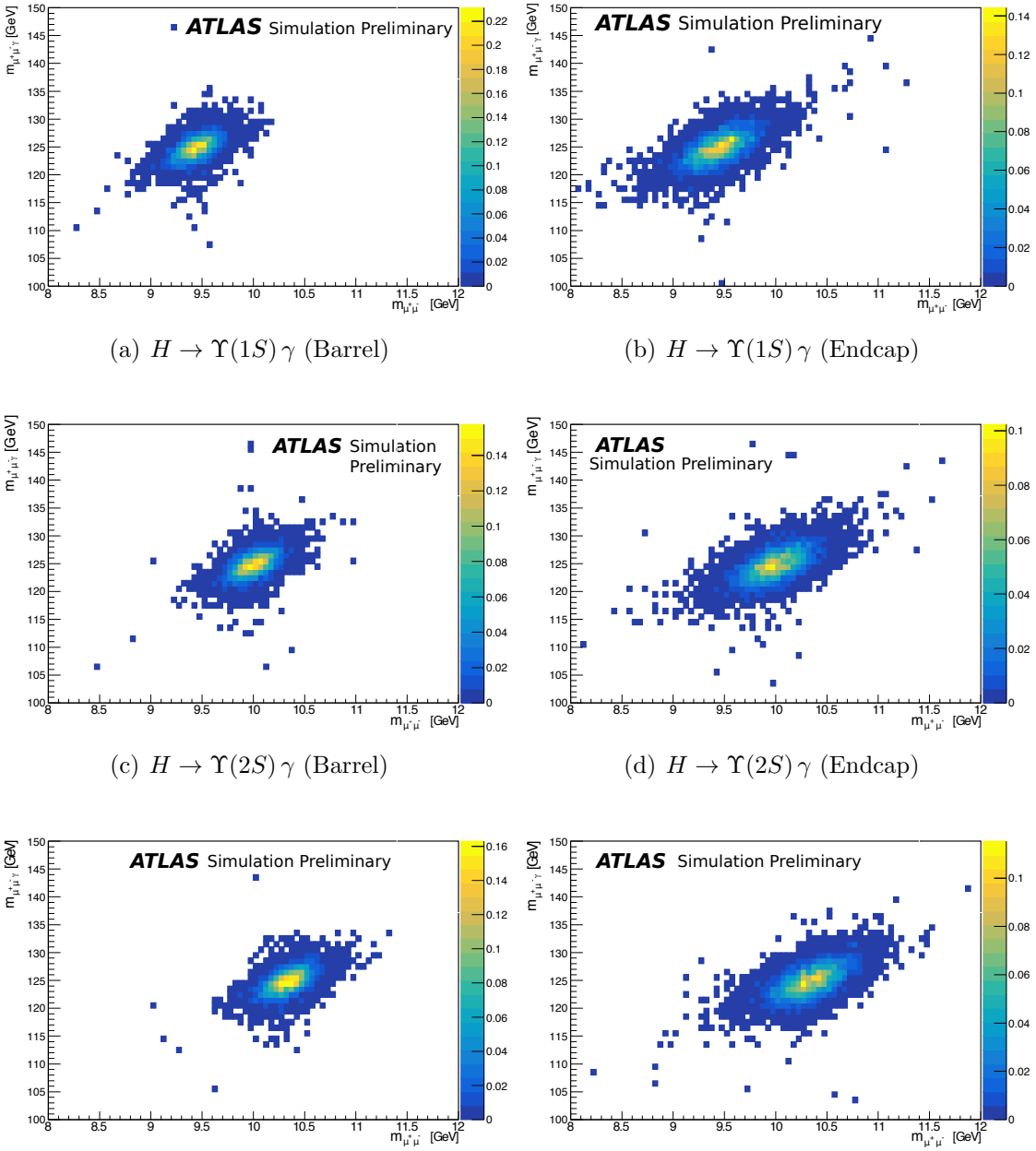

(a) $H \to \Upsilon(1S)\,\gamma$ (Barrel)

(b) $H \to \Upsilon(1S)\,\gamma$ (Endcap)

(c) $H \to \Upsilon(2S)\,\gamma$ (Barrel)

(d) $H \to \Upsilon(2S)\,\gamma$ (Endcap)

(e) $H \to \Upsilon(3S)\,\gamma$ (Barrel)

(f) $H \to \Upsilon(3S)\,\gamma$ (Endcap)

Figure 7.25: Two dimensional $m_{\mu^+\mu^-\gamma}$ and $m_{\mu^+\mu^-}$ distributions in ((a) and (b)) $H \to \Upsilon(1S)\,\gamma$, ((c) and (d)) $H \to \Upsilon(2S)\,\gamma$, and ((e) and (f)) $H \to \Upsilon(3S)\,\gamma$ MC signal events, shown for the Barrel (left) and Endcap (right) categories. A fit of a two-dimensional multivariate Gaussian yields the parameters in Table 7.1.

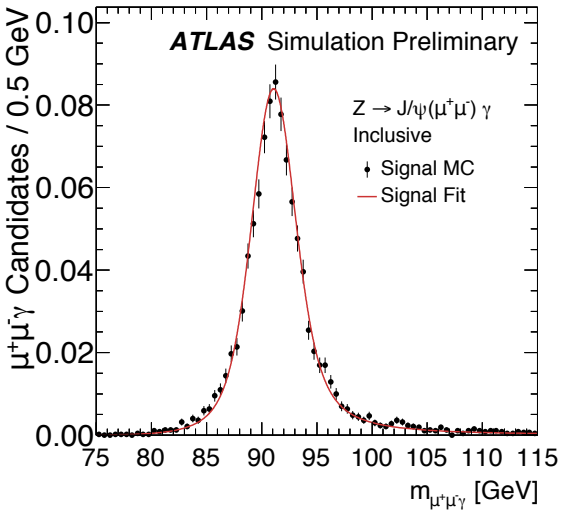

Figure 7.26: $m_{\mu^+\mu^-\gamma}$ distribution in $Z \to J/\psi\,\gamma$ MC signal events. The fit of a Voigtian distribution corrected with mass-dependent efficiency factors is also shown. The parameters of the Voigtian are given in Table 7.2.

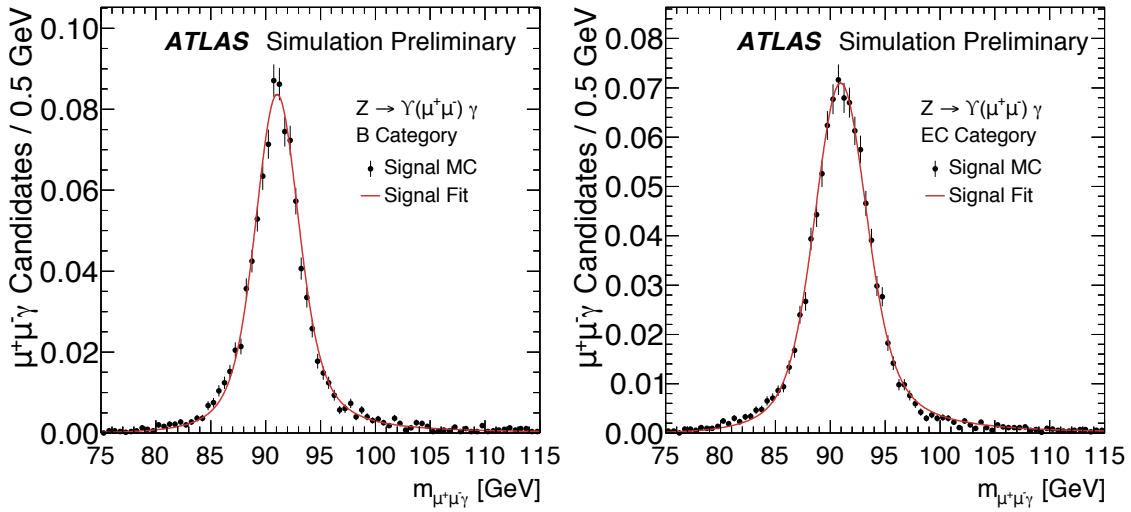

Figure 7.27: $m_{\mu^+\mu^-\gamma}$ distribution in $Z \to \Upsilon(nS)\,\gamma$ MC signal events, shown for the Barrel (left) and Endcap (right) categories. The fit of a Voigtian distribution corrected with mass-dependent efficiency factors is also shown.

Table 7.2: Parameters of the Voigtian and Gaussian models used for the Z signal. μ_Z and σ_Z describe the mean and standard deviation of the Voigtian distribution in $m_{\mu^+\mu^-\gamma}$. $\mu_{\mathcal{Q}}$ and $\sigma_{\mathcal{Q}}$ describe the mean and standard deviation of the Gaussian distribution in $m_{\mu^+\mu^-}$.

	μ_Z [GeV]	$\mu_{\mathcal{Q}}$ [GeV]	σ_Z [GeV]	$\sigma_{\mathcal{Q}}$ [GeV]
$Z \to J/\psi\gamma$	91.2	3.09	1.5	0.05
$Z \to \psi(2S)\gamma$	91.2	3.68	1.5	0.06
$Z \to \Upsilon(1S)\gamma$(barrel)	91.0	9.4	1.3	0.1
$Z \to \Upsilon(1S)\gamma$(endcap)	91.1	9.4	1.9	0.2
$Z \to \Upsilon(2S)\gamma$(barrel)	91.1	10.0	1.4	0.2
$Z \to \Upsilon(2S)\gamma$(endcap)	91.1	10.0	1.8	0.2
$Z \to \Upsilon(3S)\gamma$(barrel)	91.1	10.3	1.4	0.2
$Z \to \Upsilon(3S)\gamma$(endcap)	91.0	10.3	1.8	0.2

7.4.1 Signal Yields and Efficiency

Using the signal MC samples, the expected signal yields have been estimated in the Higgs and Z boson mass regions for events passing the SR event requirements. The signal is normalised to the SM expected cross sections described in Section 6.2 and branching fractions of $\mathcal{B}(H \to \mathcal{Q}\gamma) = 1 \times 10^{-3}$ and $\mathcal{B}(Z \to \mathcal{Q}\gamma) = 1 \times 10^{-6}$. These branching fractions are approximately the expected sensitivity of the analysis. Table 7.3 shows the expected yields for two $m_{\mu^+\mu^-\gamma}$ regions. Table 7.4 shows the efficiencies of the SR selection for each of the samples with and without the polarisation correction.

Table 7.3: Estimated yields of signal events in the three-body mass region of $120 < m_{\mu^+\mu^-\gamma} < 130$ GeV for the Higgs and $86 < m_{\mu^+\mu^-\gamma} < 96$ GeV for Z decays following the full event selection. $\mathcal{B}(H \to \mathcal{Q}\gamma) = 1 \times 10^{-3}$ and $\mathcal{B}(Z \to \mathcal{Q}\gamma) = 1 \times 10^{-6}$ are assumed, along with an integrated luminosity of 36.1fb^{-1}.

Decay	Sample	Yield	Yield
		$120 < m_{\mu^+\mu^-\gamma} < 130$ GeV	$86 < m_{\mu^+\mu^-\gamma} < 96$ GeV
$H \to J/\psi\,\gamma$	Total H Signal	21.3	-
$H \to J/\psi\,\gamma$	ggH Signal	19.7	-
$H \to J/\psi\,\gamma$	VBF Signal	1.1	-
$H \to J/\psi\,\gamma$	WH Signal	0.3	-
$H \to J/\psi\,\gamma$	ZH Signal	0.2	-
$Z \to J/\psi\,\gamma$	Z Signal	-	11.42
$H \to \psi(2S)\,\gamma$	Total H Signal	2.8	-
$H \to \psi(2S)\,\gamma$	ggH Signal	2.6	-
$H \to \psi(2S)\,\gamma$	VBF Signal	0.1	-
$H \to \psi(2S)\,\gamma$	WH Signal	0.0	-
$H \to \psi(2S)\,\gamma$	ZH Signal	0.0	-
$Z \to \psi(2S)\,\gamma$	Z Signal	-	1.5
$H \to \Upsilon(1S)\,\gamma$	Total H Signal	10.3	-
$H \to \Upsilon(1S)\,\gamma$	ggH Signal	9.5	-
$H \to \Upsilon(1S)\,\gamma$	VBF Signal	0.5	-
$H \to \Upsilon(1S)\,\gamma$	WH Signal	0.2	-
$H \to \Upsilon(1S)\,\gamma$	ZH Signal	0.1	-
$Z \to \Upsilon(1S)\,\gamma$	Z Signal	-	6.5
$H \to \Upsilon(2S)\,\gamma$	Total H Signal	7.8	-
$H \to \Upsilon(2S)\,\gamma$	ggH Signal	7.2	-
$H \to \Upsilon(2S)\,\gamma$	VBF Signal	0.4	-
$H \to \Upsilon(2S)\,\gamma$	WH Signal	0.1	-
$H \to \Upsilon(2S)\,\gamma$	ZH Signal	0.1	-
$Z \to \Upsilon(2S)\,\gamma$	Z Signal	-	4.9
$H \to \Upsilon(3S)\,\gamma$	Total H Signal	8.9	-
$H \to \Upsilon(3S)\,\gamma$	ggH Signal	8.2	-
$H \to \Upsilon(3S)\,\gamma$	VBF Signal	0.4	-
$H \to \Upsilon(3S)\,\gamma$	WH Signal	0.1	-
$H \to \Upsilon(3S)\,\gamma$	ZH Signal	0.1	-
$Z \to \Upsilon(3S)\,\gamma$	Z Signal	-	5.9

Table 7.4: Estimated efficiencies for signal events for the full event selection.

Decay	Sample	Efficiency without polarisation	Efficiency with polarisation
$H \to \psi(kS)\,\gamma$	Total H Signal	20.2%	19.4%
$H \to \psi(kS)\,\gamma$	ggH Signal	21.0%	20.2%
$H \to \psi(kS)\,\gamma$	VBF Signal	15.0%	14.5%
$H \to \psi(kS)\,\gamma$	WH Signal	13.4%	12.9%
$H \to \psi(kS)\,\gamma$	ZH Signal	13.7%	13.3%
$Z \to \psi(kS)\,\gamma$	Z Signal	10.0%	10.9%
$H \to \Upsilon(1S)\,\gamma$	Total H Signal	23.5%	22.9%
$H \to \Upsilon(1S)\,\gamma$	ggH Signal	24.5%	23.7%
$H \to \Upsilon(1S)\,\gamma$	VBF Signal	16.9%	16.5%
$H \to \Upsilon(1S)\,\gamma$	WH Signal	14.9%	14.5%
$H \to \Upsilon(1S)\,\gamma$	ZH Signal	15.5%	15.1%
$Z \to \Upsilon(1S)\,\gamma$	Z Signal	13.9%	15.0%
$H \to \Upsilon(2S)\,\gamma$	Total H Signal	23.3%	22.7%
$H \to \Upsilon(2S)\,\gamma$	ggH Signal	24.3%	23.7%
$H \to \Upsilon(2S)\,\gamma$	VBF Signal	16.8%	16.4%
$H \to \Upsilon(2S)\,\gamma$	WH Signal	14.5%	14.2%
$H \to \Upsilon(2S)\,\gamma$	ZH Signal	15.0%	14.8%
$Z \to \Upsilon(2S)\,\gamma$	Z Signal	13.8%	15.0%
$H \to \Upsilon(3S)\,\gamma$	Total H Signal	22.8%	22.2%
$H \to \Upsilon(3S)\,\gamma$	ggH Signal	23.7%	23.1%
$H \to \Upsilon(3S)\,\gamma$	VBF Signal	16.7%	16.3%
$H \to \Upsilon(3S)\,\gamma$	WH Signal	14.7%	14.4%
$H \to \Upsilon(3S)\,\gamma$	ZH Signal	15.1%	14.8%
$Z \to \Upsilon(3S)\,\gamma$	Z Signal	14.6%	15.5%

Trigger Efficiency

The trigger efficiency with respect to the offline selection is defined as the ratio of the number of events that pass the full offline selection including the trigger, to the number of events that pass the full offline selection, irrespective of the trigger decision. It is calculated using fully simulated signal samples and is shown in Table 7.5. The variations of trigger efficiency as a function of $p_{\mathrm{T}}^{\mu^+\mu^-}$ and p_{T}^{γ} are shown in Figures 7.28–7.31. It is noted that the appropriate scale factors are applied to the MC, to account for data/MC differences.

Table 7.5: The trigger efficiency, with respect to the SR analysis selection, for various decay channels, calculated from simulation.

Channel	Inclusive
$H \to J/\psi\,\gamma$	$(98.2 \pm 0.2)\%$
$Z \to J/\psi\,\gamma$	$(97.3 \pm 0.3)\%$
$H \to \Upsilon(nS)\,\gamma$	$(99.1 \pm 0.1)\%$
$Z \to \Upsilon(nS)\,\gamma$	$(98.1 \pm 0.2)\%$

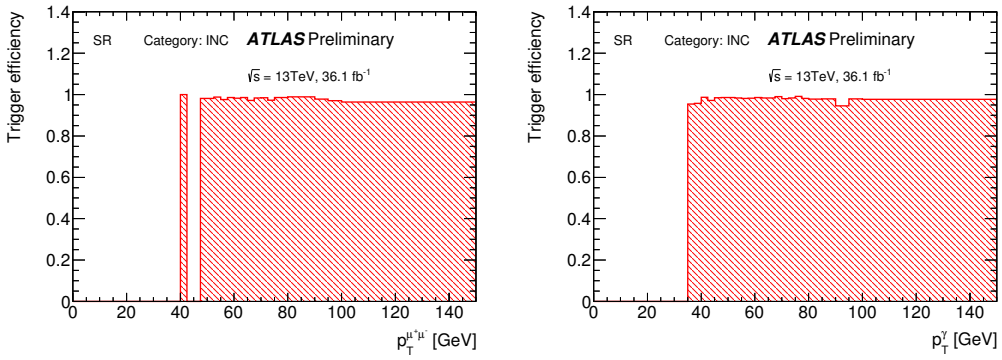

Figure 7.28: The trigger efficiency as a function of $p_{\mathrm{T}}^{\mu^+\mu^-}$ and p_{T}^{γ}, with respect to the SR analysis selection, calculated from simulated $H \to J/\psi\,\gamma$ events. Total uncertainty is around 0.2%. The gap appearing at around 45 GeV in the $p_{\mathrm{T}}^{\mu^+\mu^-}$ distribution is due to low statistics caused by the variable di-muon p_{T} requirement.

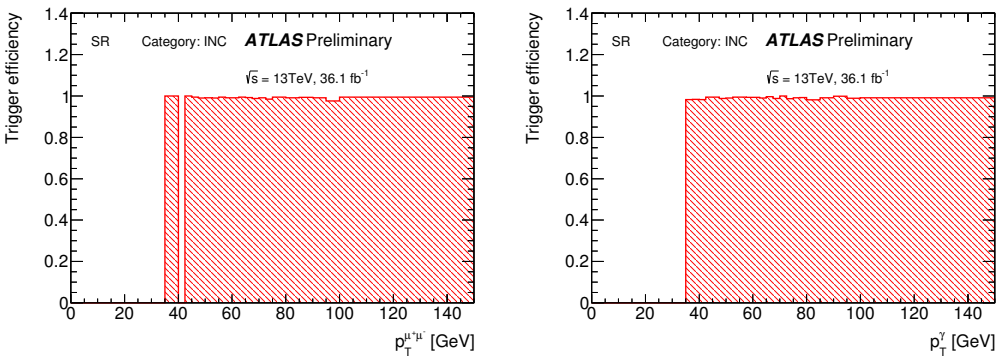

Figure 7.29: The trigger efficiency as a function of $p_{\mathrm{T}}^{\mu^+\mu^-}$ and p_{T}^{γ}, with respect to the SR analysis selection, calculated from simulated $H \to \Upsilon(nS)\,\gamma$ events. Total uncertainty is around 0.3%. The gap appearing at around 41 GeV in the $p_{\mathrm{T}}^{\mu^+\mu^-}$ distribution is due to low statistics caused by the variable di-muon p_{T} requirement.

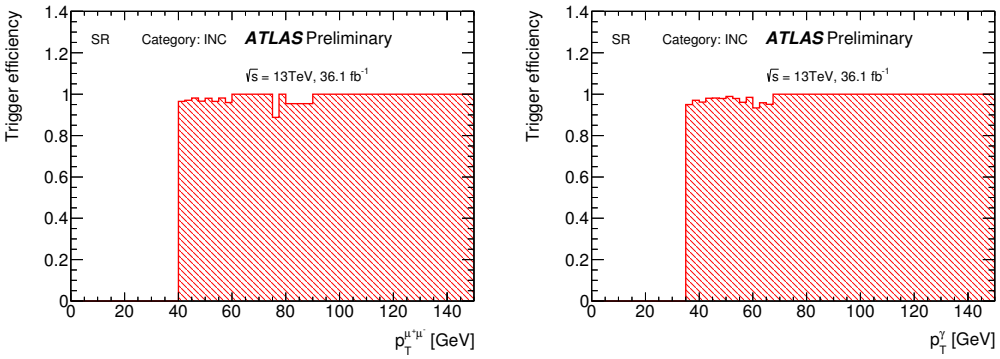

Figure 7.30: The trigger efficiency as a function of $p_{\mathrm{T}}^{\mu^+\mu^-}$ and p_{T}^{γ}, with respect to the SR analysis selection, calculated from simulated $Z \to J/\psi\,\gamma$ events. Total uncertainty is around 0.1%.

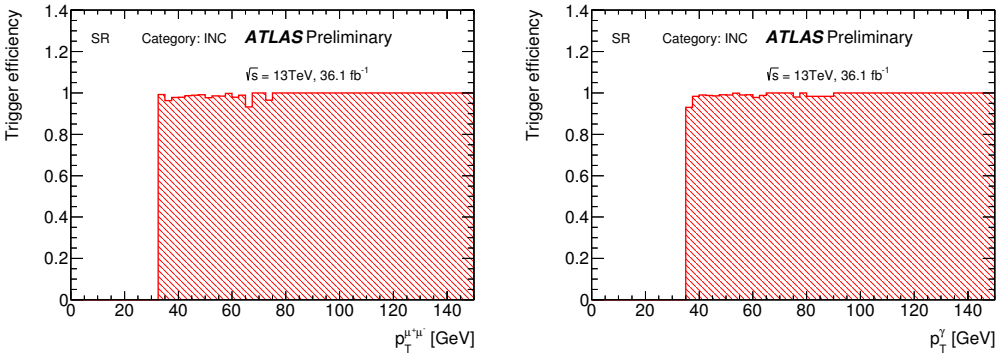

Figure 7.31: The trigger efficiency as a function of $p_{\mathrm{T}}^{\mu^+\mu^-}$ and p_{T}^{γ}, with respect to the SR analysis selection, calculated from simulated $Z \to \Upsilon(nS)\,\gamma$ events. Total uncertainty is around 0.2%.

7.5 Expected Signal Systematic Uncertainties

The expected signals are modelled using MC signal events. Many assumptions must be made to estimate the signal yields and signal shapes. The analysis must account for these by assigning systematic uncertainties for each assumption. These are input into the final fitting procedure as nuisance parameters.

7.5.1 Theoretical Systematic Uncertainties

The Higgs boson production cross section and decay branching ratios, as well as their uncertainties, are taken from Refs. [14]. The QCD scale uncertainties on the cross-section for a 125 GeV Higgs boson [125] amount to $^{+5}_{-7}$ % for the ggH process, $^{+0.4}_{-0.3}$ % for VBF, $^{+0.5}_{-0.7}$ % ($^{+3.8}_{-3.1}$ %) for the associated $WH(ZH)$ production processes, and $^{+6}_{-9}$ % for the associated $t\bar{t}H$ production process. The uncertainty on the production cross section due to uncertainties on the PDFs and the strong coupling constant, α_s, is $\pm 3\%$ for ggH processes, $\pm 2.1\%$ and $\pm 1.9(\pm 1.6)\%$ for the VBF and associated $WH(ZH)$ production processes and $\pm 3.6\%$ for the associated $t\bar{t}H$ production process.

For the Z signal the production cross section is taken from Ref. [126] to be 59 pb with an uncertainty of $\pm 2.9\%$.

QCD Modelling Acceptance Uncertainty

As well as the uncertainty on the predicted normalisation described above, considerations must also be made for how the theoretical predictions affect the shapes of the kinematic distributions and subsequently the acceptance of the analysis. The effect on the acceptance for ggH signal processes due to uncertainties on the QCD scales, PDFs, underlying event tune and parton shower are evaluated using MC events. For each source of uncertainty, truth-level samples are produced either separately or by making use of event weights. The acceptance for each uncertainty is evaluated by

implementing the reconstruction level analysis cuts. As the dominant process, the estimated ggH uncertainties are applied to all of the production processes.

Table 7.6 presents a breakdown of the estimated uncertainties. Two different sets of variations on the PDF uncertainty are considered, variations of α_s and following the *PDF4LHC* recommendations in Ref. [127]. A total uncertainty of 1.8% is obtained.

Table 7.6: Higgs acceptance uncertainties from theoretical modelling uncertainties.

Systematic Variation	Acceptance Uncertainty
PDF `alphaS` variations	0.5%
PDF `pdf4lhc` variations	0.7%
QCD Scale variations	1.3%
Showering and tune variations	0.8%
Total	1.8%

The uncertainty on the acceptance for the Z signal events is conservatively estimated by varying the generator used. A 6.0% relative acceptance change was found after generating the Z signal events using SHERPA 2.2.1 [128] and MADGRAPH5_AMC@NLO v2.2.2 [129] instead of the default POWHEG generator.

7.5.2 Signal Reconstruction Systematic Uncertainties

Trigger Efficiency

Trigger efficiencies for photons are determined from samples enriched with $Z \to e^+e^-$ events in data [130]. The systematic uncertainty on the expected signal yield associated with the trigger efficiency is estimated to be 2.0%.

Muon Reconstruction and Energy Scale

Muon momenta are measured in the MS and in the ID. The uncertainty is calculated from systematic variations in both regions. The effect of the muon reconstruction and identification efficiency uncertainty is estimated to be 2.8% [64].

The normalisation uncertainty evaluated due to the muon energy scale, including

two variations of the scale based on corrections for the measurement of the sagitta of the track trajectory, is found to be 0.16%.

Photon Reconstruction, Energy Scale and Resolution

The photon identification efficiency uncertainties, for both the converted and unconverted photons, are estimated to be 1.4% for the Higgs and Z boson signals using the enriched $Z \to e^+e^-$ events, as well as inclusive photon events and $Z \to \ell\ell\gamma$ events [67, 68].

The photon energy scale uncertainty, determined from $Z \to e^+e^-$ events and validated using $Z \to \ell\ell\gamma$ events [131, 132], is propagated through the simulated signal samples as a function of η^γ and p_{T}^γ. The uncertainty associated with the determination of the photon energy scale and resolution in the simulation is found to be 0.3% in the yields of the Higgs and Z boson signals.

The effect of the energy scale uncertainty on the mass is found to be approximately 0.23%.

7.5.3 Summary of Signal Uncertainties

The systematic uncertainties on the expected signal yields are summarised in Table 7.7.

Table 7.7: Summary of the systematic uncertainties on the expected signal yields. Table taken from Ref. [1].

Source of systematic uncertainty	Yield uncertainty $H(Z) \to \mathcal{Q}\gamma$
Total $H(Z)$ cross section	7.0% (2.9%)
Integrated luminosity	2.1%
$H(Z)$ QCD modelling effect on acceptance	1.8% (6%)
Trigger efficiency	2.0%
Photon identification	1.4%
Muon reconstruction	2.8%
Photon energy scale	0.3%
Muon momentum scale	0.2%

7.6 Results

7.6.1 Expected Sensitivity

Before the analysis selection is frozen and the data set unblinded, 95% CL limits are calculated to study the expected sensitivity of the analysis. A trial dataset is generated based on the expected background distributions. As described in Section 7.2.1, the normalisation of the inclusive background is obtained by fitting the background template to the GR data sample, whilst excluding the blinded three-body mass regions. The ratio between the resonant and non-resonant background contributions is also found from a fit to the $m_{\mu^+\mu^-}$ distributions in the GR data events. The Z FSR background normalisation is obtained using the methods described in Section 7.2.2. An estimation of the expected overall background is made by combining the individual background components and then renormalising to the total number of SR data events. This provides a sample that represents a background-only set of data. Using this dataset, the background templates and the expected signal distributions and yields, a fit can be performed to calculate the expected 95% CL branching fraction limits of the analysis. These expected limits are referred to as the "pre-fit" expected limits to avoid confusion with the expected limits obtained from the final fit to the observed data. The distinction between the two is that the pre-fit uses a

dataset formed from predicted contributions to the background, whereas the final fit estimates the contributions of background from the observed data and calculates the expected limits based on this.

At this stage, to compare the sensitivity to the Run I analysis, only the J/ψ and $\Upsilon(nS)$ states were considered (with no $\psi(2S)\,\gamma$ signal included). The $H/Z \to J/\psi\,\gamma$ pre-fit expected limits are presented in Table 7.8. The corresponding three-body and di-muon mass distributions are shown in Figure 7.32 with the signal and background templates fitted to the expected dataset. For the $\Upsilon(nS)\,\gamma$ analysis, the pre-fit expected limits are shown in Table 7.9 and the three-body and di-muon mass distributions are shown in Figures 7.33 and 7.34 for the barrel and endcap categories, respectively. In the figures, the $H(Z) \to \mathcal{Q}\,\gamma$ signal is shown for assumed branching fractions of $\mathcal{B}(H \to \mathcal{Q}\,\gamma) = 10^{-3}$ and $\mathcal{B}(Z \to \mathcal{Q}\,\gamma) = 10^{-6}$, which correspond to the expected sensitivity of the analysis. This pre-fit confirms that the fitting procedure was performed successfully. For the Higgs decays, the expected branching fraction limits improve by more than a factor of two compared to the Run I expected limits, whereas the Z decays have less of an improvement due to the Z FSR background cross section scaling with the centre-of-mass energy in the same way as the $Z \to \mathcal{Q}\,\gamma$ signal.

Table 7.8: Pre-fit expected branching fraction limits at 95% CL for $H(Z) \to J/\psi\,\gamma$. The limits are estimated with and without the complete normalisation and shape systematic uncertainties. The expected limits from the Run I $H(Z) \to J/\psi\,\gamma$ analysis at $\sqrt{s}$= 8 TeV are also shown for comparison [38].

	Expected	$\pm1\sigma$	$\pm2\sigma$	Run I Expected
Higgs $[10^{-3}]$				
No systematics	0.42	0.60/0.30	0.85/0.22	1.2
Shape+Norm	0.42	0.60/0.30	0.86/0.22	1.2
Z $[10^{-6}]$				
No systematics	1.2	1.7/0.8	2.3/0.6	2.0
Shape+Norm	1.2	1.7/0.9	2.4/0.6	2.0

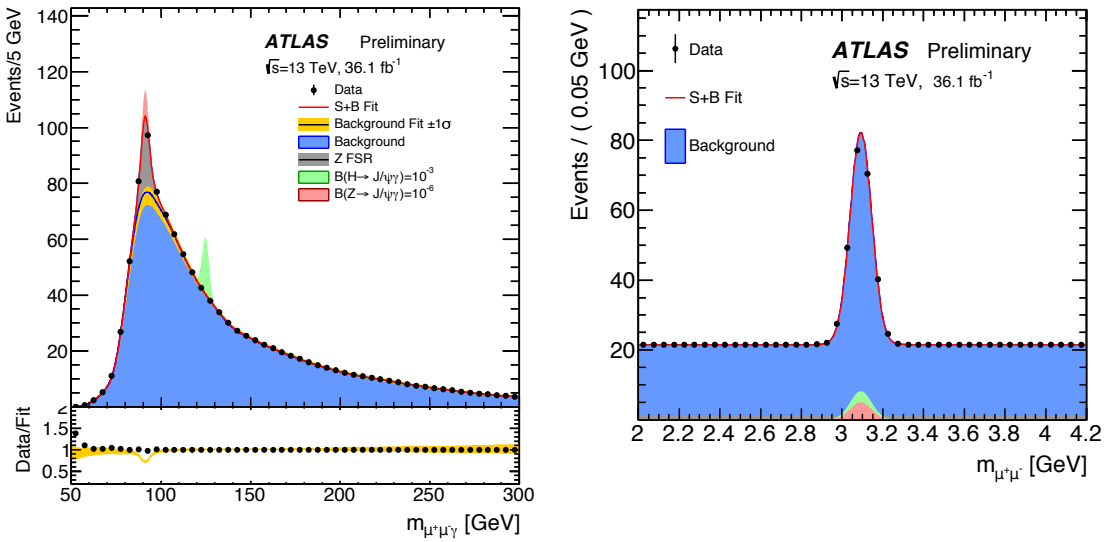

Figure 7.32: $m_{\mu^+\mu^-\gamma}$ and $m_{\mu^+\mu^-}$ distributions using a dataset equivalent to the expected background in the signal region for $H(Z) \to J/\psi\,\gamma$, including fit results. Uncertainties are the Poisson statistical uncertainty of each data point. The signal distributions for each channel are normalised to branching fractions of 10^{-3} and 10^{-6} for the Higgs and Z bosons, respectively. The red line shows the result of a combined signal-plus-background fit (all signal strengths left free in the fit).

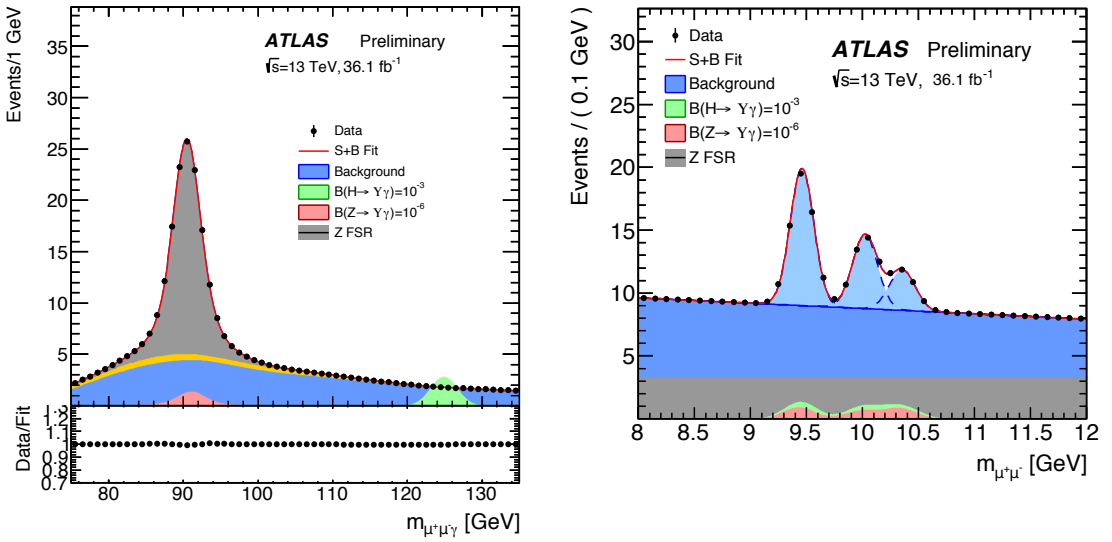

Figure 7.33: $m_{\mu^+\mu^-\gamma}$ and $m_{\mu^+\mu^-}$ distributions using a dataset equivalent to the expected background in the barrel signal region for $H(Z) \to \Upsilon(nS)\,\gamma$, including fit results. Uncertainties are the Poisson statistical uncertainty of each data point. The signal distributions for each channel are normalised to branching fractions of 10^{-3} and 10^{-6} for the Higgs and Z bosons, respectively. The red line shows the result of a combined signal-plus-background fit (all signal strengths left free in the fit).

Table 7.9: Pre-fit expected branching fraction limits at 95% CL for $H(Z) \to \Upsilon(nS)\,\gamma$. The limits are estimated with and without the complete normalisation and shape systematic uncertainties. The expected limits from the Run I $H(Z) \to \Upsilon(nS)\,\gamma$ analysis at $\sqrt{s}$= 8 TeV are also shown for comparison [38].

	Expected	$\pm1\sigma$	$\pm2\sigma$	Run I Expected
$H \to \Upsilon(1S)\gamma$ $[10^{-3}]$				
No systematics	0.58	0.81/0.42	1.1/0.31	1.7
Shape+Norm	0.60	0.83/0.43	1.1/0.32	1.8
$H \to \Upsilon(2S)\gamma$ $[10^{-3}]$				
No systematics	0.76	1.1/0.54	1.1/0.41	2.0
Shape+Norm	0.78	1.1/0.56	1.5/0.42	2.1
$H \to \Upsilon(3S)\gamma$ $[10^{-3}]$				
No systematics	0.64	0.89/0.46	1.2/0.34	1.7
Shape+Norm	0.66	0.91/0.47	1.2/0.35	1.8
$Z \to \Upsilon(1S)\gamma$ $[10^{-6}]$				
No systematics	2.8	3.9/2.0	5.2/1.5	4.8
Shape+Norm	2.9	4.0/2.1	5.4/1.6	4.9
$Z \to \Upsilon(2S)\gamma$ $[10^{-6}]$				
No systematics	3.8	5.3/2.7	7.1/2.0	6.1
Shape+Norm	3.9	5.4/2.8	7.3/2.1	6.2
$Z \to \Upsilon(3S)\gamma$ $[10^{-6}]$				
No systematics	3.1	4.3/2.2	5.7/1.6	5.3
Shape+Norm	3.1	4.4/2.3	5.9/1.7	5.4

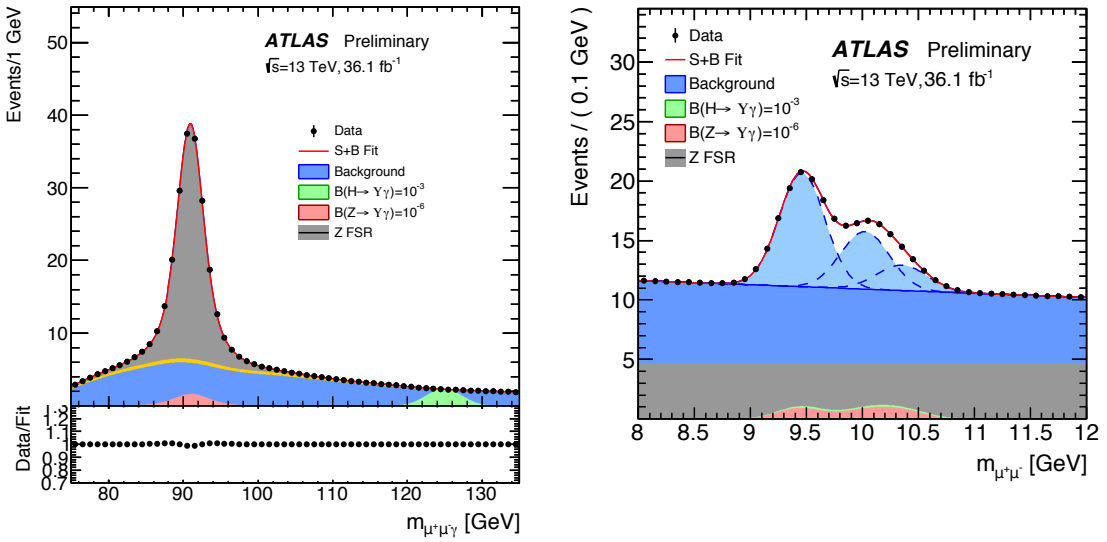

Figure 7.34: $m_{\mu^+\mu^-\gamma}$ and $m_{\mu^+\mu^-}$ distributions using a dataset equivalent to the expected background in the endcap signal region for $H(Z) \to \Upsilon(nS)\,\gamma$, including fit results. Uncertainties are the Poisson statistical uncertainty of each data point. The signal distributions for each channel are normalised to branching fractions of 10^{-3} and 10^{-6} for the Higgs and Z bosons, respectively. The red line shows the result of a combined signal-plus-background fit (all signal strengths left free in the fit).

The signal yields corresponding to the pre-fit expected 95% CL limits have been estimated and are shown in Table 7.10.

Table 7.10: Expected 95% CL branching fraction limits of each channel and the corresponding number of expected signal events.

	Expected limit	Expected signal events for this BF
$H \to J/\psi\gamma$	0.42×10^{-3}	9.6
$Z \to J/\psi\gamma$	1.2×10^{-6}	16.1
$H \to \Upsilon(1S)\gamma$	0.60×10^{-3}	6.7
$H \to \Upsilon(2S)\gamma$	0.78×10^{-3}	6.6
$H \to \Upsilon(3S)\gamma$	0.66×10^{-3}	6.3
$Z \to \Upsilon(1S)\gamma$	2.9×10^{-6}	19.7
$Z \to \Upsilon(2S)\gamma$	3.9×10^{-6}	20.0
$Z \to \Upsilon(3S)\gamma$	3.1×10^{-6}	19.2

7.6.2 Signal Injection

To test the fitting procedure further, a trial simulated signal of Higgs and Z decay events was injected into the background-only data sample and the expected limit test performed again. Values of branching fraction of 0.5 $\times 10^{-3}(10^{-6})$ were chosen for Higgs (Z) decay events to provide signal events at the lower end of the analysis sensitivity, to test the fitting procedure's ability to resolve the signal. Table 7.11 shows the fitted signal strengths (μ) for each signal when injected independently. All of the values of μ obtained from the fits were consistent with the input signals and, therefore, the results indicate that the fit is able to measure the signal contributions as expected.

Table 7.11: Signal strength, μ, values from fits after signal injection of a branching fraction of 0.5 $\times 10^{-3}(10^{-6})$ for Higgs (Z) decay.

	Signal strength
$H \to J/\psi\gamma$	$0.50 \pm 0.24 \times 10^{-3}$
$Z \to J/\psi\gamma$	$0.50 \pm 0.57 \times 10^{-6}$
$H \to \Upsilon(1S)\gamma$	$0.50 \pm 0.32 \times 10^{-3}$
$H \to \Upsilon(2S)\gamma$	$0.51 \pm 0.40 \times 10^{-3}$
$H \to \Upsilon(3S)\gamma$	$0.51 \pm 0.35 \times 10^{-3}$
$Z \to \Upsilon(1S)\gamma$	$0.49 \pm 1.37 \times 10^{-6}$
$Z \to \Upsilon(2S)\gamma$	$0.50 \pm 1.83 \times 10^{-6}$
$Z \to \Upsilon(3S)\gamma$	$0.48 \pm 1.47 \times 10^{-6}$

7.6.3 Fit Results and Limits

Once the analysis has been frozen, the fitting procedure can be run on the full unblinded dataset. Background-only and signal-plus-background fits are performed and are presented below. Performing both fits ensures that the fitting procedure is behaving as expected. The background only fit corresponds to the SM expectation of there being no observable signal present in the dataset and therefore the background model should be compatible with the dataset. The subsequent inclusion of signal components into the fit should not, therefore, drastically change the fit results. The results are then used in the procedure to obtain the 95% CL branching fraction limits, as described in Section 7.1.3.

$\psi(kS)\gamma$ Fit Results

The final fitted parameter values from the background-only and the signal-plus-background fits are shown in Table 7.12 for the $H/Z \to \psi(kS)\,\gamma$ analysis. The α parameters refer to the different signal and background shape systematic uncertainties, with $\alpha = 0 \pm 1$ being the nominal value. The a_0 parameters correspond to the gradients of the linear functions used for the non-resonant and Z FSR backgrounds. The μ parameters are the normalisations for the backgrounds and signals. The initial normalisation of each inclusive background before fitting is set to the total number of SR data events. The fit parameters all return plausible values with the background model mostly unchanged after the inclusion of the signal. The background

Table 7.12: Background-only and signal-plus-background best fit parameters for the $\psi(kS)\,\gamma$ analysis.

Floating Parameter	Background		Signal + background	
	Value	Error	Value	Error
a_0 Z FSR	0.5	1.5	0.8	1.8
a_0 Background	-0.35	0.07	-0.36	0.07
α Luminosity	0	1.0	1×10^{-4}	1.0
α Theory shower acceptance	0	1.0	-2×10^{-5}	1.0
α PDF scale	0	1.0	-7×10^{-5}	1.0
α Theory PDF α_S acceptance	0	1.0	-1×10^{-5}	1.0
α Theory PDF pdf4lhc acceptance	0	1.0	-2×10^{-5}	1.0
α QCD scale	0	1.0	-1×10^{-4}	1.0
α QCD scale acceptance	0	1.0	-3×10^{-5}	1.0
α μ reconstruction ID	0	1.0	2×10^{-4}	1.0
α γ reconstruction ID	0	1.0	9×10^{-5}	1.0
α μ reconstruction MS	0	1.0	7×10^{-6}	1.0
α Trigger	0	1.0	1×10^{-4}	1.0
α Z FSR shape	0.15	1.00	0.17	1.00
α Z model acceptance	0	1.0	4×10^{-4}	1.0
α Z cross section	0	1.0	2×10^{-4}	1.0
α Background shape $p_{\mathrm{T}}^{\mu^+\mu^-}$	-0.074	0.99	-0.11	0.99
α Background shape $\Delta\phi$	0.25	0.98	0.23	0.98
α Background shape tilt	0.78	0.66	0.59	0.67
$\mu_{H\to J/\psi\,\gamma}$	0	0	0.057	0.12
$\mu_{H\to\psi(2S)\,\gamma}$	0	0	0.48	0.60
$\mu_{\text{Background } J/\psi\,\gamma}$	0.16	0.017	0.14	0.018
$\mu_{\text{Background } \psi(2S)\,\gamma}$	9.7×10^{-3}	9.8×10^{-3}	0.011	0.011
$\mu_{\text{Background non-resonant}}$	0.85	0.036	0.85	0.037
$\mu_{Z\to J/\psi\,\gamma}$	0	0	1.2	0.61
$\mu_{Z\to\psi(2S)\,\gamma}$	0	0	-2.4	2.3
$\mu_{\text{Background } Z\text{ FSR}}$	0.82	0.44	0.80	0.46

model shape is slightly adjusted within the systematic uncertainties to incorporate the shape of the data. An upward fluctuation is observed in the $Z \to J/\psi\,\gamma$ channel, corresponding to around 2σ significance. No significant fluctuations are observed in the fit results for the Higgs decay signals.

The background-only post-fit three-body and di-muon mass distributions are shown in Figure 7.35 and the signal-plus-background distributions are shown in Figure 7.36. These distributions show that the post-fit background distributions model the data well. The upward fluctuation in the $Z \to J/\psi\,\gamma$ channel can be observed in the

signal-plus-background distribution as the small discrepancy between the red "S+B" line and the blue background distributions in Figure 7.36.

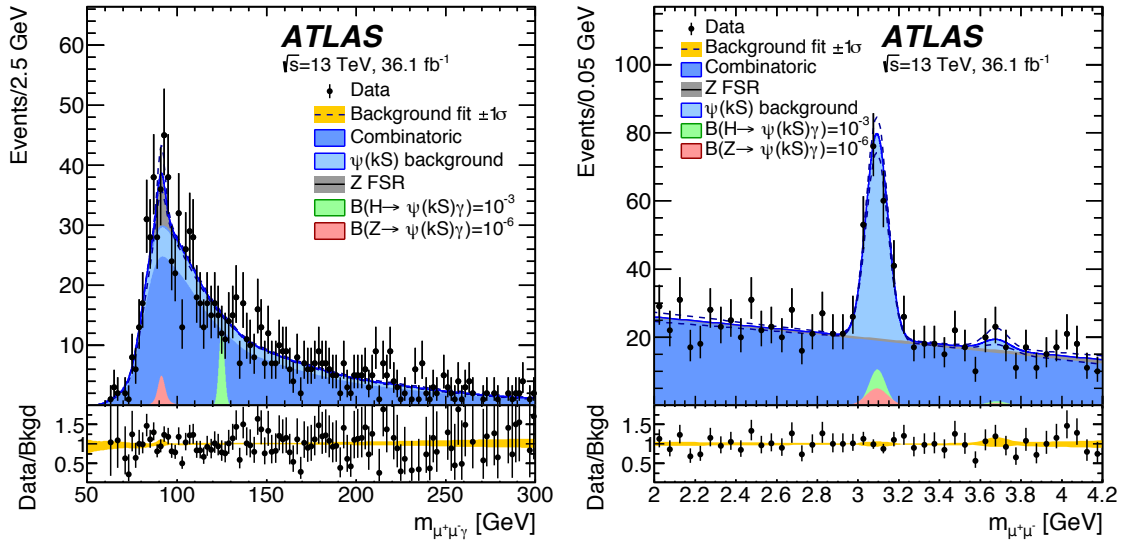

Figure 7.35: $m_{\mu^+\mu^-\gamma}$ and $m_{\mu^+\mu^-}$ background-only distributions in the signal region for the $\psi(kS)\,\gamma$ analysis, including fit results. Figure taken from Ref. [1].

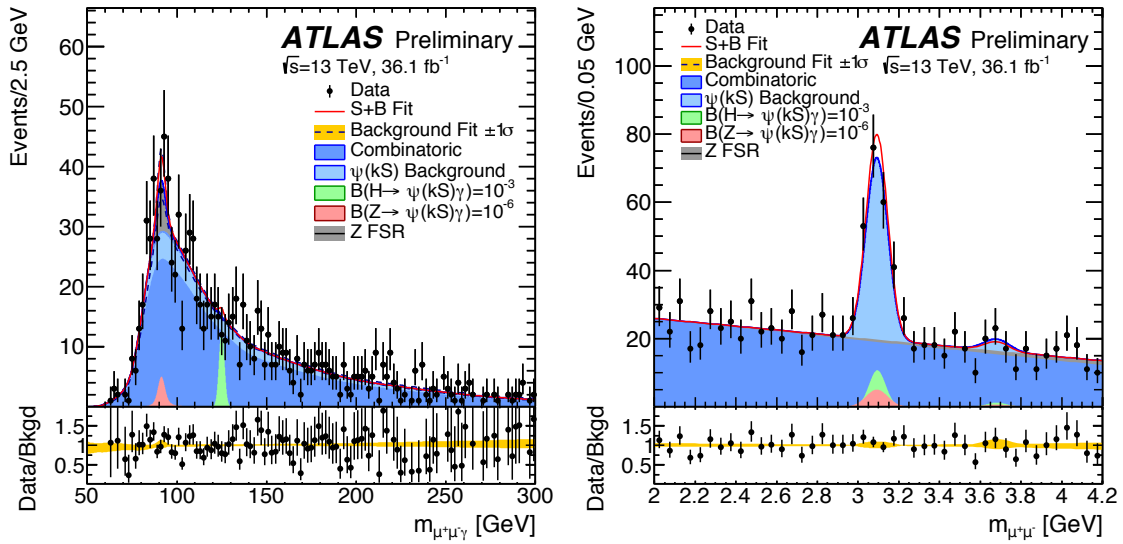

Figure 7.36: $m_{\mu^+\mu^-\gamma}$ and $m_{\mu^+\mu^-}$ signal+background distributions in the signal region for the $\psi(kS)\,\gamma$ analysis, including fit results.

$\Upsilon(nS)\gamma$ Fit Results

The final fitted parameter values from the background-only and the signal-plus-background fits are shown in Table 7.13 for the $H/Z \to \Upsilon(nS)\,\gamma$ analysis. The $\Upsilon(nS)\,\gamma$ fit is more complex than the $\psi(kS)\,\gamma$ fit due to the existence of more

resonances and with the resonances overlapping. The initial normalisation of each background contribution before fitting is based on the ratio of the number of events observed within the resonances in the fit to GR data events shown in Figure 6.8. The combined initial normalisation of the backgrounds is set to that of the SR dataset. Overall, the fit parameters behave as expected. The background model is adjusted towards the "tilt" background systematic variations quite strongly. The μ parameters have reasonable values, with some differences observed between the background-only and signal-plus-background fits. This is likely due to the large overlap between the $2S$ and $3S$ resonances and their relatively small normalisations, with a large downward fluctuation observed in $Z \to \Upsilon(2S)\gamma$.

The background-only post-fit three-body and di-muon mass distributions are shown in Figures 7.37 and 7.38 separately for events in the barrel and endcap categories, and the signal-plus-background distributions are shown in Figures 7.39 and 7.40. The post-fit background distributions model the data well in both the barrel and endcap regions for both background-only and signal-plus-background fits. The $Z \to \Upsilon(2S)\,\gamma$ downward fluctuation can be observed in Figures 7.39 and 7.40 as the discrepancy between the red "S+B Fit" line and the blue background distributions.

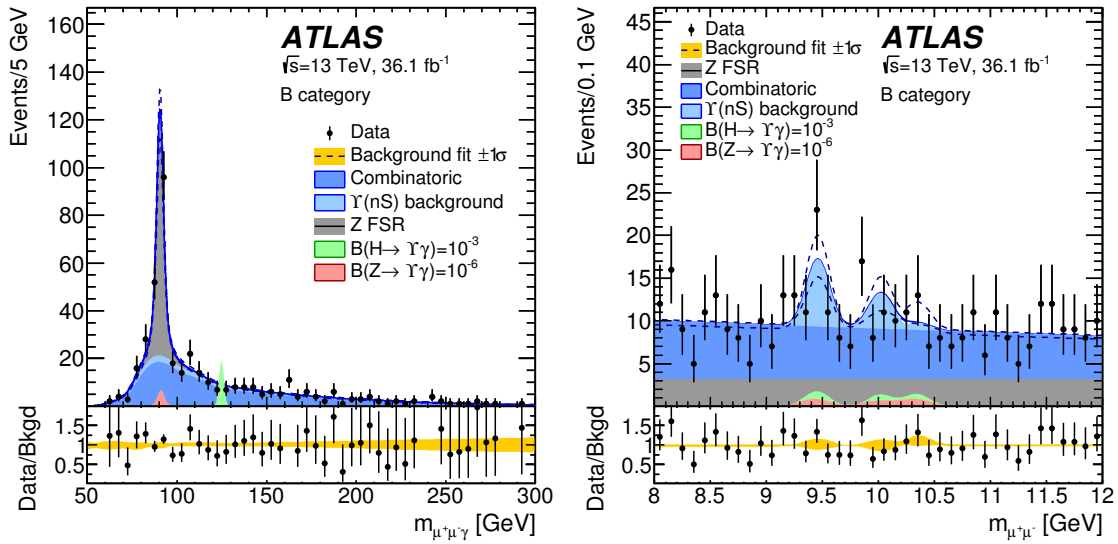

Figure 7.37: $m_{\mu^+\mu^-\gamma}$ background-only distributions in the barrel signal region for the $\Upsilon(nS)\,\gamma$ analysis, including fit results. Figure taken from Ref. [1].

Table 7.13: Background-only and signal-plus-background best fit parameters for the $\Upsilon(nS)\,\gamma$ analysis.

Floating Parameter	Background		Signal+background	
	Value	Error	Value	Error
α Luminosity	0	1	-4×10^{-5}	1.0
α Theory shower acceptance	0	1	2×10^{-7}	1.0
α PDF scale	0	1	6×10^{-7}	1.0
α Theory PDF α_S acceptance	0	1	1×10^{-7}	1.0
α Theory PDF pdf4lhc acceptance	0	1	1×10^{-7}	1.0
α QCD scale	0	1	1×10^{-6}	1.0
α QCD scale acceptance	0	1	3×10^{-7}	1.0
α μ reconstruction ID	0	1	-5×10^{-5}	1.0
α γ reconstruction ID	0	1	-2×10^{-5}	1.0
α μ reconstruction MS	0	1	-2×10^{-6}	1.0
α Trigger	0	1	-3×10^{-5}	1.0
α Z FSR shape (Barrel)	0.5	0.8	0.6	0.8
α Z FSR shape (Endcap)	0.1	0.8	0.2	0.8
α Z model acceptance	0	1	-1×10^{-4}	1.0
α Z cross section	0	1	-6×10^{-5}	1.0
α Background shape $p_{\mathrm{T}}^{\mu^+\mu^-}$ (Barrel)	-0.03	1.0	-0.03	1.0
α Background shape $p_{\mathrm{T}}^{\mu^+\mu^-}$ (Endcap)	0.4	0.9	0.4	0.9
α Background shape $\Delta\phi$ (Barrel)	0.02	1.0	0.02	1.0
α Background shape $\Delta\phi$ (Endcap)	0.2	1.0	0.2	1.0
α Background shape tilt (Barrel)	-2	2	-2	2
α Background shape tilt (Endcap)	1	1	1	1
$\mu_{H\to\Upsilon(1S)\,\gamma}$	0	0	-5×10^{-3}	0.2
$\mu_{H\to\Upsilon(2S)\,\gamma}$	0	0	-0.08	0.2
$\mu_{H\to\Upsilon(3S)\,\gamma}$	0	0	0.03	0.2
$\mu_{\text{Background}\,\Upsilon(1S)\,\gamma}$ (Barrel)	0.7	0.3	0.7	0.3
$\mu_{\text{Background}\,\Upsilon(1S)\,\gamma}$ (Endcap)	0.6	0.2	0.6	0.3
$\mu_{\text{Background}\,\Upsilon(2S)\,\gamma}$ (Barrel)	0.7	0.4	1.0	0.5
$\mu_{\text{Background}\,\Upsilon(2S)\,\gamma}$ (Endcap)	0.2	0.5	0.4	0.5
$\mu_{\text{Background}\,\Upsilon(3S)\,\gamma}$ (Barrel)	0.3	0.7	0.05	2
$\mu_{\text{Background}\,\Upsilon(3S)\,\gamma}$ (Endcap)	0.9	1	0.6	1
$\mu_{\text{Background non-resonant}}$ (Barrel)	1.1	0.10	1.1	0.10
$\mu_{\text{Background non-resonant}}$ (Endcap)	1.2	0.1	1.2	0.1
$\mu_{Z\to\Upsilon(1S)\,\gamma}$	0	0	-0.05	1
$\mu_{Z\to\Upsilon(2S)\,\gamma}$	0	0	-4	1
$\mu_{Z\to\Upsilon(3S)\,\gamma}$	0	0	2	2
$\mu_{\text{Background}\,Z\,\text{FSR}}$ (Barrel)	1.0	0.1	1	0.1
$\mu_{\text{Background}\,Z\,\text{FSR}}$ (Endcap)	0.9	0.09	0.9	0.1

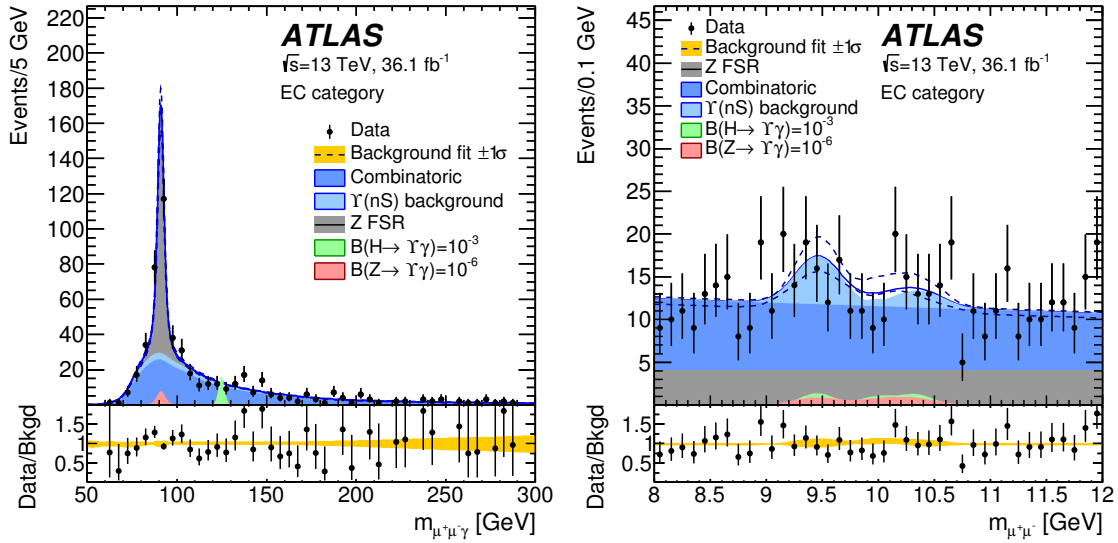

Figure 7.38: $m_{\mu^+\mu^-\gamma}$ background-only distributions in the endcap signal region for the $\Upsilon(nS)\,\gamma$ analysis, including fit results. Figure taken from Ref. [1].

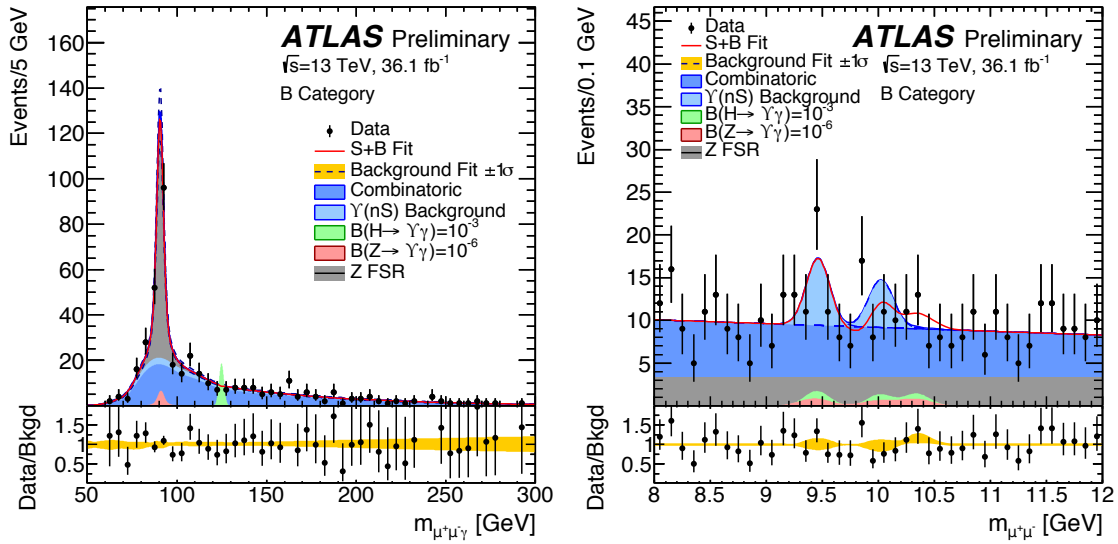

Figure 7.39: $m_{\mu^+\mu^-\gamma}$ signal+background distributions in the barrel signal region for the $\Upsilon(nS)\,\gamma$ analysis, including fit results.

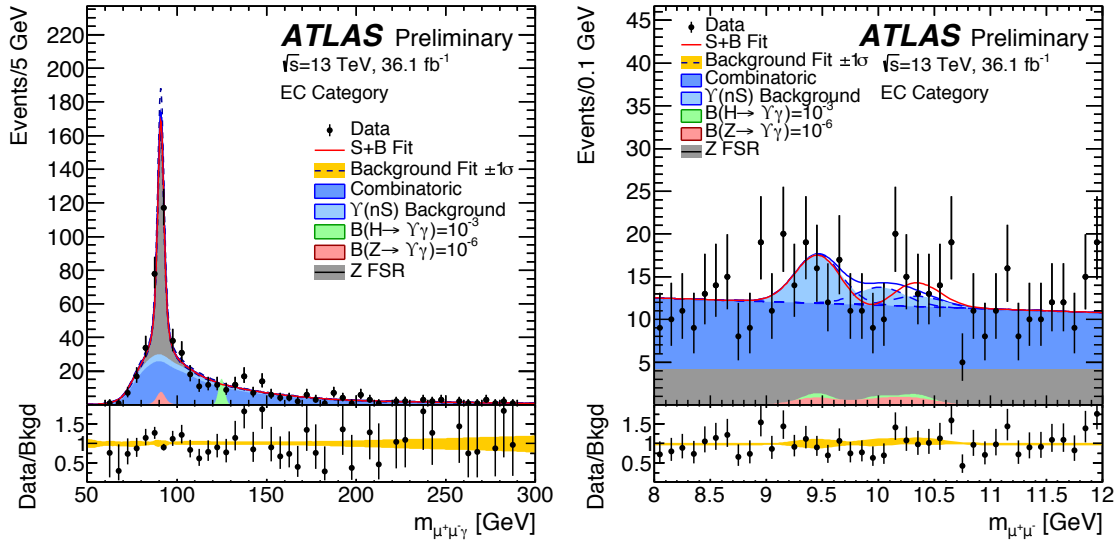

Figure 7.40: $m_{\mu^+\mu^-\gamma}$ signal+background distributions in the endcap signal region for the $\Upsilon(nS)\,\gamma$ analysis, including fit results.

Observed Limits

Using the background-only fits, the number of observed events can be compared with the expected background and to the expected Z and Higgs boson signal contributions for the assumed branching fractions. The expected and observed numbers of background events within the $m_{\mu^+\mu^-\gamma}$ ranges relevant to the Higgs and Z boson signals are shown in Table 7.14.

Table 7.14: The number of observed events and the mean expected background, with its total uncertainty, for the $m_{\mathcal{Q}\gamma}$ ranges of interest. The expected Z and Higgs boson contributions are shown for assumed branching fraction values of 10^{-6} and 10^{-3}, respectively. Table taken from Ref. [1].

$m_{\mu^+\mu^-}$ mass range [GeV]		Observed (expected background) $m_{\mu^+\mu^-\gamma}$ mass range [GeV] 81–101		120–130		Z signal for $\mathcal{B} = 10^{-6}$	H signal for $\mathcal{B} = 10^{-3}$
$J/\psi\,\gamma$	2.9–3.3	92	(89 ± 6)	20	(23.6 ± 1.3)	13.7 ± 1.1	22.2 ± 1.9
$\psi(2S)\,\gamma$	3.5–3.9	43	(42 ± 5)	8	(10.0 ± 0.8)	1.82 ± 0.14	2.96 ± 0.25
$\Upsilon(1S)\,\gamma$	9.0–10.0	115	(126 ± 8)	9	(13.6 ± 1.2)	7.8 ± 0.6	10.7 ± 0.9
$\Upsilon(2S)\,\gamma$	9.5–10.5	106	(121 ± 8)	8	(12.6 ± 1.4)	5.9 ± 0.5	8.1 ± 0.7
$\Upsilon(3S)\,\gamma$	10.0–11.0	112	(113 ± 8)	7	(10.6 ± 1.2)	7.1 ± 0.6	9.2 ± 0.8

The results from the signal-plus-background fits are summarised in Table 7.15. The observed 95% CL upper limits on the branching fractions for Higgs and Z boson decays into $J/\psi\,\gamma$ and $\psi(2S)\,\gamma$ are $(3.5, 20) \times 10^{-4}$ and $(2.3, 4.5) \times 10^{-6}$, respectively. The corresponding limits for the Higgs and Z boson decays into $\Upsilon(nS)\,\gamma$ $(n = 1, 2, 3)$ are $(4.9, 5.9, 5.7) \times 10^{-4}$ and $(2.8, 1.7, 4.8) \times 10^{-6}$, respectively. These branching fraction limits assume SM production cross sections for the Higgs and Z bosons. Since the Higgs cross section has not yet been well measured, upper limits at 95% CL on the product of the production cross section times branching fraction are determined for the Higgs boson decays, yielding 19 fb for the $H \to J/\psi\,\gamma$ decay, 110 fb for the $H \to \psi(2S)\,\gamma$ decay, and (28, 33, 32) fb for the $H \to \Upsilon(nS)\,\gamma$ $(n = 1, 2, 3)$ decays.

These upper limits improve by more than a factor of two on the $H \to J/\psi\,\gamma$ and $H \to \Upsilon(nS)\,\gamma$ branching fraction limits of 1.5×10^{-3} and $(1.3, 1.9, 1.3) \times 10^{-3}$ that were set using the $\sqrt{s} = 8$ TeV ATLAS dataset [38]. These limits remain orders of magnitude larger than the SM predicted values of the branching fractions: $\mathcal{B}(H \to$

Table 7.15: Expected and observed branching fraction upper limits at 95% CL for the $H(Z) \to J/\psi\,\gamma$, $H(Z) \to \psi(2S)\,\gamma$, and $H(Z) \to \Upsilon(nS)\,\gamma$ $(n = 1, 2, 3)$ analyses, assuming SM production for the Higgs and Z bosons. The $\pm 1\sigma$ intervals of the expected limits are also given. Table taken from Ref. [1].

Branching fraction limit (95% CL)	Expected	Observed
$\mathcal{B}(H \to J/\psi\,\gamma)\,[\,10^{-4}\,]$	$3.0^{+1.4}_{-0.8}$	3.5
$\mathcal{B}(H \to \psi\,(2S)\,\gamma)\,[\,10^{-4}\,]$	$15.6^{+7.7}_{-4.4}$	19.8
$\mathcal{B}(Z \to J/\psi\,\gamma)\,[\,10^{-6}\,]$	$1.1^{+0.5}_{-0.3}$	2.3
$\mathcal{B}(Z \to \psi\,(2S)\,\gamma)\,[\,10^{-6}\,]$	$6.0^{+2.7}_{-1.7}$	4.5
$\mathcal{B}(H \to \Upsilon(1S)\,\gamma)\,[\,10^{-4}\,]$	$5.0^{+2.4}_{-1.4}$	4.9
$\mathcal{B}(H \to \Upsilon(2S)\,\gamma)\,[\,10^{-4}\,]$	$6.2^{+3.0}_{-1.7}$	5.9
$\mathcal{B}(H \to \Upsilon(3S)\,\gamma)\,[\,10^{-4}\,]$	$5.0^{+2.5}_{-1.4}$	5.7
$\mathcal{B}(Z \to \Upsilon(1S)\,\gamma)\,[\,10^{-6}\,]$	$2.8^{+1.2}_{-0.8}$	2.8
$\mathcal{B}(Z \to \Upsilon(2S)\,\gamma)\,[\,10^{-6}\,]$	$3.8^{+1.6}_{-1.1}$	1.7
$\mathcal{B}(Z \to \Upsilon(3S)\,\gamma)\,[\,10^{-6}\,]$	$3.0^{+1.3}_{-0.8}$	4.8

$J/\psi\,\gamma) = (2.99^{+0.16}_{-0.15}) \times 10^{-6}$ [40–43], $\mathcal{B}(H \to \psi(2S)\,\gamma) = (1.03 \pm 0.06) \times 10^{-6}$ [44] and $\mathcal{B}(H \to \Upsilon(nS)\,\gamma) = (5.22^{+2.02}_{-1.70}, 1.42^{+0.72}_{-0.57}, 0.91^{+0.48}_{-0.38}) \times 10^{-9}$ [40, 41]. The upper limits for the $Z \to J/\psi\,\gamma$ and $Z \to \Upsilon(nS)\,\gamma$ branching fractions also improve on the previous limits of 2.6×10^{-6} and $(3.4, 6.5, 5.4) \times 10^{-6}$. These improvements are less dramatic, in part due to the cross-section increase with centre-of-mass energy being the same between the Z signal and the Z FSR background. They are approaching the sensitivity of the SM expectation of the values for these branching fractions, which are around 10^{-8} to 10^{-7} [45–47].

On the basis of the fits to the observed data, the largest excess observed is 2.2σ in the search for $Z \to J/\psi\,\gamma$. Table 7.16 details the significances of the observed deviations from the background-only hypothesis.

Table 7.16: Post-fit observed significances of deviations from the background-only hypotheses.

	Significance	Direction of deviation
$H \to J/\psi\,\gamma$	0.50	Up
$H \to \psi(2S)\,\gamma$	0.96	Up
$Z \to J/\psi\,\gamma$	2.2	Up
$Z \to \psi(2S)\,\gamma$	0.94	Down
$H \to \Upsilon(1S)\,\gamma$	0.03	Down
$H \to \Upsilon(2S)\,\gamma$	0.33	Down
$H \to \Upsilon(3S)\,\gamma$	0.14	Up
$Z \to \Upsilon(1S)\,\gamma$	0.04	Down
$Z \to \Upsilon(2S)\,\gamma$	2.7	Down
$Z \to \Upsilon(3S)\,\gamma$	1.4	Up

CHAPTER 8

SEARCH FOR THE HIGGS AND Z BOSON DECAYS TO $\phi\gamma$ WITH THE ATLAS DETECTOR

This chapter provides an overview of a search for the rare Higgs and Z boson decays to a ϕ meson with an associated photon. These decays are analogous to the $H(Z) \to \mathcal{Q}\gamma$ decays described in Chapters 6 and 7 and the analysis uses many of the same techniques; therefore, a general summary is given with references to the methods of the previous chapter. Some of the contents of this chapter, including figures and text, are taken from the publications, Refs. [2, 3]. The work described in this chapter was shared among an analysis team, where my primary focus was on the initial analysis development, calculation of efficiencies and production of validation plots. Section 8.6 describes an extension to the $H(Z) \to \phi\,\gamma$ analysis, with the inclusion of a separate decay of the Higgs and Z boson, to a ρ meson and an associated photon. As outlined in the Author's Contribution, this extended analysis

was mostly completed by a different member of the analysis team, whose thesis provides more details in Ref. [4].

The $H \to \phi\gamma$ decay probes the strange-quark Yukawa coupling and potentially has sensitivity to a possible deviation from the SM prediction. Prior to this analysis, no direct experimental information about the $H \to \phi\gamma$ decay mode existed. The expected SM branching fraction of this decay is $\mathcal{B}(H \to \phi\gamma) = (2.31 \pm 0.11) \times 10^{-6}$ [43]. Similarly, no constraints existed on the $Z \to \phi\gamma$ decay. The expected branching fraction is $\mathcal{B}(Z \to \phi\gamma) = (1.04 \pm 0.12) \times 10^{-8}$ [133, 134].

The decay $\phi \to K^+K^-$ is used to reconstruct the ϕ meson. In this analysis, the only signal discriminant used is the three-body mass, $m_{K^+K^-\gamma}$. The signal model distribution is determined from MC, whereas the background model comes from a data-driven non-parametric approach.

8.1 Data and Simulation Samples

The analysis is performed on the 2015 ATLAS dataset collected at $\sqrt{s} = 13$ TeV. This corresponds to an integrated luminosity of 2.7 fb^{-1} with an uncertainty of 5%, derived using the method described in Ref. [135]. The `DxAOD_HIGG2D5` derivation described in Section 6.2 is applied to the data. A different selection is required in the derivation for tracks associated with the $\phi\,\gamma$ decay:

- The event must contain two reconstructed inner detector tracks that each satisfy $p_T > 15$ GeV and which have a combined mass that is loosely consistent with that of a ϕ meson $(1020 MeV)$;
- The event must also contain one photon with $p_T^\gamma > 15$ GeV.

The same MC generation programs and methods used in the $\mathcal{Q}\gamma$ search, as described in Section 6.2, are used to generate the $\phi\gamma$ MC. The effects of the helicity of the ϕ meson on the $K^\pm$ kinematics are found to modify the acceptance by at most $\pm 1\%$,

which is corrected for in the Higgs boson case. The Z boson polarisation is less well understood and this is instead treated as a systematic uncertainty of $\pm 1\%$.

The Higgs boson production cross sections, dynamics and uncertainties were taken from Ref. [125] with the assumption of a SM Higgs boson with $m_H = 125$ GeV. The Z boson total cross section is taken from the measurement in Ref. [126].

8.2 Event Selection

8.2.1 Trigger Selection

A dedicated trigger was commissioned in September 2015, which requires an isolated photon with p_{T} greater than 35 GeV, and an isolated pair of tracks with an invariant mass, under the charged-pion hypothesis, of $200\,\mathrm{MeV} < m_{\pi^+\pi^-} < 450\,\mathrm{MeV}$, which is loosely consistent with the ϕ meson mass of 1019.5 MeV when adjusted to kaons [136]. One of the tracks must have a transverse momentum greater than 15 GeV.

The trigger efficiency for both the Higgs and Z boson signals is around 80% with respect to the full analysis selection.

8.2.2 Photon Selection

Identical photon requirements to the $H(Z) \to \mathcal{Q}\gamma$ analysis are applied, which are described in Section 6.6.2. To summarise, the photon must satisfy the "tight" photon identification criteria as outlined in Section 4.4; the transverse momentum of the photon must exceed 35 GeV; photons must be within the geometrical constraints of the ATLAS detector; and a tight photon isolation requirement is applied. These requirements are motivated by the kinematics of the photon in the decay, with the photon p_{T} shown in Figure 8.1.

8.2.3 Selection of $\phi \to K^+K^-$ Candidates

ATLAS lacks particle identification capabilities in the relevant momentum range to allow correct and consistent identification of kaons. Therefore, every charged particle satisfying the requirements described in this section is assumed to be a $K^{\pm}$ meson.

The selection requires that there are two tracks from oppositely charged particles that pass the "Loose" selection working point criteria, as outlined in Section 4.1. Both of the tracks must be within pseudorapidity $|\eta^K| < 2.5$ and have a transverse momentum greater than 15 GeV, with at least one exceeding 20 GeV. These p_{T}^K requirements are motivated in part by generator-level distributions, as shown in Figure 8.1. Track pairs with an invariant mass under the kaon hypothesis, $m_{K^+K^-}$, within ± 20 MeV of the ϕ mass are selected as $\phi \to K^+K^-$ candidates. The selected candidates have to satisfy an isolation requirement such that the scalar sum of the p_{T} of the reconstructed ID tracks from the main vertex within $\Delta R = 0.2$ of the leading track (excluding the $\phi \to K^+K^-$ tracks) is required to be less than 10% of the p_{T} of the ϕ candidate.

The ϕ candidate transverse momentum must satisfy:

$$p_T^{K^+K^-} > \begin{cases} 40 \text{ GeV}, & \text{if } m_{K^+K^-\gamma} \leq 91 \text{ GeV}, \\ 40 + 5/34 \times (m_{K^+K^-\gamma} - 91) \text{ GeV}, & \text{if } 91 \text{ GeV} < m_{K^+K^-\gamma} < 125 \text{ GeV}, \\ 45 \text{ GeV}, & \text{if } m_{K^+K^-\gamma} \geq 125 \text{ GeV}. \end{cases} \tag{8.1}$$

Using a threshold that varies linearly with three-body mass allows the analysis to be sensitive for both the Higgs and Z boson searches. The $p_{\mathrm{T}}^{K^+K^-}$ distributions for the two searches are shown in Figure 8.1.

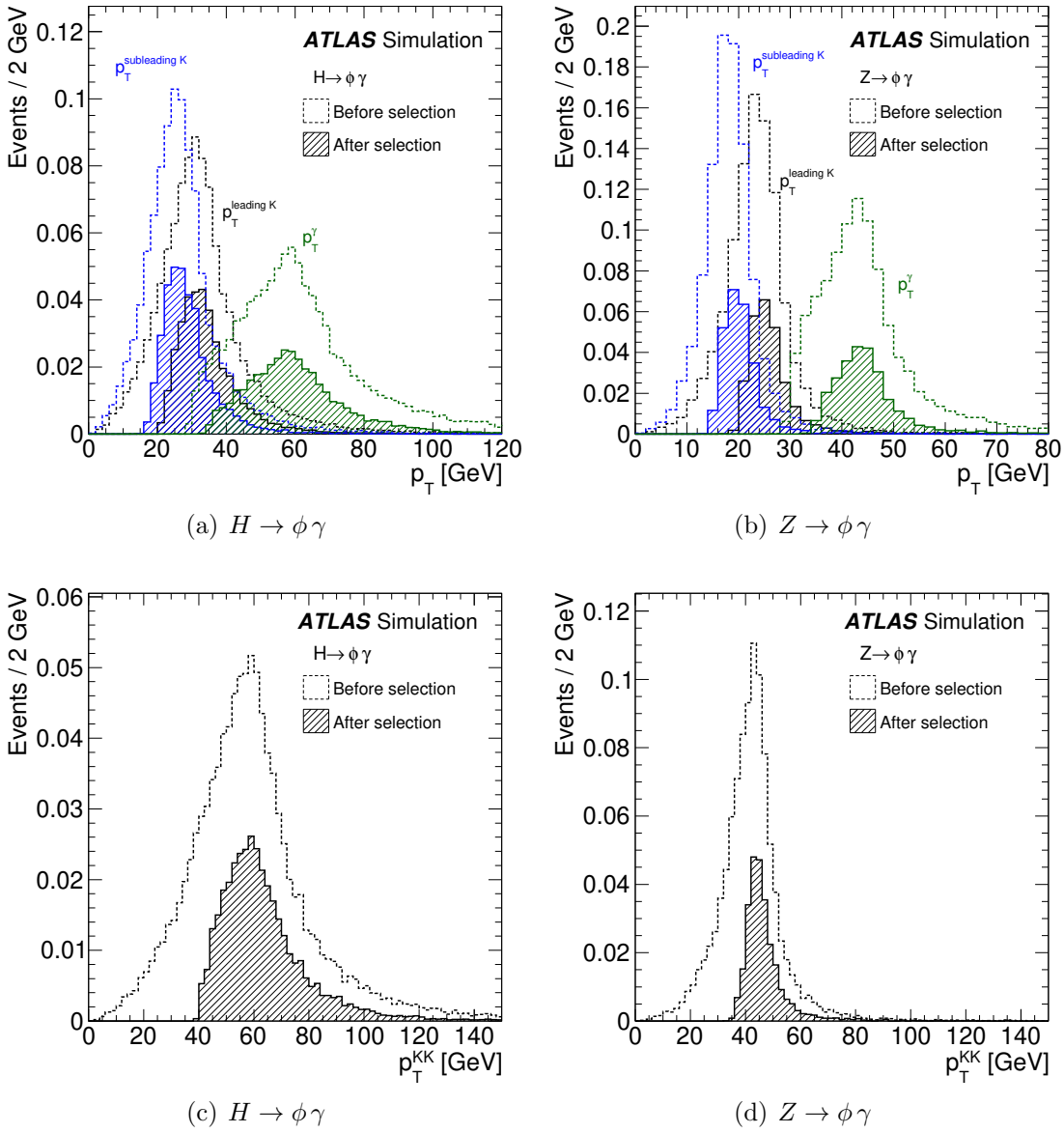

(a) $H \to \phi\gamma$ (b) $Z \to \phi\gamma$

(c) $H \to \phi\gamma$ (d) $Z \to \phi\gamma$

Figure 8.1: Generator-level p_{T} distributions of the photon and of the muons, ordered in p_{T}, for (a) $H \to \phi\gamma$ and (b) $Z \to \phi\gamma$ simulated signal events, respectively. Distributions of di-muon p_{T} are also shown for the (a) $H \to \phi\gamma$ and (b) $Z \to \phi\gamma$ simulated signal events, respectively. The hatched histograms denote the full event selection while the dashed histograms show the events at generator level that fall within the analysis geometric acceptance (both kaons are required to have $|\eta^K| < 2.5$ while the photon is required to have $|\eta^\gamma| < 2.37$, excluding the region $1.37 < |\eta^\gamma| < 1.52$). The dashed histograms are normalised to unity, and the relative difference between the two sets of distributions corresponds to the effects of reconstruction, trigger, and event selection efficiencies. Figure taken from Ref. [3].

8.2.4 Selection of $H(Z) \to \phi\gamma \to K^+K^-\gamma$ candidates

The azimuthal angle between the photon candidate and the $\phi \to K^+K^-$ candidate must satisfy $\Delta\phi(K^+K^-, \gamma) > 0.5$. In the rare cases where there is more than one $\phi \to K^+K^-$ or photon candidate within the same event that satisfy the criteria above, then the highest p_{T} photon is chosen and the ϕ candidate closest to the measured ϕ mass is chosen.

In an analogous manner to the $\mathcal{Q}\gamma$ analysis, different selection regions are defined for construction of the background, for validation of the background and for the final selection. The final baseline selection, comprising the requirements summarised above, is defined as the SR. A looser selection, which excludes the requirements on di-track p_{T} and on the photon and di-track isolations, is defined as the GR. Three further validation regions are also defined: VR1 uses GR with the inclusion of the di-track p_{T} requirement; VR2 uses GR with the inclusion of the photon isolation; and VR3 uses GR with the inclusion of the di-track isolation.

No further categorisation is used in this analysis. Using the signal MC sample, the total signal efficiencies are calculated to be 18% and 8% for the Higgs and Z boson decays, respectively.

8.3 Signal Model

The signal model is determined using simulated MC events. The MC samples are passed through the analysis selection and then the $m_{K^+K^-\gamma}$ distribution is fitted with analytical functions to best match the simulated shape. For the Higgs decay the sum of two Gaussians with a common mean is used, while for the Z decay a Voigtian function is used. The corresponding plots are shown in Figure 8.2. The $m_{K^+K^-\gamma}$ resolution is around 1.8% for both the Higgs and Z boson decays.

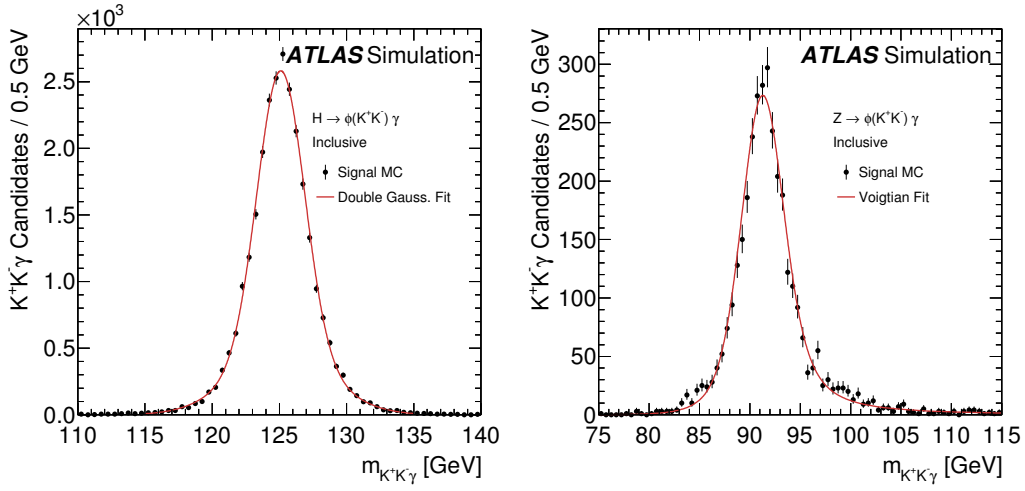

(a) (b)

Figure 8.2: $m_{K^+K^-\gamma}$ invariant mass distributions for (a) $H \to \phi\gamma$ and (b) $Z \to \phi\gamma$ simulated signal events after the analysis selection. Figure taken from Ref. [3].

8.4 Background Model

The main source of inclusive background events is from dijet production and photon + jet production, where a ϕ meson candidate is reconstructed from a pair of tracks within a jet. This background cannot be reliably modelled with MC simulation, due to the complicated mixture of the contributing processes. Instead, this component of the background is modelled using a data-driven approach similar to that used in the $H(Z) \to \mathcal{Q}\gamma$ analysis described in the previous chapter.

A sample of around 4000 GR data events was used to build the background model with the kinematic variables and their important correlations used to replicate the background distributions. The $m_{K^+K^-\gamma}$ distribution corresponding to the GR data events with the background template normalised to the GR dataset, is shown in Figure 8.6.

The contribution of exclusive backgrounds from $Z \to \ell\ell\gamma$ decays has been studied and found to be negligible after the full event selection.

Four other models are used to estimate the systematic uncertainty on the inclusive

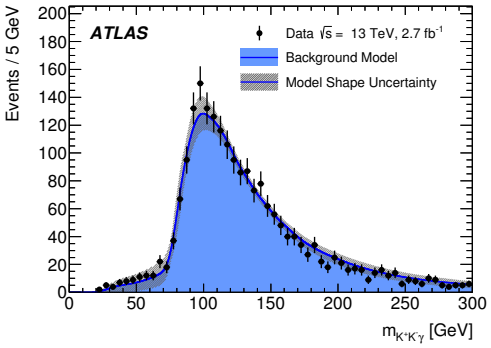

Figure 8.3: The $m_{K^+K^-\gamma}$ distribution of selected candidates passing the GR selection requirements with the background model template normalised to the dataset. Figure taken from Ref. [3].

background model. Each modification is motivated by the kinematic distributions of the data in the GR selection. The first model is distorted by shifting the di-track p_{T} distributions by ± 5 GeV when generating the background events. The second model uses a distortion of the $\Delta\phi(K^+K^-,\gamma)$ distribution by re-weighting the distribution with a factor proportional to its value of $\Delta\phi$. The third model is built by neglecting the weakest correlation between two variables in the background model. The fourth model is derived from the data/model ratio in the VR2 region ("tilt"), where there is a small discrepancy between the data and the model. These four alternatives can account for any expected variations that might occur in the data relative to the model. Figure 8.4 shows the $m_{K^+K^-\gamma}$ distribution in the data compared to the background model and alternative background models, used to assess systematic uncertainties.

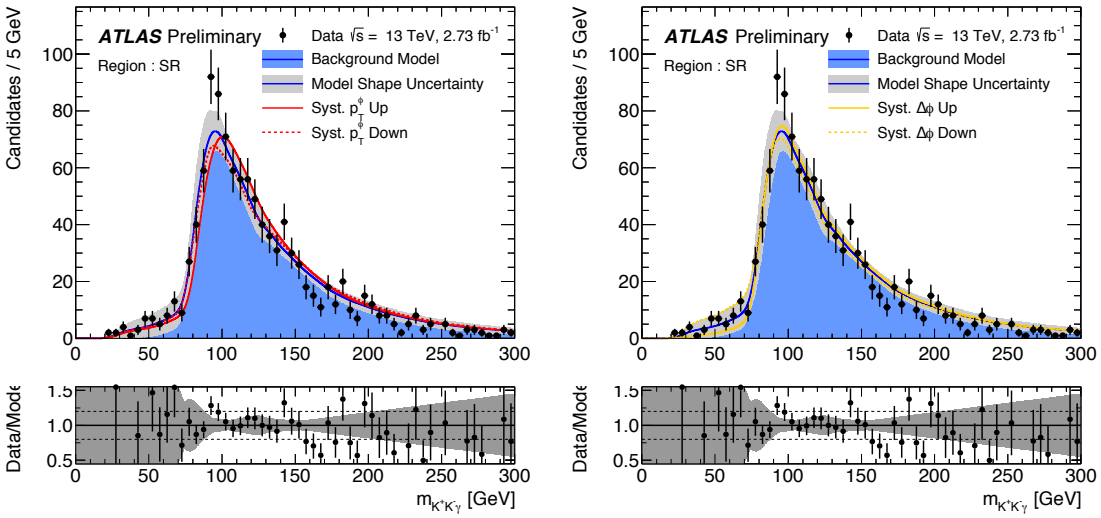

(a)

(b)

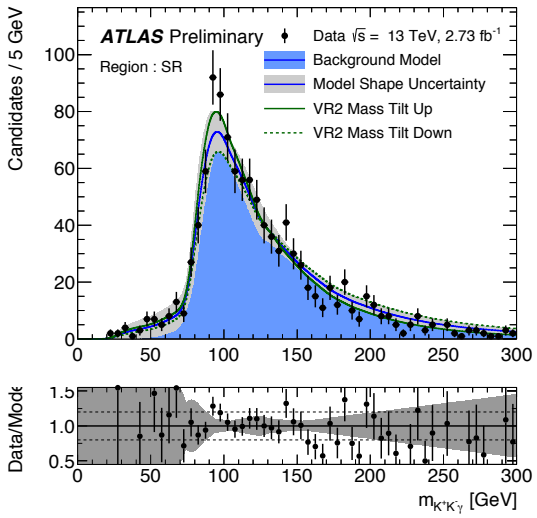

(c)

Figure 8.4: The distribution of $m_{K^+K^-\gamma}$ in data compared to the prediction of the background model. The ratio between data and background model is also shown. The alternative background models associated with variations in the (a) $p_{\mathrm{T}}^{K^+K^-}$ and (b) $\Delta\phi(\phi\gamma)$ distributions used to build the model are also shown in addition to the (c) "tilt" systematic uncertainty derived from VR2. The distributions are shown for the SR region. The alternative distribution for the removal of the weakest correlation is not included due to the variation relative to the nominal background model being small.

8.5 Results

Once the analysis was frozen, the dataset was unblinded. The $m_{K^+K^-}$ distribution is shown in Figure 8.6 after the full analysis selection has been applied, but with the di-track mass requirement loosened. Real ϕ mesons are detected giving rise to the observed peak.

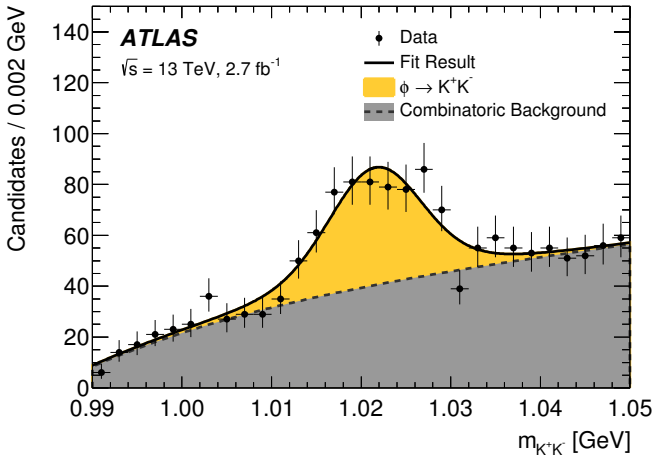

Figure 8.5: The $m_{K^+K^-}$ distribution of selected $\phi\gamma$ combinations after the complete event selection has been applied, apart from the requirement on $m_{K^+K^-}$. The data are fitted with the convolution of a Breit-Wigner distribution, using the ϕ width, and a Gaussian distribution to represent the experimental resolution. The background is modelled with an analytical function, commonly used to describe a kinematic threshold [137]. Figure taken from Ref. [3].

The expected background and observed numbers of events within the $m_{K^+K^-\gamma}$ ranges relevant to the Higgs and Z boson signals are shown in Table 8.1, as well as the expected signals assuming branching fraction values of 10^{-3} and 10^{-6}, respectively. These branching fractions are believed to represent the approximate sensitivity of the analysis and, therefore, to provide a reasonable magnitude to compare with the expected and observed background events.

Systematic uncertainties are estimated and considered in a similar manner to the $H(Z) \to \psi(kS)\,\gamma$ and $H(Z) \to \Upsilon(nS)\,\gamma$ analyses. Uncertainties pertaining to photon identification, reconstruction and triggering are calculated using the methods described in Section 7.5. An uncertainty of 6% is assigned to the track reconstruc-

Table 8.1: The numbers of observed events and the expected background yields for the two $m_{K^+K^-\gamma}$ ranges of interest. The Higgs and Z boson contributions expected for branching fraction values of 10^{-3} and 10^{-6}, respectively, estimated using Monte Carlo simulations, are also shown. Table taken from Ref. [3].

Observed (Expected background) yields			Expected signal yields	
$m_{K^+K^-\gamma}$ mass range [GeV]			Z	H
All	81–101	120–130	$\mathcal{B}[10^{-6}]$	$\mathcal{B}[10^{-3}]$
1065	288 (266 ± 9)	89 (87 ± 3)	6.7 ± 0.7	13.5 ± 1.5

tion efficiency, based on the material in the ID and the behaviour of the track reconstruction algorithm if a nearby track is present.

An unbinned maximum-likelihood fit is performed to the $m_{K^+K^-\gamma}$ distribution using the background and signal model distributions. Expected 95% CL limits are obtained from the observed data in the SR region. The result of a background-only fit is shown in Figure 8.6; a small excess of two standard deviations is observed in the Z boson mass region, estimated using the asymptotic approximation for the distribution of the test statistic [119]. The results are summarised in Table 8.2. These results correspond to being around 600 and 700 times the expected SM branching fractions for the $H \to \phi\gamma$ and $Z \to \phi\gamma$ decays, respectively. The systematic uncertainties result in a deterioration of the sensitivity to the $H \to \phi\,\gamma$ and $Z \to \phi\,\gamma$ decays by about 3% and 13%, respectively.

Table 8.2: Expected and observed branching fraction limits at 95% CL for 2.7 fb^{-1} of pp collision data at $\sqrt{s} = 13$ TeV. The $\pm 1\sigma$ intervals of the expected limits are also given. Table taken from Ref. [3].

Branching Fraction Limit (95% CL)	Expected	Observed
$\mathcal{B}(H \to \phi\,\gamma)$ [10^{-3}]	$1.5^{+0.7}_{-0.4}$	1.4
$\mathcal{B}(Z \to \phi\,\gamma)$ [10^{-6}]	$4.4^{+2.0}_{-1.2}$	8.3

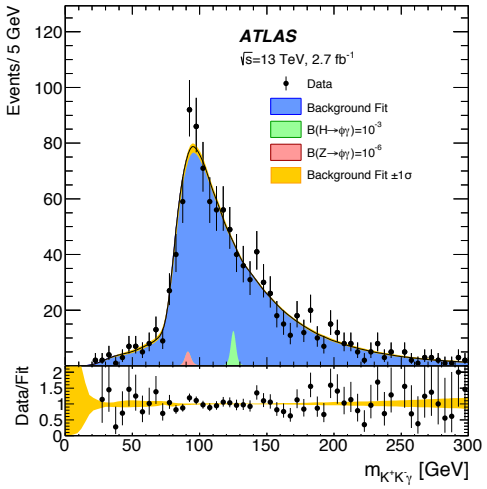

Figure 8.6: The $m_{K^+K^-\gamma}$ distribution of the selected $\phi\,\gamma$ candidates, along with the results of the maximum-likelihood fit with a background-only model. The Higgs and Z boson contributions, expected for branching fraction values of 10^{-3} and 10^{-6}, respectively, are also shown. The ratio of data to the background fit is shown in the lower plot. Figure taken from Ref. [3].

8.6 Extended $H(Z) \to \phi\gamma$ and $H(Z) \to \rho\gamma$ Searches

The $H(Z) \to \phi\gamma$ analysis described in the earlier sections of this chapter was only performed on the ATLAS dataset collected in 2015. The analysis was extended by including the 2016 ATLAS dataset, as well as the addition of a further channel, the $H(Z) \to \rho\gamma$ decay, which probes the Higgs couplings to the u and d quarks. This section briefly summarises these extended analyses.

The predicted SM branching fractions for the $H(Z) \to \rho\gamma$ decays have been calculated to be $\mathcal{B}(H \to \rho\gamma) = (1.68 \pm 0.08) \times 10^{-5}$ [43] and $\mathcal{B}(Z \to \rho\gamma) = (4.19 \pm 0.47) \times 10^{-8}$ [134].

The ϕ mesons identified in this analysis are reconstructed from their decays into K^+K^-, whereas the ρ mesons are reconstructed from their decays into $\pi^+\pi^-$. The same $H(Z) \to \phi\gamma$ trigger as described in Section 8.2.1 was used for the 2015 data. For the 2016 data the trigger requirement was improved by applying the charged kaon particle hypothesis to the tracks (instead of the charged pion hypothesis used in 2015), which allows a tighter di-track mass cut to be applied around the known

ϕ mass. The corresponding trigger for the $H(Z) \to \rho\gamma$ analysis was introduced in May 2016 and used the pion mass hypothesis for the di-track mass.

The $m_{M\gamma}$ distributions of the signal and background predictions are compared to the data using an unbinned maximum-likelihoood fit. The results of the background-only fits for the $\phi\gamma$ and $\rho\gamma$ analyses are shown in Figures 8.7(a) and 8.7(b), respectively.

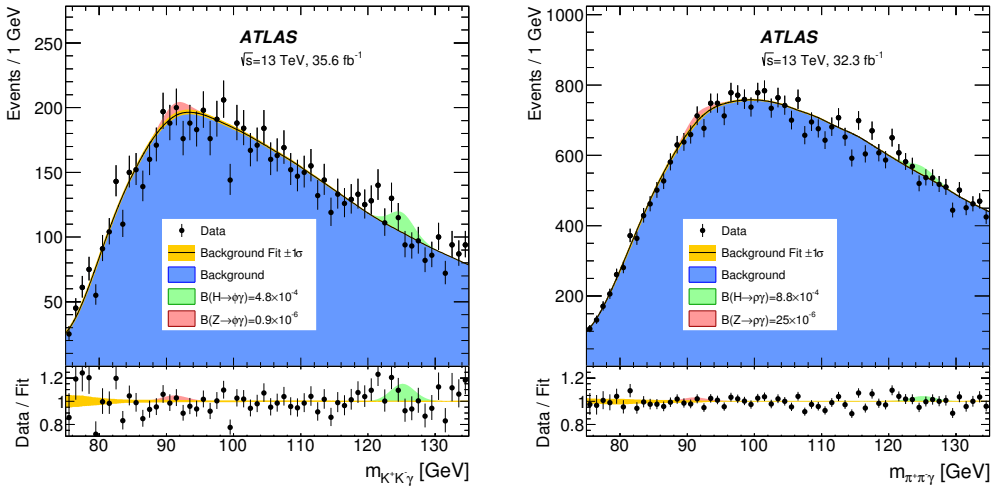

(a) (b)

Figure 8.7: The (a) $m_{K^+K^-\gamma}$ and (b) $m_{\pi^+\pi^-\gamma}$ distributions of the selected $\phi\gamma$ and $\rho\gamma$ candidates, respectively, along with the results of the maximum-likelihood fits using a background-only model. The Higgs and Z boson contributions for the branching fraction values corresponding to the observed 95% CL upper limits are also shown. Below the figures the ratio of the data to the background-only fit is shown. Figure taken from Ref. [2].

Upper limits are set on the branching fractions for the Higgs and Z boson decays into $M\,\gamma$ using the same fitting procedure as for the 2015 $H(Z) \to \phi\gamma$ analysis. The results are summarised in Table 8.3. The observed 95% CL upper limits on the branching fractions for $H \to \phi\gamma$ and $Z \to \phi\gamma$ decays are 208 and 87 times the expected SM branching fractions, respectively.

Table 8.3: Expected and observed branching fraction upper limits at 95% CL for the $\phi\gamma$ and $\rho\gamma$ analyses. The $\pm 1\sigma$ intervals of the expected limits are also given. Table taken from Ref. [2].

Branching Fraction Limit (95% CL)	Expected	Observed
$\mathcal{B}(H \to \phi\gamma)\,[\,10^{-4}\,]$	$4.2^{+1.8}_{-1.2}$	4.8
$\mathcal{B}(Z \to \phi\gamma)\,[\,10^{-6}\,]$	$1.3^{+0.6}_{-0.4}$	0.9
$\mathcal{B}(H \to \rho\gamma)\,[\,10^{-4}\,]$	$8.4^{+4.1}_{-2.4}$	8.8
$\mathcal{B}(Z \to \rho\gamma)\,[\,10^{-6}\,]$	33^{+13}_{-9}	25

CHAPTER 9

CONCLUSION

The discovery of the Higgs boson by the ATLAS and CMS collaborations in 2012 has opened a whole new spectrum of particle physics measurements aiming to test the Standard Model. Being highly sensitive to new physics, a programme of precision measurements of Higgs properties and couplings to other particles is in progress. Each year of data-taking yields new constraints on many of the key interactions of the Higgs boson. One property that has, so far, only been observed in a few channels, is the Higgs boson coupling to fermions. In particular, measuring the Higgs boson coupling to quarks is challenging due to the large background rate in the LHC and only recently has the preferred $H \to b\bar{b}$ decay mode been observed [25, 26].

A promising avenue to probe the Higgs boson coupling to quarks, whilst avoiding the large hadronic background, is to perform searches for the Higgs boson decaying into a meson and an associated photon. This decay provides a distinct topology that requires stringent selection requirements, which minimise the background contribution. For these decays, the predicted SM branching fractions are small and would

yield no observable signal at the sensitivity of current data. However, new physics has the potential to result in large increases in the decay rates, to which analyses with the current dataset could be sensitive.

This thesis outlines a number of searches for the Higgs boson decaying exclusively into a meson with an associated photon. No significant fluctuations were observed and 95% confidence level limits were set on the branching fractions. The latest search (described in Chapters 6 and 7) was performed using the decays $H \to J/\psi\,\gamma$, $H \to \psi(2S)\,\gamma$ and $H \to \Upsilon(nS)\,\gamma$, which yielded limits of 3.5×10^{-4}, 2.0×10^{-3} and $(4.9, 5.9, 5.7) \times 10^{-4}$ $(n = 1, 2, 3)$, respectively, assuming Standard Model Higgs production. A search for the decay $H \to \phi\,\gamma$ using 2.7 fb^{-1}of $\sqrt{s}$= 13 TeV ATLAS data is also presented in Chapter 8, which obtained a limit of 1.4×10^{-3} assuming Standard Model Higgs production. This $\phi\,\gamma$ search was superseded by an analysis using up to 35.6 fb^{-1}of the $\sqrt{s}$= 13 TeV dataset, with an additional search for the $H \to \rho\,\gamma$ decay, yielding limits of 4.8×10^{-4} and 8.8×10^{-4}, respectively. All of these searches set 95% confidence level branching fraction limits that are orders of magnitude greater than the SM predictions.

Similarly, 95% confidence level limits were set on branching fractions of Z boson decays to a meson and an associated photon using the same dataset as for the Higgs boson decays. For the decays into $J/\psi\,\gamma$, $\psi(2S)\,\gamma$, $\Upsilon(nS)\,\gamma$, $\phi\,\gamma$ and $\rho\,\gamma$ the searches yielded limits of 2.3×10^{-6}, 4.5×10^{-6}, $(2.8, 1.7, 4.8) \times 10^{-6}$, 0.6×10^{-6} and 25×10^{-6}, respectively.

The current ambition of the LHC is to enter a so-called "High Luminosity" era, in which the aim will be to collect a dataset with an integrated luminosity of 3000 fb^{-1}. Such an increase in luminosity will require major upgrades to the LHC and to the ATLAS detector. The ATLAS Inner Detector will undergo one of the biggest improvements, with an all-new silicon detector, which will provide higher precision measurements in a more intense radiation environment. In preparation for this upgrade, a consortium of facilities are irradiating prototype silicon sensors, to test their irradiation hardness up to the dosage level expected over the lifetime of the

high-luminosity LHC. The University of Birmingham is one of the facilities equipped to irradiate sensors in the Medical Cyclotron, as well as to test the performance of the sensors before and after irradiation using an ALiBaVa system. Some results from the early stages of this programme are shown in Chapter 5.

Should the high-luminosity era be successful, the searches described in this thesis will be performed on the full 3000 fb^{-1} dataset, where the sensitivity of the analyses will be much closer to the expected SM branching fractions. For instance, the $H \to J/\psi\,\gamma$ analysis expects to reach a sensitivity of around 15 times the Standard Model expectation [138]. The Higgs boson couplings to charm and light quarks could be constrained to levels unobtainable using direct measurements and exclude many models of new physics.

REFERENCES

[1] ATLAS Collaboration, *Searches for exclusive Higgs and Z boson decays into $J/\psi\gamma$, $\psi(2S)\gamma$, and $\Upsilon(nS)\gamma$ at $\sqrt{s} = 13$ TeV with the ATLAS detector*, Phys. Lett. **B786** (2018) 134, arXiv: 1807.00802 [hep-ex].

[2] ATLAS Collaboration, *Search for exclusive Higgs and Z boson decays to $\phi\gamma$ and $\rho\gamma$ with the ATLAS detector*, JHEP **07** (2018) 127, arXiv: 1712.02758 [hep-ex].

[3] ATLAS Collaboration, *Search for Higgs and Z boson decays to $\phi\,\gamma$ with the ATLAS Detector*, Phys. Rev. Lett. **117** (2016) 111802, arXiv: 1607.03400 [hep-ex].

[4] Rhys Owen, *Search for Rare Exclusive Decays of the Higgs and Z Bosons to a Meson and a Photon with the ATLAS Detector*, http://www.ep.ph.bham.ac.uk/publications/thesis/ro_thesis.pdf, Accessed: 2018-09-04, 2017.

[5] ATLAS Collaboration, *Observation of a new particle in the search for the Standard Model Higgs boson with the ATLAS detector at the LHC*, Phys. Lett. B **716** (2012) 1, arXiv: 1207.7214 [hep-ex].

[6] CMS Collaboration, *Observation of a new boson at a mass of 125 GeV with the CMS experiment at the LHC*, Phys. Lett. B **716** (2012) 30, arXiv: 1207.7235 [hep-ex].

[7] F. Englert and R. Brout, *Broken Symmetry and the Mass of Gauge Vector Mesons*, Phys. Rev. Lett. **13** (9 1964) 321, URL: https://link.aps.org/doi/10.1103/PhysRevLett.13.321.

[8] Peter W. Higgs, *Broken Symmetries and the Masses of Gauge Bosons*, Phys. Rev. Lett. **13** (16 1964) 508, URL: https://link.aps.org/doi/10.1103/PhysRevLett.13.508.

[9] G. S. Guralnik, C. R. Hagen, and T. W. B. Kibble,
Global Conservation Laws and Massless Particles,
Phys. Rev. Lett. **13** (20 1964) 585,
URL: https://link.aps.org/doi/10.1103/PhysRevLett.13.585.

[10] W. M. Yao et al., *Particle Data Group*, Phys. Rev. D **86** (2012),
URL: http://pdg.lbl.gov.

[11] Alexandre Deur, Stanley J. Brodsky, and Guy F. de Teramond,
The QCD Running Coupling, Prog. Part. Nucl. Phys. **90** (2016) 1,
arXiv: 1604.08082 [hep-ph].

[12] John C. Collins, Davison E. Soper, and George F. Sterman,
Factorization of Hard Processes in QCD,
Adv. Ser. Direct. High Energy Phys. **5** (1989) 1,
arXiv: hep-ph/0409313 [hep-ph].

[13] Rupert Millard, *Mexican hat potential polar*,
https://upload.wikimedia.org/wikipedia/commons/thumb/7/7b/Mexican_hat_potential_polar.svg/2000px-Mexican_hat_potential_polar.svg.png, Accessed: 2018-08-09, 2009.

[14] D. de Florian et al., *Handbook of LHC Higgs Cross Sections: 4. Deciphering the Nature of the Higgs Sector*, (2016), arXiv: 1610.07922 [hep-ph].

[15] ATLAS Collaboration, *Combined measurement of differential and total cross sections in the $H \to \gamma\gamma$ and the $H \to ZZ^* \to 4\ell$ decay channels at $\sqrt{s} = 13$ TeV with the ATLAS detector*, (2018),
arXiv: 1805.10197 [hep-ex].

[16] ATLAS Collaboration,
Measurement of the Higgs boson mass in the $H \to ZZ^* \to 4\ell$ and $H \to \gamma\gamma$ channels with $\sqrt{s} = 13$ TeV pp collisions using the ATLAS detector,
Phys. Lett. **B784** (2018) 345, arXiv: 1806.00242 [hep-ex].

[17] ATLAS and CMS Collaborations,
Combined Measurement of the Higgs Boson Mass in pp Collisions at $\sqrt{s} = 7$ and 8 TeV with the ATLAS and CMS Experiments,
Phys. Rev. Lett. **114** (2015) 191803, arXiv: 1503.07589 [hep-ex].

[18] CMS Collaboration, *Measurements of properties of the Higgs boson decaying into the four-lepton final state in pp collisions at $\sqrt{s} = 13$ TeV*,
JHEP **11** (2017) 047, arXiv: 1706.09936 [hep-ex].

[19] CMS Collaboration, *Measurements of Higgs boson properties in the diphoton decay channel in proton-proton collisions at $\sqrt{s} = 13$ TeV*,
(2018), Submitted to JHEP, arXiv: 1804.02716 [hep-ex].

[20] ATLAS and CMS Collaborations,
Measurements of the Higgs boson production and decay rates and constraints on its couplings from a combined ATLAS and CMS analysis of the LHC pp collision data at $\sqrt{s} = 7$ and 8 TeV, JHEP **08** (2016) 045,
arXiv: 1606.02266 [hep-ex].

[21] ATLAS Collaboration, *Evidence for the Higgs-boson Yukawa coupling to tau leptons with the ATLAS detector*, JHEP **04** (2015) 117, arXiv: 1501.04943 [hep-ex].

[22] CMS Collaboration, *Evidence for the* 125 *GeV Higgs boson decaying to a pair of* τ *leptons*, JHEP **05** (2014) 104, arXiv: 1401.5041 [hep-ex].

[23] CMS Collaboration, *Observation of* $\mathrm{t\bar{t}}H$ *production*, Phys. Rev. Lett. **120** (23 2018) 231801, URL: https://link.aps.org/doi/10.1103/PhysRevLett.120.231801.

[24] ATLAS Collaboration, *Evidence for the associated production of the Higgs boson and a top quark pair with the ATLAS detector*, Phys. Rev. **D97** (2018) 072003, arXiv: 1712.08891 [hep-ex].

[25] ATLAS Collaboration, *Observation of* $H \to b\bar{b}$ *decays and* VH *production with the ATLAS detector*, Phys. Lett. **B786** (2018) 59, arXiv: 1808.08238 [hep-ex].

[26] A. M. Sirunyan et al., *Observation of Higgs boson decay to bottom quarks*, Phys. Rev. Lett. **121** (2018) 121801, arXiv: 1808.08242 [hep-ex].

[27] ATLAS Collaboration, *Performance of b-Jet Identification in the ATLAS Experiment*, JINST **11** (2016) P04008, arXiv: 1512.01094 [hep-ex].

[28] ATLAS Collaboration, *Search for the Decay of the Higgs Boson to Charm Quarks with the ATLAS Experiment*, Phys. Rev. Lett. **120** (21 2018) 211802.

[29] ATLAS Collaboration, *Search for the dimuon decay of the Higgs boson in* pp *collisions at* $\sqrt{s} = 13$ *TeV with the ATLAS detector*, Phys. Rev. Lett. **119** (2017) 051802, arXiv: 1705.04582 [hep-ex].

[30] ATLAS Collaboration, *Search for the standard model Higgs boson decay to* $\mu^+\mu^-$ *with the ATLAS detector*, Phys. Lett. **B738** (2014) 68, arXiv: 1406.7663 [hep-ex].

[31] CMS Collaboration, *Search for a standard model-like Higgs boson in the* $\mu^+\mu^-$ *and* e^+e^- *decay channels at the LHC*, Phys. Lett. **B744** (2015) 184, arXiv: 1410.6679 [hep-ex].

[32] Gilad Perez et al., *Constraining the charm Yukawa and Higgs-quark coupling universality*, Phys. Rev. **D92** (2015) 033016, arXiv: 1503.00290 [hep-ph].

[33] G. D'Ambrosio et al., *Minimal flavor violation: an effective field theory approach*, Nucl. Phys. **B645** (2002) 155, arXiv: hep-ph/0207036.

[34] C. D. Froggatt and Holger Bech Nielsen, *Hierarchy of quark masses, Cabibbo angles and CP violation*, Nucl. Phys. **B147** (1979) 277.

[35] Gian F. Giudice and Oleg Lebedev, *Higgs-dependent Yukawa couplings*, Phys. Lett. B **665** (2008) 79, arXiv: 0804.1753 [hep-ph].

[36] Lisa Randall and Raman Sundrum, *Large mass hierarchy from a small extra dimension*, Phys. Rev. Lett. **83** (1999) 3370, arXiv: hep-ph/9905221.

[37] Michael J. Dugan, Howard Georgi, and David B. Kaplan, *Anatomy of a composite Higgs model*, Nucl. Phys. **B254** (1985) 299.

[38] ATLAS Collaboration, *Search for Higgs and Z boson decays to $J/\psi\,\gamma$ and $\Upsilon(nS)\,\gamma$ with the ATLAS detector*, Phys. Rev. Lett. **114** (2015) 121801, arXiv: 1501.03276 [hep-ex].

[39] CMS Collaboration, *Search for a Higgs boson decaying into $\gamma^*\gamma \to \ell\ell\gamma$ with low dilepton mass in pp collisions at $\sqrt{s} = 8$ TeV*, Phys. Lett. **B753** (2016) 341, arXiv: 1507.03031 [hep-ex].

[40] Geoffrey T. Bodwin et al., *Addendum: New approach to the resummation of logarithms in Higgs-boson decays to a vector quarkonium plus a photon*, Phys. Rev. **D96** (2017) 116014, arXiv: 1710.09872 [hep-ph].

[41] Geoffrey T. Bodwin et al., *New approach to the resummation of logarithms in Higgs-boson decays to a vector quarkonium plus a photon*, Phys. Rev. **D95** (2017) 054018, arXiv: 1603.06793 [hep-ph].

[42] Geoffrey T. Bodwin et al., *Relativistic corrections to Higgs-boson decays to quarkonia*, Phys. Rev. D **90** (2014) 113010, arXiv: 1407.6695 [hep-ph].

[43] Matthias König and Matthias Neubert, *Exclusive radiative Higgs decays as probes of light-quark Yukawa couplings*, JHEP **08** (2015) 012, arXiv: 1505.03870 [hep-ph].

[44] Geoffrey T. Bodwin et al., private communication.

[45] Geoffrey T. Bodwin et al., *Z-boson decays to a vector quarkonium plus a photon*, Phys. Rev. **D97** (2018) 016009, arXiv: 1709.09320 [hep-ph].

[46] Yuval Grossman, Matthias König, and Matthias Neubert, *Exclusive radiative decays of W and Z bosons in QCD factorization*, JHEP **04** (2015) 101, arXiv: 1501.06569 [hep-ph].

[47] Ting-Chung Huang and Frank Petriello, *Rare exclusive decays of the Z-boson revisited*, Phys. Rev. **D92** (2015) 014007.

[48] Lyndon Evans and Philip Bryant, *LHC Machine*, JINST **3** (2008) S08001.

[49] ATLAS Collaboration, *ATLAS Public Results*, https://twiki.cern.ch/twiki/bin/view/AtlasPublic, Accessed: Thursday 8th November, 2018.

[50] ATLAS Collaboration,
The ATLAS Experiment at the CERN Large Hadron Collider,
JINST **3** (2008) S08003,
URL: http://stacks.iop.org/1748-0221/3/i=08/a=S08003.

[51] ATLAS Collaboration, *Expected Performance of the ATLAS Experiment - Detector, Trigger and Physics*, (2009), arXiv: 0901.0512 [hep-ex].

[52] Alessandro La Rosa,
The ATLAS Insertable B-Layer: from construction to operation,
JINST **11** (2016) C12036, arXiv: 1610.01994 [physics.ins-det].

[53] ATLAS Collaboration, https://atlas.web.cern.ch/Atlas/GROUPS/PHYSICS/PLOTS/IDTR-2015-007/.

[54] Joao Pequenao, *Computer generated image of the ATLAS calorimeter*, http://cds.cern.ch/record/1095927, Accessed: 2018-09-05, 2008.

[55] ATLAS Collaboration, *Topological cell clustering in the ATLAS calorimeters and its performance in LHC Run 1*,
Eur. Phys. J. **C77** (2017) 490, arXiv: 1603.02934 [hep-ex].

[56] ATLAS Collaboration,
Commissioning of the ATLAS Muon Spectrometer with cosmic rays,
The European Physical Journal C **70** (2010) 875,
URL: https://doi.org/10.1140/epjc/s10052-010-1415-2.

[57] ATLAS Collaboration, *ATLAS Forward Detectors for Measurement of Elastic Scattering and Luminosity*, Technical Design Report ATLAS (2008),
URL: http://cds.cern.ch/record/1095847.

[58] ATLAS Collaboration, *The new LUCID-2 detector for luminosity measurement and monitoring in ATLAS*,
Journal of Instrumentation **13** (2018) P07017,
URL: http://stacks.iop.org/1748-0221/13/i=07/a=P07017.

[59] ATLAS Collaboration, *The Run-2 ATLAS Trigger System*,
Journal of Physics: Conference Series **762** (2016) 012003,
URL: http://stacks.iop.org/1742-6596/762/i=1/a=012003.

[60] S. Agostinelli et al., *GEANT4: a simulation toolkit*,
Nucl. Instrum. Meth. **A 506** (2003) 250.

[61] ATLAS Collaboration, *The ATLAS simulation infrastructure*,
Eur. Phys. J. **C70** (2010) 823, arXiv: 1005.4568 [physics.ins-det].

[62] ATLAS Collaboration, *Performance of the ATLAS Track Reconstruction Algorithms in Dense Environments in LHC Run 2*,
Eur. Phys. J. **C77** (2017) 673, arXiv: 1704.07983 [hep-ex].

[63] T Cornelissen, M Elsing, I Gavrilenko, W Liebig, E Moyse and A Salzburger, *The new ATLAS track reconstruction (NEWT)*,
Journal of Physics: Conference Series **119** (2008) 032014,
URL: http://stacks.iop.org/1742-6596/119/i=3/a=032014.

[64] ATLAS Collaboration, *Muon reconstruction performance of the ATLAS detector in proton proton collision data at $\sqrt{s}$ =13 TeV*, Eur. Phys. J. **C76** (2016) 292, arXiv: 1603.05598 [hep-ex].

[65] Luigi Marchese, *Muon reconstruction performance of the ATLAS detector in 2016*, tech. rep. ATL-PHYS-PROC-2017-246, CERN, 2017, URL: https://cds.cern.ch/record/2292925.

[66] ATLAS Collaboration, *Electron efficiency measurements with the ATLAS detector using the 2015 LHC proton-proton collision data*, (2016), URL: https://cds.cern.ch/record/2157687.

[67] ATLAS Collaboration, *Measurement of the photon identification efficiencies with the ATLAS detector using LHC Run-1 data*, Eur. Phys. J. **C76** (2016) 666, arXiv: 1606.01813 [hep-ex].

[68] ATLAS Collaboration, *Photon identification in 2015 ATLAS data*, tech. rep. ATL-PHYS-PUB-2016-014, CERN, 2016, URL: http://cds.cern.ch/record/2203125.

[69] W Lampl et al., *Calorimeter Clustering Algorithms: Description and Performance*, tech. rep. ATL-LARG-PUB-2008-002. ATL-COM-LARG-2008-003, CERN, 2008, URL: https://cds.cern.ch/record/1099735.

[70] Matteo Cacciari, Gavin P. Salam, and Gregory Soyez, *The Anti-k(t) jet clustering algorithm*, JHEP **04** (2008) 063, arXiv: 0802.1189 [hep-ph].

[71] P. Dervan et. al., *The Birmingham Irradiation Facility*, Nuclear Instruments and Methods in Physics Research Section A: Accelerators, Spectrometers, Detectors and Associated Equipment **730** (2013) 101, ISSN: 0168-9002, URL: http://www.sciencedirect.com/science/article/pii/S0168900213007675.

[72] ATLAS Collaboration, *ATLAS Phase-II Upgrade Scoping Document*, tech. rep. CERN-LHCC-2015-020. LHCC-G-166, CERN, 2015, URL: https://cds.cern.ch/record/2055248.

[73] LHC-Commissioning, *Nominal HL-LHC luminosity*, https://lhc-commissioning.web.cern.ch/lhc-commissioning/schedule/images/Nom-to-2037.png, Accessed: 2018-09-11, 2018.

[74] B T Huffman, *Plans for the Phase II upgrade to the ATLAS detector*, JINST **9** (2014) C02033, URL: http://stacks.iop.org/1748-0221/9/i=02/a=C02033.

[75] ATLAS Collaboration, *Letter of Intent for the Phase-II Upgrade of the ATLAS Experiment*, tech. rep. CERN-LHCC-2012-022. LHCC-I-023, CERN, 2012, URL: https://cds.cern.ch/record/1502664.

[76] Claude Leroy and Pier-Giorgio Rancoita,
Silicon solid state devices and radiation detection, World Scientific, 2012,
URL: https://cds.cern.ch/record/1492099.

[77] C. J. S. Damerell,
"Vertex detectors: The state of the art and future prospects",
The top quark and the electroweak interaction. Proceedings, 23rd Summer Institute on Particle Physics, Stanford, USA, July 10-21, 1995, URL: http://www.slac.stanford.edu/pubs/confproc/ssi95/ssi95-005.html.

[78] H. Fanchiotti, C. A. Garcia Canal, and M. Marucho,
The Landau distribution, Int. J. Mod. Phys. **C17** (2006) 1461,
arXiv: hep-ph/0305310 [hep-ph].

[79] Michael Moll, "Radiation damage in silicon particle detectors: microscopic defects and macroscopic properties", Presented on 30 Nov 1999,
PhD thesis: Hamburg Univ., URL: https://cds.cern.ch/record/425274.

[80] Y. Unno et al.,
Development of n-on-p silicon sensors for very high radiation environments,
Nuclear Inst. and Methods in Physics Research, A **636** (2011) S24.

[81] ATLAS SCT Collaboration,
Supply of Silicon Microstrip Sensors of ATLAS07 specification,
(2007), Version 4.6.

[82] Y. Unno et al., *Development of n^+-in-p large-area silicon microstrip sensors for very high radiation environments – ATLAS12 design and initial results*,
Nuclear Instruments and Methods in Physics Research Section A **765** (2014) 80, ISSN: 0168-9002, URL: http://www.sciencedirect.com/science/article/pii/S0168900214008407.

[83] ALiBaVa system, http://www.alibavasystems.com/,
Accessed: Thursday 8th November, 2018.

[84] P. Dervan et. al., *Scanning facility to irradiate mechanical structures for the LHC upgrade programme*, Proceedings of Science **419** (2014),
URL: https://cds.cern.ch/record/1999159.

[85] S. Wonsak, "Signal and Charge Collection Efficiency of n-in-p strip detectors after proton and neutron irradiation to HL-LHC fluences",
Presented at the 25^{th} RD50 workshop, CERN, 2014.

[86] P. Allport et. al., *Recent results and experience with the Birmingham MC40 irradiation facility*, Journal of Instrumentation **12** (2017) C03075,
URL: http://stacks.iop.org/1748-0221/12/i=03/a=C03075.

[87] ATLAS Collaboration, *Luminosity determination in pp collisions at $\sqrt{s} = 8$ TeV using the ATLAS detector at the LHC*, Eur. Phys. J. **C76** (2016) 653,
arXiv: 1608.03953 [hep-ex].

[88] T. Golling et al., *The ATLAS Data Quality Defect Database System*,
Eur. Phys. J. **C72** (2012) 1960, arXiv: 1110.6119 [physics.ins-det].

[89] J. Catmore et. al.,
A New Petabyte-scale Data Derivation Framework for ATLAS,
tech. rep. ATL-SOFT-PROC-2015-041. 7, CERN, 2015,
URL: https://cds.cern.ch/record/2016628.

[90] Paolo Nason, *A new method for combining NLO QCD with shower Monte Carlo algorithms*, JHEP **11** (2004) 040, arXiv: hep-ph/0409146.

[91] Stefano Frixione, Paolo Nason, and Carlo Oleari, *Matching NLO QCD computations with parton shower simulations: the POWHEG method*, JHEP **11** (2007) 070, arXiv: 0709.2092 [hep-ph].

[92] Simone Alioli et al., *A general framework for implementing NLO calculations in shower Monte Carlo programs: the POWHEG BOX*, JHEP **06** (2010) 043, arXiv: 1002.2581 [hep-ph].

[93] Simone Alioli et al., *NLO Higgs boson production via gluon fusion matched with shower in POWHEG*, JHEP **04** (2009) 002, arXiv: 0812.0578 [hep-ph].

[94] Paolo Nason and Carlo Oleari, *NLO Higgs boson production via vector-boson fusion matched with shower in POWHEG*, JHEP **02** (2010) 037, arXiv: 0911.5299 [hep-ph].

[95] Hung-Liang Lai et al., *New parton distributions for collider physics*, Phys. Rev. **D 82** (2010) 074024, arXiv: 1007.2241 [hep-ph].

[96] Torbjörn Sjöstrand, Stephen Mrenna, and Peter Skands, *A brief introduction to PYTHIA 8.1*, Comput. Phys. Commun. **178** (2008) 852, arXiv: 0710.3820 [hep-ph].

[97] Torbjörn Sjöstrand, Stephen Mrenna, and Peter Skands, *PYTHIA 6.4 physics and manual*, JHEP **05** (2006) 026, arXiv: hep-ph/0603175.

[98] ATLAS Collaboration, *Measurement of the Z/γ^* boson transverse momentum distribution in pp collisions at $\sqrt{s} = 7$ TeV with the ATLAS detector*, JHEP **1409** (2014) 145, arXiv: 1406.3660 [hep-ex].

[99] Richard D. Ball et al., *Parton distributions with LHC data*, Nucl. Phys. **B867** (2013) 244, arXiv: 1207.1303 [hep-ph].

[100] ATLAS Collaboration, ATLAS Run 1 Pythia8 tunes, tech. rep. ATL-PHYS-PUB-2014-021, CERN, 2014, URL: https://cds.cern.ch/record/1966419.

[101] J. Pumplin et al., *New generation of parton distributions with uncertainties from global QCD analysis*, JHEP **07** (2002) 012, arXiv: hep-ph/0201195.

[102] Charalampos Anastasiou et al., *Higgs boson gluon-fusion production in QCD at three loops*, Phys. Rev. Lett. **114** (2015) 212001, arXiv: 1503.06056 [hep-ph].

[103] Charalampos Anastasiou et al., *High precision determination of the gluon fusion Higgs boson cross-section at the LHC*, JHEP **05** (2016) 058, arXiv: 1602.00695 [hep-ph].

[104] Stefano Actis et al., *NLO electroweak corrections to Higgs boson production at hadron colliders*, Phys. Lett. **B670** (2008) 12, arXiv: 0809.1301 [hep-ph].

[105] Charalampos Anastasiou, Radja Boughezal, and Frank Petriello, *Mixed QCD-electroweak corrections to Higgs boson production in gluon fusion*, JHEP **04** (2009) 003, arXiv: 0811.3458 [hep-ph].

[106] M. Ciccolini, A. Denner, and S. Dittmaier, *Strong and electroweak corrections to the production of a Higgs boson + 2 jets via weak interactions at the Large Hadron Collider*, Phys. Rev. Lett. **99** (2007) 161803, arXiv: 0707.0381 [hep-ph].

[107] Mariano Ciccolini, Ansgar Denner, and Stefan Dittmaier, *Electroweak and QCD corrections to Higgs production via vector-boson fusion at the LHC*, Phys. Rev. **D 77** (2008) 013002, arXiv: 0710.4749 [hep-ph].

[108] Paolo Bolzoni et al., *Higgs boson production via vector-boson fusion at next-to-next-to-leading order in QCD*, Phys. Rev. Lett. **105** (2010) 011801, arXiv: 1003.4451 [hep-ph].

[109] Oliver Brein, Abdelhak Djouadi, and Robert Harlander, *NNLO QCD corrections to the Higgs-strahlung processes at hadron colliders*, Phys. Lett. **B579** (2004) 149, arXiv: hep-ph/0307206 [hep-ph].

[110] Ansgar Denner et al., *Electroweak corrections to Higgs-strahlung off W/Z bosons at the Tevatron and the LHC with HAWK*, JHEP **03** (2012) 075, arXiv: 1112.5142 [hep-ph].

[111] Lukas Altenkamp et al., *Gluon-induced Higgs-strahlung at next-to-leading order QCD*, JHEP **02** (2013) 078, arXiv: 1211.5015 [hep-ph].

[112] Piotr Golonka and Zbigniew Was, *PHOTOS Monte Carlo: A Precision tool for QED corrections in Z and W decays*, Eur. Phys. J. **C45** (2006) 97, arXiv: hep-ph/0506026 [hep-ph].

[113] R. Kutschke, *An Angular Distribution Cookbook*, home.fnal.gov/~kutschke/Angdist/angdist.ps, Accessed: 2018-08-22, 1996.

[114] C. Patrignani et al., *Review of particle physics*, Chin. Phys. **C40** (2016) 100001.

[115] M. Corradi, *Performance of ATLAS RPC Level-1 muon trigger during the 2015 data taking*, Journal of Instrumentation **11** (2016) C09003, URL: http://stacks.iop.org/1748-0221/11/i=09/a=C09003.

[116] ATLAS Collaboration,
Measurement of the muon reconstruction performance of the ATLAS detector using 2011 and 2012 LHC proton-proton collision data,
Eur. Phys. J. **C74** (2014) 3130, arXiv: 1407.3935 [hep-ex].

[117] Alexander L. Read, *Presentation of search results: the CL_s technique*,
J. Phys. **G 28** (2002) 2693.

[118] J. Neyman and E. S. Pearson,
On the Problem of the Most Efficient Tests of Statistical Hypotheses,
Philosophical Transactions of the Royal Society of London. Series A, Containing Papers of a Mathematical or Physical Character **231** (1933) 289,
ISSN: 02643952, URL: http://www.jstor.org/stable/91247.

[119] Glen Cowan et al.,
Asymptotic formulae for likelihood-based tests of new physics,
Eur. Phys. J. **C71** (2011) 1554, [Erratum: Eur. Phys. J. **C73** (2013) 2501],
arXiv: 1007.1727 [physics.data-an].

[120] Max Baak et al., *Interpolation between multi-dimensional histograms using a new non-linear moment morphing method*, (2014),
arXiv: 1410.7388 [physics.data-an].

[121] ATLAS Collaboration,
Measurement of the differential cross-sections of inclusive, prompt and non-prompt J/ψ production in proton-proton collisions at $\sqrt{s} = 7$ TeV,
Nucl. Phys. **B850** (2011) 387, arXiv: 1104.3038 [hep-ex].

[122] M.P. Wand and M.C. Jones, *Kernel Smoothing*,
Chapman & Hall/CRC Monographs on Statistics & Applied Probability,
CRC Press, 1994, ISBN: 9781482216127,
URL: https://books.google.co.uk/books?id=lUFZDwAAQBAJ.

[123] J. S. Conway,
Incorporating Nuisance Parameters in Likelihoods for Multisource Spectra,
(2011) 115, arXiv: 1103.0354 [physics.data-an].

[124] Bernard Flury, "The Multivariate Normal Distribution",
A First Course in Multivariate Statistics, Springer New York, 1997 171,
ISBN: 978-1-4757-2765-4,
URL: https://doi.org/10.1007/978-1-4757-2765-4_3.

[125] LHC Higgs Cross Section Working Group et al.,
Handbook of LHC Higgs Cross Sections: 3. Higgs Properties,
CERN-2013-004 (CERN, Geneva, 2013), arXiv: 1307.1347 [hep-ph].

[126] ATLAS Collaboration, *Measurement of $W^{\pm}$ and Z-boson production cross sections in pp collisions at $\sqrt{s} = 13$ TeV with the ATLAS detector*,
Phys. Lett. **B759** (2016) 601, arXiv: 1603.09222 [hep-ex].

[127] Jon Butterworth et al., *PDF4LHC recommendations for LHC Run II*,
J. Phys. **G43** (2016) 023001, arXiv: 1510.03865 [hep-ph].

[128] T. Gleisberg et al., *Event generation with SHERPA 1.1*, JHEP **02** (2009) 007, arXiv: 0811.4622 [hep-ph].

[129] J. Alwall et al., *The automated computation of tree-level and next-to-leading order differential cross sections, and their matching to parton shower simulations*, JHEP **07** (2014) 079, arXiv: 1405.0301 [hep-ph].

[130] ATLAS Collaboration, *Performance of the electron and photon trigger in p-p collisions at $\sqrt{s} = 7$ TeV with the ATLAS detector at the LHC*, ATLAS-CONF-2011-114 (2011), URL: http://cds.cern.ch/record/1375551.

[131] ATLAS Collaboration, *Electron and photon energy calibration with the ATLAS detector using LHC Run 1 data*, Eur. Phys. J. C **74** (2014) 3071, arXiv: 1407.5063 [hep-ex].

[132] ATLAS Collaboration, Electron and photon energy calibration with the ATLAS detector using data collected in 2015 at $\sqrt{s} = 13$ TeV, ATL-PHYS-PUB-2016-015, CERN, 2016, URL: https://cds.cern.ch/record/2203514.

[133] Ting-Chung Huang and Frank Petriello, *Rare exclusive decays of the Z boson revisited*, Phys. Rev. D **92** (1 2015) 014007, URL: https://link.aps.org/doi/10.1103/PhysRevD.92.014007.

[134] Yuval Grossman, Matthias König, and Matthias Neubert, *Exclusive radiative decays of W and Z bosons in QCD factorization*, Journal of High Energy Physics **2015** (2015) 101, ISSN: 1029-8479, URL: https://doi.org/10.1007/JHEP04(2015)101.

[135] ATLAS Collaboration, *Luminosity Determination in pp Collisions at $\sqrt{s} = 7$ TeV Using the ATLAS Detector at the LHC*, Eur. Phys. J. **C71** (2011) 1630, arXiv: 1101.2185 [hep-ex].

[136] K.A. Olive and Particle Data Group, *Review of Particle Physics*, Chinese Physics C **38** (2014) 090001, URL: http://stacks.iop.org/1674-1137/38/i=9/a=090001.

[137] BaBar Collaboration, *Measurement of the $D^*(2010)^+$ natural line width and the $D^*(2010)^+ - D^0$ mass difference*, Phys. Rev. **D88** (2013) 052003, [Erratum: Phys. Rev.D88,no.7,079902(2013)], arXiv: 1304.5009 [hep-ex].

[138] *Search for the Standard Model Higgs and Z Boson decays to $J/\psi\,\gamma$: HL-LHC projections*, tech. rep. ATL-PHYS-PUB-2015-043, CERN, 2015, URL: http://cds.cern.ch/record/2054550.